SOLAR ACTIVITY AND MIDDLE ATMOSPHERIC DYNAMICS

by

EDUARDO P. OLAGUER

S.M., Massachusetts Institute of Technology
(1982)

Submitted to the Department of Earth, Atmospheric and Planetary Sciences in Partial Fulfillment of the Requirements for the Degree of

DOCTOR OF PHILOSOPHY

in

METEOROLOGY

at the

MASSACHUSETTS INSTITUTE OF TECHNOLOGY

October 1986

Signature of Author _____
Center for Meteorology and Physical Oceanography
Department of Earth, Atmospheric and Planetary Sciences
October 23, 1986

Certified by _____
Ronald G. Prinn
Thesis Supervisor

Accepted by _____
Chairman, Departmental Committee on Graduate Students

SOLAR ACTIVITY AND MIDDLE ATMOSPHERIC DYNAMICS

by

EDUARDO P. OLAGUER

Submitted to the Department of Earth, Atmospheric,

and Planetary Sciences on October 23, 1986

in partial fulfillment of the requirements for

the degree of Doctor of Philosophy in Meteorology

ABSTRACT

An efficient three-dimensional spectral radiative-dynamical-chemical model was developed for the purpose of simulating the response of the middle atmosphere to a solar flare-generated high-latitude ozone deficit. In addition to solving the global balance equations, the model includes detailed on-line ozone photochemistry and transport, a band model and Curtis matrix calculation of infrared cooling, and a Rayleigh friction and vertical eddy diffusion parameterization of breaking gravity wave turbulence. When compared with the observations reported by Wu, et al (1984), the model successfully reproduces the observed zonally-averaged climatological circulation of the middle atmosphere, but underpredicts the strength of the eddy circulation by a factor of two.

The result of a solar proton-induced odd nitrogen injection into the model upper stratosphere comparable to the massive event which occurred on August 4, 1972 was a decrease in the photochemical acceleration rate near the polar stratopause, followed consequently by the growth of planetary waves in the high-latitude mesosphere. Accompanying the changes in the eddy circulation was a 10% enhancement of the mesospheric zonal wind speed at mid-latitudes. The zonal wind acceleration was brought about by a thermally-direct mean meridional circulation induced by the diabatic heating changes resulting from the high-latitude ozone deficit. No significant response was obtained at levels below the upper stratosphere, thus disproving any short-term connection between solar activity-related ozone variability and the tropospheric circulation.

Thesis Supervisor: Dr. Ronald G. Prinn

Title: Professor of Meteorology

Οιδαμεν δε οτι τοις αγαπωσιν τον θεον παντα συνεργει
εις αγαθον, τοις καταπροθεσιν κλητοις ουσιν.

αλλ' εν τουτοις πασιν υπερνικωμεν δια του αγαπησαντος
υμας. πεπεισμαι γαρ οτι ουτε θανατος ουτε ζωη ουτε
αγγελοι ουτε αρχαι ουτε ενεστοτα ουτε μελλοντα ουτε
δυναμεις ουτε υψωμα ουτε βαθος ουτε τις κτισις ετερα
δυνησεται ημας χωρισαι απο της αγαπης του θεου της
εν Χριστου Ιησου τω κυριω ημων.

-Προς Ρωμαιους

Acknowledgements

I would like to thank my advisor, Prof. Ronald Prinn for his patience and for his valuable assistance, without which this thesis could not have been possible.

I would also like to thank Drs. Cunnold and Alyea, and Carlos Cardelino for their helpful suggestions regarding a number of technical details pertaining to the model.

Lastly, I would like to thank all my friends whose moral support has enabled me to persevere despite innumerable obstacles.

-Ad majorem Dei gloriam

TABLE OF CONTENTS

LIST OF TABLES

LIST OF FIGURES

I. INTRODUCTION

1.1 Statement of the Problem

The dynamics of the middle atmosphere has received increased attention in the past decade, largely out of concern for the ozone layer in the earth's stratosphere. A major goal of middle atmospheric research has been to identify the processes by which natural and anthropogenic changes in ozone occur, and to understand the consequences that ozone variability may have for tropospheric weather and climate. For some time now there has been much speculation over the possibility that solar activity leads to observable changes in stratospheric ozone, and that these changes in turn lead to noticeable signals in the troposphere (see for instance Willet, 1962; Heath, et al, 1977; Reiter, 1979; Callis, et al, 1985). Much of the recent research into this particular problem has been fueled by a hypothesis first stated by Hines (1974), who proposed that solar disturbances modulate planetary wave activity in the earth's middle atmosphere, thereby influencing meteorological processes below. The energetics of this is such that a "trigger" mechanism is excited which results in the redistribution of energy already present in the atmosphere itself. This feature of Hines' hypothesis negates the standard criticism of most solar-terrestrial mechanisms which claims that the minute energy associated with solar disturbances at the highest levels of the atmosphere cannot directly force the circulation at lower levels (see Willis, 1976).

The thermal and dynamical balance of the middle atmosphere depends significantly on the distribution of ozone, which is sensitive to the solar output. The principal goal of this thesis is to examine whether or not changes in ozone induced by solar activity are sufficient to cause observable changes in the amplitudes and phases of planetary waves, primarily in the stratosphere and

mesosphere, and secondarily in the troposphere. We shall investigate this problem using a numerical model designed to take into account all the major feedbacks in a sufficiently detailed way. Our model is unique in that no other current middle atmospheric three-dimensional model combines a dynamical prediction with: an explicit solar and infrared radiative transfer and heating computation, extensive on-line ozone photochemistry, and on-line ozone transport. The value of this thesis lies therefore in its being the first fairly complete three-dimensional numerical simulation of the effects of a solar-induced ozone perturbation on the dynamics of the middle atmosphere.

1.2 Solar-Terrestrial Correlations in the Lower and Middle Atmosphere

A vast number of correlations between solar activity and meteorological phenomena have been reported in the literature. These correlations cover time scales ranging from a day (usually associated with irregular events such as solar flares and geomagnetic storms), to 11 years, which is the period of the well-known sunspot cycle. There are also correlations associated with the 27-day rotation of the sun and the associated interplanetary magnetic field. A detailed review of the more plausible correlations and postulated mechanisms put forward in the last decade is provided by Pittock (1983). In this thesis, we shall concentrate exclusively on short-term connections between solar variability and the lower and middle atmosphere- in particular, correlations with time scales of the order of 27 days or less.

The study of Wilcox, et al (1974), which purported to show a connection between tropospheric cyclonic activity and the sector structure of the interplanetary magnetic field has not only generated considerable controversy, but has also been responsible for an upsurge of interest in sun-weather connections. In that study, Wilcox, et al analyzed Northern Hemisphere data from the winters of 1963-1973 and reported that cyclonic activity at 300 mb as measured by the vorticity area index (VAI: defined as the area in square kilometers over which the absolute vorticity exceeds 2×10^{-4} s^{-1}) decreases significantly one day after the passage of a solar magnetic sector boundary (MSB). The effect is supposedly stronger during sunspot activity. An independent skeptical analysis of the data by Hines and Halevy (1977) appeared to confirm the statistical significance of the VAI phenomenon; however, an extension of the analysis to the winters of 1974-1977 by Williams and Gerety (1978) failed to reproduce the effect reported by Wilcox, et al (1974). Williams (1978) and Williams and Gerety (1980) examined the energetics of the

atmosphere in connection with sector boundary transits and found correlations of marginal significance between MSB passage and the kinetic energy of planetary wavenumber 5. They concluded that the simplest interpretation of their results was that they were a statistical fluctuation.

Padgaonkar and Arora (1981) conducted their own superposed epoch analysis using vorticity data from 1947-1957 and 1963-1974 and concluded that the atmosphere at 500 mb did not respond in the manner observed by Wilcox, et al (1974). They also studied VAI as a function of geomagnetic disturbances and found a minimum either on the same day or one day after a large geomagnetic storm. Shah (1980) looked at the behavior of VAI during solar proton events and also found a dip in cyclonic vorticity one day after the key date. However, he reported that the effect was evident only during the summer and was observed from 1954-1969, but was not evident from 1970-1972.

King, et al (1977) examined correlations between 500 mb geopotential height waves and the 27-day solar rotation. The morphology of their solar-induced perturbations suggested that planetary wavenumbers 1 and 2 are modulated by solar activity. Schafer (1979), however, claimed that the correlation was not statistically significant, arguing that the persistence of planetary disturbances with quasi-periods near 27 days will occasionally produce coincidentally high correlations with the solar rotation.

Zerefos (1974) studied circulation changes in the atmosphere associated with energetic solar proton events and found 24-hour height decreases in the lower stratosphere and upper troposphere of the order of 20 geopotential meters (gpm) at high latitudes. Schuurmans (1979) reported similar height changes one day after a solar flare, but noted a later effect following after 2-4 days.

Nastrom and Belmont (1978) and Venne, et al (1982) correlated stratospheric wind variations with the 10.7 cm solar radio flux ($F_{10.7}$) and found only marginally significant correlations at periods of 27.1 and 13.6 days- i.e., the

first and second harmonics of the solar rotation period. Venne, et al (1982) concluded that the results, derived from rocketsonde data from the years 1960-1976, were near or below the level of detection. Ebel, et al (1981) and Ebel and Schwister (1983), on the other hand, found correlations between lower stratospheric waves and $F_{10.7}$ at periods of 25, 15.1, and 13.6 days. The height perturbations associated with these waves were of the order of 10 gpm at high latitudes. Ebel, et al explained the occurence of a 25-day wave as the result of the modulation of a 27-day wave by the well-known annual quasi-stationary wave in the lower stratosphere. The 15-day wave, on the other hand, showed evidence of being a westward-traveling external wave, which Ebel, et al (1981) related to the well-known traveling 15-day wave in the lower and middle atmosphere.

It is apparent from the various observational studies quoted here that the evidence for solar-induced meteorological signals in the lower stratosphere and upper troposphere, while suggestive, is controversial and often contradictory. Its primary value with regard to our own study is to furnish typical characteristics of planetary wave changes putatively asssociated with solar activity which may be compared to our modelling results. Thus the significance of this thesis can be measured in terms of whether it can clearly demonstrate the feasibility or infeasibility of the Hines mechanism (see Section 1.1) in producing planetary wave amplitude changes of the order of 10-20 gpm in the lower stratosphere and upper troposphere.

1.3 Solar Variability Effects on Ozone

There are a number of potential mechanisms by which solar disturbances may induce short term changes in stratospheric ozone. Ruderman and Chamberlain (1975) and Chamberlain (1977) have hypothesized that modulation of galactic cosmic rays (GCR) by solar activity leads to a modulation of odd nitrogen compounds (NO_x) in the stratosphere. Since NO_x acts as a catalyst in the destruction of ozone, any change in the concentration of stratospheric NO_x could affect the radiative balance of the middle atmosphere. Suda and Wada (1978) performed a superposed epoch analysis of GCR intensity with MSB passage as the key date. They found short term variations in GCR flux of the order of one per cent. Since GCR radiation is important primarily in the lower stratosphere where catalytic removal of ozone is least effective, it is doubtful that such minor variations in GCR flux can produce detectable changes in ozone. In contrast to the more energetic galactic cosmic rays, solar protons yield peak NO_x production at altitudes above 25 km, where catalytic destruction of ozone is far more efficient than at lower levels. Yet another mechanism involving energetic particles was proposed by Thorne (1977,1980), who noted that precipitation of outer zone electrons during geomagnetically disturbed periods can enhance the ionization rate throughout the mesosphere by several orders of magnitude over quiet time values. Although the relativistic primary electrons generated during such events do not penetrate below 50 km, they produce large fluxes of bremsstrahlung X-rays which penetrate deep into the stratosphere before ionizing and exciting neutral gas molecules, leading in turn to increased concentrations of NO_x. Finally, it has been observed by Heath (1975) that the solar output of ultraviolet (UV) radiation varies with solar activity. Heath showed that the full-disk solar UV intensity tends to maximize at a time when a solar magnetic sector boundary is near central meridian on the sun. The

magnitude of this variation is of the order of one per cent. Changes in solar UV intensity influence ozone concentrations through photodissociation and UV heating.

Whether or not stratospheric ozone exhibits variations in response to solar activity is still a matter of dispute. The solar proton event (SPE) of August 4, 1972, in which a zonally averaged decrease of 20% in the ozone column above 4 mb was observed at altitudes above 75N (Heath, et al, 1977), is perhaps the most obvious and dramatic instance of such an effect. The changes associated with this event were long-lived and persisted for approximately one month. This, however, is highly unusual in that most SPE's do not result in significant ozone changes beyond a few hours (McPeters and Jackman, 1985). Other connections between solar activity and atmospheric ozone are indicated in studies by Reiter and Litfass (1977) and Reiter (1979), who observed that stratospheric air intrusions at Zugspitze, West Germany are 40% more frequent after solar flares and MSB crossings. In conjunction with this, Reiter (1979) found a significant maximum in atmospheric total ozone (TOZ) on the day before a solar flare when the active region approached central meridian on the sun, a phenomenon which he attributed to Forbush decreases in GCR intensity reaching the lower stratosphere. Heath and Prasad (1976) studied BUV measurements and found that high latitude ozone was enhanced 4 days prior to sector boundary crossings and that the Northern Hemispheric average of TOZ appeared to be slightly depressed after MSB passage. However, an attempt by Weinbeck and Yarger (1978) to deduce a relationship between atmospheric ozone profiles and MSB crossings using 18 years of Umkehr data from Arosa, Switzerland proved negative. Weinbeck and Yarger (1978) also examined more than 100 energetic solar flares but found no significant ozone trends associated with these events. Rao and Nair (1980) tested the behavior of TOZ with the day of central meridian passage of the solar MSB as the key date, but did not find any evidence

to suggest that solar UV variability had any effect on ozone. Chandra and Maeda (1980) searched for a correlation between geomagnetic activity and TOZ as measured by the Nimbus 4 BUV experiment. They found an apparent correlation at high latitudes in winter, but suggested that this was due to planetary waves which by coincidence have periods comparable to magnetic activity. Chandra (1985) analyzed the Nimbus 4 data for 1970-1972 and found tropical temperature and ozone to be correlated with $F_{10.7}$. However, these oscillations were not regional phenomena but manifestations of high latitude oscillations that were 180° out of phase, suggesting that the oscillations were not excited directly by solar UV variations, but rather were planetary-wave induced. Meanwhile, several other authors have put forward observational evidence for a solar rotation-atmospheric ozone connection (see Gille, et al, 1984; Keating, et al, 1985; Heath and Schlesinger, 1985; Hood, 1986; Eckman, 1986a,b). Substantial disagreement still remains over the interpretation of these results, particularly concerning the phase of the observed ozone response. We conclude by noting that, as was true for the circulation-solar activity connections discussed in the previous section, the case for short-term modulation of atmospheric ozone by solar activity is at best controversial, being well-established only for major solar disturbances such as the SPE of August, 1972.

1.4 Dynamical Models of Solar-Terrestrial Coupling

Planetary wave coupling between the troposphere and the middle atmosphere is by now a well-understood phenomenon. Theoretical studies by several authors have shown that the transmissivity of upward propagating planetary disturbances is determined largely by the mean zonal wind, the background static stability, and the mechanical and thermal dissipation rates (see for instance Charney and Drazin, 1961; Dickinson, 1969; Matsuno, 1970; Schoeberl and Geller, 1977; Schmitz and Grieger, 1980). Hines' (1974) hypothesis hinges on whether solar disturbances can alter these quantities sufficiently so as to change the structure of planetary waves in the middle atmosphere, thereby changing the nature of the wave pattern below, as the waves tend to be reflected by the background winds at certain levels. That the troposphere is indeed sensitive to stratospheric changes in zonal wind and static stability was shown by Bates (1977), who used an analytical quasi-geostrophic model of steady-state stationary waves. Bates showed that the meridional heat flux of planetary waves in the troposphere, as well as their amplitudes and phases, is influenced by the wind and temperature structure at higher levels. In another paper Bates (1980) also demostrated the sensitivity of planetary wave structure to the thermal dissipation rate in the stratosphere. Geller and Alpert (1980) used a numerical steady-state quasi-geostrophic model wherein the zonal wind was arbitrarily decreased by 20% at various levels. They found that wind changes at or below the 35 km level give rise to changes in the tropospheric wave pattern at middle and high latitudes comparable with observed interannual differences. They also found that the alterations in wave structure do not propagate downwards to more than 3 scale heights beneath the level where the zonal wind is perturbed.

The above studies do not demonstrate that solar disturbances are capable of producing effects in the troposphere since the changes made in the background

state of the atmosphere were prescribed rather than induced through an explicit mechanism. To date, only two models have incorporated realistic short-term solar-induced ozone perturbations; both of these models were intended to mimic the effects of a solar flare of the same magnitude as the August 1972 SPE. The first of these was a zonally-averaged quasi-geostrophic model employed by Schoeberl and Strobel (1978), who found a negligible response to their prescribed ozone density reductions of about 22% at the polar stratopause. The second was an 18-level hemispheric general circulation model with annual mean insolation, used in a numerical experiment by Hunt (1981). In this experiment, ozone deficits of 6% of the total amount were inserted at high latitudes, resulting in an enhancement of the zonal wind speed near the tropopause some 20-24 days after the initial perturbation. Accompanying the zonal wind changes was a 14% increase in the eddy kinetic energy in the upper troposphere. The problem with Hunt's model, however, is that the bulk of the prescribed ozone reduction occurred unrealistically at the top of the model at 37.5 km, so that it is probable that the effects of the perturbation were strongly distorted by the reflecting rigid lid at the upper boundary. Moreover, neither Hunt's model nor that of Schoeberl and Strobel (1978) incorporated any photochemical feedback, thus limiting their applicability to the real atmosphere.

I propose here to reexamine the effects of a major solar flare using a numerical model whch not only incorporates all of the major feedbacks not taken into account in previous modelling studies, but does so at relatively low cost owing to its computational efficiency. Because of the nature of the problem and the time and budget constraints involved, I decided to base the model in part on a pre-existent one available to me from previous research done at MIT. I stress, however, that my model is a significant improvement on this base model. As mentioned previously, no three-dimensional model other than the one presented in this thesis combines detailed simulation of all major aspects of the

radiation, chemistry and dynamics of the middle atmosphere pertaining to extra-tropical latitudes suitable for studying sun-ozone-circulation connections.

II. THE NUMERICAL MODEL

2.1 The Governing Equations

The model we have chosen for our numerical experiments is a highly improved derivative of a global stratospheric model originally developed at MIT by Drs. Cunnold, Alyea, Phillips, and Prinn (henceforth referred to as CAPP). Designed so as to incorporate the effects of radiative transfer, photochemical processes, and fluid motions on the large scale circulation of the middle atmosphere, the CAPP model went through three versions which differed slightly in detail. The first of these, known as RUN12, is described in Cunnold, et al (1975), while the results of the second, known as RUN17, can be found in Cunnold, et al (1980). Aspects of the third, known as RUN34, are presented in Golombek and Prinn (1986). The primary objective of the CAPP model was to simulate the climatological behavior of ozone in the lower stratosphere, rather than any short-term fluctuations such as those which concern us in this study. This being the case, we found it necessary to make substantial changes in order to ensure adequate performance, particularly in the upper stratosphere and mesosphere, where solar activity effects are likely to be more pronounced than at lower altitudes. What motivated these changes were a number of defects in the original model which included:

1) a radiative heating scheme that underestimated the strength of the diabatic forcing above 40 km; and

2) the lack of an adequate damping mechanism at mesospheric levels.

In this chapter, we discuss the details of the model used in our solar-terrestrial experiment.

The basic variables and symbols employed in our discussion are defined as follows:

t = time

λ = longitude [measured positive eastward from Greenwich]

θ = latitude

$\mu = \sin \theta$

P = pressure in atmospheres

$Z = -\ln P$

∇ = spherical gradient operator at constant Z

$\underline{k}$ = vertical unit vector

ψ = horizontal velocity stream function

$\partial X/\partial P$ = horizontal velocity potential

$\zeta = \nabla^2\psi$

$W = dZ/dt$

T_0 = standard horizontally averaged temperature [$\equiv T_0(Z)$]

T = temperature

z = geopotential height

n_{O_3} = ozone number density

n_m = neutral atmospheric number density

$\chi O_3 = n_{O_3}/n_m$ [i.e., the ozone number mixing ratio]

Ω = angular velocity of the earth

g = acceleration due to gravity

$f = 2\Omega\mu$ [i.e., the Coriolis parameter]

H_0 = atmospheric scale height

R = ideal gas constant

c_p = specific heat at constant pressure

$\kappa = R/c_p$

$\sigma = dT_0/dZ + \kappa$ [i.e., the stability parameter]

K_d = vertical austausch coefficient

$\underline{S}$ = frictional stress

K_H= horizontal fourth-order diffusion coefficient

q = diabatic heating rate per unit volume

ρ = neutral atmospheric mass density

$Q = q/\rho c_p$

G = photochemical source term

$\bar{(\ )}$ = horizontal average

$(\ )'$= deviation from horizontal average

The model employs the global balance approximation, and thus does not retain all the dynamical modes necessary to faithfully represent equatorial processes, particularly the Kelvin mode (Moura, 1976). While this may somewhat affect circulation patterns elsewhere, we nevertheless expect our model to give results which are, at the very least, qualitatively similar to processes in the real atmosphere, particularly at mid and high latitudes.

Diagnostic relations include the hydrostatic equation, the condition for quasi-geostrophic balance, and the continuity equation, which we write repectively as:

$$RT' = g\,\partial z'/\partial Z \tag{2-1}$$

$$g\,\nabla^2 z' = \nabla\cdot f\nabla\psi \tag{2-2}$$

$$PW = \nabla^2 X \tag{2-3}$$

Furthermore, the model predicts vorticity, temperature, and ozone mixing ratios as follows:

$$\partial\zeta/\partial t = -\underline{k} \times \nabla\psi\cdot\nabla(f+\zeta) - \nabla\cdot f\nabla\partial X/\partial P - \nabla\cdot\partial(P\underline{S})/\partial P + K_H\nabla^4\zeta \tag{2-4}$$

$$\partial T'/\partial t = -\underline{k} \times \nabla\psi\cdot\nabla T' - \sigma W + Q' + K_H\nabla^4 T' \tag{2-5}$$

$$\partial\chi_{O_3}'/\partial t = -\underline{k} \times \nabla\psi\cdot\nabla\chi_{O_3}' - W\partial\bar{\chi}_{O_3}/\partial Z + \partial[P(W\chi_{O_3}')']/\partial P - (1/H_0^2)\partial(K_d P\partial\chi_{O_3}'/\partial Z)/\partial P + G' \tag{2-6a}$$

$$\partial\bar{\chi}_{O_3}/\partial t = \partial[P(\overline{W\chi_{O_3}'})]/\partial P - (1/H_0^2)\partial(K_d P\partial\bar{\chi}_{O_3}/\partial Z)/\partial P + \bar{G} \tag{2-6b}$$

Note that we do not predict any deviation of $\bar{T}$ from its reference distribution,

given by $T_0(Z)$. Moreover, the model assumes a constant static stability, which is necessary in order to derive proper energy integrals, following Lorenz (1960).

Table 2.1 summarizes the essential differences between the CAPP model and our improved version. Among the changes we have made is the inclusion of the vertical flux convergence term in the prediction equation for the ozone deviation, so that with this addition eqs.(2-6a,b) can be combined together to form a single equation for χ_{O_3}:

$$\partial\chi_{O_3}/\partial t = -\underline{k} \times \nabla\psi\cdot\nabla\chi_{O_3} - \nabla\cdot\overline{\chi}_{O_3}\nabla\partial X/\partial P + \partial(PW\chi_{O_3})/\partial P - (1/H_0^2)\partial(K_d P\partial\chi_{O_3}/\partial Z)/\partial P + G \qquad (2\text{-}7)$$

The model atmosphere extends vertically from Z=0 at the surface to $Z=Z_{top}\simeq 10.14$ where a rigid lid is imposed, so that $W(Z=Z_{top})=0$. At the bottom, the flow is determined by the orography $z_0(\lambda,\mu)$. Thus the lower boundary condition may be expressed approximately as:

$$W(Z=0) = \underline{k} \times \nabla\psi\cdot\nabla z_0/H_0 \qquad (2\text{-}8)$$

For the ozone prediction equations, we use the boundary condition that the vertical diffusive flux at the bottom equals the surface destruction rate, which is assumed to be proportional to the concentration, i.e.

$$(K_d/H_0)\partial\chi_{O_3}/\partial Z = d\chi_{O_3} \qquad (2\text{-}9)$$

The constant d is assigned the value of .08 cm s^{-1} so as to be consistent with the results of Fabian and Junge (1970). At the top of the model, we assume that the vertical diffusive flux vanishes- an expedient mitigated by the fact that ozone in the presence of sunlight is in photochemical equilibrium at high levels.

2.2 Numerical Scheme and Energetics

The dynamics of the stratosphere is governed primarily by the propagation of planetary Rossby-type waves, unlike the troposphere where synoptic and convective scales are important. In the mesosphere, the situation is somewhat modified by the dissipation of gravity waves with length scales estimated by Fritts, et al (1984) from VHF echo observations to be of the order of a thousand kilometers. Nevertheless, because planetary waves do tend to dominate the energy spectrum above the troposphere, it is adequate for our purposes to adopt a numerical scheme which parameterizes rather than explicitly predicts the effects of scales of the order of the Rossby radius of deformation. Accordingly, the dynamical fields in our model are represented by truncated series of spherical harmonics, so that for instance:

$$\psi(\lambda,\mu,Z,t) = \sum_{m=-M}^{M} \sum_{n=m}^{N_m} \Psi_{mn}(Z,t)\Pi_n^m(\mu)\exp(im\lambda) \qquad (2\text{-}10)$$

where $\Pi_n^m(\mu)$ is the associated Legendre polynomial of order m and degree n, normalized so that $\int_{-1}^{1}[\Pi_n(\mu)]^2\, d\mu = 2$. Similar representations are used for χO_3, W,T', and z_0. The truncation used is the same as in the CAPP model, i.e. M=6 and N_m equal to 6,6,7,8,9,10,11 for $|m|$=0,1,2,3,4,5,6 respectively. The orographic spectral coefficients employed in our model, however, give a realistic Southern Hemisphere, as opposed to previous versions which assumed topographic symmetry about the equator.

The vertical representation of the various fields is achieved by dividing the atmosphere into 25 layers, each of thickness $\Delta Z = \ln 3/2$, corresponding to a height increment of ≈2.89 km. The grid is staggered so that the variables ψ and $\partial X/\partial P$ are evaluated at the middle of each layer, while W,T', and χ_{O_3} are evaluated at the interfaces. Table 2.2 shows the vertical coordinate, pressure, standard temperature, stability parameter, and approximate height at each level. It should be mentioned that our adopted values of the static stability

are identical to those of RUN12, which in turn differ from the values adopted in RUN17 and RUN34 in that they are ≈25% less in the lower troposphere.

The time-differencing scheme employed is a Lorenz "4-cycle", with four 1 hr time steps in each cycle. At every time step, W is evaluated by solving the vertical finite difference and horizontal spectral equivalent of the following continuous equation, obtained by elimination of $\partial\psi/\partial t$ and $\partial T'/\partial t$ from equations (2-1) to (2-5):

$$R\sigma\nabla^2 W + [(\nabla\cdot f\nabla)\nabla^{-2}]^2\partial[(1/P)\partial(PW)/\partial Z]/\partial Z = R\nabla^2 G_1 - [(\nabla\cdot f\nabla)\nabla^{-2}]\partial G_2/\partial Z \quad (2\text{-}11)$$

where $G_1 = -\underline{k} \times \nabla\psi\cdot\nabla T' + Q' + K_H\nabla^4 T'$

$G_2 = -\underline{k} \times \nabla\psi\cdot\nabla(f+\zeta) - \nabla\cdot\partial(P\underline{S})/\partial P + K_H\nabla^4\zeta$

The Jacobian advection terms in G_1 and G_2 are evaluated by the method of interaction coefficients, whereas the transform method is used for the transcendentally nonlinear diabatic heating term. The three-dimensional grid employed for the heating calculation has 16 points in longitude and 15 in latitude, the latter providing exact quadrature for quadratic products (see Table 2.3). Once the G_j's are known, W for the current time step can then be found by matrix methods and ψ and T' may then be predicted for the next time step from equations (2-4) and (2-5). (We postpone the discussion of the ozone prediction scheme until section 2.5.)

The energetics of the governing equations is described as follows. First let the kinetic energy per unit mass and the available potential energy per unit mass be defined by:

$$K = (1/2)\nabla\psi\cdot\nabla\psi$$

$$A = RT'^2/2\sigma$$

Denoting the integral of a quantity over the mass of the entire atmosphere by $\int(\ )dM$, we derive from equations (2-1) to (2-5) the relations:

$$\int\partial K/\partial t\ dM = \int RWT'\ dM + (p_0/g)\int\psi(\nabla\cdot f\nabla)\nabla^{-2}W\Big|_S\ dS$$

$$+ \int \psi \nabla \cdot \partial(P\underline{S})/\partial P \, dM + \int \psi K_H \nabla^4 \zeta \, dM \qquad (2\text{-}12)$$

$$\int \partial A/\partial t \, dM = -\int RWT' \, dM + \int (R/\sigma) Q'T' \, dM + \int (R/\sigma) T' K_H \nabla^4 T' \, dM \qquad (2\text{-}13)$$

where S is the horizontal surface at pressure $p_0 = 10^6$ dyn cm^{-2}. The term $\int RWT' \, dM$ represents the conversion between available potential and kinetic energy, while the second term on the right hand side of equation (2-12) is the energy change due to orography. The term $\int \psi \nabla \cdot \partial(P\underline{S})/\partial P \, dM$ on the other hand, is the rate of frictional dissipation, whereas the term $\int (R/\sigma) Q'T' \, dM$ represents the generation of available potential energy by the diabatic heating. The last terms of both energy equations are non-zero only if K_H is horizontally dependent.

2.3 Heating

The general circulation of the terrestrial atmosphere is highly dependent on the distribution of the diabatic heating. In the stratosphere and mesosphere, this heating consists primarily of the absorption of direct solar radiation by ozone molecules and the radiative cooling due to infrared emission by atmospheric molecules, mainly carbon dioxide and ozone. The CAPP model employed the Newtonian cooling approximation to parameterize the infrared contribution to the radiative forcing. However, Ramanathan and Grose (1978) and more recently, Fels, et al (1980) and Wehrbein and Leovy (1982) have shown that when more accurate radiative algorithms are employed, the large scale circulation is found to be much stronger than is suggested by simpler calculations. This is because Newtonian cooling, which models the thermal relaxation of the atmosphere as being proportional to the deviation from a specified equilibrium temperature, seriously underestimates the differential radiative forcing between the equator and the pole. In the case of the CAPP model, this equilibrium temperature is identical to the horizonally averaged temperature, so that the Newtonian cooling parameterization may predict anomalous heating in cold regions such as the polar night, where only cooling occurs. We have therefore found it necessary to resort to a more sophisticated treatment of radiation than that employed by the the CAPP model.

For convenience, we shall partition the diabatic heating rate in the following manner:

$$q = q_{UV} + q_{IR}$$

where q_{UV} is the diabatic heating due to absorption of visible and ultraviolet light, and q_{IR} is that due to infrared emission and absorption. q_{UV}, like in the original model, is calculated as a diurnal average from the empirical formula:

$$q_{UV} = (H/2.05\pi)[q^{\dagger}(\xi=\xi_1) + q^{\dagger}(\xi=\xi_2)] \qquad (2\text{-}14)$$

where ξ_1 and ξ_2 are the zenith angles at the solar hour angle corresponding to local noon H/4 and local midnight 3H/4, while $q^{\dagger}$ is given by:

$$q^{\dagger}(\xi) = n_{O_3}\int\alpha(\lambda')I(\lambda')\varepsilon(\lambda')\exp(-\alpha N\sec\xi)\, d\lambda' \qquad (2\text{-}15)$$

where:

λ'= wavelength

α = absorption coefficient

I = solar flux at the top of the atmosphere

ε = energy of a photon

N = ozone column amount

The infrared heating rate, on the other hand, is calculated as follows. First we let

$$q_{IR} = q_{CO_2} + q_{O_3}$$

where q_{CO_2} and q_{O_3} are the heating due to the 15μ band of carbon dioxide and the 9.6μ band of ozone, respectively. For either absorber, but for CO_2 in particular, the contribution to the atmospheric heating rate may be expressed as:

$$q_{CO_2} = \pi\int_0^{\infty} dT_{\nu}(z,z')/dz\ dB_{\nu}(z')/dz'\ dz' \qquad (2\text{-}16)$$

where B_{ν} is the Planck function evaluated at the band center, and T_{ν} is the flux transmission function between levels z and z' for the wavenumber interval $\Delta\nu$ (cm^{-1}), expressed as:

$$T_{\nu}(z,z') = (2/\Delta\nu)\int_{\Delta\nu} d\nu\int_1^{\infty}\exp[-x\tau_{\nu}(z,z')]\ dx/x^3 \qquad (2\text{-}17)$$

In eq.(2-17), τ_{ν} is the monochromatic optical depth between levels z and z', while the dummy variable x represents the secant of the angle of incidence of the diffuse radiation.

Curtis (1956; see also Goody, 1964) developed a method wherein the effects of temperature and absorber distribution are separated via a "Curtis matrix". The basic principle underlying this method is as follows: the atmosphere is

divided into n equally-spaced reference levels (taken as model levels 1 to 26) at each of which the temperature and heating rate are evaluated. The Planck function between the levels is then represented by some interpolation formula so that the heating rate at the ith level reduces to a linear combination of the n Planck functions, i.e.

$$q_i = \sum_{j=1}^{26} R_{ij} B(T_j)$$

Integrating eq.(2-16) by parts and approximating the result by finite differences, we obtain the following expression for the Curtis matrix elements:

$$R_{ij} = (\pi/\Delta z)[A_{i+1,j+1} - A_{i+1,j} - A_{i,j+1} + A_{ij}] \qquad (2\text{-}18)$$

where Δz is the spacing between the levels, and A_{ij} is the matrix of absorptance, defined as:

$$A_{ij} = [1 - T_\nu(z_i, z_j)]\Delta\nu$$

Wehrbein and Leovy (1982) found that cooling rates in the upper stratosphere and lower mesosphere are not very sensitive to the method of treating line strength distribution, as these rates are closely tied to the fundamental band of CO_2. We shall take advantage of this fact by adopting a simple formula for the absorptance which neglects the contribution of the hot and isotopic bands, following Houghton (1977). In the limit of strong absorption, the absorptance of a single line may be expressed as:

$$A = 2(s\gamma u)^{1/2} \qquad (2\text{-}19)$$

where s is the line strength, γ the line half-width, and u the absorber amount. The line half-width is assumed to depend linearly on pressure, so that

$$\gamma = \gamma_0 P$$

We shall use the Curtis-Godson approximation to calculate the average line half-width between levels i and j, so that assuming a uniform amount of absorber of fractional concentration c, this average is given by

$$\bar{\gamma} = (1/2)\gamma_0(P_i + P_j)$$

The absorber amount, on the other hand, is given by

$$u = (5/3)\int_z^\infty c\rho \, dz' \tag{2-20}$$

where 5/3 is the well-known diffusivity factor, which takes into account the fact that the radiation is incident at various angles. Using the hydrostatic approximation, eq.(2-20) reduces to

$$u = (5cp_0/3g)\left|P_i - P_j\right|$$

so that, neglecting the effects of temperature on line structure, we find that for the entire band:

$$A_{ij} = \left\{(10cp_0/3g)\left|P_i^2 - P_j^2\right|\right\}^{1/2}\sum_k (s_k\gamma_{0k})^{1/2} \tag{2-21}$$

where $\sum(s_k\gamma_{0k})^{1/2}$ is the sum of the square roots of the product of the line strength and line half-width at STP within the band. Table 2.4 gives spectral band information for the strongest CO_2 lines, derived from McClatchey, et al (1973), from which we conclude that

$$A_{ij} = (2.0 \times 10^3)\left|P_i^2 - P_j^2\right|^{1/2} \text{ cm}^{-1}$$

For the 9.6μ band of ozone, we use the cooling-to-space approximation, since the contribution of this band to the net heating is only of the order of -1 K/day. Thus we may write

$$q_{O_3} = \pi B_\nu(T)dA(z,\infty)/dz \tag{2-22}$$

To evaluate q_{O_3}, we employ the empirical band absorptance formula of Ramanathan (1976), given by:

$$A(U,\beta) = 2\Delta\nu \ln\left\{1 + U/[4 + U(1+\beta^{-1})]^{1/2}\right\} \tag{2-23}$$

where

$$U = (5/3)\int_z^\infty (S/\Delta\nu)P_{O_3}dz'$$

$$\beta = (4\gamma_0/\delta U)\int_0^U P dU'$$

P_{O_3} = ozone partial pressure in atm

S = total band intensity = 387 $\text{cm}^{-2}\text{atm}^{-1}$STP

γ_0 = mean line half-width = 0.076 cm^{-1}

δ = mean line spacing = 0.1 cm^{-1}

$\Delta\nu$ = band wavenumber width = 39 cm^{-1}

[See Cess and Tiwari (1972) for the definition of the band intensity.]

The quantity β in eq.(2-23) is essentially a dimensionless measure of the line structure within the band, while U is a dimensionless measure of the absorber amount. Figs. 2.1(a),(b) show typical infrared and net heating rates at solstice as computed by our model. The infrared rates may be compared with those of Freeman and Liou (1979), who employed the discreet-ordinates method for radiative transfer. Their results for the lower stratosphere are shown in Fig. 2.2(a). Fig. 2.2(b), on the other hand, illustrates the profile of net diabatic heating in the upper stratosphere and mesosphere generated by the radiative algorithm of Wehrbein and Leovy (1982). Note how our computed heating rates compare remarkably well with those resulting from more detailed modelling studies.

The computational procedure described thus far in this section is applied only to levels above 20 km (Z>2.84). Below 20 km, we use a much more empirical representation of the net heating, which is a somewhat modified version of the tropospheric heating scheme employed by the CAPP model. This heating may be expressed as:

$$q' = \rho c_p h(Z)(T^{\dagger} - T') \qquad (2\text{-}24)$$

where $T^{\dagger}(\lambda,\mu,Z,t)$ is an "equilibrium temperature" defined such that

$$T^{\dagger} = q'_{obs}/\rho c_p h(Z) + T'_{obs}$$

where q'_{obs} and T'_{obs} are the observed seasonal distributions of q' and T'. Eq.(2-24) may therefore be rewritten as

$$q' = q'_{obs} + \rho c_p h(Z)(T'_{obs} - T') \qquad (2\text{-}25)$$

The second term on the right hand side of eq.(2-25) is a relaxation term, which represents the heating not explicitly taken into account in the model, such as the effects of synoptic and convective scales.

We shall partition the equilibrium temperature into an annual mean and a seasonal sine wave, so that

$$T^{\dagger} = T^{\dagger}_a(\lambda,\mu,Z) + \sin[\delta_0(t-\phi_0)]T^{\dagger}_s$$

where t=0 at the vernal equinox, $\delta_0 = 2\pi/(360 \text{ days})$, and $\phi_0 = 30$ days. The quantity ϕ_0 is a mild time lag introduced in the troposphere to account for delayed ocean warmth. Following Trenberth (1973), we shall assume symmetry about the sub-solar point so that $T^{\dagger}_a$ contains only even polynomials and $T^{\dagger}_s$ only odd polynomials. This means that the annual average term will be a symmetric function of latitude, while the seasonal term will be antisymmetric with respect to the equator. Moreover, $T^{\dagger}$ may be further subdivided into longitudinally dependent and longitudinally independent components. Thus,

$$T^{\dagger} = T^{\dagger}_{zonal} + T^{\dagger}_{long}$$

where

$$T^{\dagger}_{zonal} = T^{\dagger}_2\Pi^0_2 + T^{\dagger}_4\Pi^0_4 + \sin[\delta_0(t-\phi_0)](T^{\dagger}_1\Pi^0_1 + T^{\dagger}_3\Pi^0_3) \qquad (2\text{-}26a)$$

and

$$T^{\dagger}_{long} = w(Z) \sum_{m=1,2} \left[\sum_{n=m,m+2} + \sin[\delta_0(t-\phi_0)] \sum_{n=m+1,m+3} \right] \times [c^m_n \cos(m\lambda) + s^m_n \sin(m\lambda)]\Pi^m_n \qquad (2\text{-}26b)$$

In (2-26a), $T^{\dagger}_i(Z) = 1.1[a_i(Z) + b_i(Z)/h(Z)]$. Table 2.5 gives the variation with height of the Newtonian cooling coefficient h(Z). The values of h in the upper troposphere are similar to those adopted in RUN34, which in turn are taken from Trenberth (1973). The values near the surface, on the other hand, are somewhat greater than those in RUN34 and may be compared to the value h=0.48 day^{-1} used by Bushby and Whitelam (1961) to represent convection effects over the North Atlantic in a three-level numerical weather prediction model. Tables 2.6-2.7 give the values of the coefficients used for each expansion in eqs.(2-26). These were calculated to fit the data of Newell, et al (1972) for the zonal forcing, and Katayama (1964) for the non-zonal forcing. The quantity w(Z) in eq.(2-26b) is a weighting factor, which in the original version of the

model was set equal to unity at levels below 10 km ($Z<1.42$) and zero elsewhere. In our version of the model, the profile of w(Z) below 10 km (levels 23-25) has been adjusted so that

$$w(Z_j) = \frac{P(Z_j)h(Z_j)}{\sum_{j=23}^{25} P(Z_j)h(Z_j)} \qquad (2\text{-}27)$$

Moreover, the even terms in eq.(2-26b) were found to be produced primarily by equatorial forcing, to which our model may not respond realistically because of the global balance assumption. Hence in our new version, these terms are suppressed. Finally, the values of the coefficients b_i in Table 2.6 differ slightly from those used in the CAPP model at the lowest levels. Most of the revisions in Tables 2.6-2.7 were suggested by the recent work of Drs. Alyea, Cunnold, and Cardelino (personal communication) who have incorporated these changes into a version of the CAPP model in which the resolution was increased to include zonal wavenumbers up to eighteen.

2.4 Sub-Grid Scale Dynamics

One of the serious defects associated with the CAPP model was the lack of an adequate damping mechanism that would prevent the spurious energy reflected by the rigid lid at the top of the model from contaminating the numerical solution in the upper stratosphere and mesosphere. As a result of this deficiency, the model failed to predict the observed closing of the polar night jet and the associated reversal of the meridional temperature gradient above a height of 60km. It is by now generally agreed that the closing of the jets in the mesosphere is caused by turbulence generated by gravity waves which saturate as their lapse rates become convectively unstable (Lindzen, 1981; Holton, 1983; Fritts, 1984). The breaking level of these waves is determined by their wavelengths and phase speeds, and is also influenced by radiative damping (Schoeberl, et al, 1983) and by eddy diffusion caused by the breaking waves themselves (Holton and Zhu, 1984). Above the breaking level, gravity wave dissipation results in enhanced vertical diffusion and in a decelerating drag which Lindzen (1981) showed to be proportional to $([u]-c)^3$ where [u] is the mean zonal wind and c the gravity wave phase speed.

Unfortunately, Lindzen's gravity wave parameterization is difficult and time consuming to implement in a spectral global balance model such as ours, as it involves the calculation of a cubic term and, moreover, requires the specification of gravity wave characteristics, observations of which are sparse. This being the case, we have resorted to a lower order scheme based on the work of Smith and Lyjak (1985), who used the residual method (Hartmann, 1976; Hamilton, 1983) to evaluate the effect of gravity wave breaking on the momentum budget of the middle atmosphere below 0.3 mbar. Smith and Lyjak estimated their momentum residuals from the primitive equations using daily LIMS data from Nimbus 7, from which they also derived a height-dependent Rayleigh

friction coefficient suitable for parameterizing the effects of gravity wave turbulence in the upper stratosphere and lower mesosphere. It must be warned, however, that their Rayleigh friction parameter is not a dependable measure of forcing by small-scale waves at levels below 1 mb, since their calculated residuals were not consistent over adjacent latitudes, levels, and months in the middle and lower stratosphere. With this caveat in mind, we have nevertheless decided to adopt Smith and Lyjak's Rayleigh friction parameterization in addition to the vertical eddy diffusion already employed in the model. The frictional stress term in the vorticity equation is then expressed as:

$$\underline{S} = \begin{cases} \kappa_R \nabla\psi & , Z=0 \\ \kappa_R \nabla\psi - (K_d/H_0^2)\partial\nabla\psi/\partial P & , \Delta Z \leq Z \leq Z_{top} - \Delta Z \\ 0 & , Z=Z_{top} \end{cases} \qquad (2\text{-}28)$$

where the vertical variation of κ_R above 0.3 mb is given by the formula:

$$\kappa_R = [0.3(Z/Z_{top})^4 + 3.0(Z/Z_{top})^{32}] \text{ day}^{-1} \qquad (2\text{-}29)$$

Eq.(2-29) is effectively an extrapolation of the Smith and Lyjak (1985) results, chosen so that it yields wind decelerations at the top of the model (≈72 km) comparable to those calculated by Holton and Zhu (1984) in a one-dimensional model employing Lindzen's (1981) wavebreaking parameterization and a gravity wave spectrum similar to that used by Matsuno (1982). Our adopted profile of κ_R is illustrated in Fig. 2.3, which in addition shows an equivalent Rayleigh friction coefficient which we have computed using winter zonal wind speeds and deceleration rates taken from Holton and Zhu (1984). Fig. 2.3 also shows the Rayleigh friction coefficient used by Holton and Wehrbein (1980) in a semi-spectral model that employed the Newtonian cooling approximation. Note how the observations imply significantly larger damping than is assumed in models which underestimate the radiative forcing.

The profile of vertical eddy diffusion employed in the model is illustrated in Fig. 2.4 together with that derived by Holton and Zhu (1984) for the winter

solstice. The values of K_d were chosen to account for three things: (a) gravity wave turbulence, (b) the effects of other scales not resolved due to the model truncation, and (c) the reflection of waves by the model rigid lid. It is clear from Lindzen's theory that the zonal wind deceleration and the vertical eddy momentum diffusion due to gravity wave breaking are closely linked. For this reason, K_d at the top of the model (middle mesosphere) was set to agree with the corresponding value from Holton and Zhu (1984). In the troposphere and lower stratosphere, the profile of eddy diffusion is similar to that used by Wofsy and McElroy in a one-dimensional chemical-diffusive model of methane, and in our model is intended to represent the vertical transport due to absent or unresolved convective and synoptic-scale motions. In between these two regions, the diffusion coefficient increases monotonically with altitude, but the rate of increase is somewhat arbitrary. The adopted K_d is greater in the lower mesosphere than that of Holton and Zhu (1984) so as to minimize reflection of wave energy by the rigid lid, and decreases smoothly to the tropopause value in order to avoid similar reflection problems due to rapid variations in K_d.

We have found it necessary to include additional numerical dissipation in the dynamical equations to prevent spurious energy from building up at higher wavenumbers. Puri and Bourke (1974) demonstrated that low resolution spectral models tend to exhibit such "spectral blocking" as a result of neglecting interactions involving components outside the truncation limits. This motivated our inclusion of the fourth order diffusion terms in eqs. (2-4) and (2-5), where we have allowed K_H to vary with both latitude and height according to:

$$K_H = 5 \times 10^{18}\ m^4 s^{-1}\ (\alpha(Z) + \mu^6) \qquad (2\text{-}30)$$

where

$$\alpha(Z) = \begin{cases} 1 & ,Z \geq 5 \\ (Z/5)^5 & ,Z < 5 \end{cases}$$

The values of K_H in eq.(2-30) give roughly similar damping times for the smallest retained horizontal scales as does the value 5×10^{16} $m^4 s^{-1}$ used by Bridger (1981) in a semi-spectral primitive equation model with a meridional resolution of 5 degrees in latitude. The latitudinally varying part of K_H was chosen deliberately in order to suppress spurious wave disturbances near the poles, particularly in the troposphere. (Multiplication of a spectral field by μ^6 has the advantage of being easily computed via recursion relations involving associated Legendre polynomials.) The vertical variation, on the other hand, tends to curb the formation of high-latitude jets in the upper stratosphere which result from anomalous wave-wave interactions (see Chapter III for a more detailed discussion).

2.5 Photochemistry

The chemistry of the stratosphere and mesosphere consists of a complex array of reactions involving several minor constituents- among them oxygen, hydrogen, nitrogen, and chlorine compounds, to be referred to respectively as O_x, NO_x, HO_x, and ClO_x. We have extensively updated the photochemistry employed in RUN34 of the CAPP model by including an extra three-body reaction involving the recombination of atomic oxygen and by using the latest rate constants taken from Baulch, et al (1982). Table 2.8 is a list of the various photochemical reactions included in the model, as well as their reaction rates, denoted by the k_i's. We also use the notation J_i to denote the photo-dissociation rate for the ith species, where

$$J_i = \int \alpha_i(\lambda')I(1')\exp(-\alpha_i N_i \sec\xi)\, d\lambda'$$

NO_x, HO_x, and ClO_x are all assumed to be in photochemical equilibrium, so that:

$$k_3[NO][O_3] + k_{32}[ClO][NO] + k_{38}[NO][HO_2] = k_4[NO_2][O] + [NO_2]J_{NO_2} \quad (2\text{-}31)$$

$$k_{14}[OH][O] = k_{16}[H][O_2][M] + k_{17}[H][O_3] \quad (2\text{-}32)$$

$$k_{17}[H][O_3] + k_{18}[HO_2][O] + k_{38}[NO][HO_2] + k_{20}[HO_2][O_3] = k_{12}[OH][O_3] + k_{14}[OH][O] \quad (2\text{-}33)$$

Moreover, the O/O_3 balance is determined by the principal terms only:

$$[O_3]J_{O_3} = l_{25}[O][O_2][M] \quad (2\text{-}34)$$

Eqs.(2-31) to (2-33) imply the following expression for the chemical loss of odd oxygen:

$$[M](\partial\chi_{O_3}/\partial t)_c = 2[O_2]J_{O_2} - 2k_4[NO_2][O] - 2k_{12}[OH][O_3] - 2k_{14}[OH][O] - 2k_{22}[O_3][O] - 2k_{31}[ClO][O] - 2l_{37}[O]^2[M] + 2k_{38}[NO][HO_2] \quad (2\text{-}35)$$

Two-dimensional distributions of the mixing ratios of the catalytic

species/families NO_x, ClO_x, and OH are specified in the model and are assumed to evolve sinusoidally in an annual wave throughout the year. These These distributions have been provided by Dr. Dak Sze from the work of Ko, et al (1985, 1986), who utilized a zonal mean model in isentropic coordinates in modelling the advection of stratospheric tracers by the diabatic circulation. Number densities at solstice for each of these catalytic species/families are shown in Figs. 2.5(a),(b),(c).

Eqs.(2-34) and (2-35) together allow us to evaluate the photochemical source term G in the ozone prediction equation. The computation of this term, like the calculation of the diabatic heating rate, is performed in grid space, after which G is transformed into spectral space and added along with the other terms in eq.(2-6). Because of the rapidity of the reaction rates in the upper part of the model, χ_{O_3} was assumed to be in photochemical equilibrium above 48 km ($Z>6.89$). Moreover, we assumed the complete absence of chemistry in the polar night. We also set G equal to zero at levels below 12 km ($Z<1.62$), which is an artifice since there is in situ photochemical generation of O_3 in the troposphere. However, since we are concerned with the troposphere only as a sink for stratospheric ozone via downward transport, accurate simulation of tropospheric ozone is unnecessary for our purposes. As a further expedient, we also set the term $\partial[P(W\chi_{O_3}')']/\partial P$ equal to zero below 12 km to avoid extra spectral to grid transformations. (This term was also evaluated by the transform method and not the interaction coefficient method so that it could be computed simultaneously with the diabatic heating terms, thus saving computer time.) At the surface, the boundary condition (2-9) allows χ_{O_3} to be expressed in terms of its value at $Z=\Delta Z$ as follows:

$$\chi_{O_3}(Z=0) = \chi_{O_3}(Z=\Delta Z)/[1 + dH_0\Delta Z/K_d] \qquad (2\text{-}36)$$

III. MODEL PERFORMANCE

3.1 Preliminary Experiments

The success of our solar-terrestrial experiment depends on our generating control runs which adequately simulate climatological conditions in the middle atmosphere especially during the winter when planetary wave activity is most intense. An important part of our work therefore was to sufficiently improve the model so as to eliminate any spurious response to external forcing in the regions of interest. Our aim was to produce satisfactory control fields for the month of February, hence we decided to generate these fields by integrating the governing equations forward in time starting from rest on model day 0, corresponding to November 30 of the model year. During this process we encountered some interesting behavior which corresponded to the sudden warmings periodically observed in the winter stratosphere. In this chapter we present the results of two simulations for the model time period beginning on day 30 and ending on day 40 of the model year. The first of these simulations, henceforth referred to as RUN35, includes all the dynamical improvements described in the previous chapter, except for the fourth order diffusion terms in the vorticity and thermodynamic equations. Moreover, RUN34 chemistry is used, as well as the RUN34 profile of h(Z). The second, known as RUN36, differs from the first only in that the relaxation term in eq.(2-25) has been omitted from the zonal components of q'. Figs. 3.1 through 3.5 show the various background fields for day 30 generated by each run. For comparison's sake, the corresponding fields from day 390 of RUN34 of the CAPP model are also shown. This comparison is, of course, limited by the fact that the wave fields for RUN35 and RUN36 are not yet fully developed; however, our purpose here is merely to indicate the effects of the various improvements we have made in the model physics.

Figs. 3.1(a)-(c) illustrate the net diabatic heating q' for each run. Note the drastic difference between RUN34 and the others above 40 km. From this it is clear that the Newtonian cooling parameterization of infrared emission seriously underestimates the strength of the diabatic forcing in the upper stratosphere and mesosphere. We attribute this partly to the fact that the radiative equilibrium temperature used in the CAPP model is not a local equilibrium temperature but rather the horizontal mean $\bar{T}$. As alluded to earlier, the use of $\bar{T}$ as the equilibrium temperature leads to heating in the polar night where $T<\bar{T}$, contrary to the expected cooling due to the absence of UV absorption in the region. The resulting temperature distribution for each run is shown in Figs. 3.2(a)-(c) whereas Fig. 3.2(d) depicts the observed distribution as presented by Newell (1969). The interesting features of RUN34 are the very cold stratopause and the warm tropopause in the region of the polar night. RUN36, on the other hand, most successfully reproduces the observed pattern, except that it gives an equatorial tropopause temperature minimum that is several degrees warmer than observed. Apparently, without the zonal relaxation terms, the thermal forcing at the equator is poorly simulated, perhaps owing to the adjustment made in the tropical tropospheric heating (see Section 2.3). RUN35 shows somewhat similar features, but differs from RUN36 in that it gives a cooler stratopause and warmer lower stratospheric temperatures in polar regions, as does RUN34. As we shall see, this is due to the sudden warming progressing at around this time in the simulation.

One key feature worthy of note is that in both RUN35 and RUN36 there is a reversal of the meridional temperature gradient near the winter mesopause. This reversal indicates a closing of the polar night jet based on the thermal wind relation, as is indeed shown in Figs. 3.3(b),(c), which together with Fig. 3.3(a) illustrate the zonal wind distribution in each case. The observed zonal wind pattern from Newell (1969) is shown in Fig. 3.3(d). Fig. 3.3(a) exhibits,

apart from the large mesospheric jets, a band of easterlies extending across almost the entire lower stratosphere. In addition, there is a single tropospheric jet core which is centered around 10N. In contrast to this, RUN35 and RUN36 give two tropospheric jets, with stratospheric easterlies confined to the Southern Hemisphere, as is observed. We found from intermediate runs that the splitting of the tropospheric jet is associated with a more realistic polar night jet, which is in turn due primarily to the enhanced mechanical dissipation at mesospheric levels. This may be due to the fact that changes in the shape of the polar night jet lead to alterations in the refractive index of the longest planetary waves, which then modify the distribution of the eddy transports near the tropopause, as shown by Bates (1977; see Section 1.4). On the other hand, the improved tropospheric jet structure might also be attributed to decreased reflection by the rigid lid in the cases of RUN35 and RUN36, rather than to changes in the actual wind values in the mesosphere. Nevertheless, hints of a dynamical coupling between the middle and lower atmospheres can be found in the work of Koermer, et al (1983), who used a primitive equation spectral model with orographic forcing to study the sudden warming phenomenon. They found that the strength and shape of the polar night jet were crucial to the development of the warming, as demonstrated by two experiments in which they varied the initial intensity of the jet. Their Figure 14 illustrates the effect on the tropospheric zonal wind structure in that the core changes position significantly in the second case in which the initial mesospheric jet was stronger (see later discussion in Section 3.3 including Fig. 3.36).

Other changes we have made in the model that affected the zonal wind distribution in the troposphere were the lower static stability of the current model compared to that of RUN34 and, in the case of RUN36, the elimination of the relaxation term in the zonal components of q'. The former helped only slightly in pushing the winter tropospheric jet more towards 30N. The latter,

however, clearly had a significant effect, resulting among other things in a more realistic Southern Hemispheric jet. Changes in the model topography, on the other hand, did not seem to generate significant differences in the circulation pattern, probably because the Southern Hemisphere was in summer, when wave activity is less effective.

Meridional circulation patterns for all three simulations and for observations are presented in Figs. 3.4(a)-(d), which show contours of the mass-weighted meridional stream function, defined by:

$$X_M = 2\pi(p_0/g)\cos\theta\ \partial[X]/\partial\theta \qquad (3\text{-}1)$$

The tropospheric cells in all three cases bear some resemblance to the observed circulation, particularly in the Northern Hemisphere. The differences in the diabatic heating schemes, however, result in qualitatively different circulations above 40 km. The cell between 10 and 50 mb in the polar night in RUN35 is an indication of a sudden warming taking place, and is a direct result of the eddy heat and momentum transports in that vicinity. The descending branch of this cell corresponds to adiabatic warming which maintains the relatively warm temperature at 50 mb compared to that in RUN36. On the other hand, the ascending branch of the cell at the polar stratopause in RUN34 explains the relatively cold temperature in that region. The resulting distributions of ozone in the lower stratosphere for each run and for observations are shown in Figs. 3.5(a)-(d). We see that the circulation pattern of RUN36 results in a larger pole-to-equator gradient in ozone concentration, owing to its poleward and downward character at high latitudes. This circulation, however, does not correspond to observations (Louis, et al, 1975), which indicate an extension of the tropospheric Ferrel cell into the lower stratosphere. In reality, the latitudinal gradient of ozone is maintained not only by the mean meridional circulation, but also by tracer transport due to planetary waves, which in RUN36 are less active during this time period than in

the other two runs.

It is interesting to compare the energetics of the three simulations described above. In order to do this we first partition the available and kinetic energies into zonal and eddy components after Lorenz (1955). The "Lorenz energy cycle" consistent with the governing equations is then as follows:

$$\begin{aligned}
\partial A_Z/\partial t &= G_Z - C_A + C_Z \\
\partial A_E/\partial t &= G_E + C_A - C_E \\
\partial K_Z/\partial t &= C_K - C_Z - D_Z + B_Z \\
\partial K_E/\partial t &= C_E - C_K - D_E + B_E
\end{aligned} \tag{3-2}$$

where:

$$A_Z = \int R[T']^2/2\sigma \, dM$$

$$A_E = \int R[T^{*2}]/2\sigma \, dM$$

$$K_Z = \int (1/2)\nabla[\psi]\cdot\nabla[\psi] \, dM$$

$$K_E = \int (1/2)[\nabla\psi^*\cdot\nabla\psi^*] \, dM$$

$$C_A = \int -(R/\sigma a)[v^*T^*]\partial[T]/\partial\theta \, dM$$

$$C_K = \int [u^*v^*][\nabla^2\psi] \, dM$$

$$C_Z = \int -R[W][T'] \, dM$$

$$C_E = \int R[W^*T^*] \, dM$$

$$G_Z = \int R[Q'][T']/\sigma \, dM$$

$$G_E = \int R[Q^*T^*]/\sigma \, dM$$

$$D_Z = \int [F][\psi] \, dM$$

$$D_E = \int [F^*\psi^*] \, dM$$

$$B_Z = (p_0/g)\int_{\text{boundary}}[\psi](\nabla\cdot f\nabla)\nabla^{-2}P[W] \, dS$$

$$B_E = (p_0/g)\int_{\text{boundary}}[\psi^*(\nabla\cdot f\nabla)\nabla^{-2}PW^*] \, dS$$

$$u^* = (1/a)\partial\psi^*/\partial\theta$$

$$v^* = -(1/a)\partial\psi^*/\partial\lambda$$

$$F = \nabla\cdot\partial(\underline{PS})/\partial P$$

a = radius of earth

[ ] = zonal average

$[\ ]^*$ = deviation from zonal average

In deriving eqs.(3-2) we have assumed that K_H=0, as is the case in RUN34, RUN35, and RUN36. Recall also that the term F includes the effects of both Rayleigh friction and vertical eddy diffusion.

Fig. 3.6 shows the energetics of the atmosphere as deduced by Oort and Peixoto (1983) for the winter months, while Figs. 3.7(a)-(c) illustrate the Lorenz energy cycle for the troposphere, stratosphere, and mesosphere averaged over the time period beginning on model day December 30 and ending on January 10, corresponding to the last day of RUN35 and RUN36.

In the troposphere we find that the energy storage terms of RUN36 come closest to observations, particularly in the total amount of eddy kinetic energy. RUN34, on the other hand, has an overactive tropospheric circulation, probably as a result of the larger eddy forcing in the diabatic heating. This surplus of eddy kinetic energy results in an anomalous boundary flux into the stratosphere causing transience and eventually sudden warmings, which lead to the formation of easterlies during the winter. Fig. 3.8 shows Lorenz energy cycle diagrams for the stratosphere before and after an observed warming, as computed by Julian and Labitzke (1965). From the direction of the various conversions we see that the stratospheric energy cycle of RUN34 indeed fits a postwarming pattern, a pattern which to a lesser degree fits that of RUN35. In the mesosphere we find that the improved radiation code of the current model results in a net generation of zonal available potential energy, in marked contrast to the net dissipation of RUN34. Moreover, the difference in the meridional circulation between the two models is reflected in the differing signs in the conversion terms C_Z and C_E. It also comes as no surprise to find that the kinetic energy dissipation terms of RUN35 and RUN36 are several

times larger than those of RUN34, indicating the effect of breaking gravity waves in the mesosphere.

3.2 The Theory of Sudden Warmings

The sudden warming phenomenon plays an important role in meteorology, not only because it contributes significantly to the overall budgets of heat, momentum, energy, and trace constituents in the stratosphere, but also because it provides a convenient natural test of our understanding of planetary atmospheric dynamics. Observational aspects of the sudden warmings have been reviewed extensively by McInturff (1978) and more briefly by Schoeberl (1978), while theoretical aspects of the phenomenon are discussed by Holton (1980) and by McIntyre (1982). A concise statement of the current theory of stratospheric sudden warmings can be made following Holton (1980):

1) Quasi-stationary planetary waves of zonal wavenumber 1 or 2 amplify in the troposphere and propagate into the stratosphere.
2) As a consequence of the thermal wind constraint, the eddy momentum and heat fluxes associated with the growing waves induce a mean meridional circulation which causes adiabatic warming in the lower stratosphere at polar latitudes.
3) The temperature changes associated with the sudden warming result in the deceleration and distortion of the polar night jet.
4) Major warmings occur when critical levels (where $[u]=0$) are formed, which block further upward transfer of wave energy and result in the appearance of easterlies as the critical level moves downward.

A physical explanation of the sudden warming phenomenon hinges on the theory of wave-mean flow interaction (Charney and Drazin, 1961; Eliassen and Palm, 1961; Andrews and McIntyre, 1976; Boyd, 1976). What follows is an elucidation of this theory from an Eulerian standpoint using the notation of the previous chapter. Following Holton (1975), the linearized equations governing the mean zonal wind and temperature are as follows:

$$\partial[u]/\partial t = f[v] - (1/a\cos^2\theta)\partial([u^*v^*]\cos^2\theta)/\partial\theta \quad (3\text{-}3)$$

$$\partial[T']/\partial t = -\sigma[W] - (1/a\cos\theta)\partial([v^*T^*]\cos\theta)/\partial\theta \quad (3\text{-}4)$$

where we have ignored the effects of dissipation. Furthermore, the mean meridional circulation conserves mass, so that

$$(1/a\cos\theta)\partial([v]\cos\theta)/\partial\theta - \partial(P[W])/\partial P = 0 \quad (3\text{-}5)$$

We now introduce the residual mean meridional circulation $(v^\dagger, W^\dagger)$, defined by:

$$v^\dagger = [v] + \partial(P[v^*T^*]/\sigma)/\partial P \quad (3\text{-}6)$$

$$W^\dagger = [W] + (1/a\cos\theta)\partial([v^*T^*]\cos\theta/\sigma)/\partial\theta \quad (3\text{-}7)$$

With this transformation, eqs.(3-3) to (3-5) can then be rewritten as follows:

$$\partial[u]/\partial t = fv^\dagger + [E] \quad (3\text{-}8)$$

$$\partial[T']/\partial t = -\sigma W^\dagger \quad (3\text{-}9)$$

$$(1/a\cos\theta)\partial(v^\dagger\cos\theta)/\partial\theta - \partial(PW^\dagger)/\partial P = 0 \quad (3\text{-}10)$$

where [E] is the divergence of the Eliassen-Palm flux, given by:

$$[E] = -(1/a\cos^2\theta)\partial([u^*v^*]\cos^2\theta)/\partial\theta - f\partial(P[v^*T^*]/\sigma)/\partial P$$

It can be shown that [E] is just the meridional transport of potential vorticity, that is

$$[E] = [q_0{}^*v^*]$$

where

$$q_0{}^* = (1/a\cos^2\theta)\partial\Phi^*/\partial\lambda^2 + (f^2/a^2\cos\theta)\partial(\cos\theta\ \partial\Phi^*/\partial\theta/f^2)/\partial\theta - f\partial(PT^*/\sigma)/\partial P \quad (3\text{-}11)$$

In eq.(3-11), Φ^* is the perturbation geopotential so that:

$$u^* = -(1/fa)\partial\Phi^*/\partial\theta \quad (3\text{-}12)$$

$$v^* = (1/fa\cos\theta)\partial\Phi^*/\partial\lambda \quad (3\text{-}13)$$

Combining eqs.(3-8) to (3-10) with the equation for thermal wind balance:

$$f\partial[u]/\partial Z = -(R/a)\partial[T']/\partial\theta \quad (3\text{-}14)$$

we get the following elliptic equation for the residual mean meridional velocity:

$$(R\sigma/a^2)\partial((1/\cos\theta)\partial(v^\dagger\cos\theta)/\partial\theta)/\partial\theta + f^2\partial^2 v^\dagger/\partial Z$$
$$= f\partial[E]/\partial Z - f\partial^2[E]/\partial Z^2 \qquad (3\text{-}15)$$

Eq.(3-15) demonstrates that it is the transport of both heat and momentum by the waves which induces the residual mean meridional circulation. Whenever this transport vanishes and assuming that dissipation is absent and that $v^\dagger$ vanishes on the boundary, then the residual mean meridional circulation will also vanish, and there will be no deceleration or warming, according to eqs.(3-8) to (3-10).

We may ask under what conditions will planetary waves transport potential vorticity. Again assuming no dissipation, we may answer this by appealing to the conservative nature of the potential vorticity, so that to first order in wave amplitude,

$$\partial q_0^*/\partial t + [\omega]\partial q_0^*/\partial\lambda = -(v^*/a)\partial[q_0]/\partial\theta \qquad (3\text{-}16)$$

where $[\omega] = [u]/(a\cos\theta)$ and $\partial[q_0]/\partial\theta$ is the latitudinal gradient of the zonal mean potential vorticity, given in spherical coordinates by the formula:

$$\partial[q_0]/\partial\theta = \{\, 2(\Omega + [\omega]) - \partial^2[\omega]/\partial\theta^2 + 3\tan\theta\,\partial[\omega]/\partial\theta$$
$$- (f^2a^2/R)\partial((P/\sigma)\partial[\omega]/\partial Z)/\partial P \,\}\cos\theta \qquad (3\text{-}17)$$

Multiplying eq.(3-16) by q_0^* and zonally averaging, we obtain:

$$[q_0^* v^*] = -(a/2)\partial[q_0^{*2}]/\partial t/(\partial[q_0]/\partial\theta) \qquad (3\text{-}18)$$

Eq.(3-18) implies that wave transience will lead to potential vorticity transport, and hence to deceleration of the zonal mean flow. On the other hand, if the wave is stationary the term $\partial q_0^*/\partial t$ in eq.(3-16) will vanish, in which case eq.(3-13) implies that

$$[u][q_0^* v^*] = 0$$

Thus $[q_0^* v^*] = 0$ unless $[u] = 0$ --i.e., wave mean flow interaction will occur in the vicinity of a critical level.

Eliassen and Palm (1961) showed that the heat and momentum transports of long waves are related to their wave energy flux as follows:

$$[v^*\Phi^*] = [u]\{(\partial[u]/\partial Z)[v^*T^*]/\sigma - [u^*v^*]\}$$

$$[W^*\Phi^*] = [u]\{(f - (1/a)\partial[u]/\partial\theta)[v^*T^*]/\sigma - [u^*v^*]\}$$

For quasi-geostrophic waves in the stratosphere, these reduce approximately to

$$[v^*\Phi^*] = -[u][u^*v^*]$$

$$[W^*\Phi^*] = f[u][v^*T^*]/\sigma$$

From these last two equations we see that a poleward heat flux is associated with an upward energy flux, while a poleward momentum flux corresponds to an equatorward energy flux. A poleward heat flux is in turn associated with a westward phase tilt of the wave with height, while a westward phase tilt with decreasing latitude is indicative of poleward momentum transfer.

One key feature of sudden warmings as discerned from observations is that focussing of wave energy into polar latitudes is essential if a major warming is to occur (O'Neill and Taylor, 1979; Kanzawa, 1982; O'Neill and Youngblut, 1982; Palmer, 1981a). This is because the small mass and moment of inertia of the polar region maximizes the effects of wave energy on the background flow. For focussing to occur there must be equatorward momentum transport in the stratosphere. What determines whether or not this will actually occur during a particular warming? This question was investigated by Butchart, et al (1982) with a three-dimensional primitive equation model in connection with the unusual wavenumber 2 major warming of February, 1979. They concluded from their numerical experiments that it is the initial zonal wind structure which determines whether a wave is focused towards the pole. It is quite well known that the refractive index of planetary waves is related to the basic zonal state (Charney and Drazin, 1961). Matsuno (1970) used a quasi-geostrophic model with spherical geometry to look at the propagation of waves in the presence of realistic wind profiles. He reduced the governing equations to a single equation for the wave geopotential of the form:

$$L_z\Phi^* + L_\theta\Phi^* + Q_m\Phi^* = 0$$

where L_z and L_θ are vertical and horizontal operators and Q_m is the refractive index squared, written as:

$$Q_m = \partial[q_0]/\partial\theta \; (1/[\omega]\cos\theta) - m^2/\cos^2\theta - f^2a^2/4\sigma^2R^2 \qquad (3\text{-}19)$$

m representing the zonal wavenumber. A given wave will become evanescent when Q_m is negative and will propagate towards regions where Q_m is both large and positive. The simpler Charney and Drazin theory, on the other hand, showed that stationary planetary waves would propagate vertically only if

$$0 < [u] < \beta/k^2$$

where $\beta = 2\Omega\cos\theta/a$ and $k = m/(a\cos\theta)$, so that planetary waves tend to be trapped by easterlies and by critical levels, as well as by strong zonal winds. One immediate consequence of eq.(3-19) is that shorter waves avoid polar regions more easily than do longer ones. This is undoubtedly one reason why sudden warmings dominated by wavenumber 2 are rare in comparison to those dominated by wavenumber 1.

Kanzawa (1984) found that the field of $\partial[q_0]/\partial\theta$ is a good indicator of wave focussing by the basic state. It is, after all, the background gradient of potential vorticity which allows planetary waves to grow in amplitude as they extract potential enstrophy from the mean flow (Schoeberl, 1982). McIntyre (1982) theorized that irreversible potential vorticity mixing by planetary waves outside polar latitudes preconditions the basic state so that wave focussing becomes possible.

The onset of a sudden warming is, as mentioned earlier, preceded by an amplification of wave energy in the troposphere. It is currently understood that the vacillations in the amplitudes of planetary waves propagating into the stratosphere are caused primarily by the interference between westward traveling external Rossby waves and quasi-stationary waves generated by flow over orography (Madden, 1983). The period of this vacillation cycle is that of the traveling wave and is of the order of two weeks. It is further hypothesized

that resonant amplification of topographic waves can occur if the basic state evolves such that a free mode of the atmosphere becomes stationary (Tung and Lindzen, 1979). Schoeberl and Strobel (1980a) used a quasi-geostrophic semi-spectral model to simulate wavenumber 1 and wavenumber 2 sudden warmings and found that in the case of the former, oscillations of wave amplitude and of the mean flow resulted from the interference between the topographically forced wave and a trapped, westward-propagating planetary wave excited by the switch-on of the forcing. More recently, Robinson (1985) explored the dynamics of wave vacillations using a truncated three-dimensional quasi-geostrophic β-channel model and found that the vacillation of wavenumber 2 in the stratosphere could be explained by wave-wave interactions between stationary wavenumber 2 and the traveling and stationary components of wavenumber 1. Moreover, he was able to account for the observed anticorrelation between the two wavenumbers in the winter stratosphere (Hirota and Sato, 1969; Labitzke, 1981; Smith, 1983a,b; Smith, et al, 1984).

3.3 Model Sudden Warmings

The differences in tropospheric heating between RUN35 and RUN36 had important consequences for the succeeding time development of their respective fields. The more efficient conversion of available energy into eddy kinetic energy in the case of the former led to a larger wave energy flux into the stratosphere. The transience associated with this upward flux initiated a major sudden warming which resulted in the development of easterlies in the upper stratosphere and a substantial deceleration of the polar night jet. This is shown in Figs. 3.9(a),(b) which represent the zonal wind patterns during days 35 and 40 of RUN35. Note how the tropospheric jet core in the Northern Hemisphere has been shifted southward probably as a result of the buildup of wavenumber 1 in the troposphere together with the lack of momentum transport due to synoptic scale waves. Figs. 3.10(a),(b) show the temperature changes that accompanied the RUN35 warming. In addition to the warming of the polar lower stratosphere, we see that the upper stratosphere and the lower mesosphere have undergone significant cooling at high latitudes. This mesospheric cooling has been known to accompany observed warmings (Labitzke, 1972; Hirota and Barnett, 1977), as well as simulated warmings such as that of Schoeberl and Strobel (1980a), who attributed the temperature changes to the induced secondary meridional circulation.

Figs. 3.11-3.13 show the time development in RUN35 of the zonal wind and of the geopotential height amplitudes of wavenumbers 1 and 2 at 50N up to day 40. The warming actually commences around day 22 as both wavenumbers 1 and 2 become transient. By day 29, wavenumber 1 begins to decrease in amplitude while wavenumber 2 continues to build up until stratospheric easterlies appear on day 33, a sequence of events akin to Schoeberl's (1978) "Type A" pattern of observed warmings, except that wavenumber 2 plays a larger role than usual. The role of

wavenumber 1 appears to be that of a precursor which conditions the basic state thus paving the way for wavenumber 2 to produce the major effects, much like in the observed warming of February 1979 (McIntyre, 1982). Schoeberl and Strobel (1980b) extended their study of stratospheric sudden warmings by adding a troposphere to their earlier model, so that both wavenumbers 1 and 2 were simultaneously forced by orography. They found that because of the relatively slow development of wavenumber 1, their simulated warming was dominated by wavenumber 2, although wavenumber 1 tended to moderate the strength of the warming by decelerating the polar night jet and allowing wavenumber 2 energy to escape into the mesosphere. The importance of wavenumber 2 in our simulated warming in RUN35 can be appreciated from the RUN35 zonal winds (Fig. 3.9(b)) where unlike in most major warmings the stratospheric easterlies are not confined to the polar region where wavenumber 1 is dominant, but extend as far southwards as 40N. This may be partly due to the fact that the equatorial critical line, which tends to reflect wave energy back towards high latitudes, does not advance poleward as in other modelling studies (e.g., Schoeberl and Strobel, 1980a,b; Dunkerton, et al, 1981; Koermer, et al, 1983). Another possible explanation, further elaborated in connection with RUN36, may be that owing to the limited truncation of the model, wave-wave interactions are not properly simulated thus resulting in a spurious growth of wavenumber 2.

Figs. 3.14-3.17 illustrate the geopotential height amplitude and phase contours of wavenumbers 1 and 2 in the Northern Hemisphere during the RUN35 warming sequence. By day 40, wavenumber 2 becomes confined to the lower stratosphere indicating that it has been trapped by the background flow. This is confirmed by the phase contours of Fig. 3.17(c), which show eastward phase tilt with height in the upper stratosphere and mesosphere. This in turn can be explained by referring to the field of the latitudinal gradient of potential vorticity which, as discussed earlier, is a measure of the refractive index of

planetary waves. Indeed, Figs. 3.18(a),(b),(c), which illustrate the potential vorticity gradients during the warming, show a tongue of negative $\partial[q_0]/\partial\theta$ developing between 1 and 20 mb at high latitudes near the appearing easterlies. Wavenumber 1 also seems to be trapped at high latitudes on day 35 (see Fig. 3.15(b)) owing to the region of negative $\partial[q_0]/\partial\theta$ between 0.2 and 5 mb.

Figs. 3.19(a)-(c) and 3.20(a)-(c) show the eddy transports of zonal momentum and heat during the period of the RUN35 sudden warming. Note how equatorward momentum transport appears in the lower stratosphere in the vicinity of the developing easterlies. Moreover, we see that the flux distributions of both momentum and heat in the troposphere undergo significant evolution during the warming. In particular, the maximum in the eddy momentum flux seems to migrate northwards by about 10 degrees. Profiles of the Eliassen-Palm flux divergence are depicted in Figs. 3.21(a)-(c), which show large convergences coinciding with critical levels, indicating intense wave-mean flow interaction in these regions.

The case of RUN36 is very different from that of RUN35. Figs. 3.22-3.29 show the corresponding development of the zonal winds and of the amplitudes and phases of geopotential wavenumbers 1 and 2. The first feature worthy of note is that the onset of transience in RUN36 is slower than in RUN35 so that no easterlies form in the upper stratosphere. However, a minor warming does take place which results in a significant decrease in the strength of the polar night jet owing to an anomalous buildup of wavenumber 2. Moreover, the jet undergoes a sudden distortion in the vicinity of the polar stratopause, which is accompanied by a drastic decrease in the amplitude of wavenumber 1 by day 40 of the simulation. This evanescence of wavenumber 1 is evident from the phase contours of Fig. 3.27(c) which show almost no phase variation with height in the upper stratosphere.

Figs. 3.30(a),(b),(c) show $\partial[q_0]/\partial\theta$ to be decreasing in the upper

stratosphere and increasing in the lower stratosphere at around 60N, an indication that wave energy is being guided into polar regions by the basic zonal state. This fact is further confirmed by the large equatorward eddy momentum transport appearing by day 35 in Figs. 3.31(a)-(c). Meanwhile, the tropospheric maximum in the eddy momentum flux migrates southwards and upwards, while that of the eddy heat flux moves northwards and downwards as depicted in Figs. 3.32(a)-(c). As a result of these changes, the tropospheric jet core has once again moved southwards as is evident from Figs. 3.25(a)-(c). Contours of [E] during the warming are illustrated in Figs. 3.33(a)-(c). Note the large divergences at the polar stratopause as well as the strong convergences near the core of the mesospheric jet that develop by day 40.

The time development of the kinetic energy spectrum at 1 mb during the period of the warming is shown in Fig. 3.34. Here we see the anomalous growth of wavenumbers 3 and 4 at the expense of wavenumber 1 which occurs at this level. The sudden energy cascade explains why the shape of the polar night jet becomes distorted in the neighborhood of the polar stratopause, as the transience resulting from the decrease in amplitude of wavenumber 1 causes a local acceleration of the jet according to eqs. (3-8) and (3-18). Apparently the spurious growth of wavenumber 2 results in a significant decrease in the background potential vorticity at high latitudes, making propagation less feasible for wavenumber 1. A cascade towards higher wavenumbers (which tend to avoid polar regions) is then triggered, resulting in the appearance of high latitude jets in the upper stratosphere.

Evidence that such high latitude jets accompany at least some warmings was put forward by Palmer (1981b), who analyzed the major warmings of February 1979 and February 1980. Figs. 3.35(a)-(d) show meridional cross sections of the mean zonal wind appropriate to these events, both of which were preceded by a minor warming which preconditioned the basic state so that succeeding planetary waves

were more easily focused towards the high latitude stratosphere. Palmer attributed the appearance of high latitude polar night jet cores prior to both major warmings to the previous decay of a wavenumber 1 pulse in the polar mid-stratosphere. Koermer, et al (1983), in the modelling study noted earlier, developed such high latitude stratospheric jets in their simulations of major and minor warmings (Figs. 3.36(a)-(h)). Associated with these displaced jets was the growth of wavenumber 3 in the upper stratosphere, coinciding with the rapid weakening of wavenumber 1 and the intensification of wavenumber 2 in that region. Palmer and Hsu (1983) and Matsuno (1984) used simplified numerical models to show that wave-wave interactions were indispensable to the formation of high latitude westerly jets during minor warmings. Both of these simulations confirmed the hypothesis due to McIntyre (1982) who, as mentioned earlier, suggested that the preconditioning of the basic state during a minor warming is a result of irreversible mixing of potential vorticity by planetary waves in the outer regions of the polar vortex. Accompanying this mixing would be the breaking of upward propagating wavenumber 1 due to nonlinear interactions with other waves, primarily wavenumber 2.

Since it is the anomalous growth of wavenumber 2 which apparently triggers the decay of wavenumber 1 and not vice-versa, we believe the energy cascade accompanying the warming of RUN36 to be an artifact of the model truncation. We believe that the limited horizontal resolution of the model also explains why the amplitude of wavenumber 1 in the troposphere is a maximum at high latitudes rather than at mid latitudes as indicated by observations (van Loon, et al, 1973; Wu, et al, 1984). Since the associated Legendre polynomials of high meridional mode number tend to have large values near the poles, limited spectral truncation can result in large errors in these regions. It should be stated that the most recent observations (see Wu, et al (1984), also Chapter IV and Figs. 4.5, 4.11, 4.15) do indicate high latitude jets to be common in the

winter stratosphere, but in the context of wave amplitudes that are very different from those which develop in RUN36. Ultimately, we believe that proper simulation of these jets can only be attained with a model of greater horizontal resolution than our own.

3.4 Effects of Fourth Order Diffusion

RUN35 and RUN36 served as instructive precursors to runs of the "complete" model as described in Chapter II. Important differences between RUN35 and RUN36 and the complete model run are the inclusion of "fourth-order" diffusion and the updated photochemistry in the complete model. The inclusion of numerical fourth order diffusion in the vorticity and thermodynamic equations, in particular, resulted in decisive improvements in the model circulation. This is demonstrated in Figs. 3.37-3.46, which illustrate various fields at solstice output by the complete model. Like the fields for day 30 in RUN35 and RUN36, these were obtained by running the model for 30 days starting from rest on day 0. Firstly, it should be noted that the winter mesosphere of Fig. 3.37 is somewhat colder than in either RUN35 or RUN36, a development which we attribute to the updated photochemical reaction rates used in the complete model. The stronger thermal contrasts associated with these changes led in turn to the closing of the Southern Hemisphere mesospheric jet, as is evident in Fig. 3.38. The primary effects of the added numerical dissipation, on the other hand, were twofold. On one hand, the height-dependent component of K_H was responsible for retarding the growth of geopotential wavenumber 2 (Fig. 3.41) in the stratosphere, thus allowing wavenumber 1 to develop more rapidly than in the previous numerical experiments (Fig. 3.39). Moreover,it prevented the development of high latitude jets in the vicinity of the stratopause further on in the simulation (see Chapter IV). The μ^6 variation, on the other hand, enabled the amplitude of wavenumber 1 to maximize at mid-latitudes in the upper troposphere and lower stratosphere, a fact confirmed by the westward phase tilts of Fig. 3.40, which compared to the phase tilts in the lower stratosphere of Fig. 3.15(a) show greater evidence of upward energy propagation at 50N. This feat, however, was achieved at the expense of reducing the amplitudes of the

highest wavenumbers, which are affected most, not only by the ∇^4 operator, but also by the μ^6 variation in K_H, as it is precisely these wavenumbers which tend to have large values near the poles. The result of the severe amplitude reduction of these waves was to drastically decrease the eddy transports in the lower troposphere where the waves are most important (see Figs. 3.43-3.44). This, in turn, led to a decrease in the strength of the mid-latitude westerlies near the surface and a subsequent trapping of wave energy at the lowest levels.

One of the bonuses obtained from the added numerical dissipation in the troposphere and lower stratosphere is a mean meridional circulation which bears much closer resemblance to the observed pattern (Fig. 3.45). In particular, the mid-latitude Ferrel cell now extends to the lower stratosphere as in the observations. Moreover, a distinct polar cell is now evident in the Northern Hemisphere, in contrast to the two-cell pattern of previous experiments. As a result of this high-latitude circulation, the Arctic maximum in ozone concentration is now more intense than in RUN35 and RUN36 (Fig. 3.46). One drawback of this new circulation, however, is that its strength in the troposphere is roughly a third of that in the observed circulation (see Fig. 3.4(d)), owing to the reduction in the eddy momentum trasport due to the higher wavenumbers. Since we are primarily interested in the stratosphere and mesosphere, however, we do not regard this as a major problem for the purposes of this thesis.

The improved model, like the parent CAPP model, is remarkably efficient. With vectorization of most of the code, running time for the model is currently 38 seconds per day of integration on the Goddard Cyber 205. Despite the many approximations made which lead to this efficiency, the quality of our results compares favorably with those of more detailed and computationally demanding general circulation models (GCM's). For example, Fig. 3.47(a) illustrates the zonal wind field for January obtained from the GFDL "SKYHI" general circulation model (Mahlman and Umscheid, 1984), which incorporates a sophisticated radiation

code along with fairly complete dynamical and tropospheric physical processes in a primitive equation model with 40 vertical levels and 5° latitude by 6° longitude resolution. The GFDL model winds exhibit several defects not evident in our results, including an overly strong mesospheric circulation (no large external damping is incorporated), mid-latitude surface easterlies, and a Southern Hemisphere jet stream several degrees north of its observed position. Fig. 3.47(b), on the other hand, shows the January mean zonal wind profile resulting from the latest version of the NCAR Community Climate Model (Boville, 1986), which like our model includes a Rayleigh friction parameterization based on that of Smith and Lyjak (1985) in a 33-level primitive equation spectral GCM with 15 zonal wavenumbers. The NCAR model mesospheric circulation is somewhat deficient in comparison to observations and to our model results, owing (according to the author) to its specification of uniform ozone mixing ratios above the 0.49 mb level.

There are also defects in our model resulting from the approximations which lead to its computational efficiency. The least of these is the constant static stability which must be assumed by all energetically consistent quasi-geostrophic models. Of greater consequence is the balance assumption, which prevents us from accurately simulating the behavior of the equatorial zero-wind line. Also, the limited truncation of the model does not allow us to resolve (nonlinear) interactions involving high wavenumber components of large amplitude. Our solution to the problems associated with truncation, which involved the inclusion of the fourth-order damping term, meant the curtailment of significant eddy transport by higher wavenumbers in the troposphere, which in turn resulted in the trapping of orographic waves near the surface. We have experimented with simple horizontal eddy diffusion-type parameterizations of these transports in the lowest layers, but thus far no paramaterization has been found of sufficient sensitivity to the basic state so as to correct the problem.

IV. THE UNPERTURBED MIDDLE ATMOSPHERE EXPERIMENT

4.1 Purpose of the Experiment

In the preceding chapter we discussed the various improvisations that went into the design of our model with a view to understanding both its capabilities and limitations in simulating the behavior of the real atmosphere. Our ultimate aim is, of course, to be able to predict the atmosphere's response to changes in the external forcing- in particular, the changes associated with solar variability on time scales of the order of several days to a few weeks. In modelling the atmosphere's sensitivity to such changes, we first need to understand its behavior in the absence of any perturbations in order to appreciate both qualitatively and quantitatively the significance of the presumed solar signal. In this chapter we present the climatology of the model during the late winter and early spring in the form of monthly averaged statistics for January (days 31-60), February (days 61-90), and March (days 91-120). These statistics were the result of continuing the run already discussed partially in Section 3.4, which dealt with the model output for day 30 of the simulation.

Our choice of time period for the experiment is dictated by the goal of this thesis, which is to test the viability of the Hines mechanism as a causal chain linking solar activity to changes in atmospheric circulation in the troposphere. Doing this requires two things: a) the presence of sunlight at the latitudes of interest, and b) significant planetary wave activity in the stratosphere and mesosphere during the time period of the simulation. The first of these is made necessary by the presumption that ozone is the triggering link which instigates changes in planetary wave behavior. The second requirement restricts the time period of interest to the winter and spring. As such, our

control fields will be taken from February and March, by which time the model should have already reached quasi-equilibrium.

4.2 Climatology of the Zonal Mean Flow

We begin our discussion of the model climatology with a description of those background fields which determine the propagation characteristics of planetary waves, primarily the zonal wind and temperature. Before this we need to consider the background radiative forcing, which is illustrated in Figs. 4.1(a)-(c). From these we see that as the sub-solar point progresses northwards, the diabatic heating field throughout the entire depth of the atmosphere becomes more and more symmetric with respect to latitude, a characteristic also typical of the field of temperature, as shown in Figs. 4.2(a)-(c). Because of the thermal wind relation, the resulting decrease in the meridional temperature gradient implies a weakening of the winter mesospheric jet and a progression of the zero-wind line from equatorial regions to mid-latitudes, as is the case in Figs. 4.3(a)-(c).

Figs. 4.4-4.5 display observations of temperature and zonal wind taken from the years 1978-1982 as reported by Wu, et al (1984). A few comments are in order regarding the relationship between the observed climatology of the middle atmosphere and that produced by the model. Firstly, the model extremes in the temperature field are generally lesser in magnitude than the corresponding extremes in the observations. In the tropical tropopause, this discrepancy may be due partly to the balance assumption and partly to the adjustments in the tropical diabatic forcing as discussed in Section 3.1. In the vicinity of the polar lower stratosphere, the very cold temperatures of observations are associated with the presence of high latitude jets in the upper stratosphere which, as mentioned earlier cannot be simulated properly by the model owing to its limited truncation. This lack of horizontal resolution may also explain why the Northern Hemisphere tropospheric jet stream is located somewhat south of its observed position, as intermediate and synoptic scales would normally contribute

significantly to the zonal momentum budget of the upper troposphere. On the whole, though, agreement between the model and observations seems adequate. Contours of potential vorticity gradient consistent with the model basic state are shown in Figs. 4.6(a)-(c) for future reference. Notice the decrease in potential vorticity available to planetary waves from winter to spring.

Meridional circulation patterns for the three months are illustrated in Figs. 4.7(a)-(c), while Figs. 4.8(a)-(c) show the corresponding distribution of ozone. Note that as a consequence of the lower stratospheric extension of the mid-latitude Ferrel cell, coupled with the decrease in lateral mixing by planetary waves during the spring, the Arctic maximum in ozone concentration occurs further south in February and March than in January.

4.3 Wave Climatology

We now proceed to examine the structure of the planetary waves in the model as compared to the observations of Wu, et al (1984). Figs. 4.9-4.10 illustrate the climatology of model geopotential wavenumber 1, while the corresponding observed climatology is demonstrated in Figs. 4.11-4.12. An important feature of the comparison is that the model amplitudes are somewhat weaker than those implied by the observations (by a factor of two at 10 mb), a fact we attribute to the trapping of wave energy at the lowest layer owing to the diminished eddy momentum transport in the troposphere. The phase contours of Figs. 4.10(a)-(c), apart from showing clear signs of westward propagation in the stratosphere and mesosphere, exhibit little variation in their structure from month to month. This is different from the apparent transience in the phase contours corresponding to observations (Figs. 4.12(a)-(c)), which is probably indicative of sudden warming activity, particularly in the late winter. Since the accurate simulation of wave transience depends on satisfactory resolution of wave-wave interactions in both the troposphere and stratosphere, as is apparently indicated by the most recent modelling studies (see Section 3.2), we cannot expect our model to duplicate the observational features associated with this aspect of planetary wave behavior. Agreement between the behavior of the model and the observations is better for geopotential wavenumber 2 than for wavenumber 1, as is demonstrated by Figs. 4.13-4.16.

Figs. 4.17-4.19 show the eddy transports and resulting decelerations of the zonal flow for the model waves, while Figs.4.20-4.22 give their observational counterparts for the standing eddies. Here again we see a difference of a factor of two between the model fields and the observations, a defect linked to the failure of the model to simulate properly the buildup of wavenumber 1 amplitude in the winter and spring.

4.4 Model Energetics

To complete the discussion of the climatology of the model atmosphere, we present an analysis of the energetics of the general circulation, as illustrated in Figs. 4.23(a)-(c). Note that we have not explicitly included the effects of the fourth-order dissipation in the analysis, as only the latitudinally varying component of this dissipation contributes to the horizontally averaged energy cycle. Since this component decays rapidly away from the poles and affects primarily the higher wavenumbers, it is important only in the high-latitude troposphere, which contains a relatively small fraction of the total atmospheric mass.

Comparison of the three-month average of the tropospheric energy storage terms of Figs. 4.23(a)-(c) with those of Oort and Peixoto (1983; see Fig. 3.6) shows good agreement between the model and observations, except in the case of the eddy kinetic energy, which in the model is ≈80% less than the observed value. This is undoubtedly due to the drastic decrease in the amplitudes of intermediate scale planetary waves enforced by the fourth-order diffusion terms. Since much of this energy in the real atmosphere is found in synoptic scale motions, this is not in itself a serious problem.

In the stratosphere, there is a general weakening of the model circulation from winter to spring as net zonal available energy is no longer generated but dissipated by the radiative forcing. This available energy is related to the reservoir of potential vorticity gradient in the basic state, which supplies the fuel for the growth of planetary waves in the stratosphere. As this supply diminishes, the amplitudes of the waves decrease, leading to a reduction in the magnitudes of the eddy storage terms and in the conversion terms representing the exchange of energy between the zonal mean and eddy circulations. Moreover, the reversal of the meridional circulation in the Southern Hemisphere

stratosphere during the spring (see Fig. 4.7) results in a change in the sign of the conversion between zonal kinetic and available energies.

The directions of the energy transformations in the model mesosphere differ from those in the stratosphere in that the mesospheric eddies draw energy from the zonal flow, rather than vice-versa. In the case of the available energy conversion, this is due to the differing signs of $\partial[T]/\partial\theta$ between the stratosphere and mesosphere (see Fig. 4.2). On the other hand, the focusing of wave energy in the polar lower stratosphere leads to an equatorward momentum flux (Fig. 4.20), which in turn leads to an acceleration of the zonal flow at high latitudes (Fig. 4.22). This is the opposite of what occurs in the mesosphere, where poleward momentum transfer predominates, thus implying a difference of sign in the term C_K in eqs.(3-2) compared to that in the stratosphere.

V. A SOLAR-TERRESTRIAL EXPERIMENT

5.1 Solar Flare Simulation

The numerical model discussed in the previous two chapters provides an especially suitable tool with which to investigate the hypothesized link between solar activity and middle atmospheric planetary-scale waves. The experiment we have designed for this purpose is similar to that of Schoeberl and Strobel (1978) in that we simulate the effects of a major solar flare on the general circulation of the stratosphere and mesosphere. Our model, however, provides a more valid test of atmospheric response to such a perturbation in that the radiative and photochemical effects are consistently calculated. Moreover, Schoeberl and Strobel used a zonal mean model and ignored wave-mean flow interactions, without which the atmosphere may be less sensitive to changes in external forcing.

The strength of our simulated solar flare is comparable to that of the August 1972 solar proton event as analyzed by Reagan, et al (1981), and can be measured in terms of the total odd nitrogen production resulting from the flare (see Figs. 5.1-5.2). In our primary experiment, this is given approximately by the formula:

$$\Delta n_{NO_x} = (2 \times 10^9 \text{ mol/cc}) \Lambda(\theta) \exp[-0.169(Z-6.49)^2] \qquad (5\text{-}1)$$

where the latitudinal distribution is given by

$$\Lambda(\theta) = \begin{cases} 1 & , \theta \geq 69^\circ \\ \exp[(\theta - 69^\circ)/11.5^\circ] & , \theta < 69^\circ \end{cases}$$

(We do not consider the direct heating of the atmosphere due to the fast protons themselves, as only a negligible fraction of their energy goes directly into translational energy of atmospheric molecules.) Note that the above

distribution of solar flare-produced odd nitrogen is asymmetric with respect to the equator. Actual measurements indicate that the distribution is symmetric for high energy (≈100 MeV) protons, whereas for less energetic particles, this may not necessarily be the case (see Chivers and Hargreaves, 1965; Wescott, 1966), hence we also conducted an experiment wherein we employed a symmetric distribution of perturbation NO_x. As we are interested primarily in the Northern Hemisphere, we will first discuss the results of the asymmetric distribution experiment, which has the advantage of minimizing the effects of any spurious dynamical coupling between the hemispheres due to our use of the global balance assumption. This will be followed by a discussion of the symmetric distribution experiment, but we note parenthetically that the Northern Hemisphere results in this case are similar to those in the asymmetric case.

The NO_x perturbation is not added instantaneously (a precaution against computational instability), but is instead added in equal increments per time step over the first two days of the experiment. Meanwhile, the perturbation NO_x is advected according to:

$$\begin{aligned}\partial\chi''_{NO_x}/\partial t = &-\underline{k} \times \nabla\psi\cdot\nabla\chi''_{NO_x} - \nabla\cdot\overline{\chi}''_{NO_x}\nabla\partial X/\partial P \\ &+\partial(PW\chi''_{NO_x})/\partial P \\ &-(1/H_0^2)\partial(K_d P\partial\chi''_{NO_x}/\partial Z)/\partial P\end{aligned} \qquad (5\text{-}2)$$

where χ''_{NO_x} is the perturbation NO_x mixing ratio. As in the ozone prediction equation, we assume that the diffusive flux of perturbation NO_x vanishes at the top of the atmosphere.

Implicit in eq.(5-2) is that we are ignoring changes in the prescribed background NO_x concentration due to circulation changes induced by the solar flare. Thus we are effectively treating the prescribed background and predicted perturbation NO_x as separate tracers, the former being externally specified as in the unperturbed run (see Chapter IV). Furthermore, we shall not consider the

effect of a transient injection of HO_x which usually accompanies a solar flare, as the photochemical perturbations due to this injection have a timescale of only a few hours (Solomon and Crutzen, 1981). We are also ignoring HNO_3 as a temporary sink for perturbation NO_x via the reactions:

$$OH + NO_2 + M \rightarrow HNO_3 + M \qquad (5\text{-}3)$$

$$HNO_3 + h\nu \rightarrow OH + NO_2 \qquad (5\text{-}4)$$

HNO_3 is only important as a NO_x reservoir in the lower stratosphere where ozone is in any case controlled primarily by dynamics rather than by photochemistry.

In implementing the numerical scheme for advecting perturbation NO_x, we encountered the common problem of negative mixing ratios- a difficulty we resolved by the technique of "borrowing-and-filling" whereby the negative ratios were set equal to zero and the difference extracted proportionally from the positive values in the same horizontal level. The resulting mixing ratios were then added to the prescribed background NO_x to form a field of total NO_x. This total NO_x was then used in the calculation of the photochemical source term G in the ozone prediction equation.

It should be remembered that the solar proton event of August 1972 was an unusually strong one in comparison to most solar flares, so that our experiment is not necessarily indicative of the effects of corpuscular radiation accompanying more regular events, such as solar sector boundary crossings. Rather, the experiment provides an upper limit test case wherein the result of a major ozone perturbation with spatial and temporal characteristics typical of solar-terrestrial signal can be evaluated. Moreover, this experiment is, to the best of our knowledge, the first detailed simulation of an odd nitrogen injection into the upper atmosphere using a three-dimensional model capable of resolving all the major feedbacks, whether radiative, dynamical, or photochemical.

5.2 Model Response to Solar Forcing

We now discuss the results of two month-long simulations of a (hemispherically asymmetric) solar proton event, the first proton event being in February, representing late winter conditions, and the second in March, representing the spring. In each experiment, the solar flare begins at the end of the first day of the month, reaching its peak in integrated NO_x production two days later- a computational expediency designed, as noted earlier, to avoid spurious advection of NO_x due to large gradients in species concentration. Since the model is non-diurnal, we cannot hope to properly resolve circulation changes occurring within a day, so that the time scale of interest is on the order of a week. Figs. 5.3-5.10 illustrate the changes (perturbed case minus unperturbed case) in geopotential amplitude and phase for wavenumbers 1 and 2 at 60N during each day of the simulation. (The amplitudes and phases for each experiment are computed separately before the subtraction.) In each case, the figures show initially growing disturbances above 45 km, which begin much earlier in the March event than in the February event. This may be attributed to the fact that sunlight penetrates higher latitudes only towards the middle of February, so that changes in ozone due to the injected NO_x and its subsequent effects are activated sooner in March, when the photochemically and thermodynamically important sunlight is more readily available. The maximum absolute changes for the two months are of the same order of magnitude and are comparable to the day-to-day variations in mesospheric wave amplitudes and phases. However, because the circulation is stronger in winter than in spring, the relative changes are smaller in February ($\approx$4%) than in March ($\approx$10%). For this reason, we shall analyze the March experiment in greater detail.

Figs. 5.11(a)-(d) show the development of the field of perturbation NO_x during March. The apparent result of the mean meridional circulation is to

advect NO_x downwards to the lower stratosphere, while the planetary waves tend to diffuse the species out towards the equator. The effects of this spreading perturbation on ozone and on the diabatic heating are shown in Figs. 5.12(a)-(d) and 5.13(a)-(d). The maximum ozone decrease occurs near the pole at around 45 km and is of the order of 2 ppmv, representing a relative change of around -25%. The ozone changes, like the NO_x perturbation, propagate downwards in time as the increase in the ambient NO_x results in greater catalytic destruction of ozone. The ozone decrease, in turn, leads to a decrease in absorption of ultraviolet light and hence to a reduction in the net diabatic heating as shown in Figs. 5.13(a)-(d). The heating changes are of the order of -0.2 K/day near 45 km and represent a 10% reduction of the unperturbed values. Note in particular how the effects of the perturbation diminish as the additional NO_x sinks towards those levels where dynamics becomes dominant over photochemistry in the ozone prediction equation.

Changes in temperature and zonal wind accompanying the solar flare are illustrated in Figs. 5.14(a)-(d), which show maximum temperature decreases of the order of 1K near the pole. The perturbation cooling apparently intensifies the meridional temperature gradient, which in turn leads to an increase in the zonal wind speed in the mesosphere of the order of 2 m/s near 40N, as may be seen from Figs. 5.15(a)-(d). This is an appreciable change, considering that the mean zonal wind in this region is of the order of 20 m/s in late March. That this is not a secondary effect induced by planetary waves is demonstrated by the contours of the change in the Eliassen-Palm flux divergence in Figs. 5.16(a)-(d). These show the maximum decelerations due to the "perturbation waves" to be several degrees north of the largest zonal wind deviations. The actual acceleration of the mesospheric jet is accomplished by the Coriolis torques associated with a mean meridional circulation induced by the diabatic heating perturbation, illustrated in Figs. 5.17(a)-(d). Notice how the

descending branches of the meridional cells coincide with the region of major perturbation cooling in the upper stratosphere.

Figs. 5.18(a)-(d) portray the time development of the change in the latitudinal gradient of potential vorticity during the solar proton event. The relative change of this quantity in the mesosphere at 60N is of the order of 3%, whereas the relative zonal wind deviations in the same vicinity are of the order of 5%. Examination of the first term on the right hand side of eq.(3-19) reveals that the relative changes in the square of the refractive index implied by the perturbations in zonal wind and potential vorticity gradient are no larger than 3% at high latitudes.

The actual dependence of wave amplitude on refractive index is quite complicated, but it is nevertheless instructive to explore what would happen in a simpler analytical model if the refractive index of the basic state were to be perturbed by the same relative amount as in our numerical experiment. An appropriate model is that of Charney and Drazin (1961; see also Section 3.2), who used the quasi-geostrophic potential vorticity equation on a mid-latitude β-plane to determine the vertical structure of steady waves in the presence of a constant mean zonal wind. The refractive index squared (denoted by r) corresponding to the case of geostationary disturbances is then:

$$r = (R\sigma/f_0^2)[\beta/[u] - k^2] - 1/4 \qquad (5\text{-}5)$$

where f_0 is the Coriolis parameter at the center of the β-plane. In eq.(5-5) we have made the additional assumption that the waves have an infinite latitudinal scale, as did Hirota (1971), who employed a linearized lower boundary condition of the form:

$$W(Z=0) = ik[u](h/H)\exp(ikx) \qquad (5\text{-}6)$$

together with the Charney-Drazin model in deriving the following expression for the density-weighted amplitude of the perturbation geopotential:

$$\left|\Phi_0^*\right| = 2R\sigma(h/H)/(1+4r)^{1/2} \qquad (5\text{-}7)$$

We can relate the simple Charney-Drazin (1961) refractive index to the Matsuno (1970) index by noting that the horizontal curvature of the mean zonal wind changes the effective value of β "felt" by the waves, whereas the meridional scale of the waves themselves may be taken into account by setting $k^2=n(n+1)/a^2$.

Differentiating eq.(5-7) with respect to r, we get:

$$d\left|\Phi_0^*\right|/dr = -4R\sigma(h/H)/(1+4r)^{3/2} \qquad (5\text{-}8)$$

so that:

$$\Delta\left|\Phi_0^*\right|/\left|\Phi_0^*\right| \approx -[2r/(1+4r)]\Delta r/r$$

Setting $k^2=12/a^2$, $\beta=2\Omega/a$, [u]=20 m/s, $f_0=10^{-4}$ s^{-1}, and σ=83K, we obtain:

$$\Delta\left|\Phi_0^*\right|/\left|\Phi_0^*\right| \approx -0.44(\Delta r/r)$$

so that a 3% increase in the refractive index squared would imply a 1.3% decrease in wave amplitude. Even though the analytical model employed above is relatively simple, it would seem from our order-of-magnitude calculation that the 10% increase in the amplitude of wavenumber 1 resulting from the solar flare cannot be explained by alterations in the basic state. It is far more likely that planetary waves are excited directly by the diabatic heating perturbations associated with the flare, as we now proceed to demonstrate.

The spatial structure of the waves excited by the solar protons is illustrated in Figs. 5.19-5.22, which show the time variations of the amplitudes and phases of the "perturbation" wavenumbers 1 and 2 (calculated in the same manner as in Figs. 5.3-5.10). The decrease in ozone heating in the upper stratosphere apparently resulted in the growth of planetary waves above the region of maximum change in the thermal forcing. The phase contours of Figs. 5.20(a)-(d) and 5.22(a)-(d), however, show primarily eastward tilt with height in the high latitude mesosphere. This would seem to imply a diminishing of upward energy propagation from the stratosphere, contrary to the evidence afforded by the amplitudes of Figs. 5.19(a)-(d) and 5.21(a)-(d). We resolve this paradox in the following manner.

The energy diagrams of Fig. 4.23(c) show that the net effect of the diabatic heating in the stratosphere and mesosphere is to dissipate the eddy circulation. Strobel (1979) showed that the damping rate associated with this radiative dissipation above 40 km can be parameterized as follows:

$$\alpha_T = a + (CH/T^2)\Psi \qquad (5\text{-}5)$$

where a is the Newtonian infrared cooling coefficient, C a positive constant, H the ozone heating rate, and Ψ a function of the ozone column amount, N, representing opacity effects. The transmission function Ψ is, in turn, empirically given by the formula

$$\Psi = 13.47 - 0.325 \ln N \qquad (5\text{-}6)$$

The second term on the right hand side of eq.(5-5) takes into account the buffering effect of ozone on temperature perturbations, known as "photochemical acceleration" (Leovy, 1964; Blake and Lindzen, 1973), which comes about because of the temperature dependence of photochemical reactions in the upper atmosphere. The most sensitive quantity controlling the magnitude of the photochemical acceleration term is, in fact, the ozone heating rate, so that a decrease in this quantity may produce a comparable relative increase in wave amplitude owing to the reduced thermal dissipation. This would seem to be the case for wavenumber 1, whereas wavenumber 2 does not appear to be as significantly affected by the solar perturbation presumably because it is guided further equatorward of the maximum ozone changes than is wavenumber 1. Above the region of maximum perturbation cooling, the atmosphere would tend to relax towards radiative-photochemical equilibrium with much the same time constant as in the unperturbed case. We show in the Appendix that radiative dissipation leads to a decrease in the westward tilt with height of vertically propagating planetary waves, a fact which probably explains the eastward tilt of the phase contours in Figs. 5.20 and 5.22.

A concise summary of the mechanism we believe to be responsible for the

solar activity effects noted above is as follows:

1) Solar flare protons are dumped in the high latitude stratosphere generating significant concentrations of odd nitrogen species as a result of the ionization of chemically inert nitrogen molecules.
2) The odd nitrogen produced by the solar flare is advected downward and equatorward to regions where sunlight is available. The sunlight then activates the odd nitrogen, resulting in the catalytic destruction of ozone, which in turn reduces the photochemical acceleration rate in the upper stratosphere around 60N.
3) Planetary wave amplitudes increase in the vicinity of the maximum radiative changes. The excited waves propagate through the mesosphere acquiring an eastward tilt with height as a result of the atmosphere's relaxation to radiative-photochemical equilibrium away from the thermal forcing.
4) Independent of the changes in the eddy circulation, the high latitude stratospheric cooling resulting from the solar flare induces a thermally direct mean meridional circulation at mid-latitudes. The Coriolis torques associated with this cell accelerate the zonal wind in the mesosphere around 40N.
5) As the solar flare-generated odd nitrogen reaches the lower stratosphere where photochemistry is no longer dominant in comparison to the dynamics, solar activity effects diminish so that no significant changes in atmospheric circulation are found below 30 km.

We repeated the March experiment using a hemispherically symmetric distribution of perturbation NO_x and found a slightly larger response in the Northern Hemisphere. In the case of the amplitude of planetary wavenumber 1, the maximum changes were around 19 gpm instead of the 16 gpm maximum amplitude deviation in the previous experiment, whereas the maximum zonal wind increase

was 3 m/s, compared to 2 m/s in the asymmetric case. The differences between the two cases are perhaps not significant considering the uncertainties introduced by the global balance approximation in assessing cross-equatorial coupling between the hemispheres.

The major result of our numerical experiments is ultimately a negative one in that we have demonstrated the infeasibility of ozone-circulation coupling as an important trigger mechanism linking solar activity to observable meteorological signals in the lower atmosphere.

VI. SUMMARY AND CONCLUSION

In the introduction to this thesis, we briefly reviewed the evidence concerning possible short-term solar-terrestrial coupling in the neutral atmosphere- evidence which, while suggestive, remains as yet inconclusive. One of the difficulties in interpreting the available observations is that there are dynamical processes in the atmosphere which have natural time scales nearly coincident with those of solar activity, so that an accidental correlation involving such processes might easily be mistaken for a solar signal. Given the tentativeness of many claimed solar-terrestrial correlations, there exists a great need for plausible mechanisms by which such evidence may be properly evaluated. One such mechanism, proposed by Hines (1974), postulates the existence of an atmospheric trigger, which when activated by solar disturbances, results in the modulation of planetary wave activity in the stratosphere and/or mesosphere, leading to signals in the troposphere. The primary contribution to sun-weather research in this thesis has been to provide a rigorous test of a variant of the Hines mechanism, one which presupposes ozone to be the necessary trigger. The test involved the only indubitable solar-induced ozone perturbation known to occur, namely that associated with an energetic solar proton event.

In order to provide an accurate test of the role of stratospheric ozone in a sun-weather hypothesis, it was first necessary to construct a numerical model which included all the major feedbacks involving the chemistry, radiative transfer, and dynamics of the middle atmosphere. The one which I have developed and used for the solar-terrestrial experiment is, to my knowledge, the most detailed middle atmospheric global balance radiative-dynamical-chemical three-dimensional model currently available. It successfully reproduces many important features of the observed circulation, such as the mesospheric polar

night jet and the mean meridional circulation of the troposphere and stratosphere. An important part of this thesis involved the development and subsequent analysis of various components of the model in order to ensure proper simulation of the phenomenon of interest.

The model's response to the simulated solar proton event consisted of the following chain of events: (a) a decrease in ozone concentrations of 25% at the polar stratopause, (b) a subsequent change in the diabatic heating rate of about -0.3 K/day in the same vicinity, (c) an increase in mesospheric wave amplitude of 10-20 gpm resulting from the decreased photochemical acceleration rate in the upper stratosphere, and (d) an acceleration of the mid-latitude mesospheric zonal wind due to a solar-flare induced thermally-direct mean meridional circulation. The changes in both zonal wind ($\approx$2 m/s) and geopotential height accompanying the simulated solar flare are below the level of detection of satellite measurements, so that no observationally important circulation effects can be expected to result from a real solar flare. Our negative result implies that for the Hines mechanism to be valid, some triggering link other than stratospheric ozone must be involved, particularly one which is more effective at producing changes in the lower stratosphere. One such possible link, proposed by Dickinson (1975), involves the influence of galactic cosmic rays (whose fluxes are modulated by solar activity) on the aerosol content, and hence the radiative and thermal budget of the atmosphere.

In the future, the model developed for the purposes of this thesis may be usefully applied to the study of other problems involving the ozone layer, such as the effects of fluorocarbon pollution on stratospheric chemistry. It can also be used to address the current controversy over the origin of the dramatic springtime minimum in the Antarctic ozone column, which some have linked to the 11-year solar cycle (Callis and Natarajan, 1986).

In addressing possible future improvements to the model, perhaps the most

serious shortcoming is the model's limited truncation, which necessitated the inclusion of an artificial fourth-order diffusion term in the governing equations. This resulted in an underprediction of the strength of the eddy circulation in the middle atmosphere as well as the exclusion of certain transient features associated with nonlinear wave interactions. The underprediction problem may probably be addressed by employing an as yet unspecified parameterization of intermediate and synoptic scale eddy transports in the lower troposphere. Such a parameterization should adjust the mid-latitude surface westerlies to allow greater vertical energy propagation into the upper levels. The exclusion of transient features is more serious, and would probably require an extension of the model resolution. The model's inability to simulate the appearance of high latitude jets in the stratosphere ("sudden cooling") could conceivably have a bearing on the results of our solar-terrestrial experiment. Such high-latitude jets would focus waves more towards polar regions, where solar-induced ozone changes are greater and would, in addition, reflect more wave energy down towards lower levels, possibly resulting in detectable signals in the upper troposphere. However, we have noted that the ozone concentration and diabatic heating changes due to NO_x injections require the presence of sunlight, which when present at high latitudes diminishes the available supply of background potential vorticity gradient, hence rendering such "sudden coolings" unlikely. We conclude, therefore, that our numerical experiments provide a realistic assessment of the atmosphere's response to a major solar-induced ozone perturbation.

VII. TABLES AND FIGURES

Table 2.1

Model Physics	CAPP Model Scheme	Current Model	Reason
Infrared Emission	Newtonian Cooling Parameterization	Explicit Band Model and Curtis Matrix Calculation	CAPP Model Underestimated Diabatic Forcing
Mechanical Dissipation	Eddy Diffusion	Eddy Diffusion Plus Rayleigh Friction	Simulation of Breaking Gravity Wave Turbulence
Tropospheric Heating	Observed Zonal Heating Plus Zonal and Non-zonal Relaxation Terms	Non-Zonal Forcing Adjusted	Better Tropospheric Boundary Flux
Synoptic Scale Motions	Truncation at Wavenumber 6	Fourth Order Diffusion	Curbs Spectral Blocking
Photochemistry	Reaction Rates Circa 1974	Updated Reaction Rates Plus Additional 3-Body Reaction	Improved Mesospheric Circulation
Ozone Transport	Vertical Flux Convergence Term Neglected	Vertical Flux Convergence Term Included	Better Ozone Transport
Orographic Forcing	Topographic Symmetry About Equator	Realistic Southern Hemisphere	More Realistic Topography

Table 2.2

Level j	P_j (mb)	Z_j	z (km)	$\overline{T}_j$ (K)	σ (K)
1	0.040	10.137	71.6	211	41.0
2	0.059	9.731	69.0	219	43.1
3	0.089	9.326	66.3	226.5	46.1
4	0.134	8.920	63.5	234	48.2
5	0.200	8.515	60.6	241.5	49.7
6	0.301	8.109	57.6	249.5	50.0
7	0.451	7.704	54.5	258.5	52.0
8	0.677	7.298	51.4	267	64.9
9	1.01	6.893	48.2	267.5	82.9
10	1.52	6.488	45.0	261.5	90.3
11	2.28	6.082	41.9	254.5	88.2
12	3.43	5.677	38.8	248.5	85.3
13	5.14	5.271	35.9	242.5	82.9
14	7.71	4.866	33.0	237	81.4
15	11.6	4.460	30.2	231	80.5
16	17.3	4.055	27.5	225	78.1
17	26.0	3.649	24.8	219.5	75.1
18	39.0	3.244	22.2	214.5	70.9
19	58.5	2.838	19.6	211.5	64.9
20	87.8	2.433	17.1	210.5	58.0
21	132	2.027	14.6	213	46.4
22	198	1.622	12.0	222	37.4
23	296	1.216	9.3	234	29.9
24	444	0.811	6.4	248	20.9
25	667	0.405	3.4	266	20.9
26	1000	0.0	0.1	287	23.9

Table 2.3

Standard Latitudes (degrees)	Standard Longitudes (degrees)
81.1N	0
69.6N	22.5E
58.0N	45E
46.4N	67.5E
34.8N	90E
23.2N	112.5E
11.6N	135E
0	157.5E
11.6S	180E
23.2S	157.5W
34.8S	135W
46.4S	112.5W
58.0S	90W
69.6S	67.5W
81.1S	45W
	22.5W

Table 2.4

Wavenumber Interval (cm^{-1})	$\sum_k (s_k \gamma_{0k})^{1/2}$ ($gm^{-1/2}$)
625-650	301.5
650-675	890.8
675-700	354.7

Spectral Band Data for 15μ Band of CO_2 (McClatchey, et al, 1973)

Table 2.5: Newtonian Cooling Coefficient

Level	$h(day^{-1})$
20	.02
21	.02
22	.03
23	.09
24	.22
25	.50
26	1.00

Table 2.6: Zonal Tropospheric Heating Coefficients

Level	a_1	a_2	a_3	a_4	b_1	b_2	b_3	b_4
	(deg)				(deg/day)			
20	3.2	8.4	3.2	-3.0	.14	-.20	.02	-.02
21	2.6	7.4	3.0	-2.3	.10	-.10	.00	.02
22	2.9	0.0	1.3	-0.1	.07	-.11	-.05	.13
23	3.7	-7.5	0.2	0.1	.11	-.15	-.10	.29
24	4.0	-8.9	0.1	-0.3	.24	-.53	-.13	.28
25	4.5	-10.0	0.1	-0.8	.34	-.20	.15	-.25
26	5.5	-11.5	0.5	-1.5	.20	.06	.08	-.24

Table 2.7: Non-zonal Tropospheric Heating Coefficients

m	n	c_n^m	s_n^m
1	2	1.12	8.05
1	4	-2.09	-1.48
2	3	-8.57	2.15
2	5	-1.23	2.14

Table 2.8

1. $NO + O_3 \rightarrow NO_2 + O_2$	$k_3 = 3.6\times10^{-12}\exp(-1560/T)$
2. $NO_2 + O \rightarrow NO + O_2$	$k_4 = 9.3\times10^{-12}$
3. $NO_2 + h\nu \rightarrow NO + O$	J_{NO_2}
4. $OH + O_3 \rightarrow HO_2 + O_2$	$k_{12} = 1.9\times10^{-12}\exp(-1000/T)$
5. $OH + O \rightarrow H + O_2$	$k_{14} = 2.3\times10^{-11}\exp(110/T)$
6. $H + O_2 + M \rightarrow HO_2 + M$	$k_{16} = 5.9\times10^{-32}(T/300)$
7. $H + O_3 \rightarrow OH + O_2$	$k_{17} = 1.4\times10^{-10}\exp(-480/T)$
8. $HO_2 + O \rightarrow OH + O_2$	$k_{18} = 3.7\times10^{-11}$
9. $HO_2 + O_3 \rightarrow OH + 2O_2$	$k_{20} = 1.4\times10^{-14}\exp(-600/T)$
10. $O_3 + O \rightarrow 2O_2$	$k_{22} = 1.8\times10^{-11}\exp(-2300/T)$
11. $O_3 + h\nu \rightarrow O + O_2$	J_{O_3}
12. $O + O_2 + M \rightarrow O_3 + M$	$1_{25} = 6.2\times10^{-34}(T/300)^{-2}$
13. $O_2 + h\nu \rightarrow 2O$	J_{O_2}
14. $ClO + O \rightarrow Cl + O_2$	$k_{31} = 7.5\times10^{-11}\exp(-120/T)$
15. $ClO + NO \rightarrow Cl + NO_2$	$k_{32} = 6.2\times10^{-12}\exp(294/T)$
16. $O + O + M \rightarrow O_2 + M$	$1_{37} = 4.8\times10^{-38}\exp(900/T)$
17. $NO + HO_2 \rightarrow NO_2 + OH$	$k_{38} = 3.7\times10^{-12}\exp(240/T)$

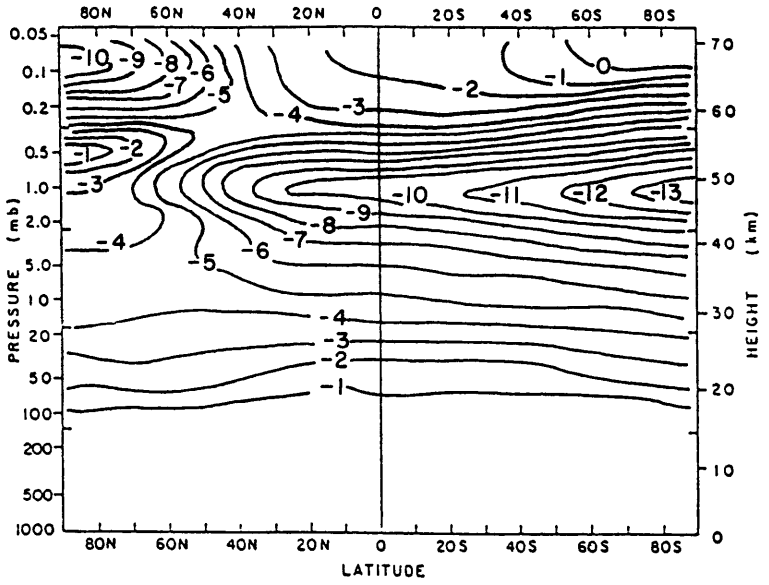

(a)

Figs. 2.1: Model Diabatic Heating (K/day) at Solstice; (a) IR, (b) Net

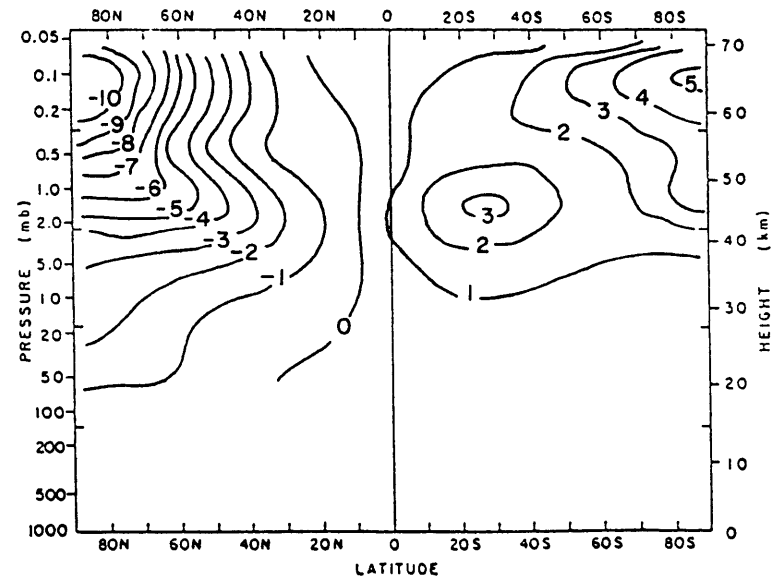

(b)

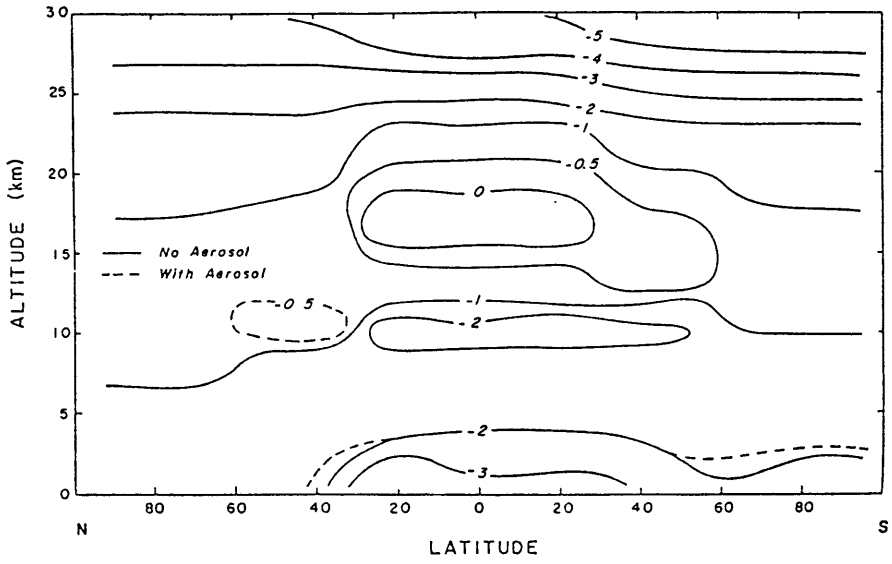

Fig. 2.2(a): IR Heating Based on Observed January T (after Freeman and Liou, 1979)

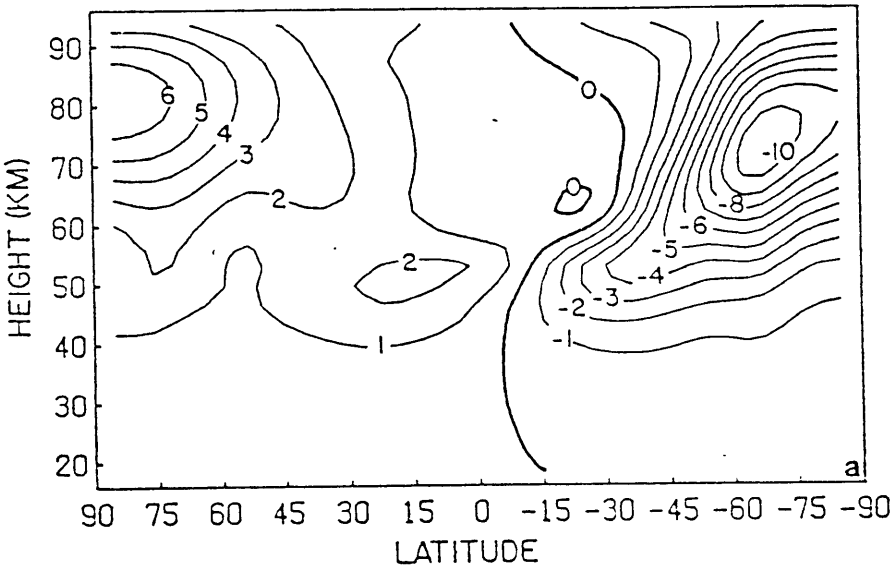

Fig. 2.2(b): Net Diabatic Heating at Summer Solstice Based on Observed T (after Wehrbein and Leovy, 1982)

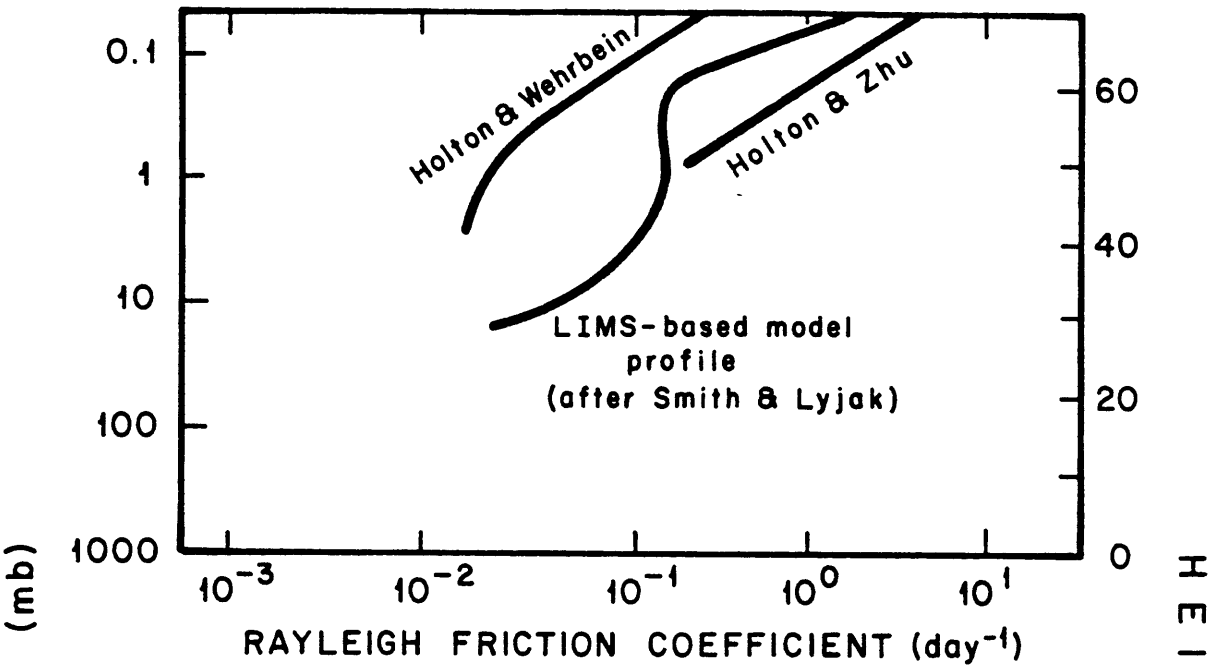
0.1
1
10
100
1000
PRESSURE (mb)
60
40
20
0
HEIGHT (KM)
Holton & Wehrbein
Holton & Zhu
LIMS-based model
profile
(after Smith & Lyjak)
10^{-3}
10^{-2}
10^{-1}
10^{0}
10^{1}
RAYLEIGH FRICTION COEFFICIENT (day^{-1})

Fig. 2.3

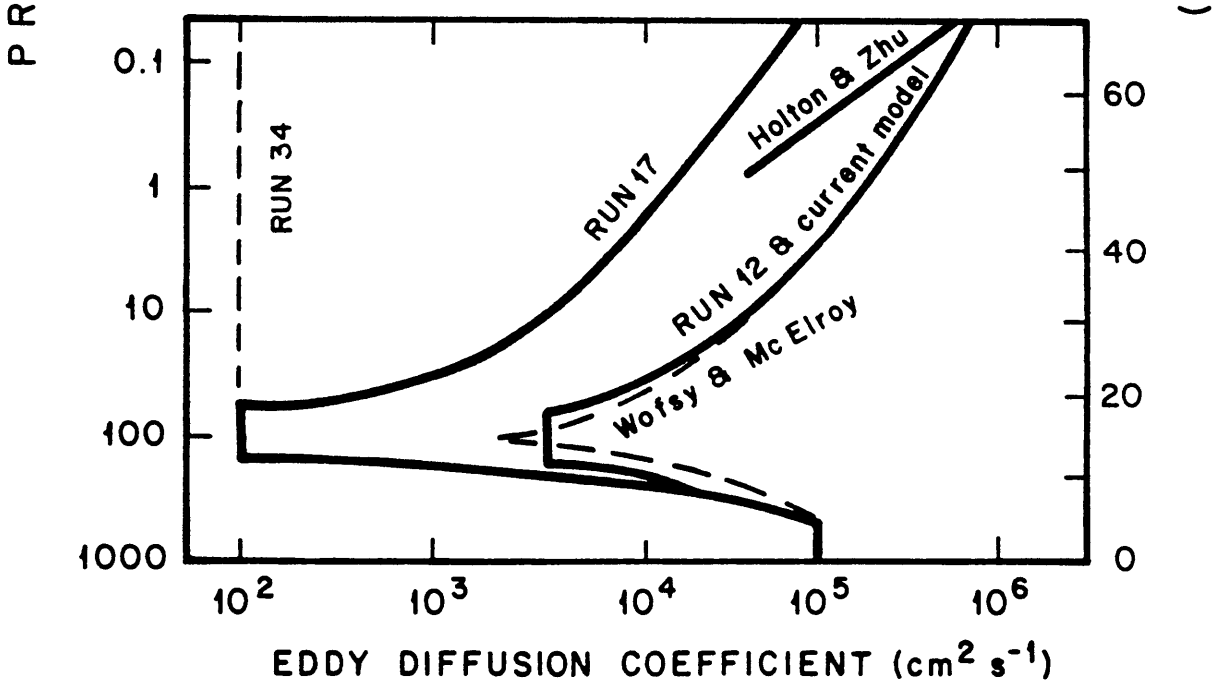
0.1
1
10
100
1000
60
40
20
0
RUN 34
RUN 17
Holton & Zhu
RUN 12 & current model
Wofsy & McElroy
10^{2}
10^{3}
10^{4}
10^{5}
10^{6}
EDDY DIFFUSION COEFFICIENT ($cm^2\ s^{-1}$)

Fig. 2.4

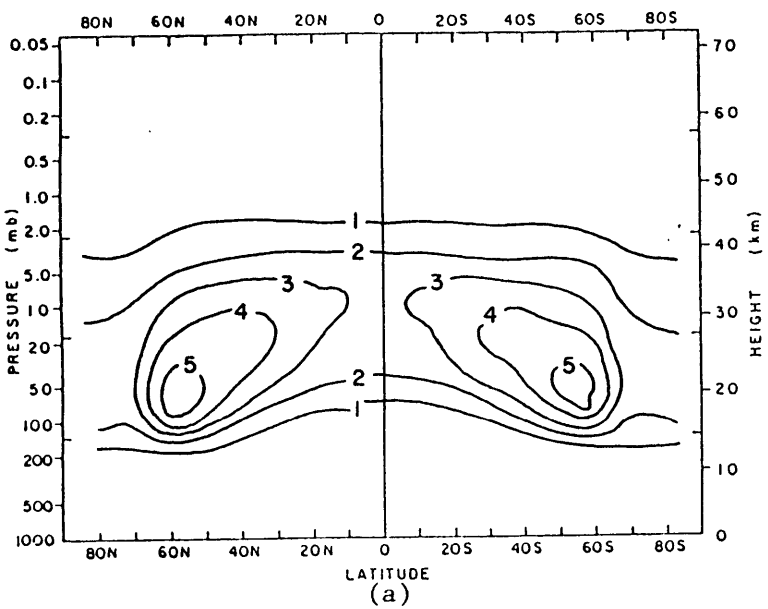

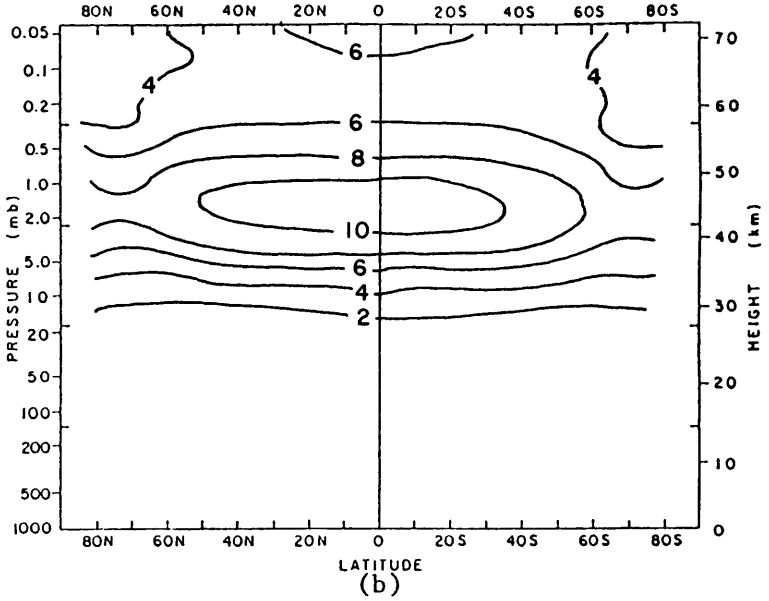

Figs. 2.5 (a) $[n_{NO_x}]$ (10^9 cm^{-3}), (b) $[n_{HO_x}]$ (10^7 cm^{-3}), (c) $[n_{ClO_x}]$ (10^7 cm^{-3})

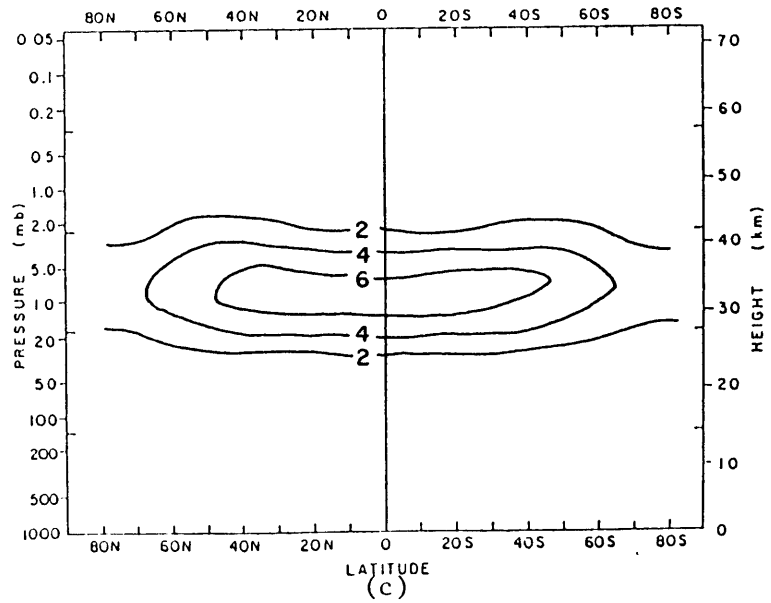

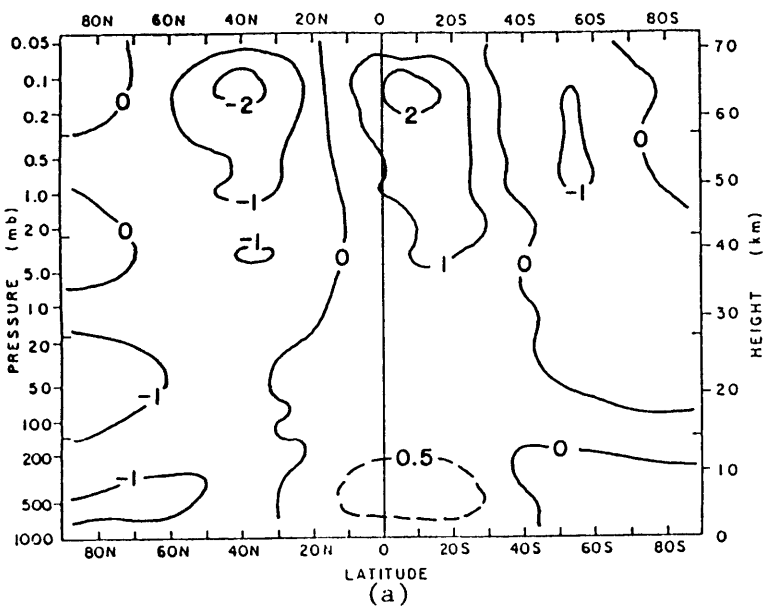

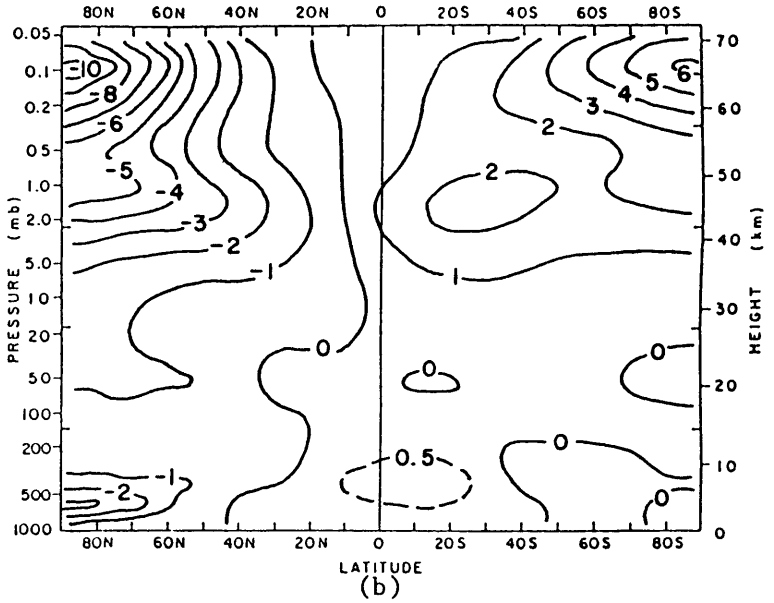

Figs. 3.1 [Q] (K/day) at Solstice for: (a) RUN34, (b) RUN35, (c) RUN36

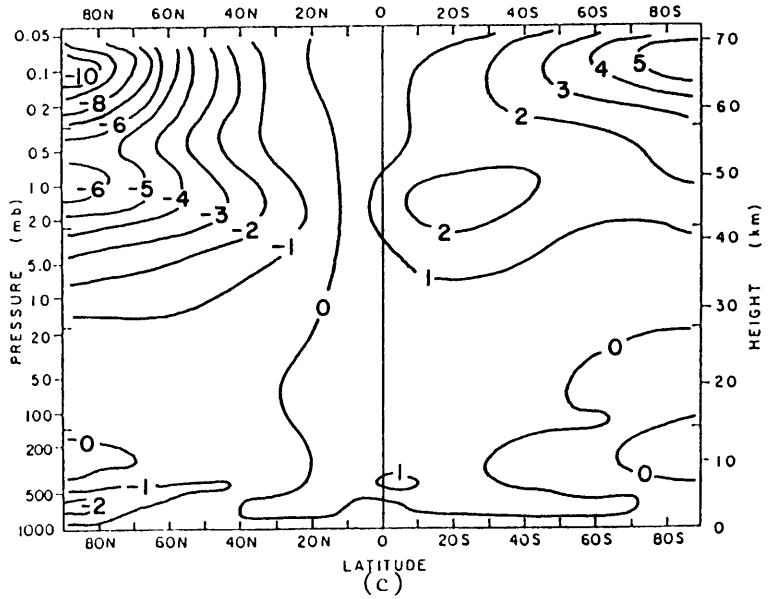

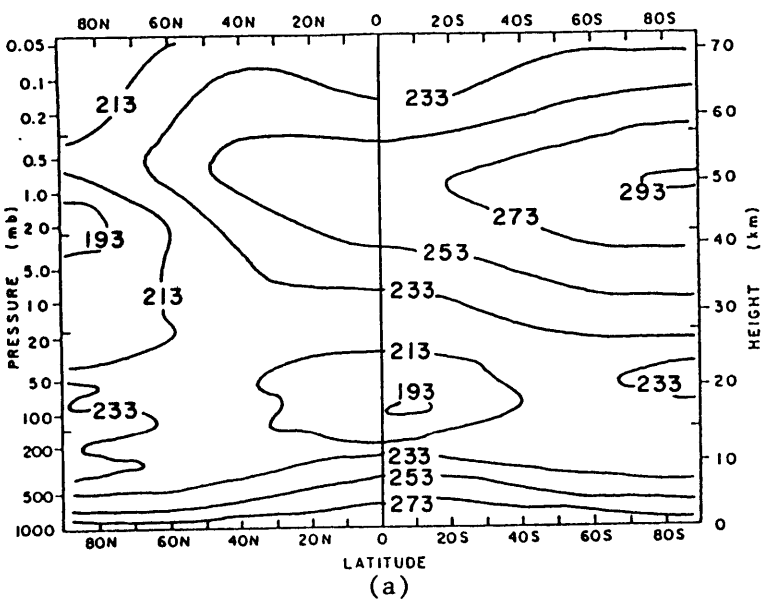

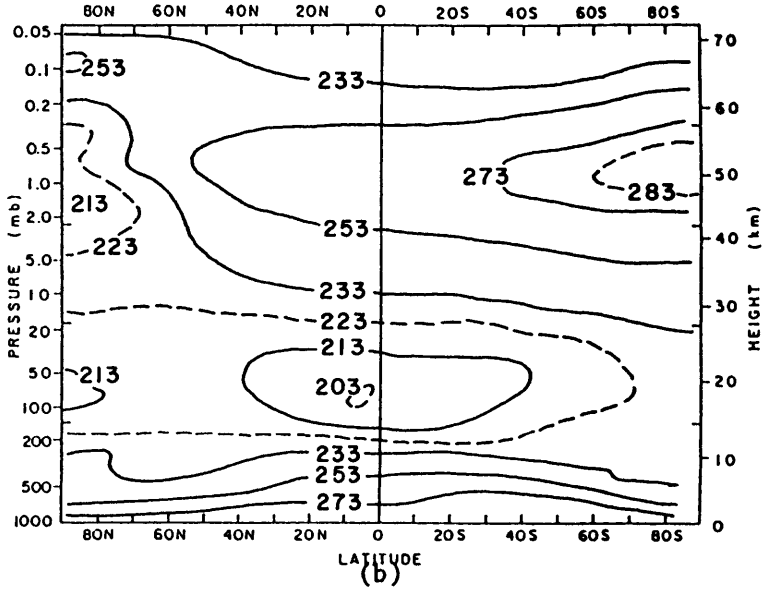

Figs. 3.2 [T] (K) at Solstice for: (a) RUN34, (b) RUN35, (c) RUN36, (d) Observations (after Newell, 1969)

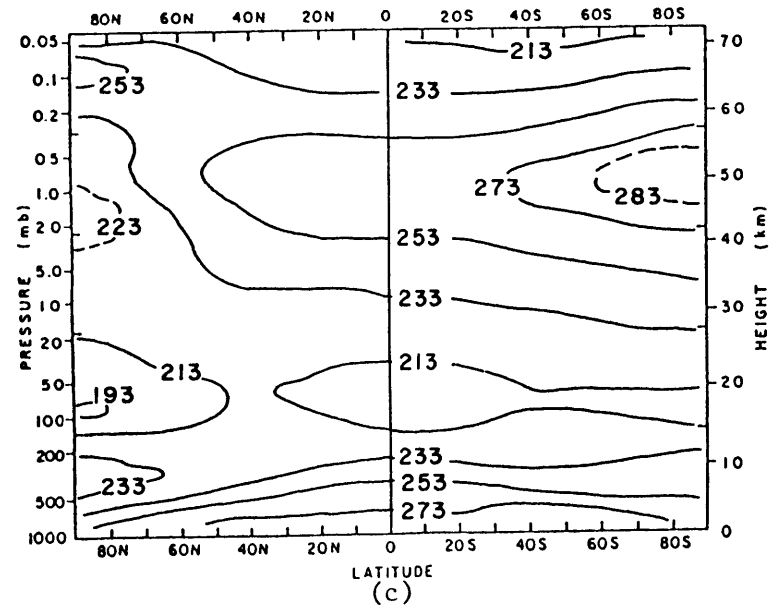

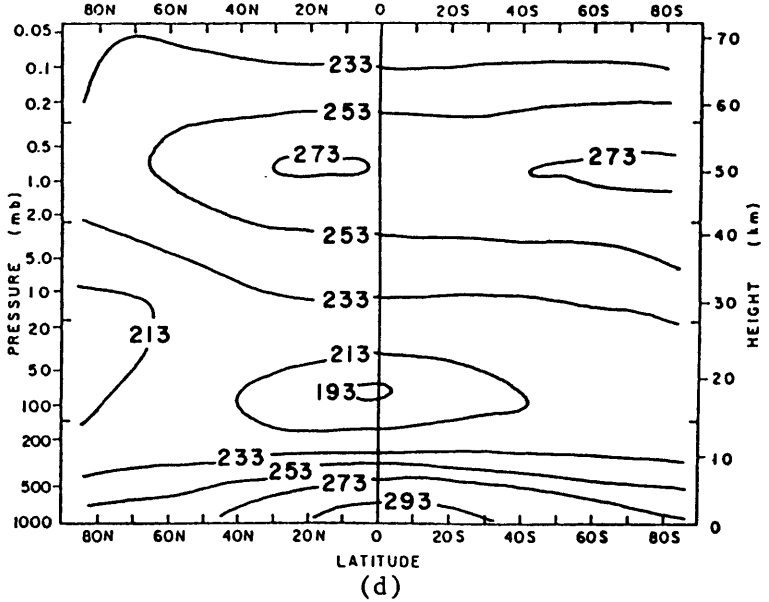

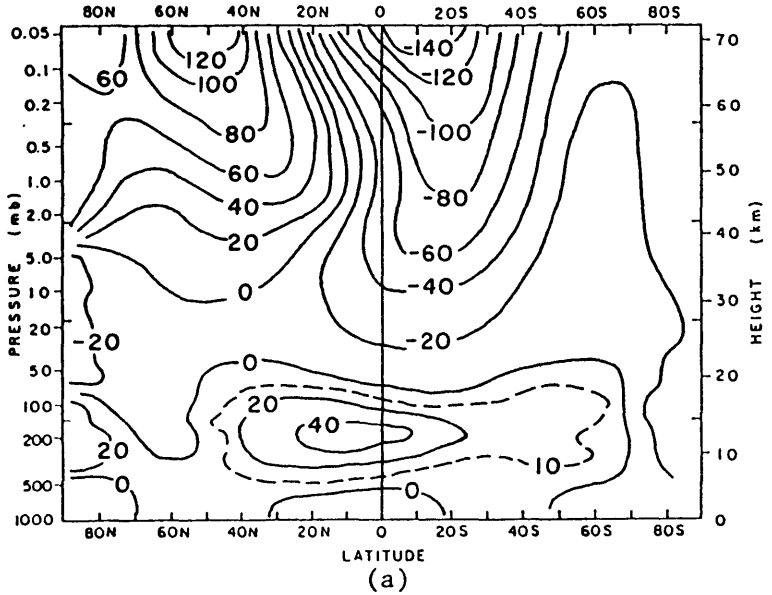

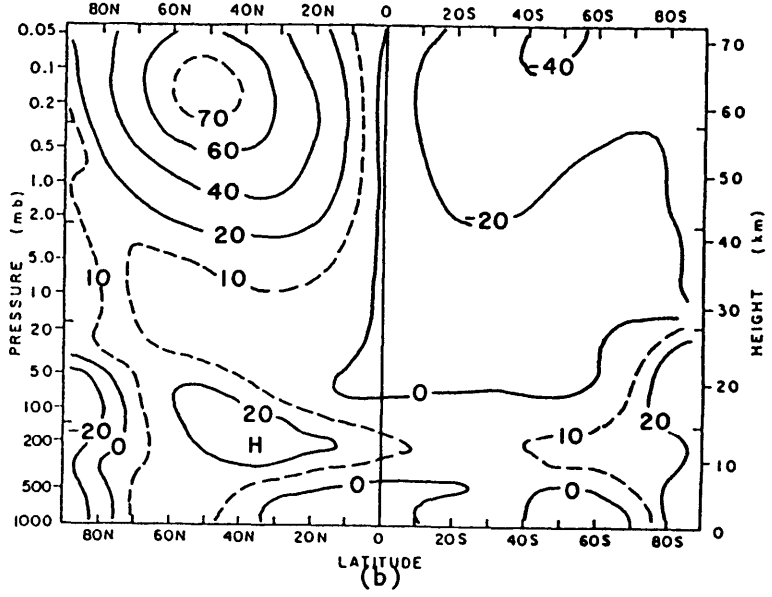

Figs. 3.3 [u] (m/s) at Solstice for: (a) RUN34, (b) RUN35, (c) RUN36, (d) Observations (after Newell, 1969)

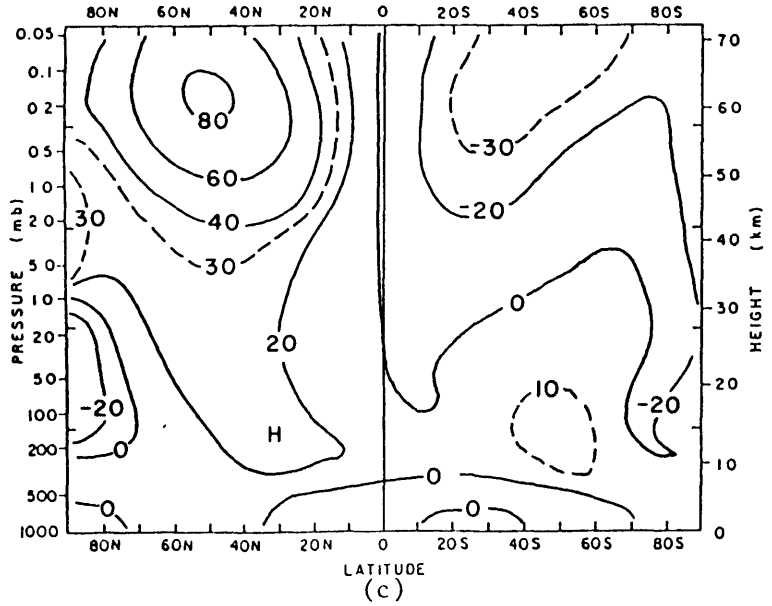

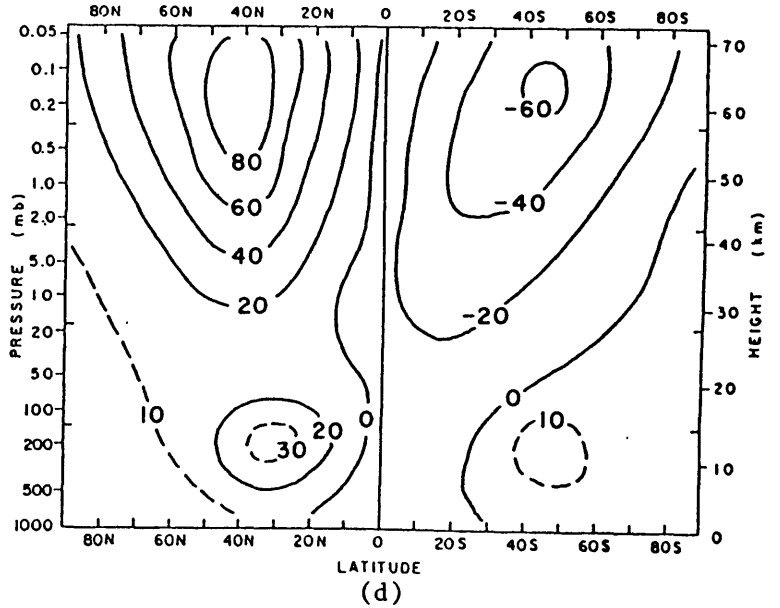

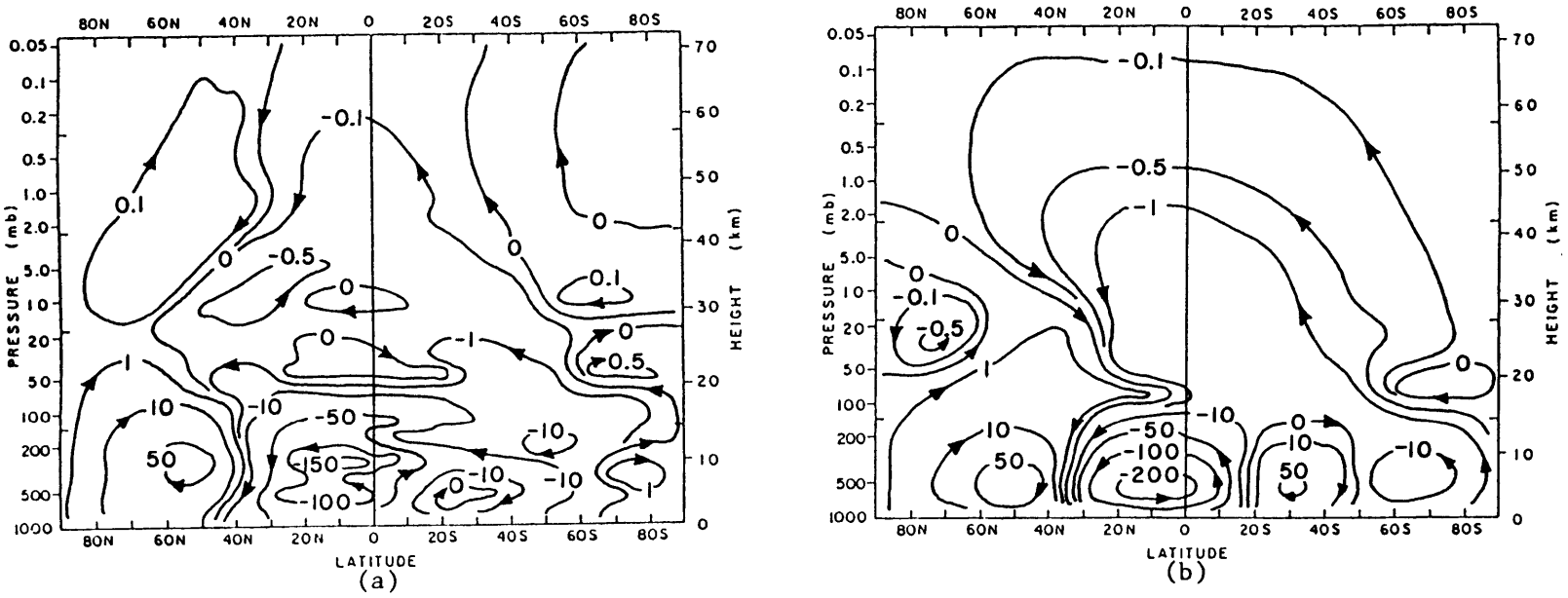

Figs. 3.4 X_M (10^{12} gm/s) at Solstice for: (a) RUN34, (b) RUN35, (c) RUN36

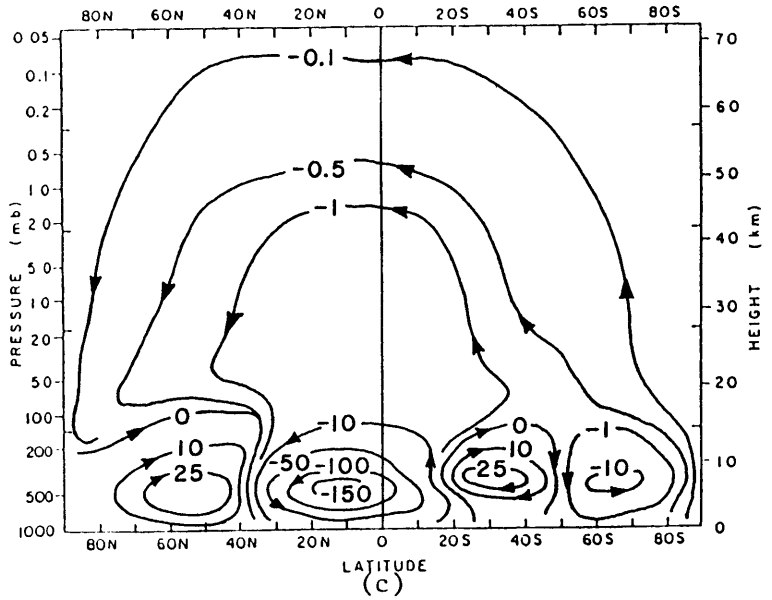

Fig. 3.4(d) X_M (10^{12} gm/s) Based on Observations for December-February (after Louis, 1975)

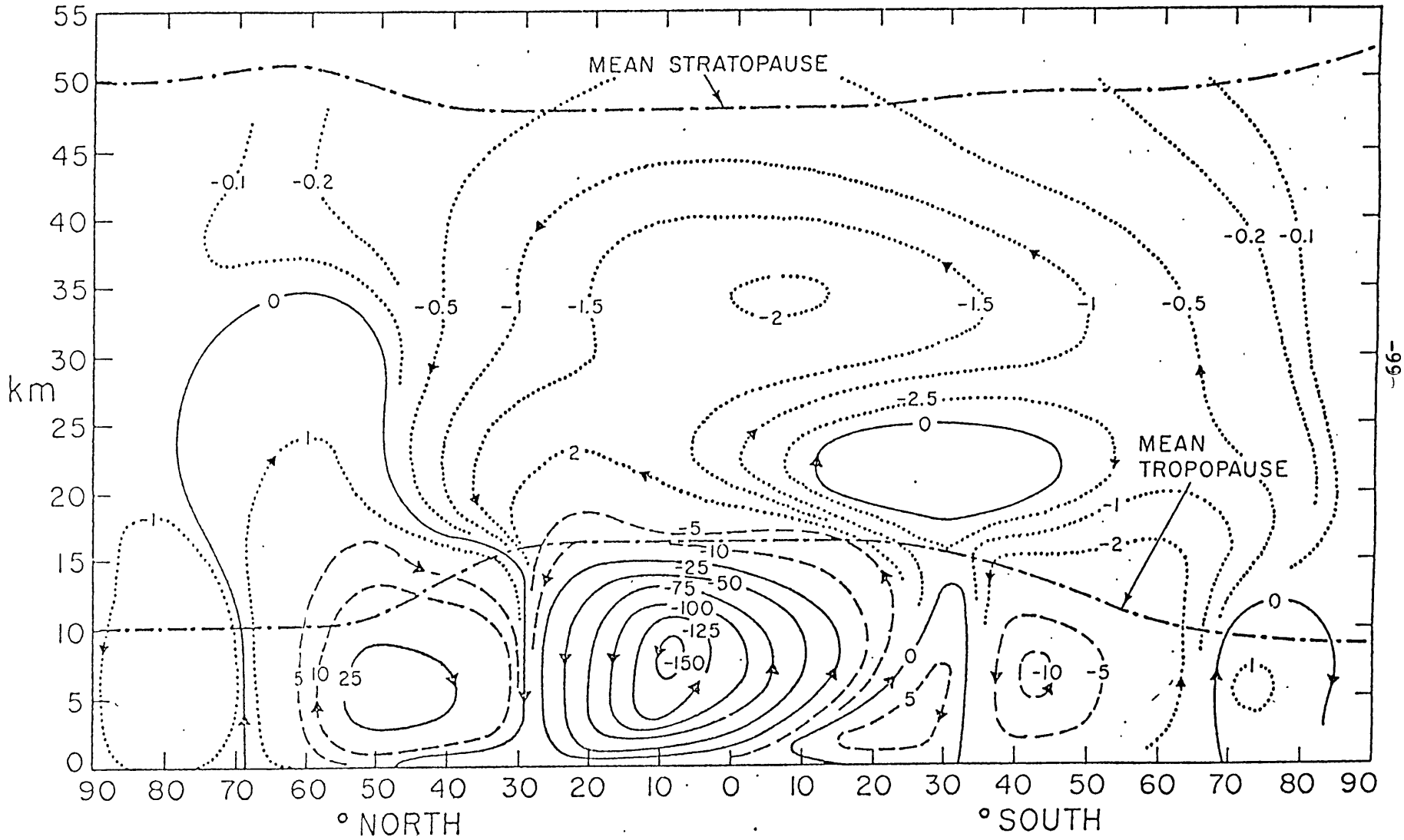

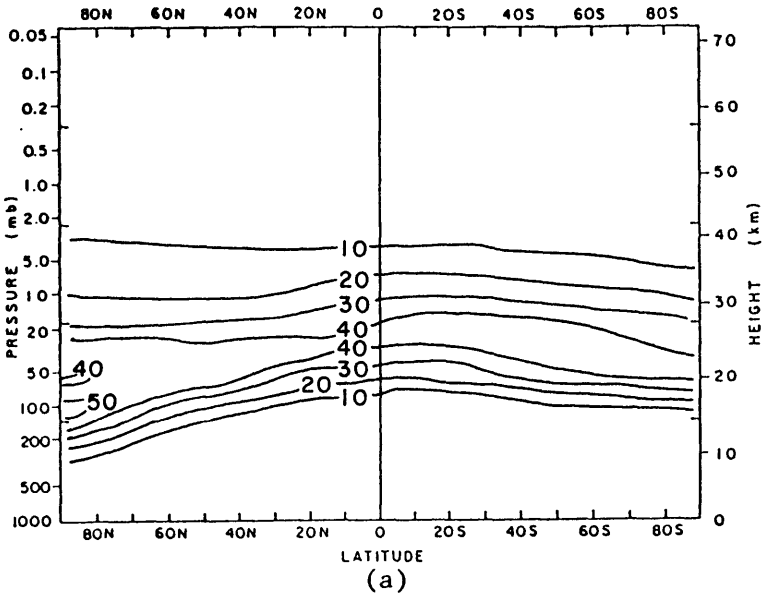

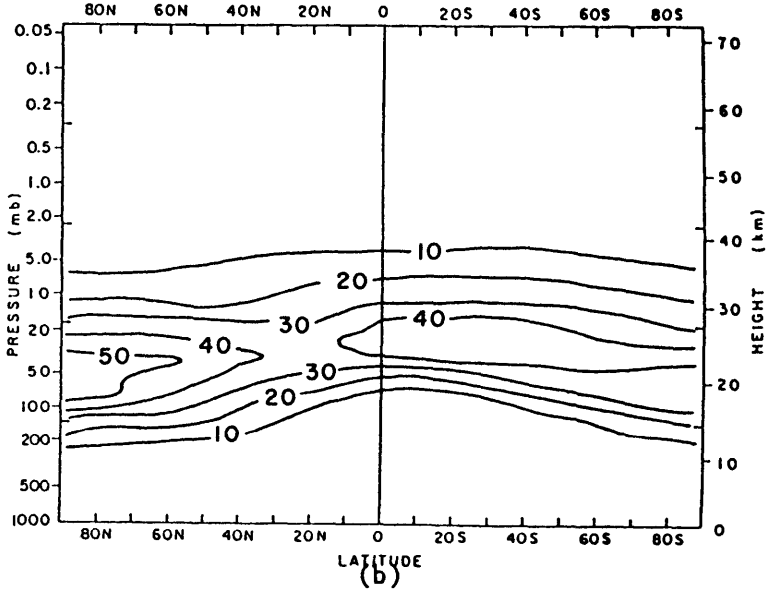

Figs. 3.5 $[n_{O_3}]$ (10^{11} cm^{-3}) at Solstice for: (a) RUN34, (b) RUN35, (c) RUN36, (d) Observations (after Wu,1973)

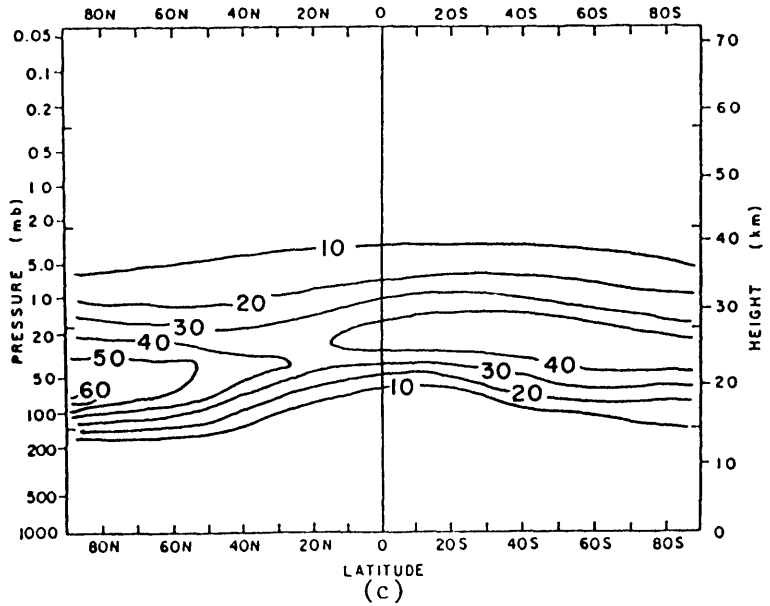

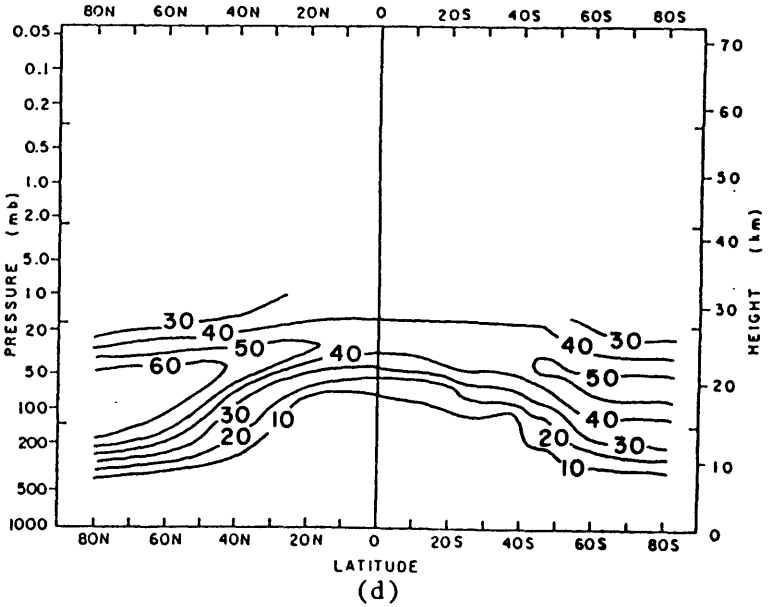

DECEMBER - FEBRUARY

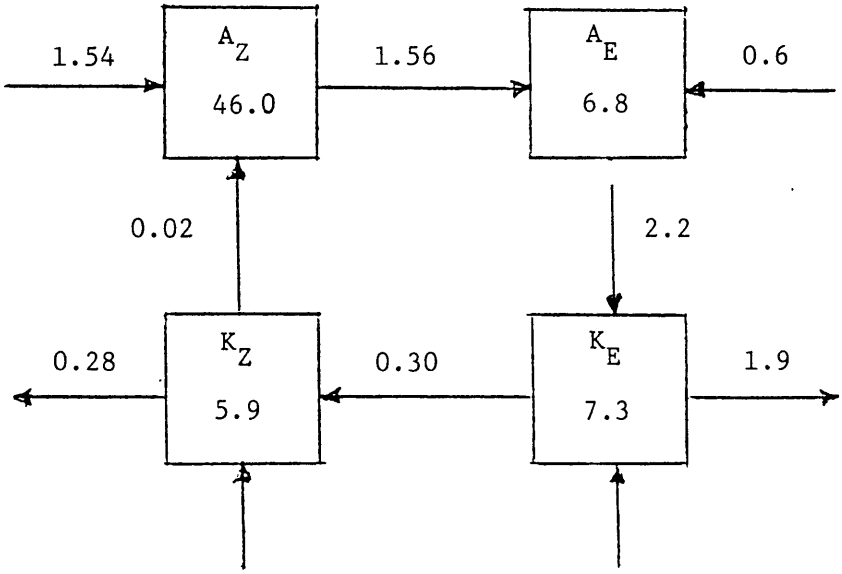

Units: 10^5 J/m^2, W/m^2

OBSERVED TROPOSPHERIC ENERGY CYCLE (Oort and Peixoto, 1983)

Fig. 3.6

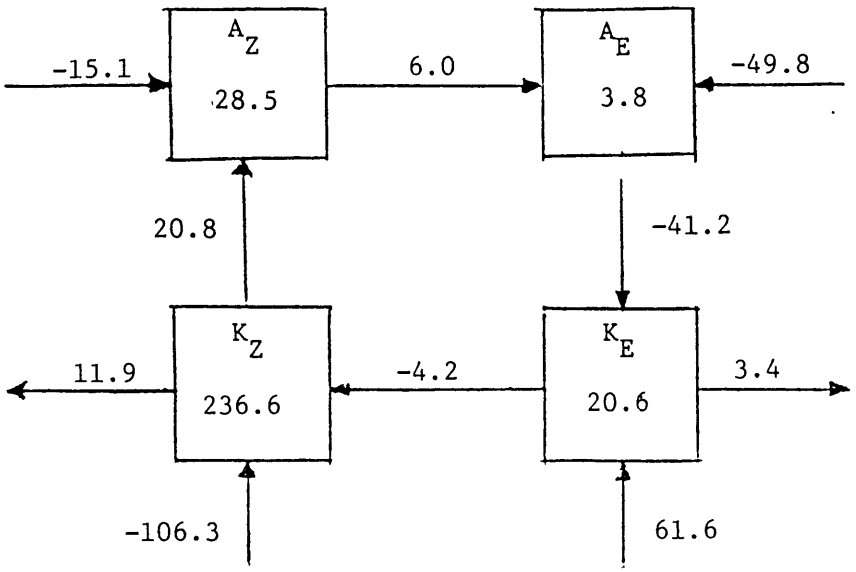

MESOSPHERE
(Levels 1-8)

Units: 10^2 J/m^2, 10^{-4} W/m^2

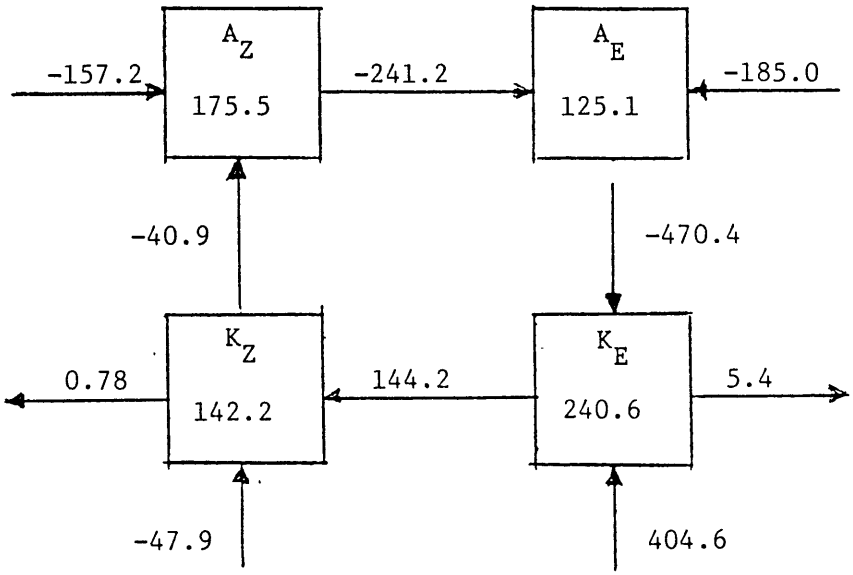

STRATOSPHERE
(Levels 9-19)

Units: 10^3 J/m^2, 10^{-3} W/m^2

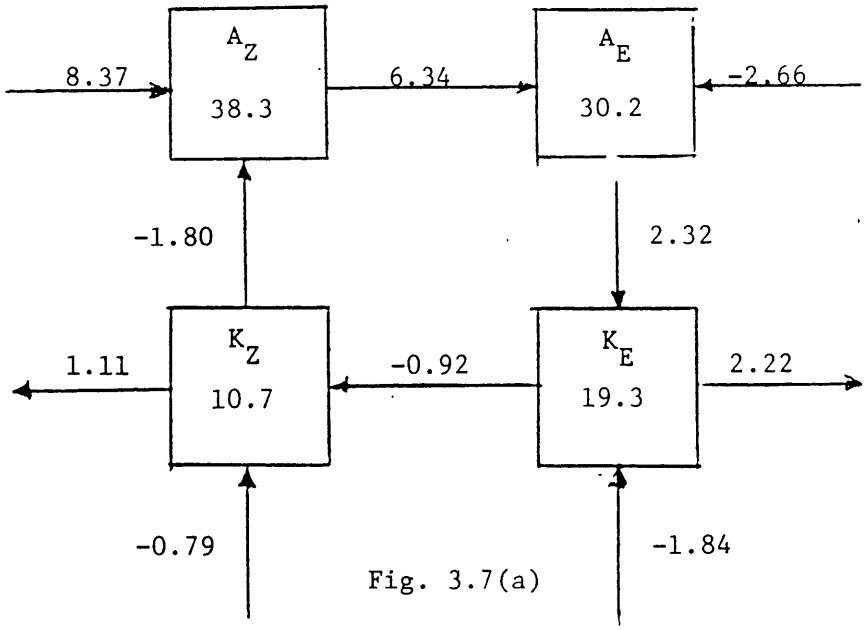

TROPOSPHERE
(Levels 20-26)

Units: 10^5 J/m^2, W/m^2

Fig. 3.7(a)

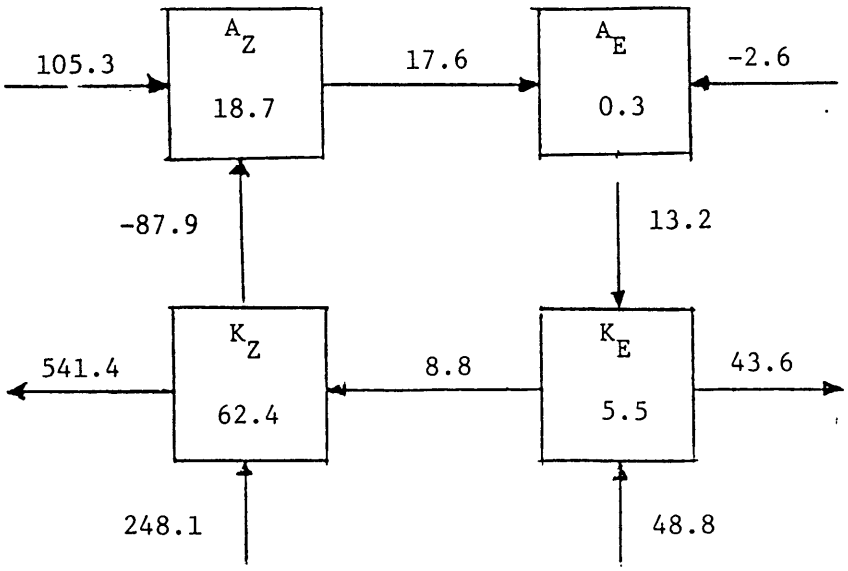

MESOSPHERE
(Levels 1-8)

Units: 10^2 J/m^2, 10^{-4} W/m^2

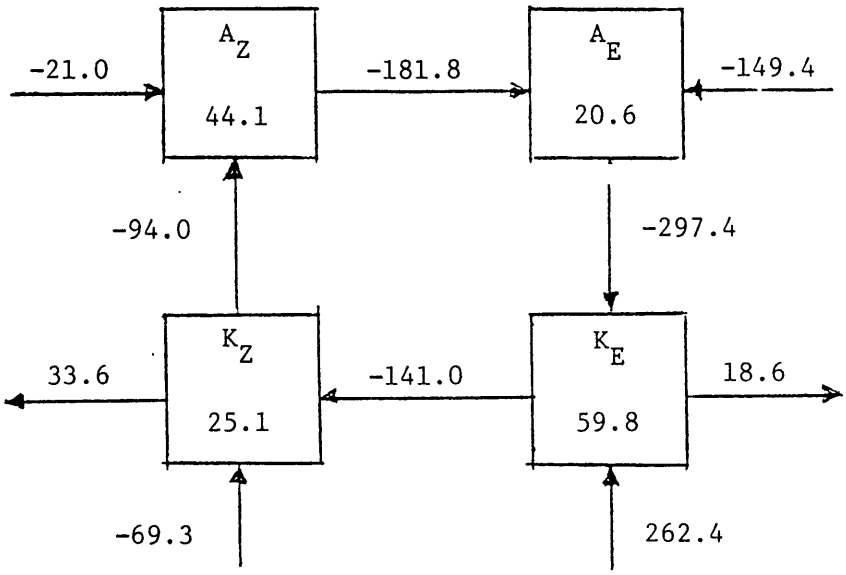

STRATOSPHERE
(Levels 9-19)

Units: 10^3 J/m^2, 10^{-3} W/m^2

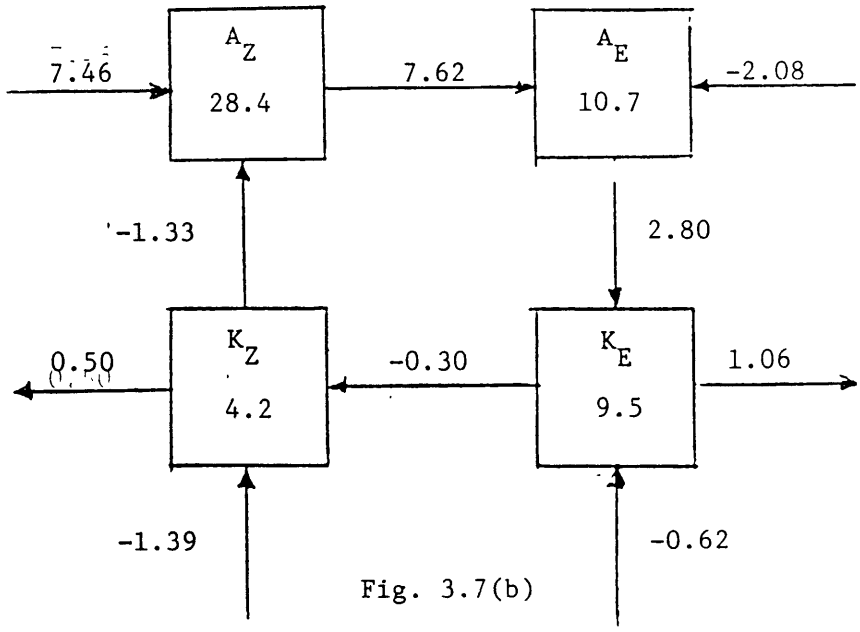

TROPOSPHERE
(Levels 20-26)

Units: 10^5 J/m^2, W/m^2

Fig. 3.7(b)

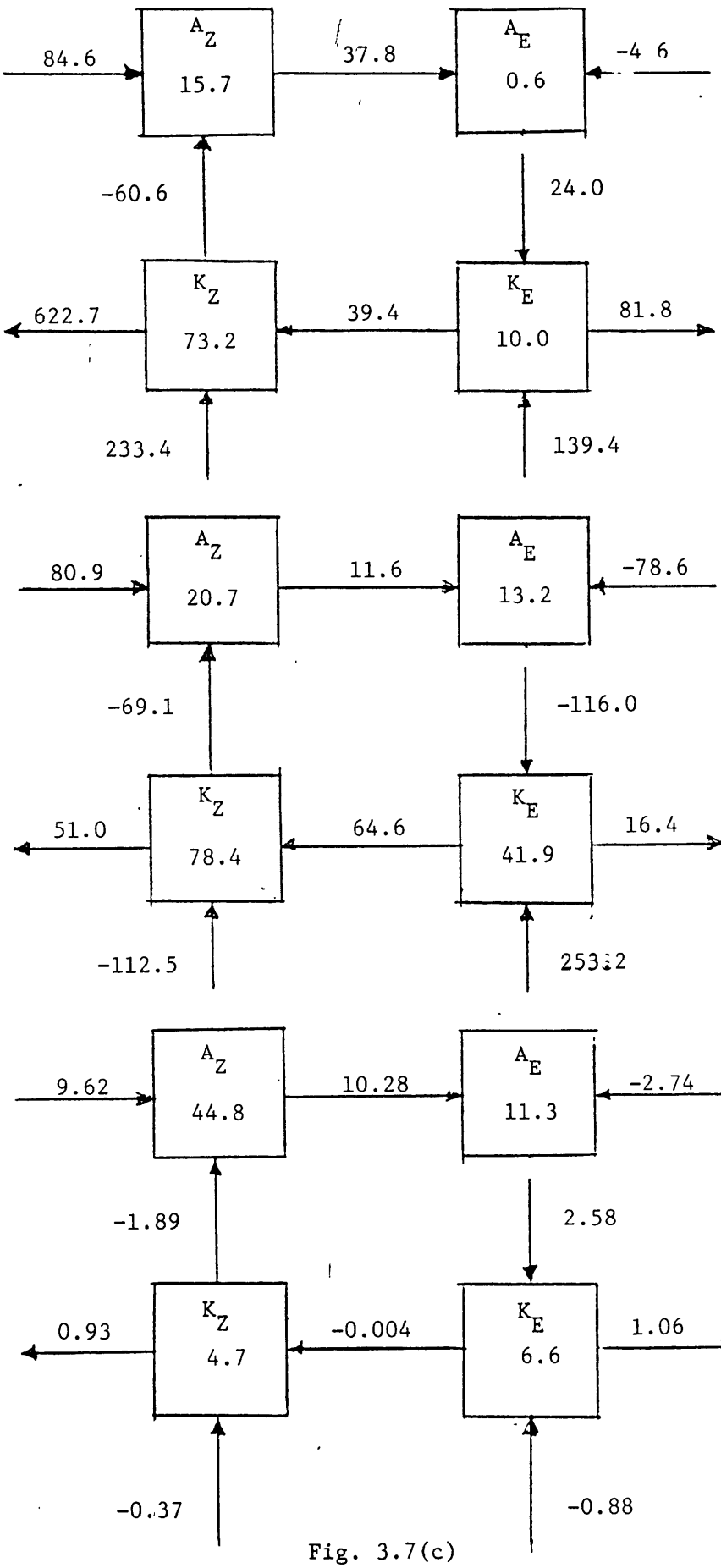
MESOSPHERE
(Levels 1-8)
A_Z 15.7
A_E 0.6
84.6
37.8
-4 6
-60.6
24.0
K_Z 73.2
K_E 10.0
622.7
39.4
81.8
233.4
139.4
Units: 10^2 J/m^2, 10^{-4} W/m^2
STRATOSPHERE
(Levels 9-19)
A_Z 20.7
A_E 13.2
80.9
11.6
-78.6
-69.1
-116.0
K_Z 78.4
K_E 41.9
51.0
64.6
16.4
-112.5
Units: 10^3 J/m^2, 10^{-3} W/m^2
TROPOSPHERE
(Levels 20-26)
A_Z 44.8
A_E 11.3
9.62
10.28
-2.74
-1.89
2.58
K_Z 4.7
K_E 6.6
0.93
-0.004
1.06
-0.37
-0.88
Units: 10^5 J/m^2, W/m^2

Fig. 3.7(c)

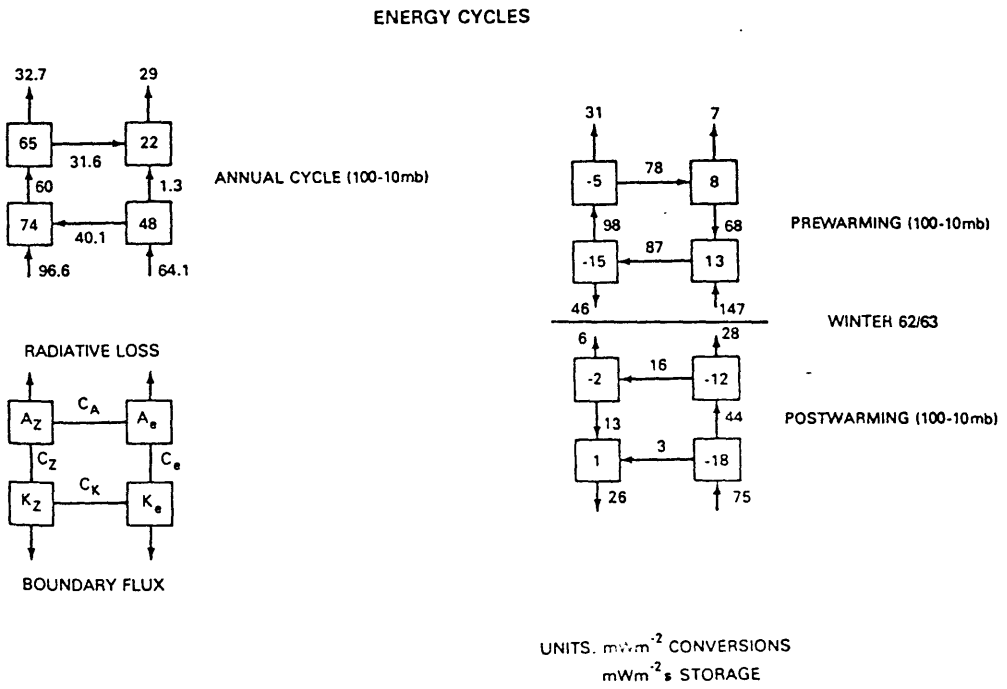

Fig. 3.8: Observed Stratospheric Energy Cycles (after Julian and Labitzke, 1965)

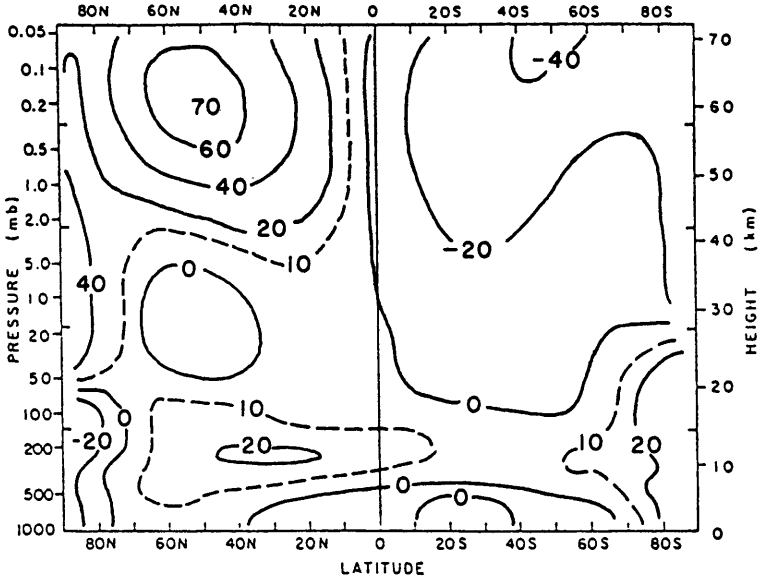

(a)

Figs. 3.9 RUN35 [u] (m/s) for: (a) day 35, (b) day 40

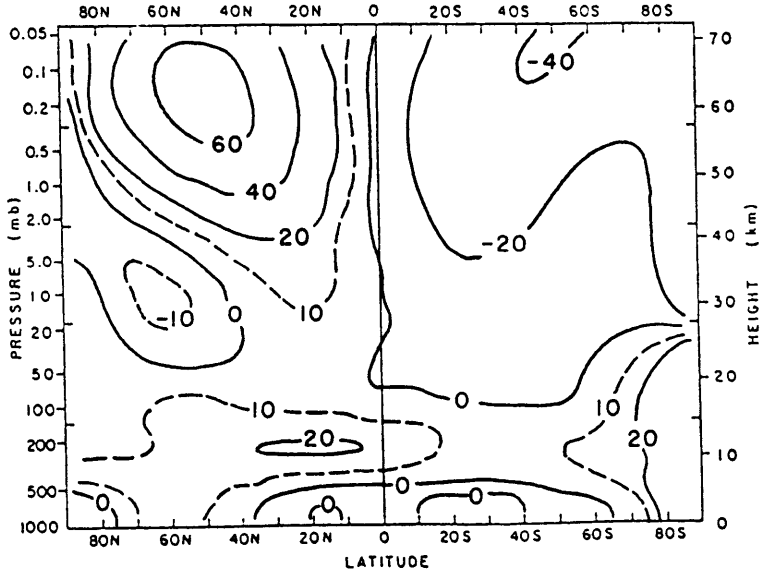

(b)

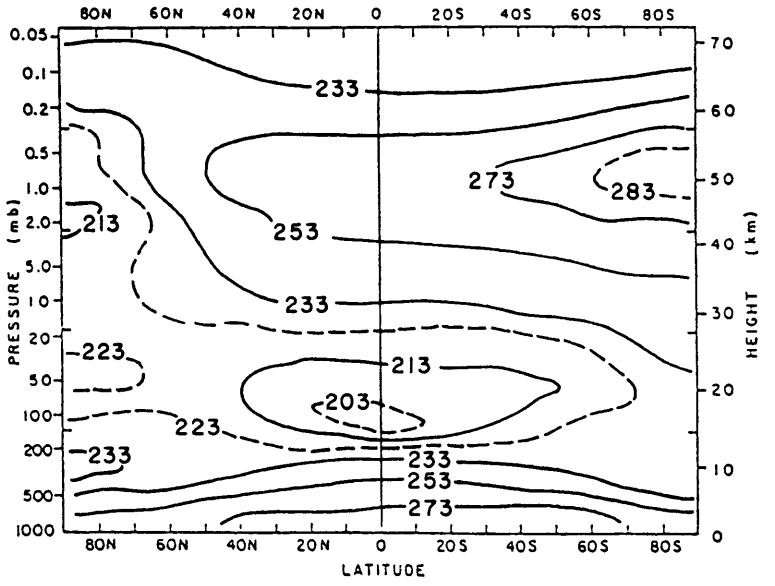

(a)

Figs. 3.10 RUN35 [T] (K) for: (a) day 35, (b) day 40

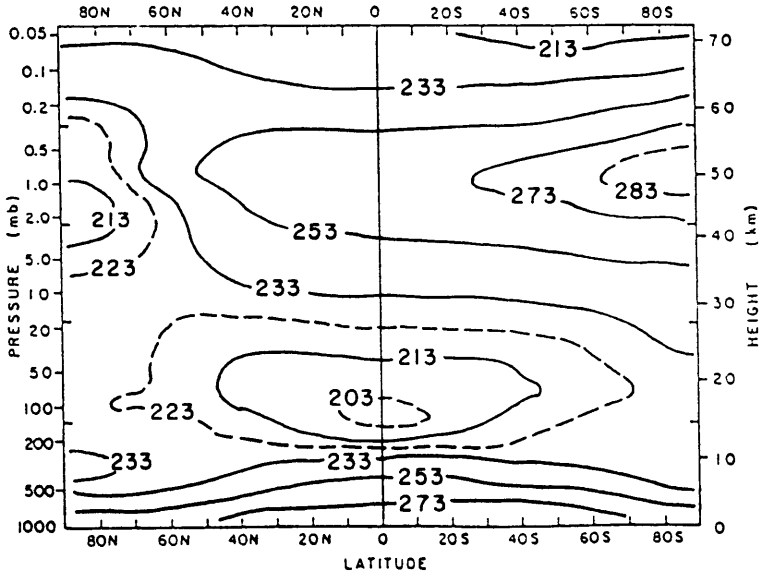

(b)

Fig. 3.11: RUN35 [u] (m/s) at 50N

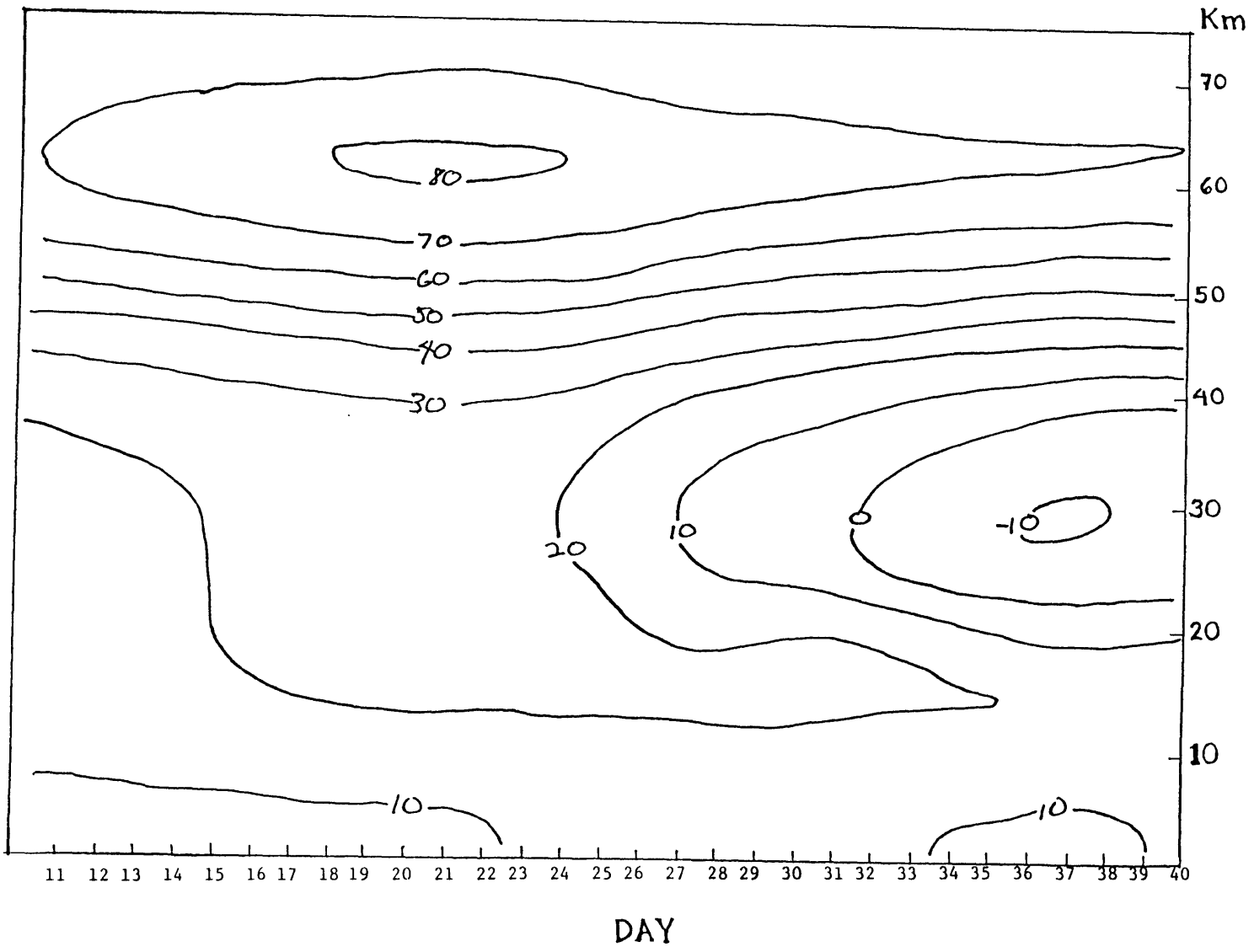

Fig. 3.12: RUN35 Wavenumber 1 Amplitude (gpm) at 50N

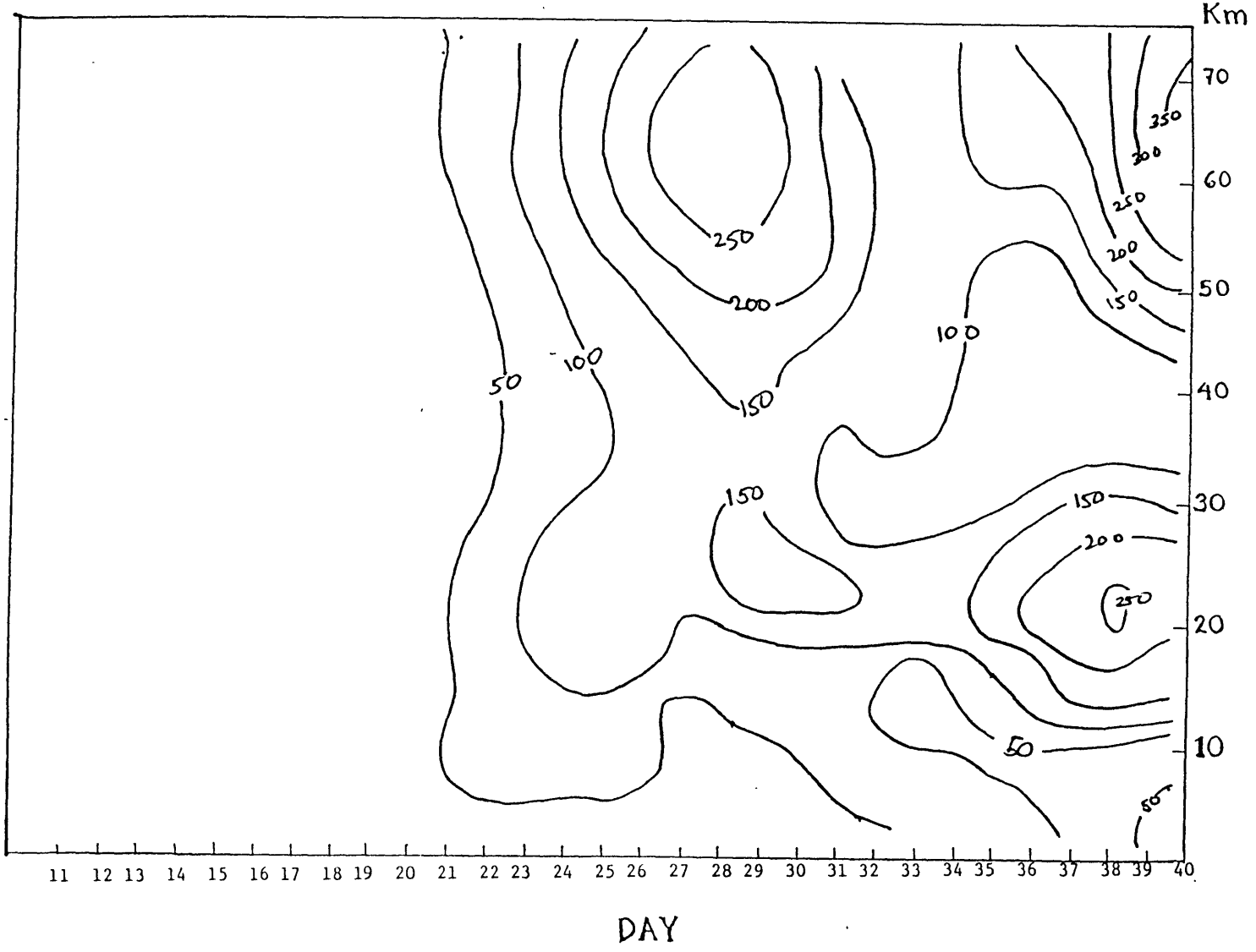

Fig. 3.13: RUN35 Wavenumber 2 Amplitude (gpm) at 50N

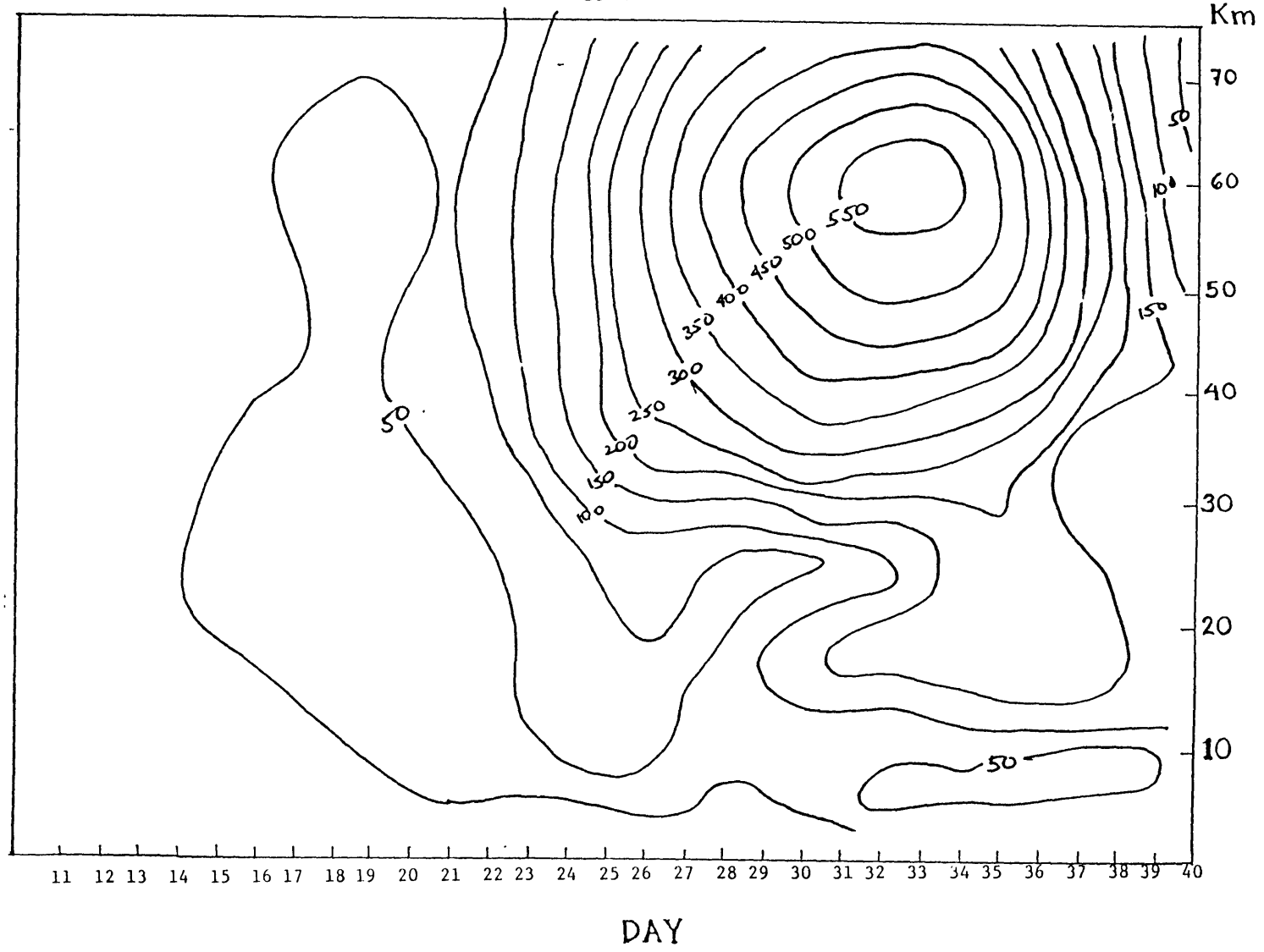

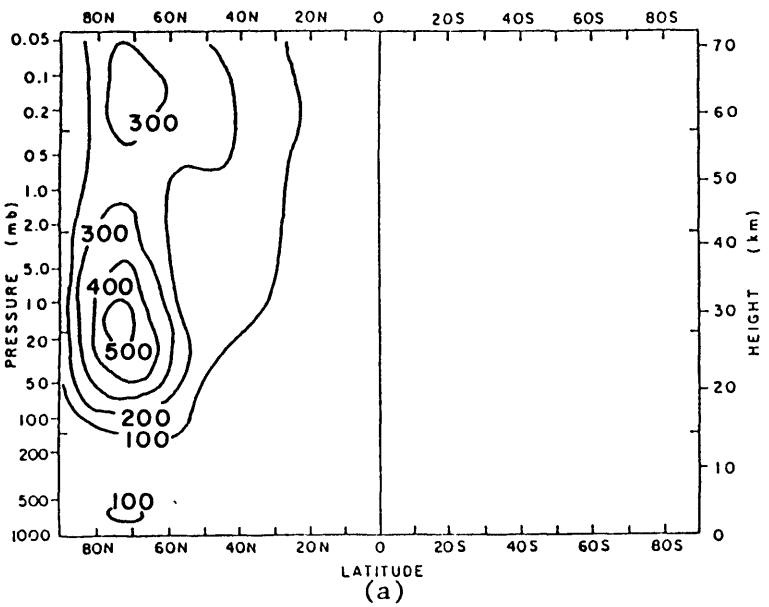

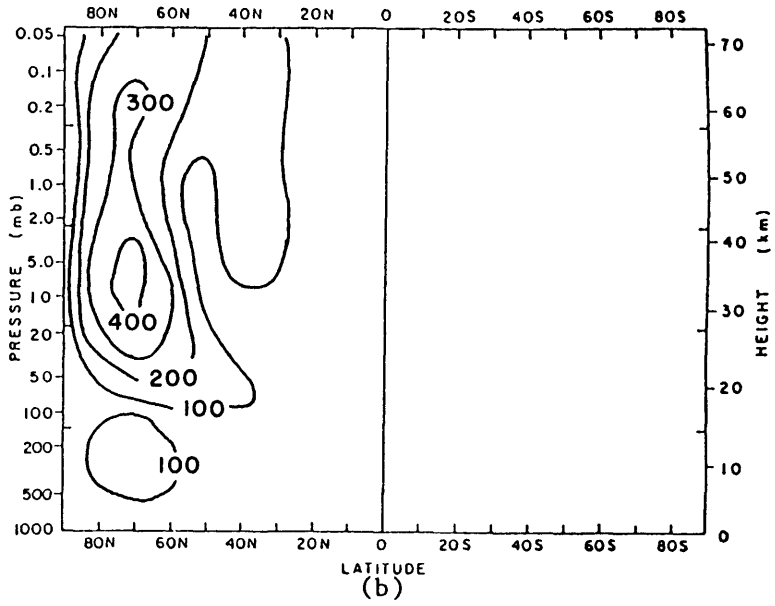

Figs. 3.14 RUN35 Wavenumber 1 Amplitude (gpm) for: (a) day 30, (b) day 35, (c) day 40

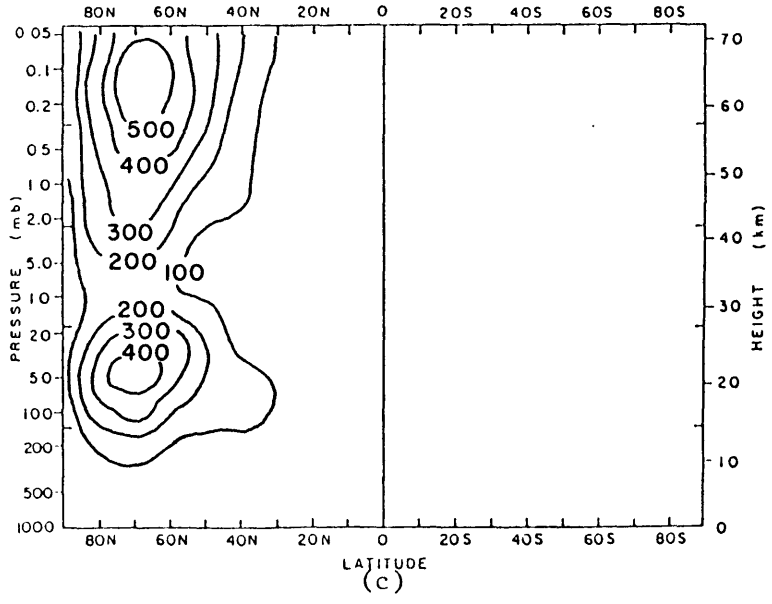

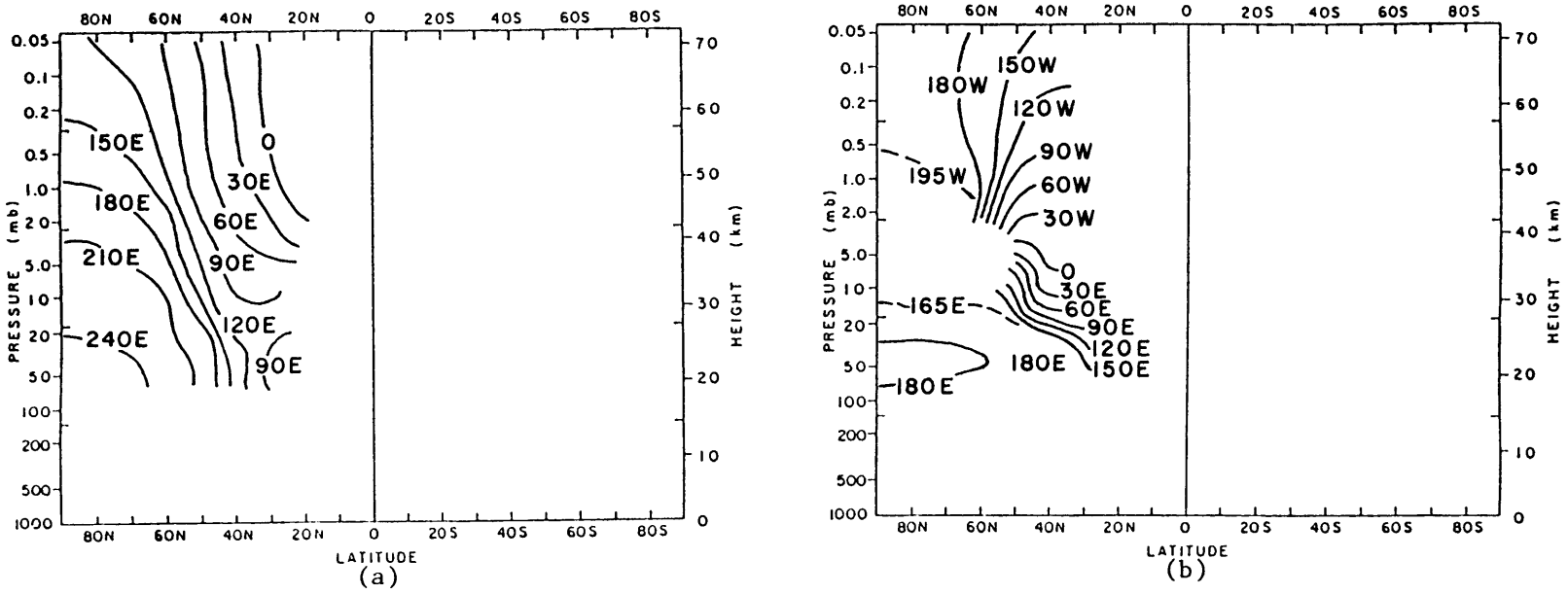

Figs. 3.15 RUN35 Wavenumber 1 Phase (deg) for: (a) day 30, (b) day 35, (c) day 40

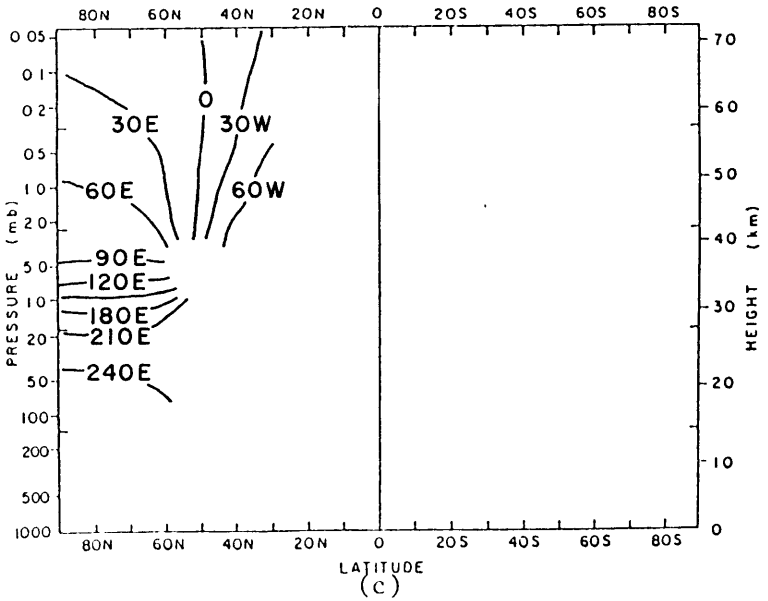

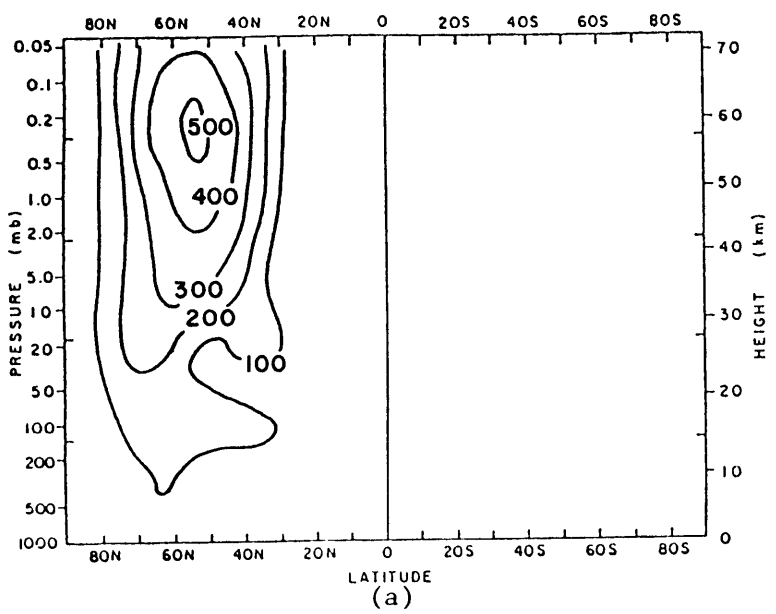

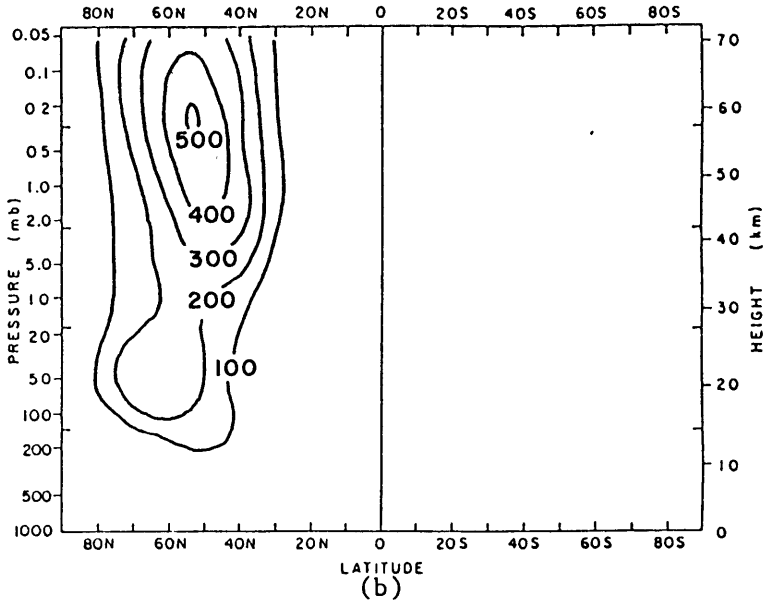

Figs. 3.16 RUN35 Wavenumber 2 Amplitude (gpm) for: (a) day 30, (b) day 35, (c) day 40

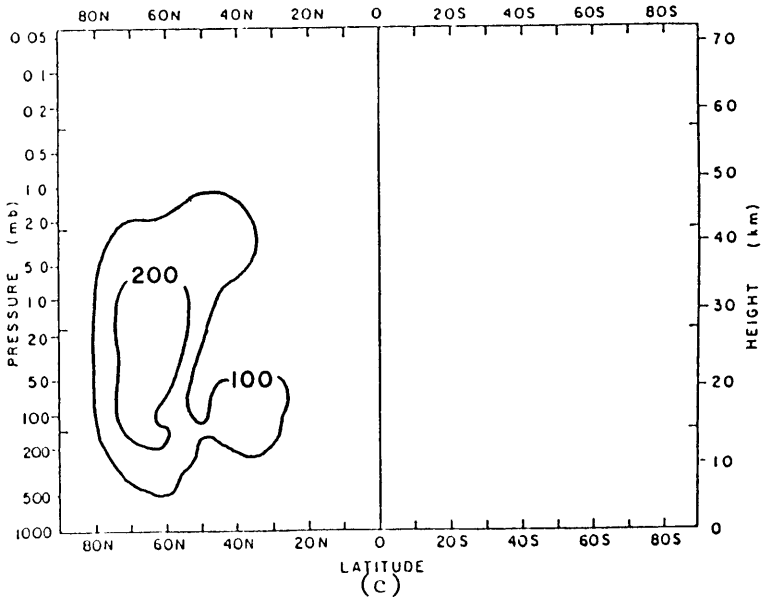

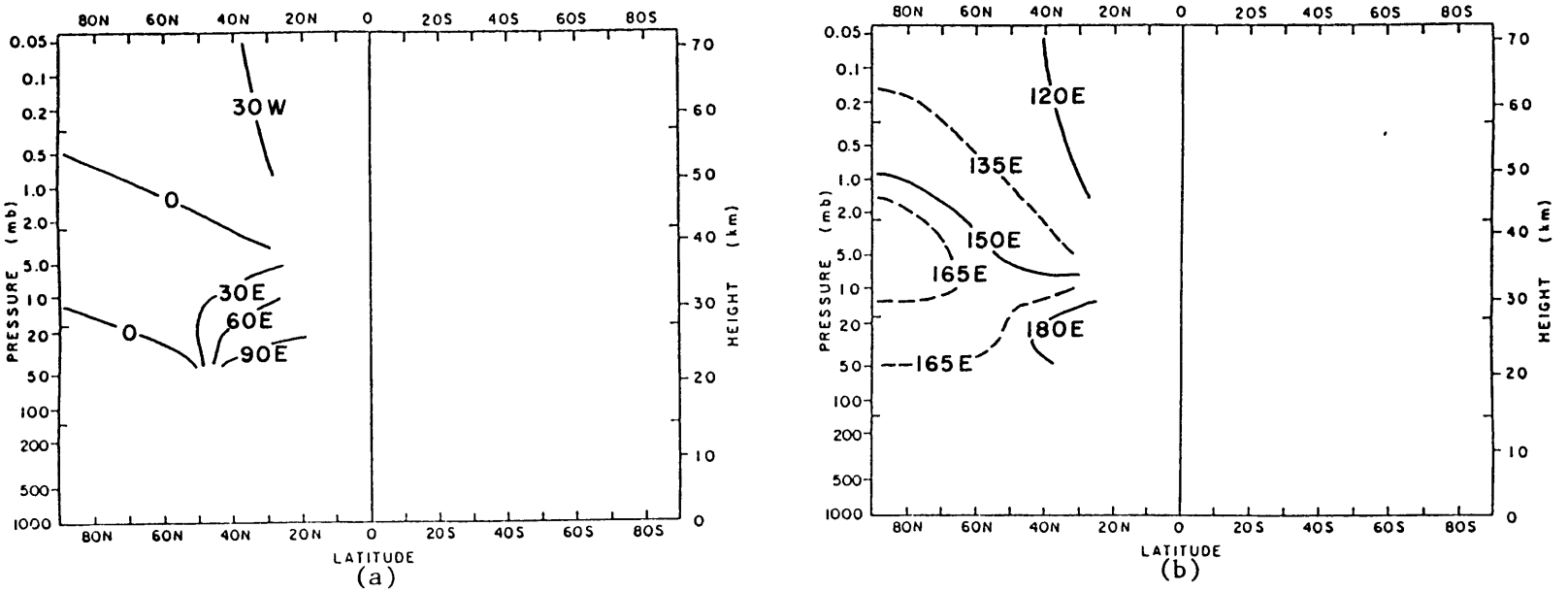

Figs. 3.17 RUN35 Wavenumber 2 Phase (deg) for: (a) day 30, (b) day 35, (c) day 40

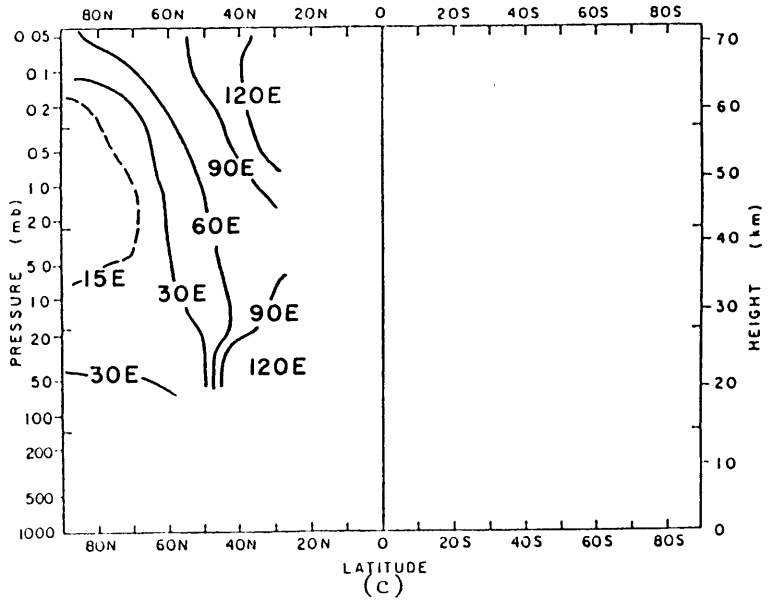

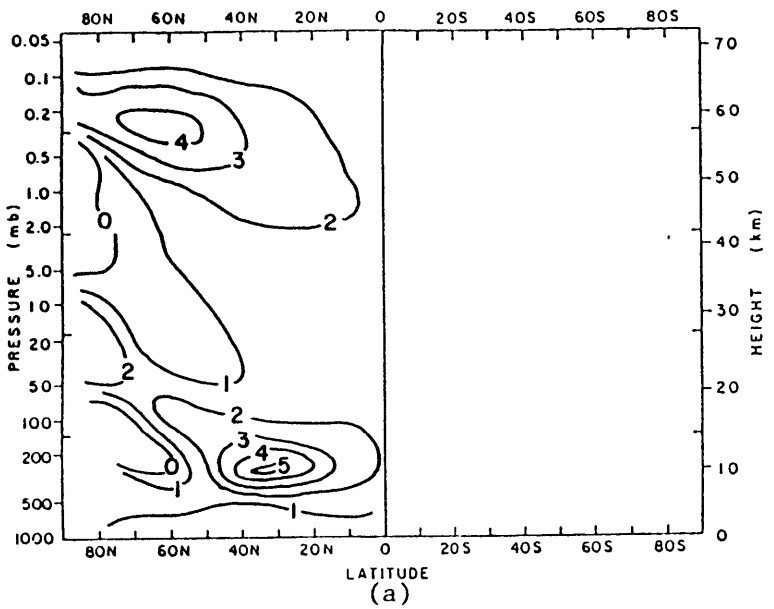

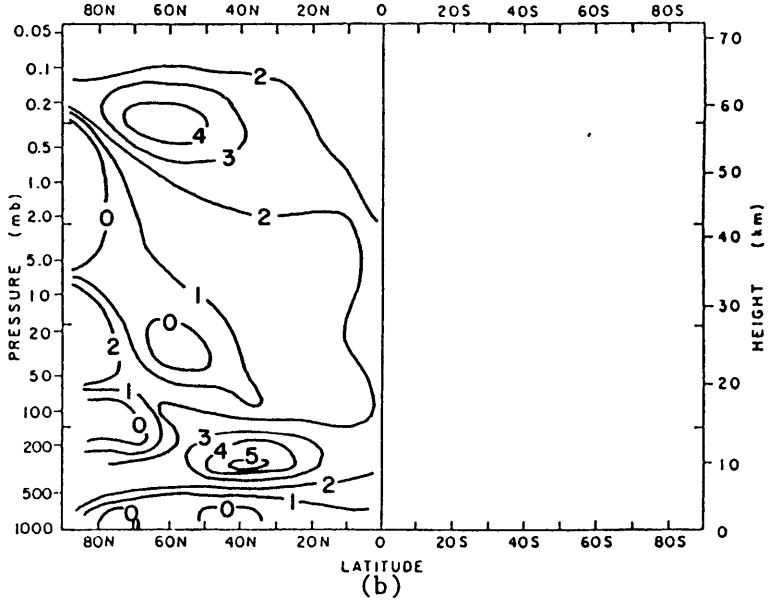

Figs. 3.18 RUN35 Latitudinal gradient of potential vorticity (units of omega) for: (a) day 30, (b) day 35, (c) day 40

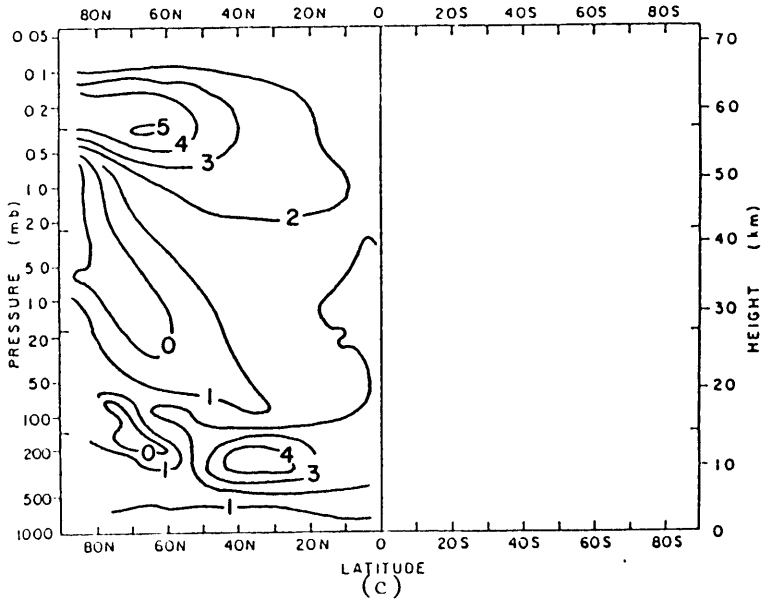

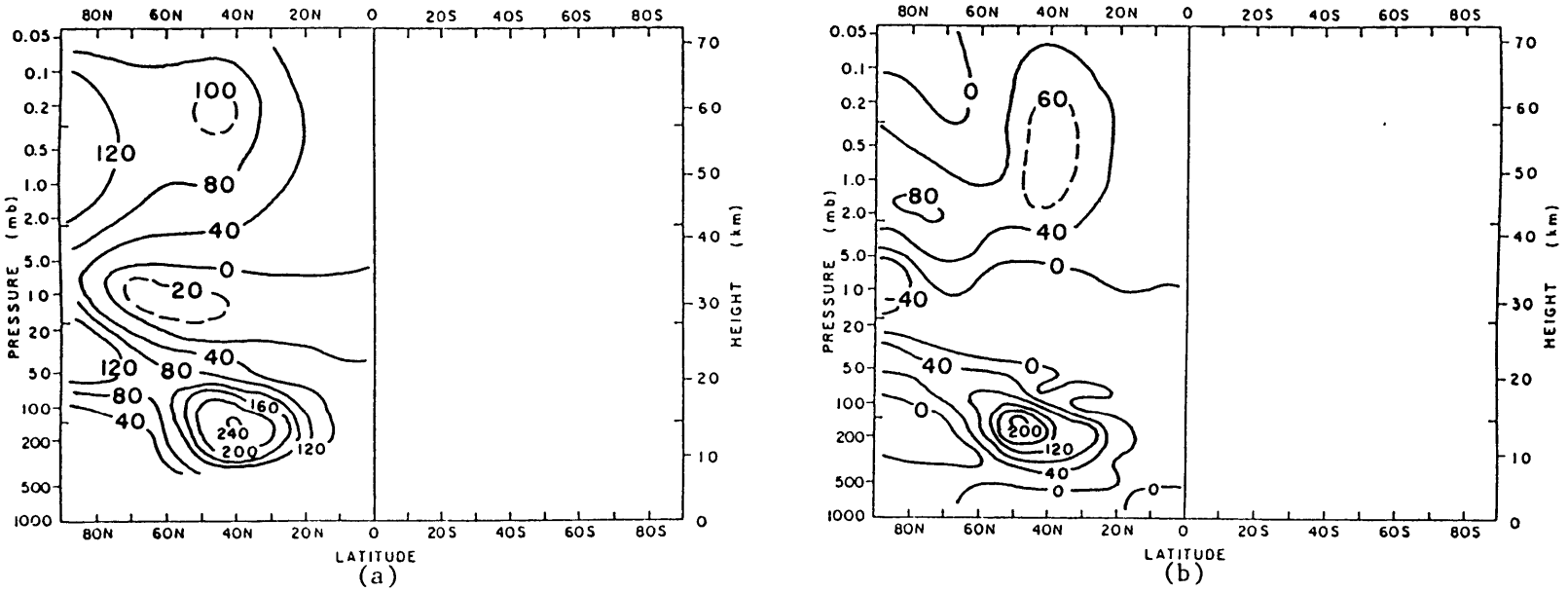

Figs. 3.19 RUN35 $[u^* v^*]$ (m^2/s^2) for: (a) day 30, (b) day 35, (c) day 40

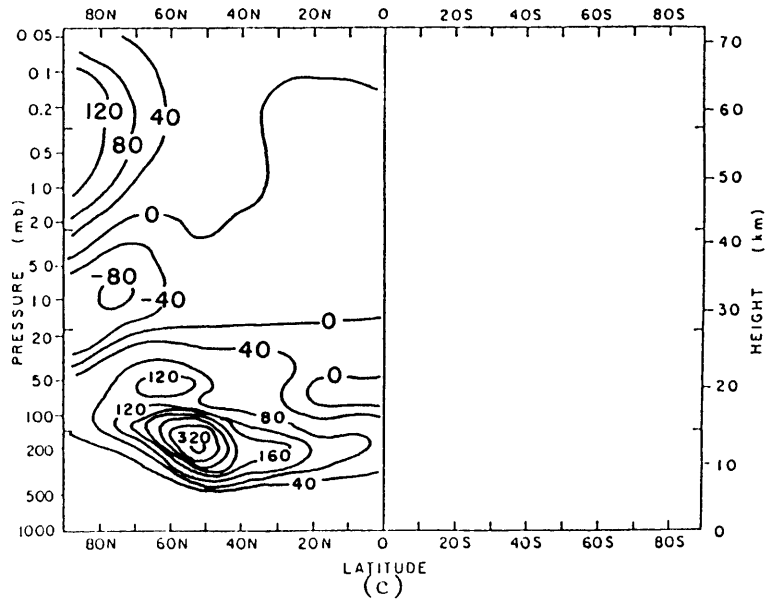

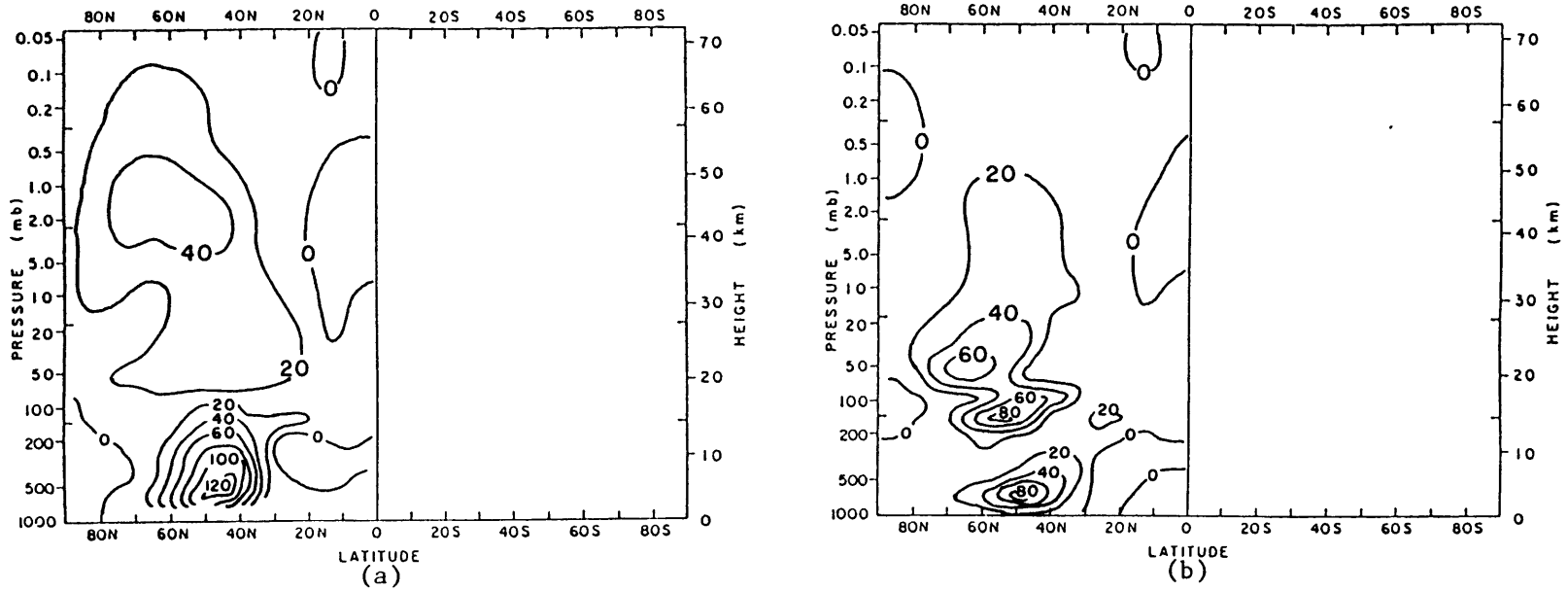

Figs. 3.20 RUN35 [$v^{*}T^{*}$] (K-m/s) for: (a) day 30, (b) day 35, (c) day 40

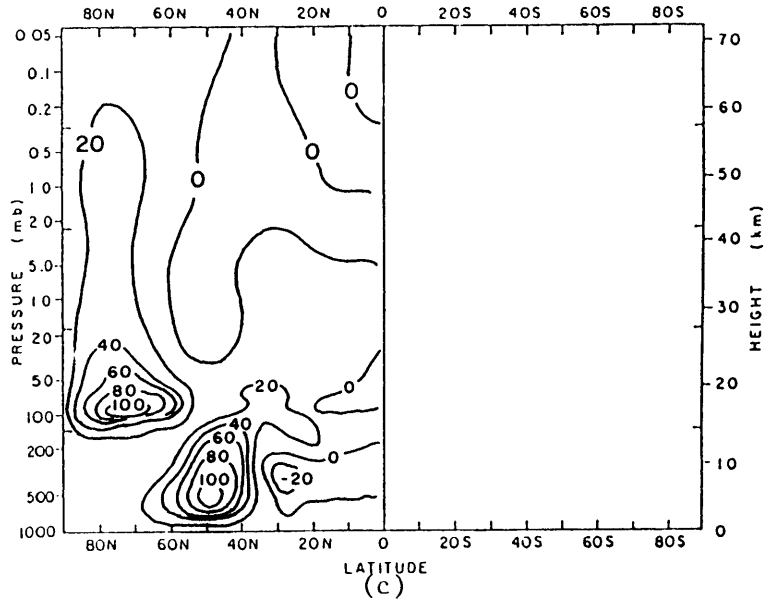

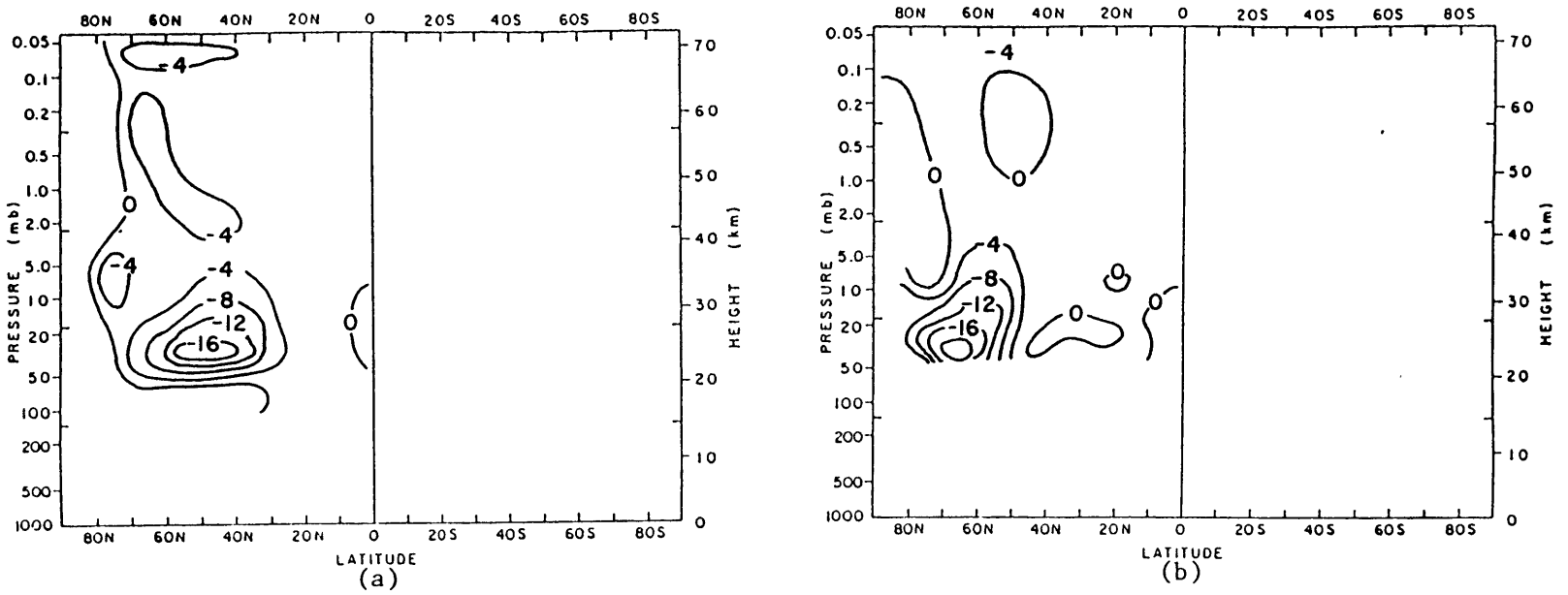

Figs. 3.21 RUN35 Eliassen-Palm flux divergence (10^{-5} m/s^2) for: (a) day 30, (b) day 35, (c) day 40

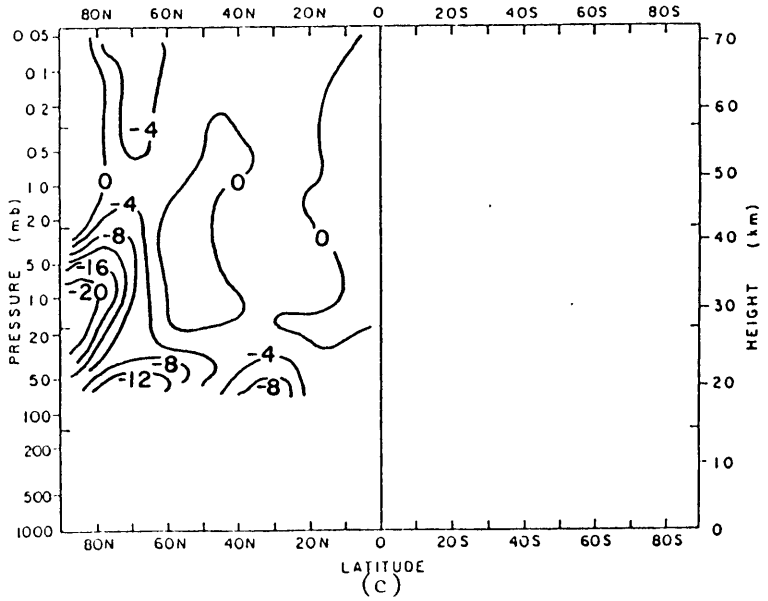

Fig. 3.22: RUN36 [u] (m/s) at 50N

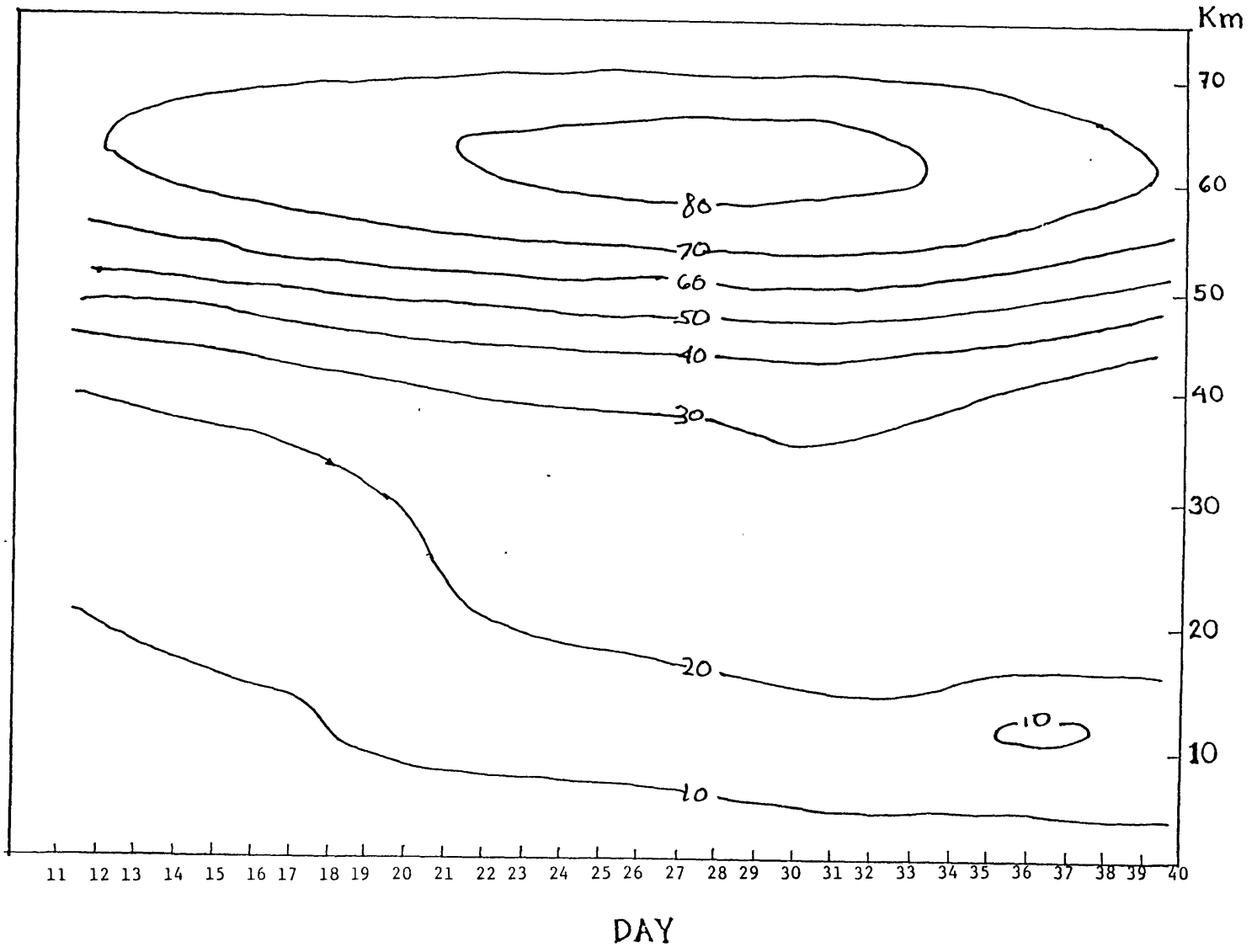

Fig. 3.23: RUN36 Wavenumber 1 Amplitude (gpm) at 50N

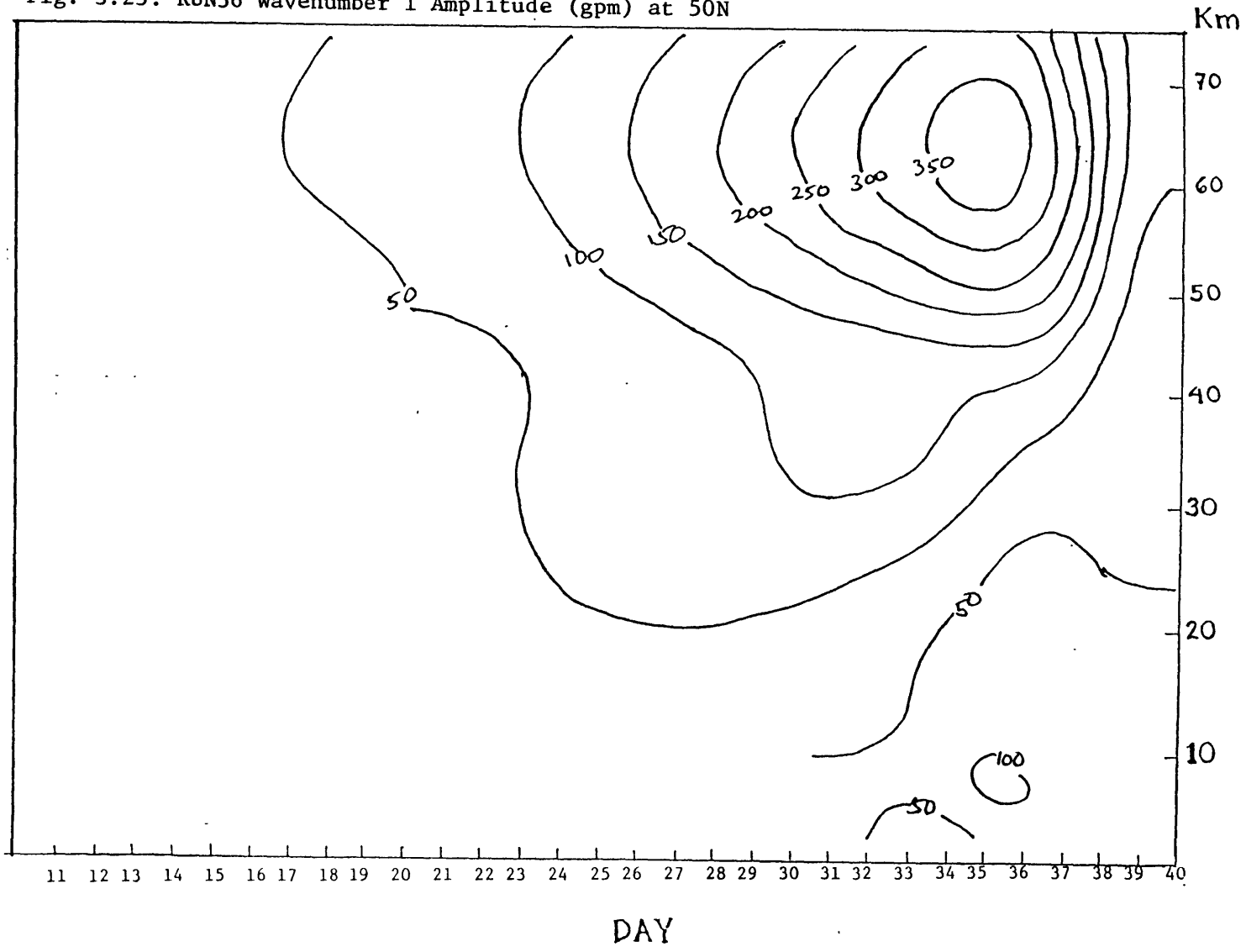

Fig. 3.24: RUN36 Wavenumber 2 Amplitude (gpm) at 50N

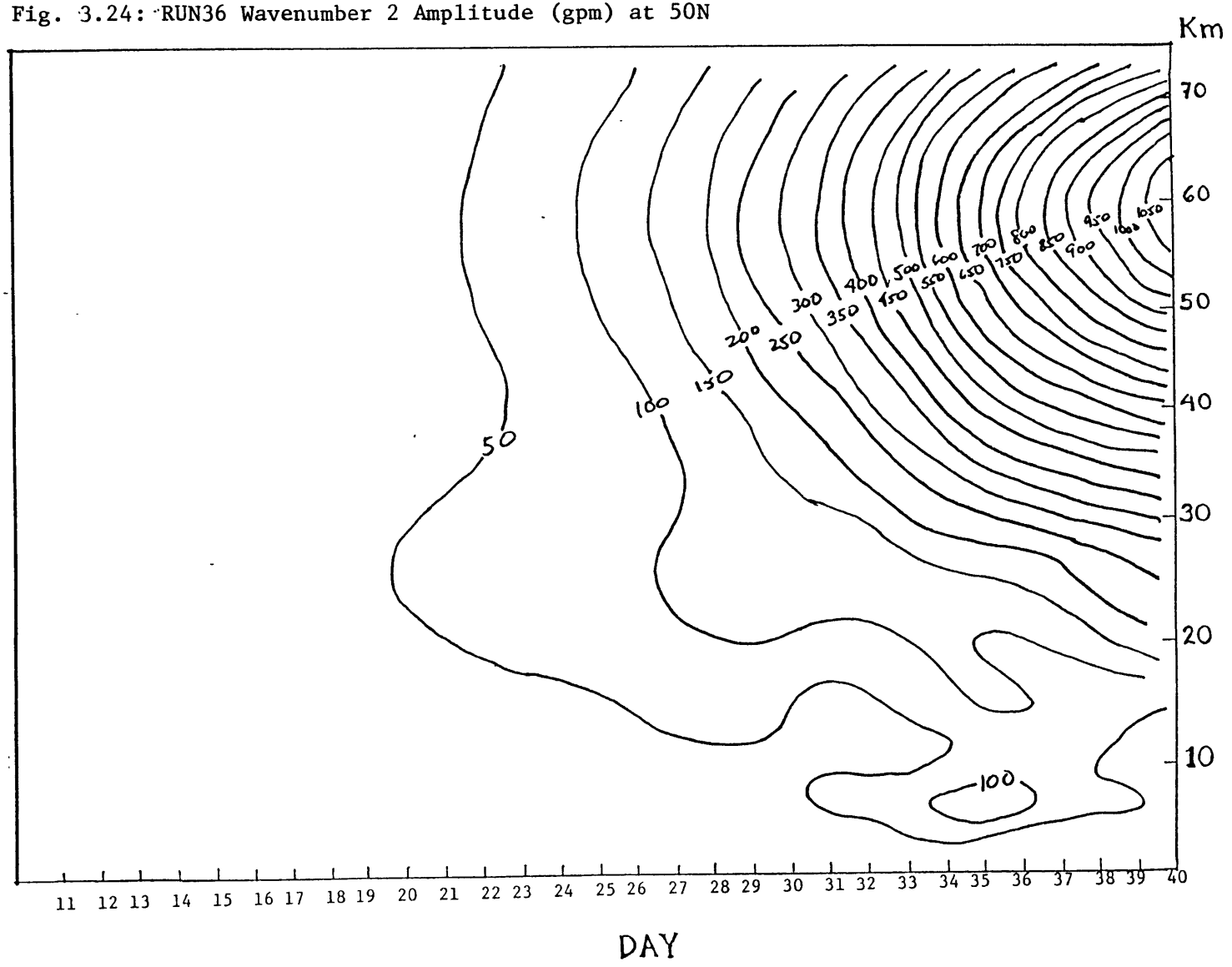

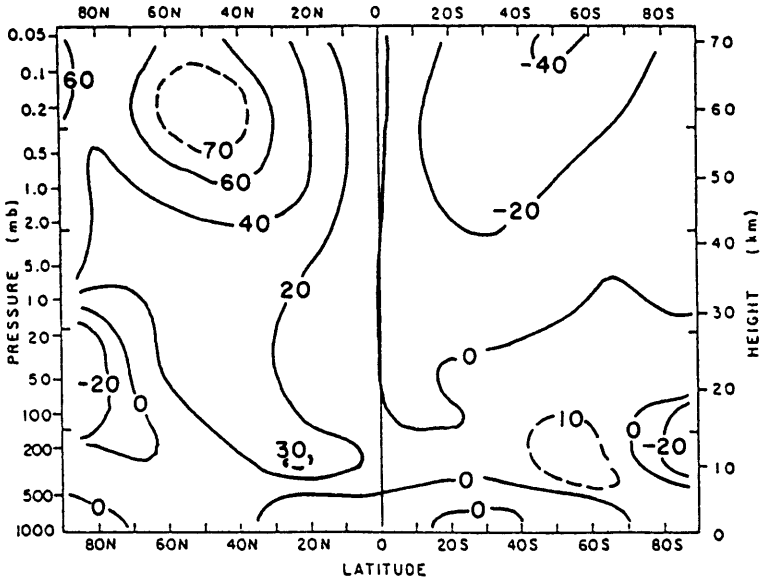

(a)

Figs. 3.25 RUN36 [u] (m/s) for: (a) day 35,
(b) day 40

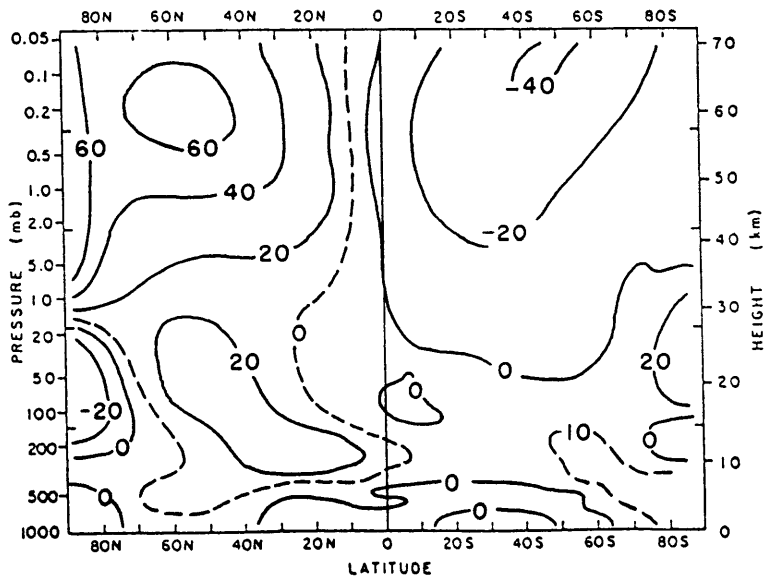

(b)

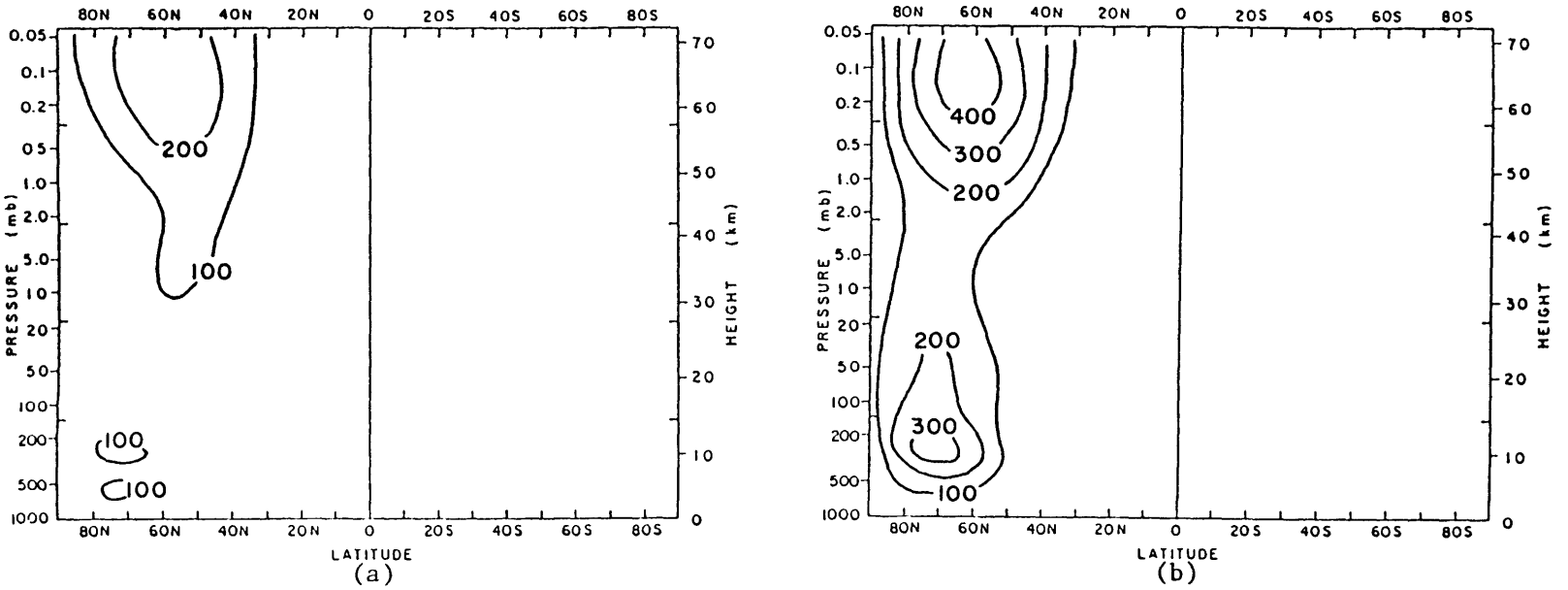

Figs. 3.26 RUN36 Wavenumber 1 Amplitude (gpm) for: (a) day 30, (b) day 35, (c) day 40

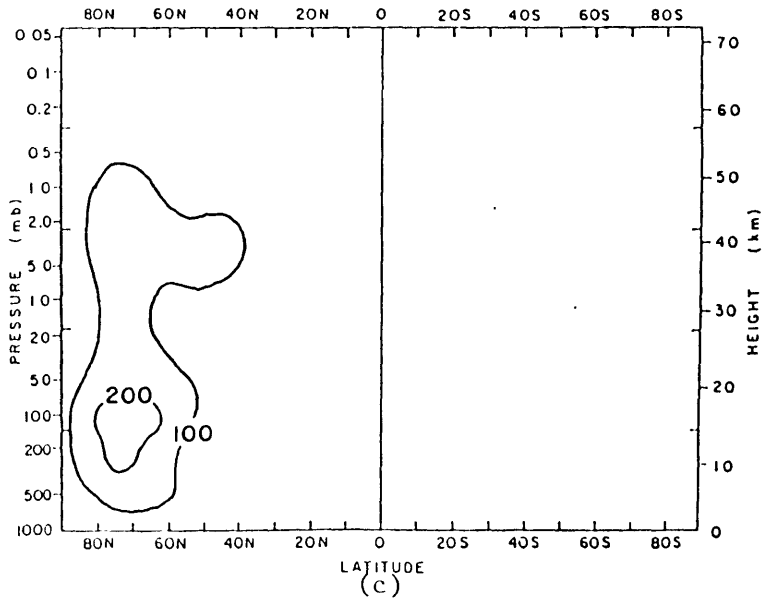

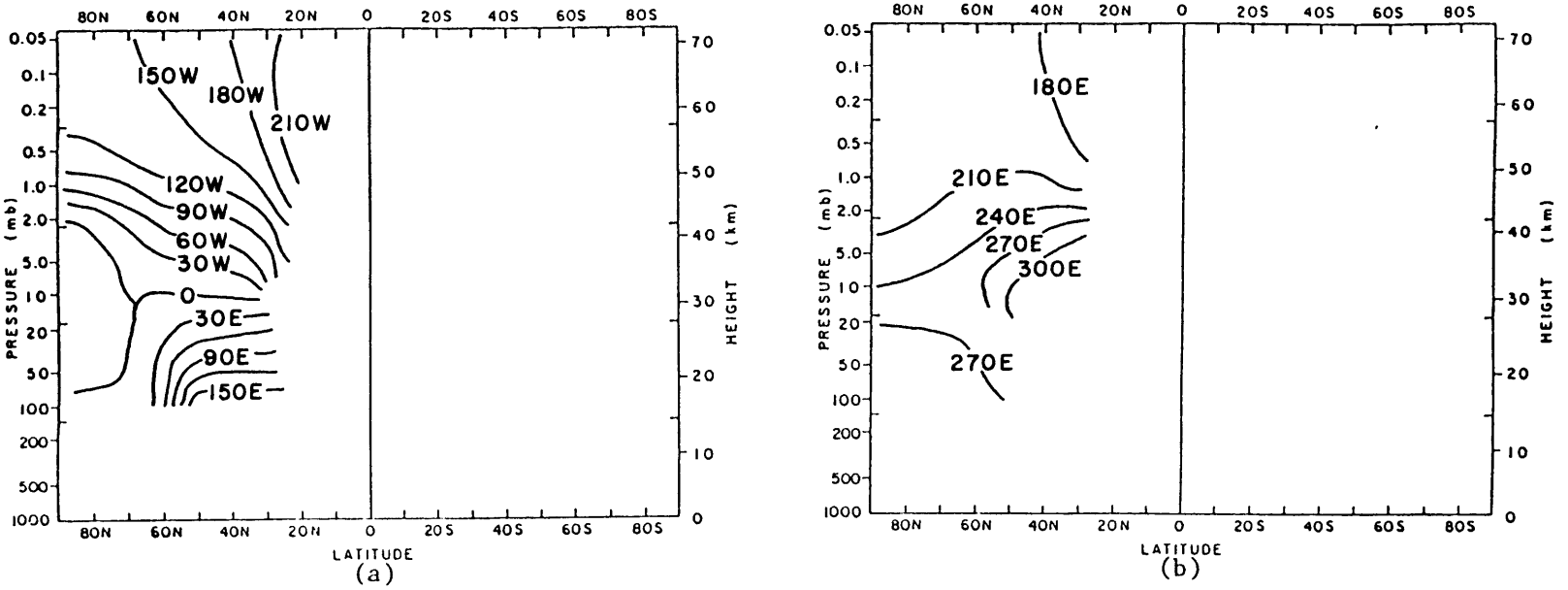

Figs. 3.27 RUN36 Wavenumber 1 Phase (deg) for: (a) day 30, (b) day 35, (c) day 40

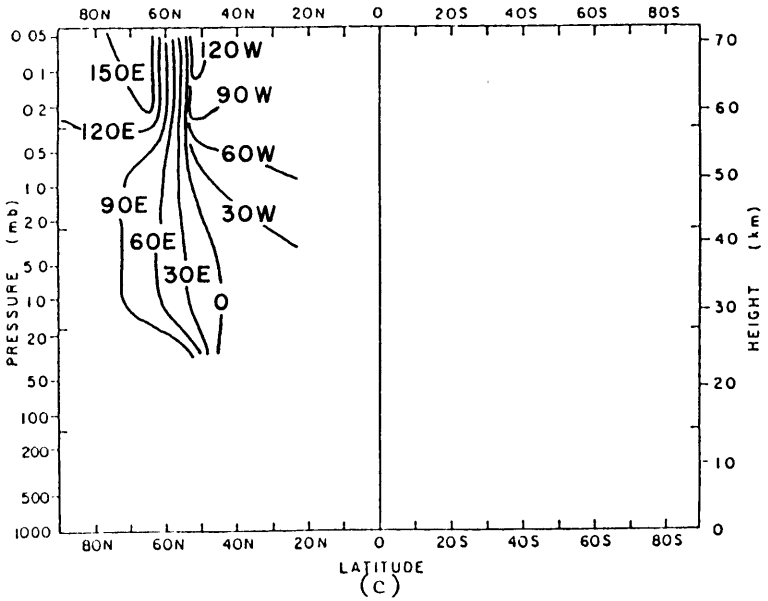

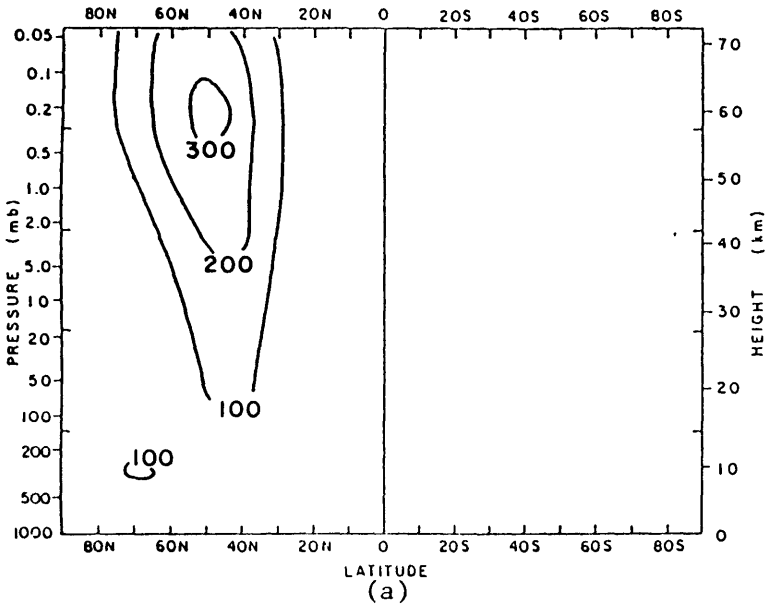

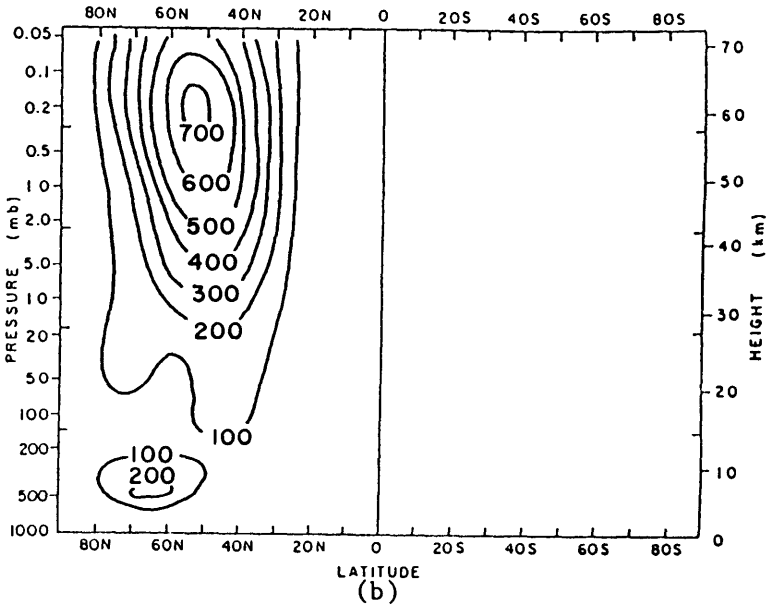

Figs. 3.28 RUN36 Wavenumber 2 Amplitude (gpm) for: (a) day 30, (b) day 35, (c) day 40

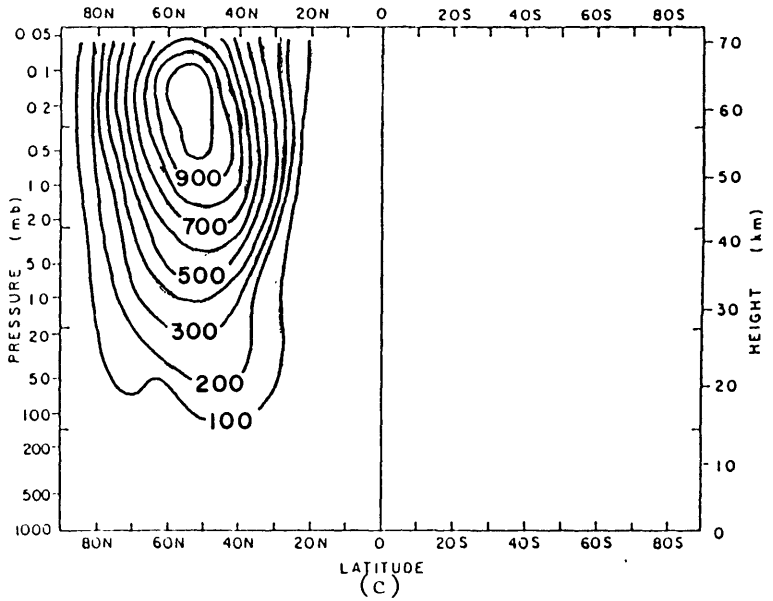

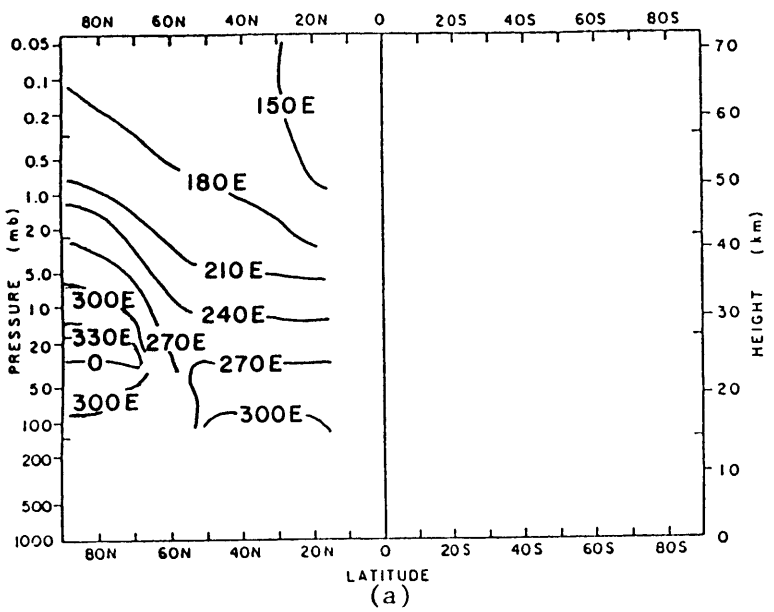

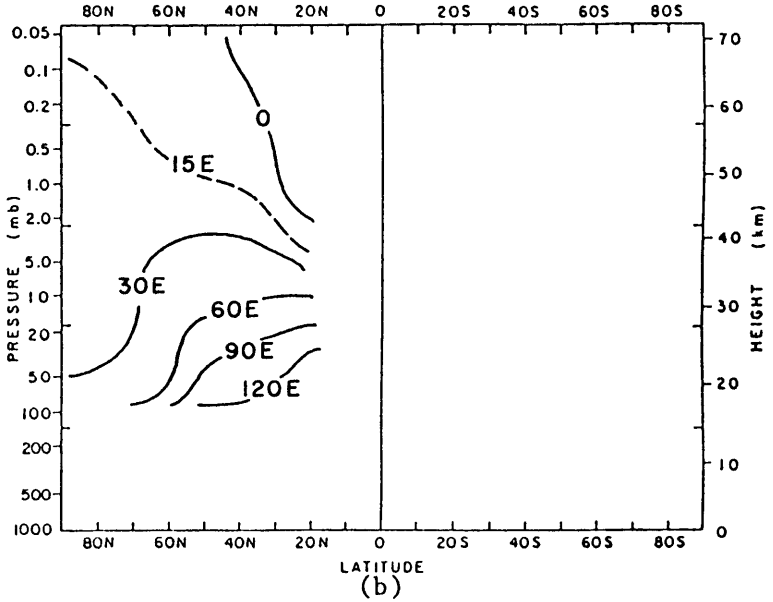

Figs. 3.29 RUN36 Wavenumber 2 Phase (deg) for: (a) day 30, (b) day 35, (c) day 40

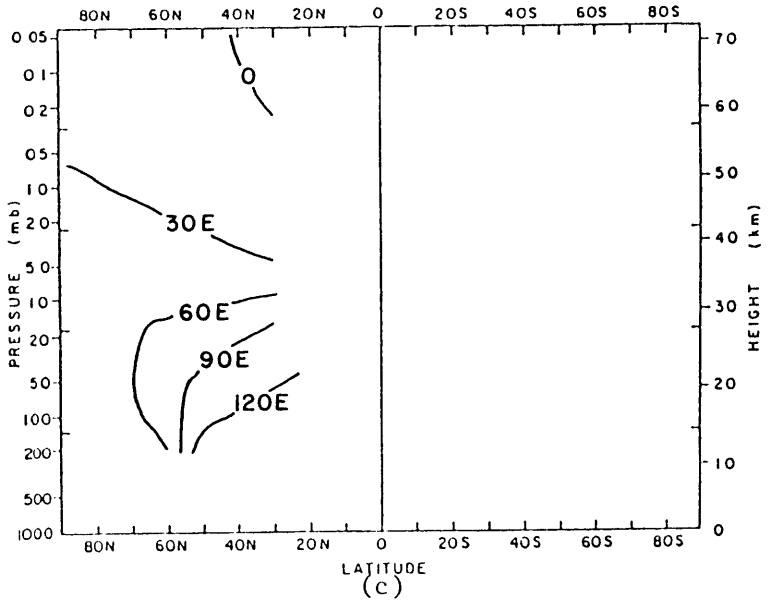

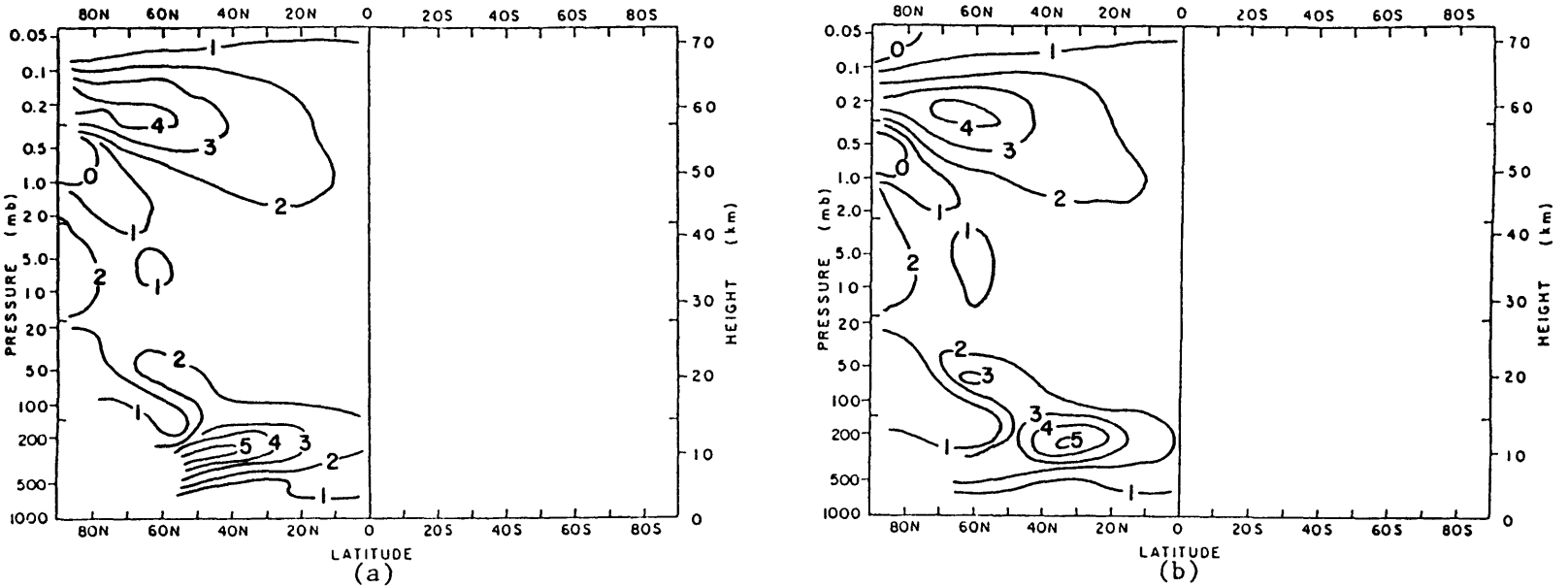

Figs. 3.30 RUN36 Latitudinal gradient of potential vorticity (units of omega) for: (a) day 30, (b) day 35, (c) day 40

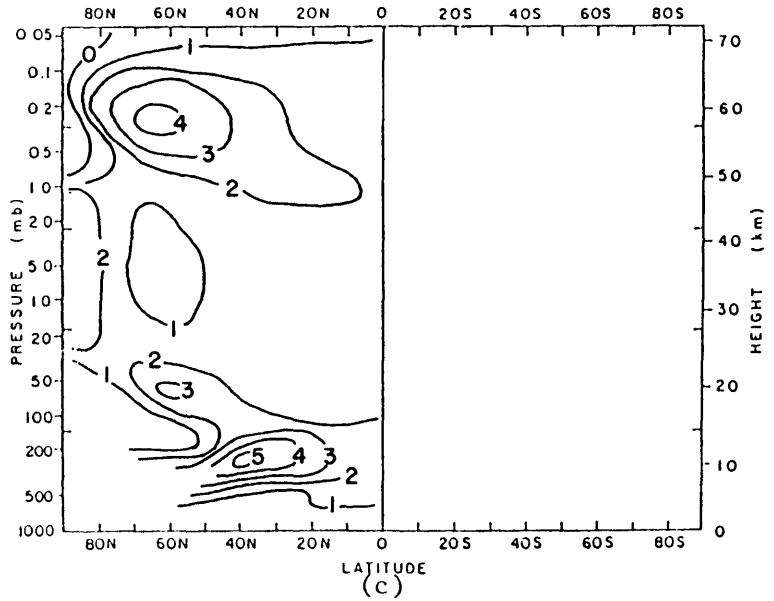

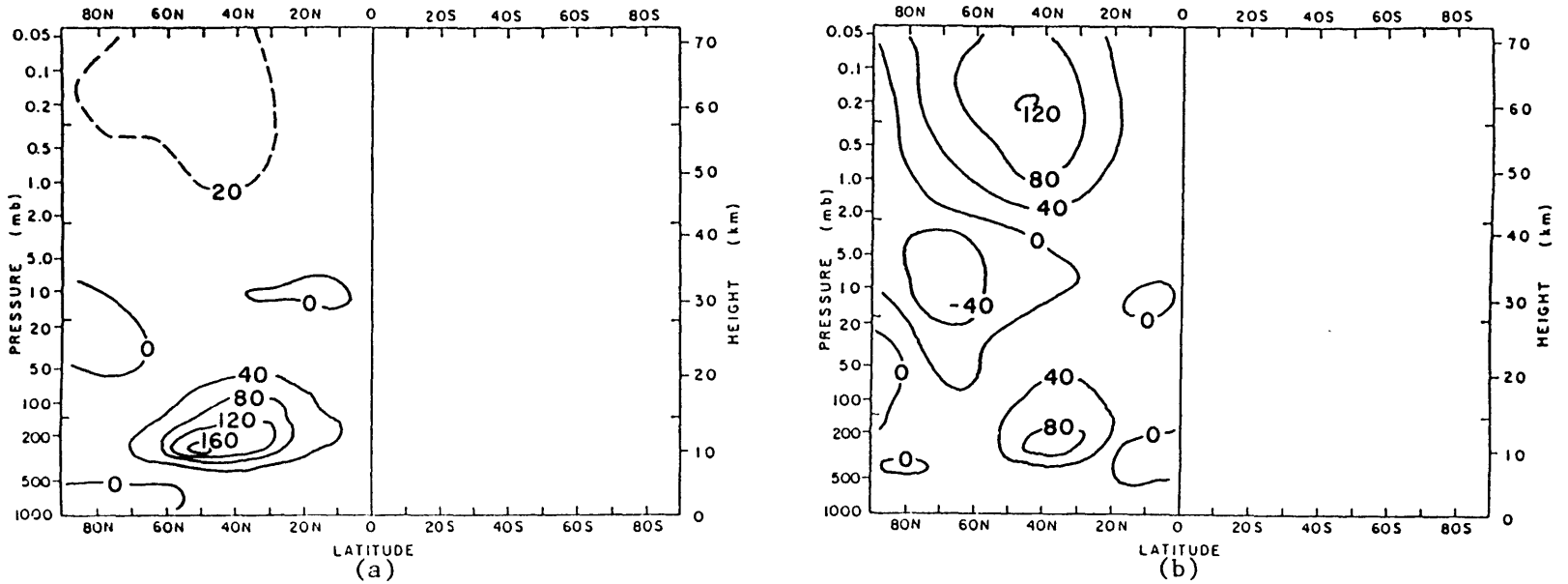

Figs. 3.31 RUN36 [$u^* v^*$] (m^2/s^2) for: (a) day 30, (b) day 35, (c) day 40

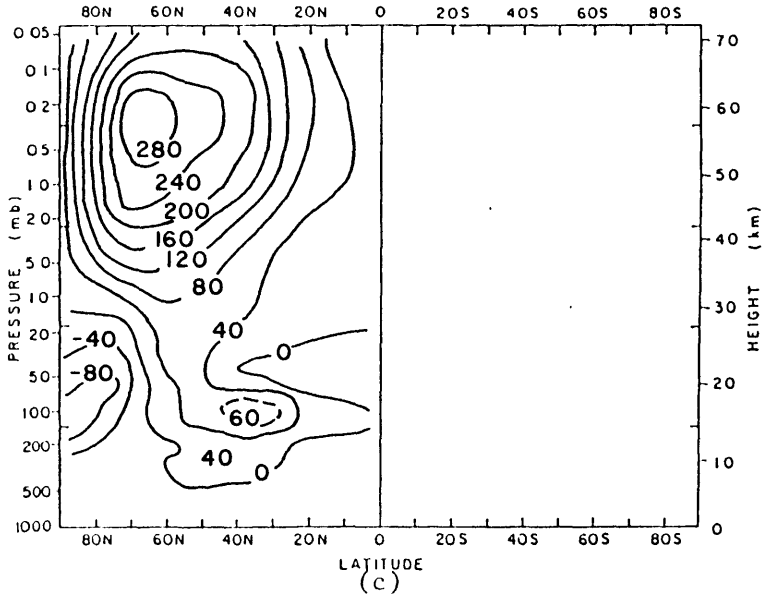

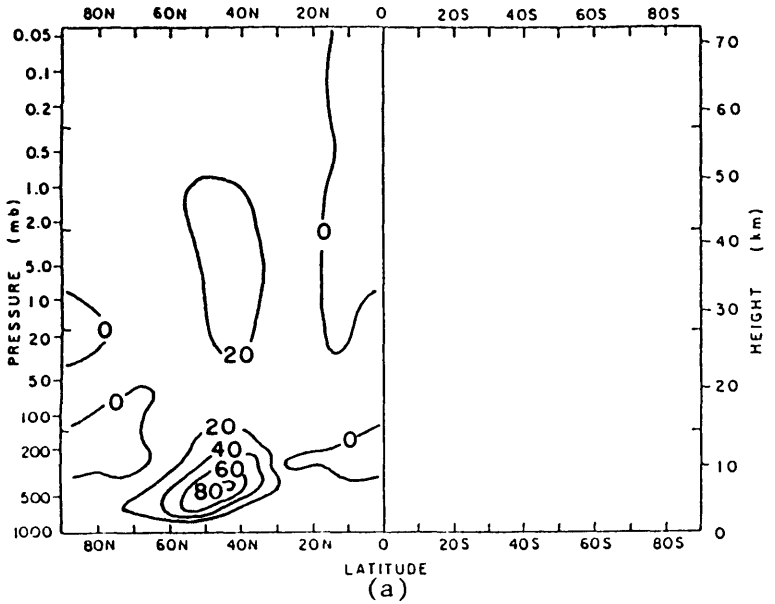

(a)

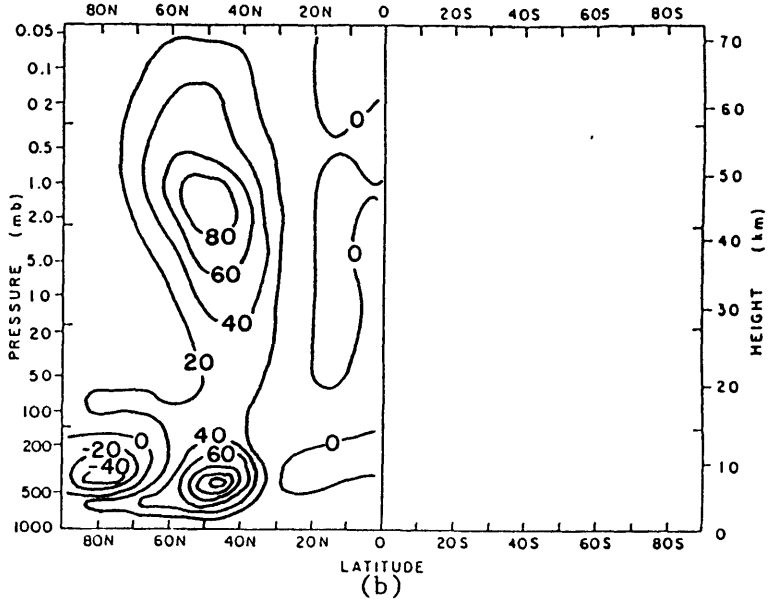

(b)

Figs. 3.32 RUN36 [$v^{*}T^{*}$] (K-m/s) for: (a) day 30, (b) day 35, (c) day 40

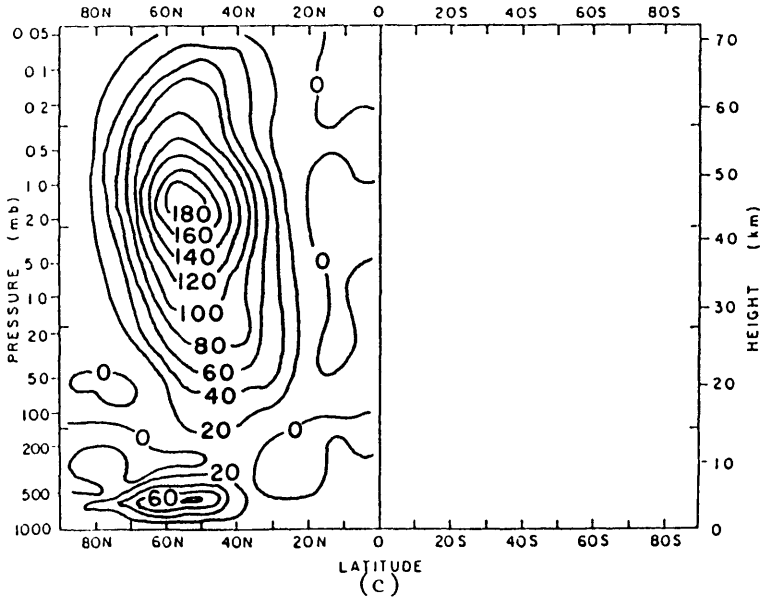

(c)

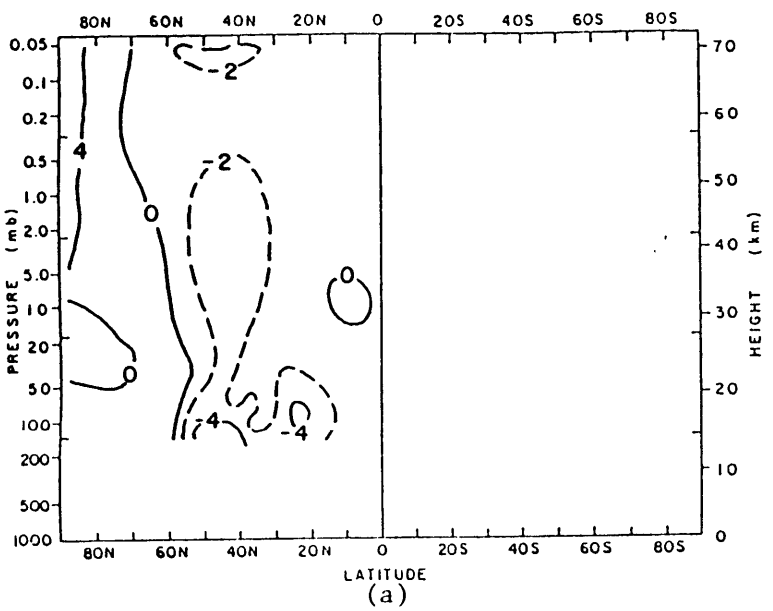

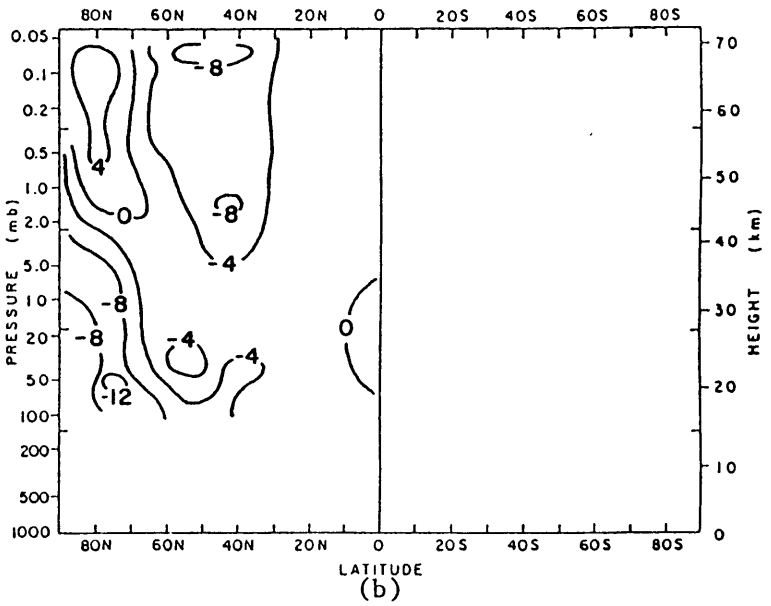

Figs. 3.33 RUN36 Eliassen-Palm flux divergence (10^{-5} m/s^2) for: (a) day 30, (b) day 35, (c) day 40

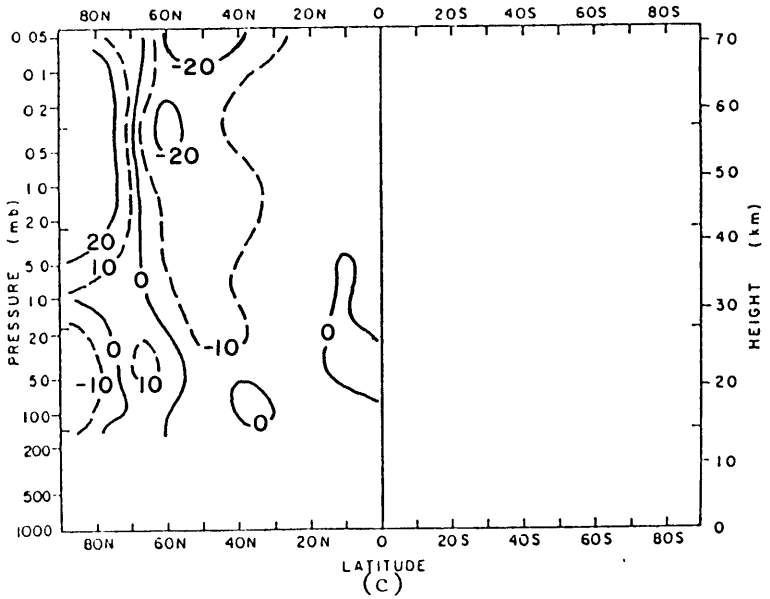

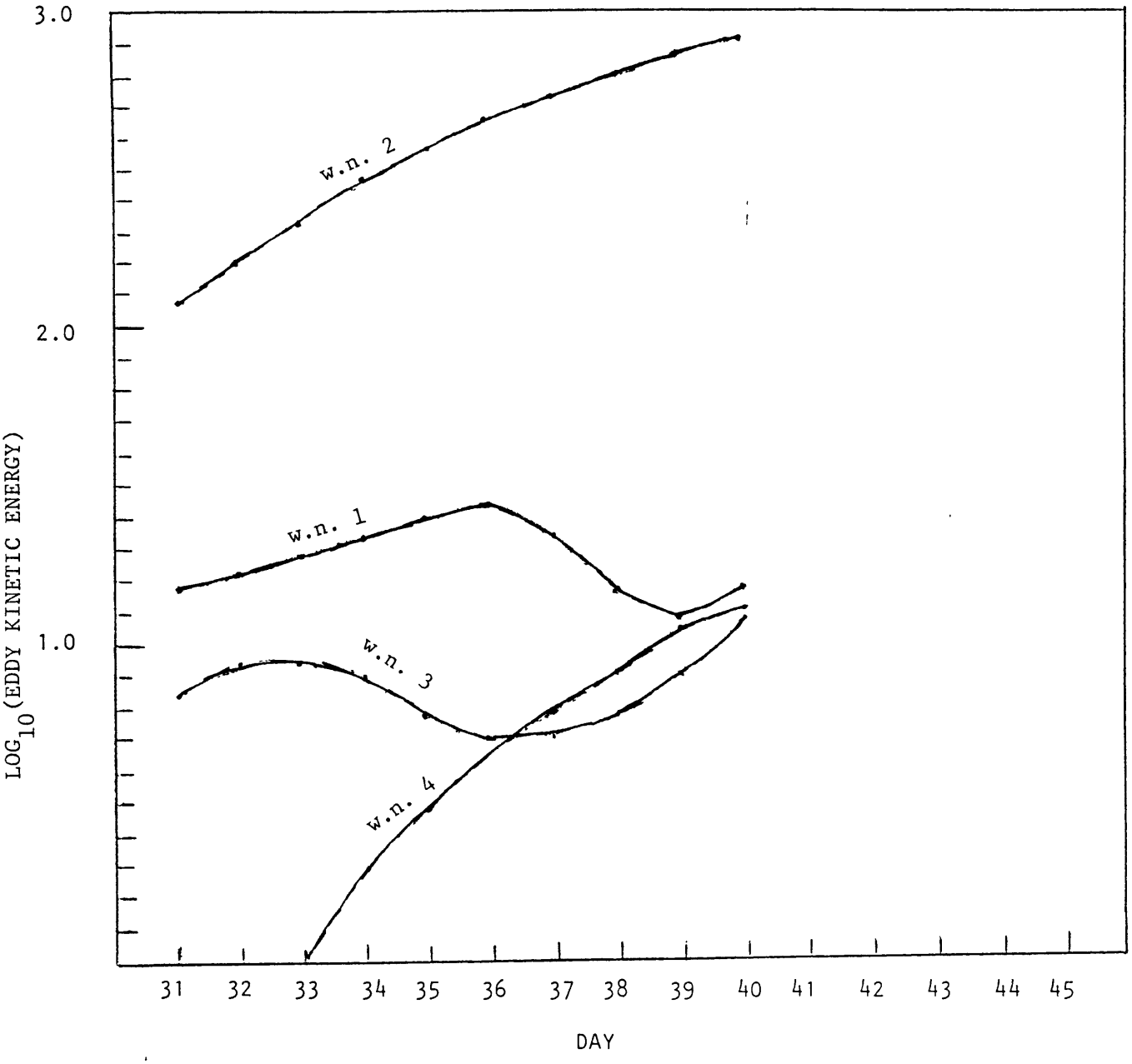

Fig. 3.34

RUN36 Horizontal Average Eddy Kinetic Energy Spectrum at 1 mbar (J/m^2)

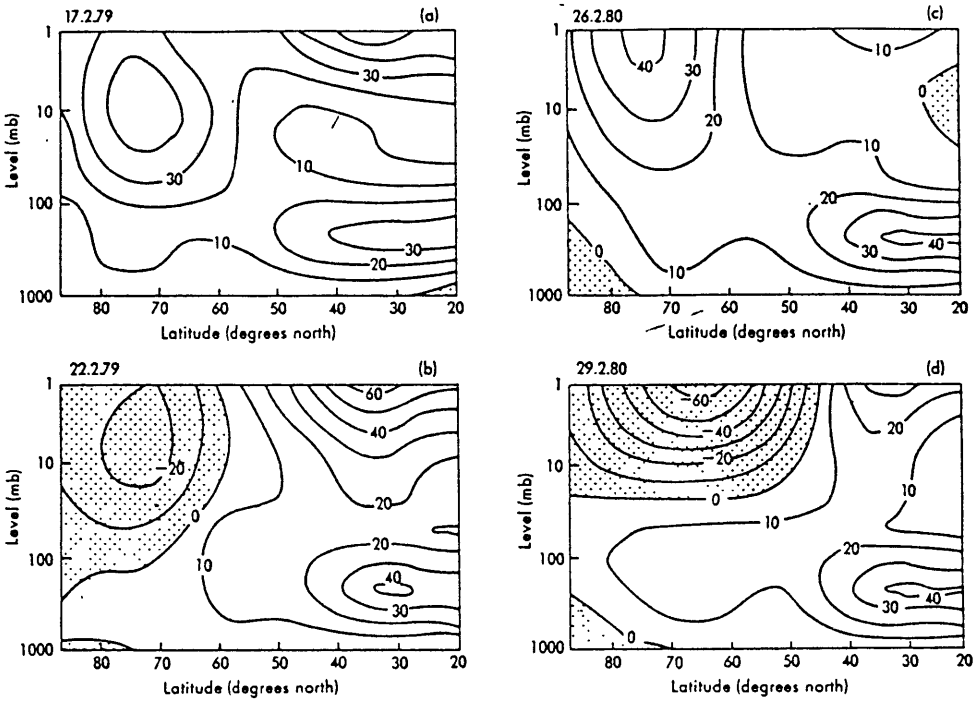

Meridional cross section of zonal mean wind velocity (m s^{-1}). Regions of easterly winds are stippled (*a*) February 17, 1979; (*b*) February 22, 1979; (*c*) February 26, 1980; (*d*) February 29, 1980.

Figs. 3.35

(Observations after Palmer, 1981b)

Case 1

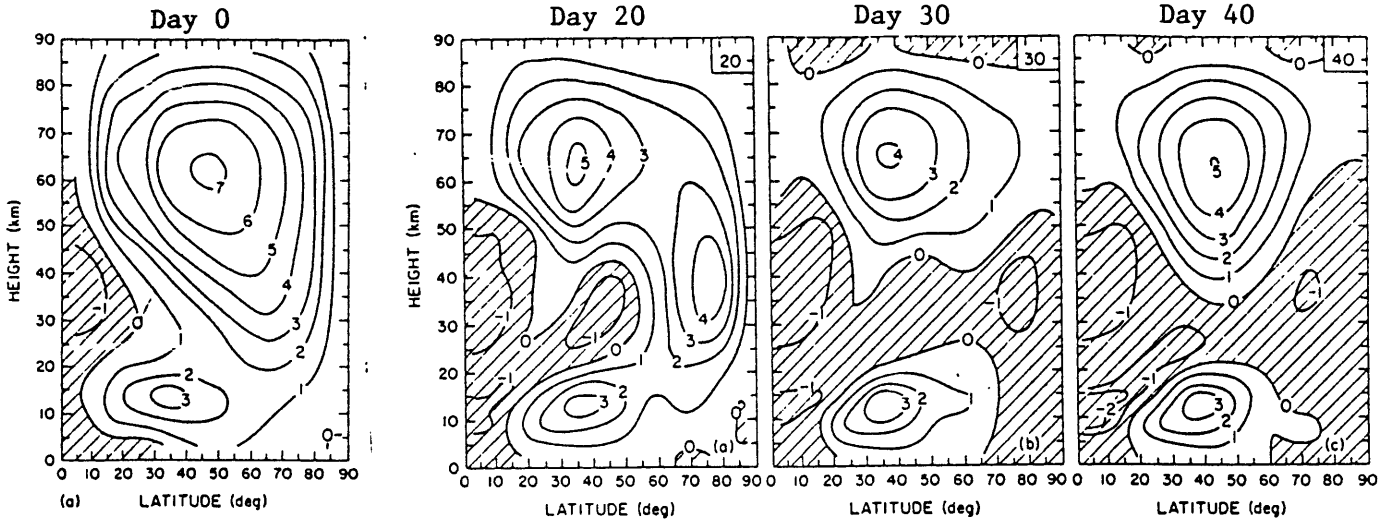

Figs. 3.36: Zonal Wind (10 m/s) for Cases 1 and 2 from Koermer, et al (1983)

Case 2

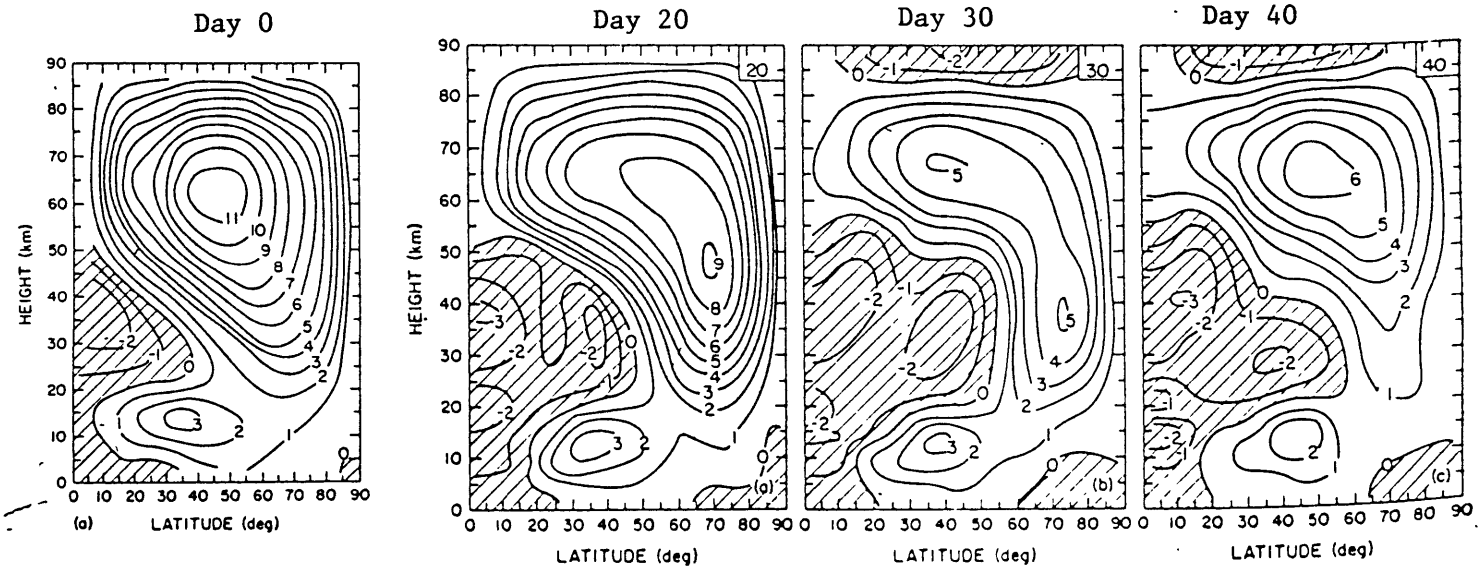

Model [T] (K) for day 30

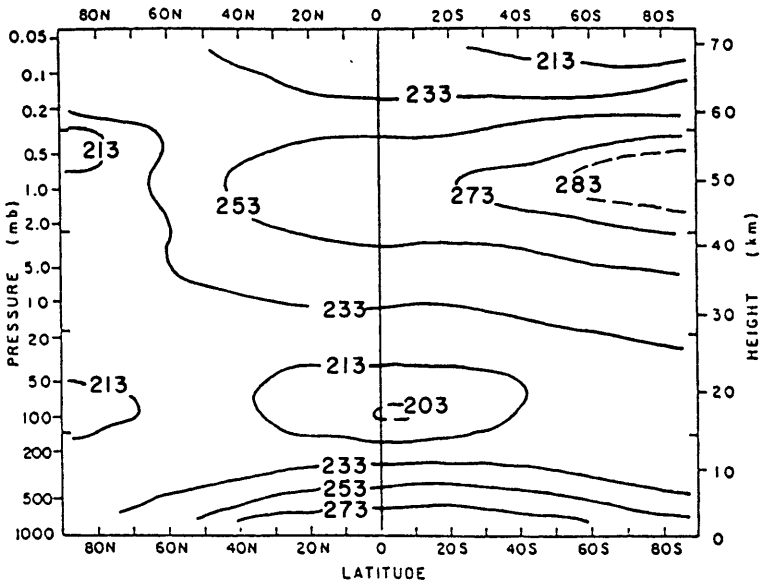

Fig. 3.37

Model [u] (m/s) for day 30

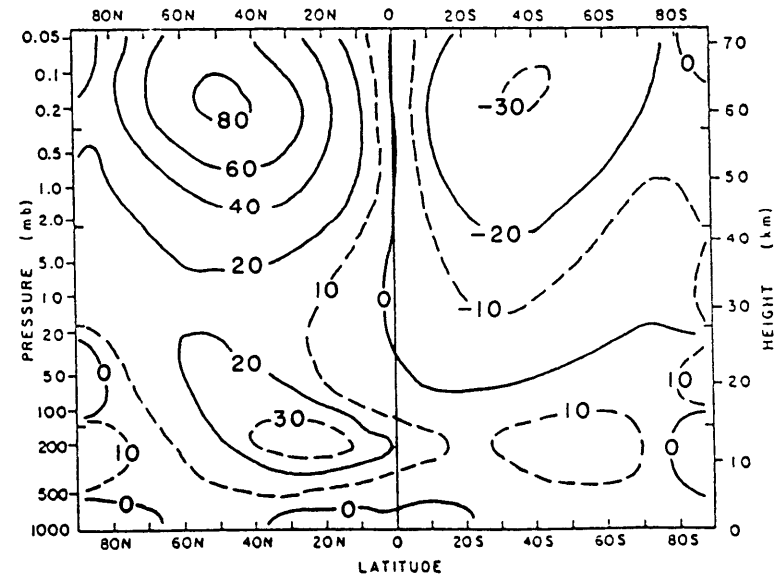

Fig. 3.38

Model Wavenumber 1 Amplitude (gpm) for day 30

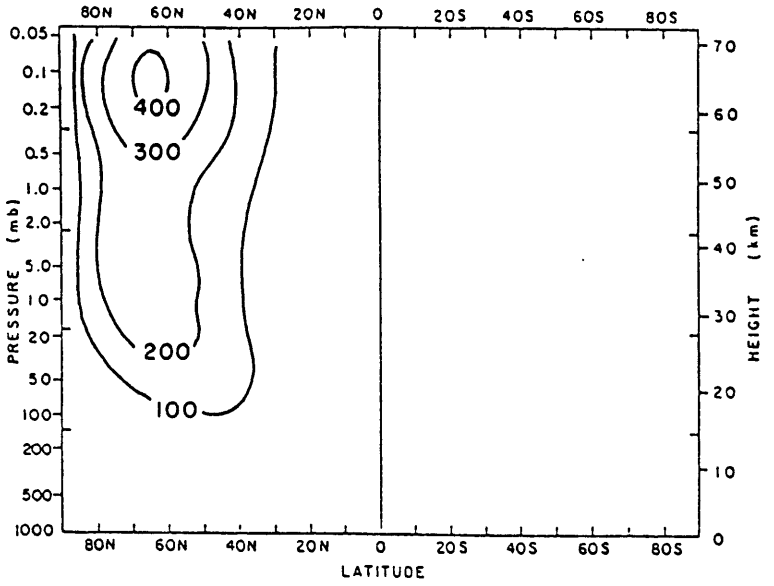

Fig. 3.39

Model Wavenumber 1 Phase (deg) for day 30

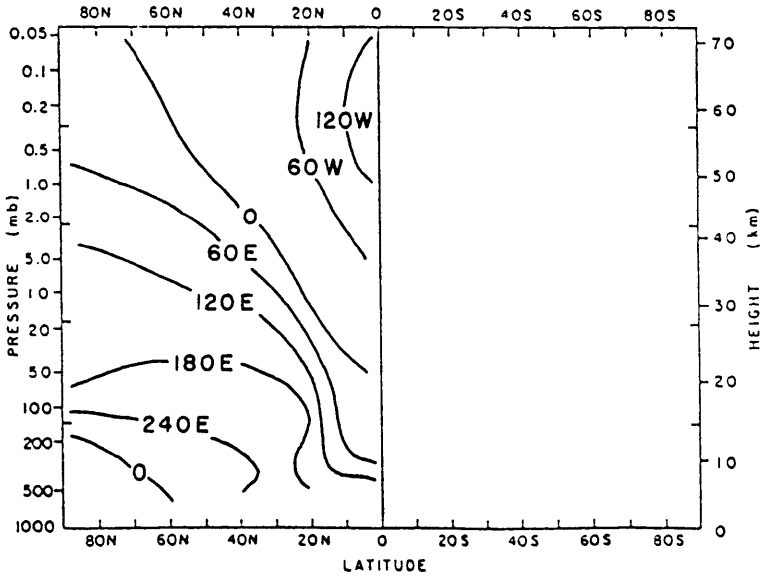

Fig. 3.40

Model Wavenumber 2 Amplitude (gpm) for day 30

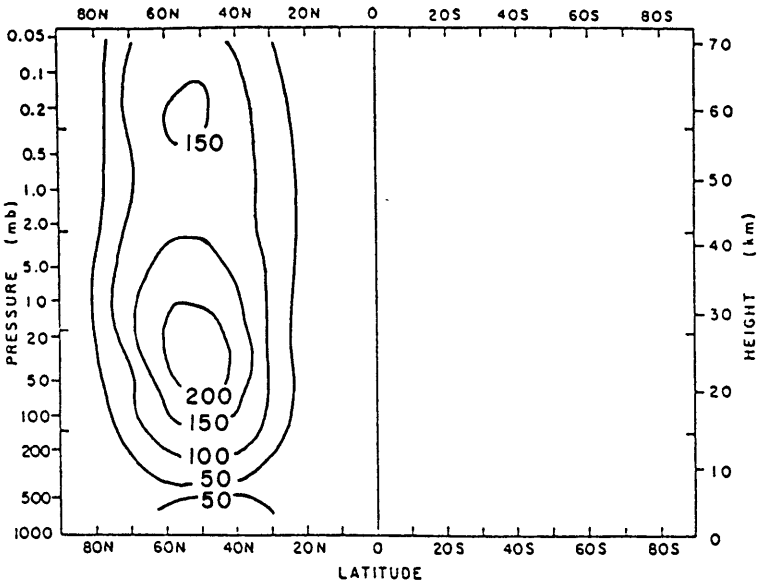

Fig. 3.41

Model Wavenumber 2 Phase (deg) for day 30

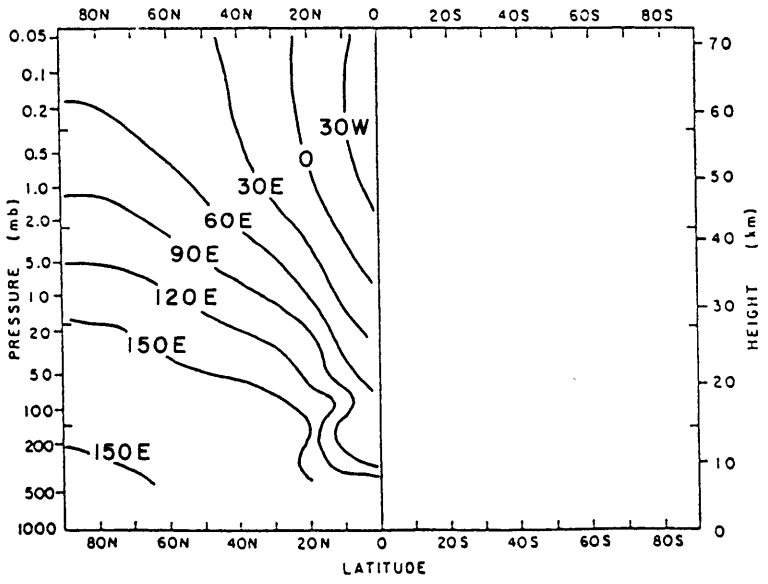

Fig. 3.42

Model $[u^*v^*]$ (m^2/s^2) for day 30

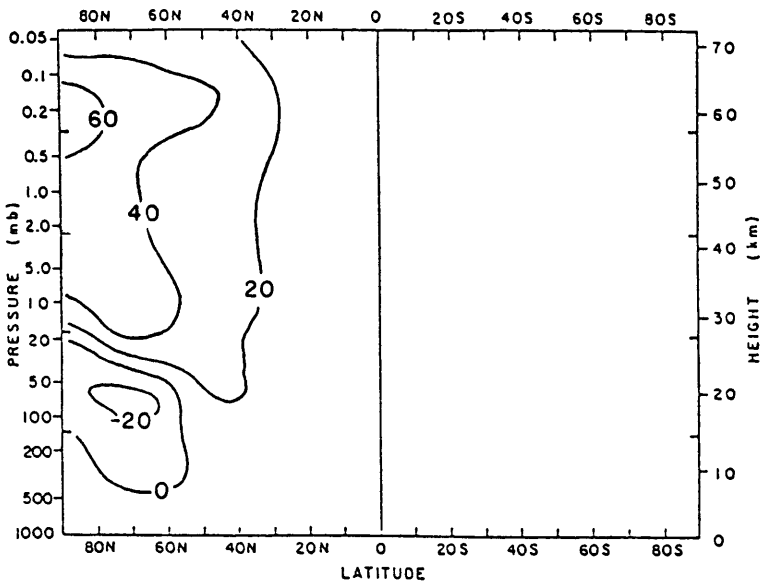

Fig. 3.43

Model $[v^*T^*]$ (K-m/s) for day 30

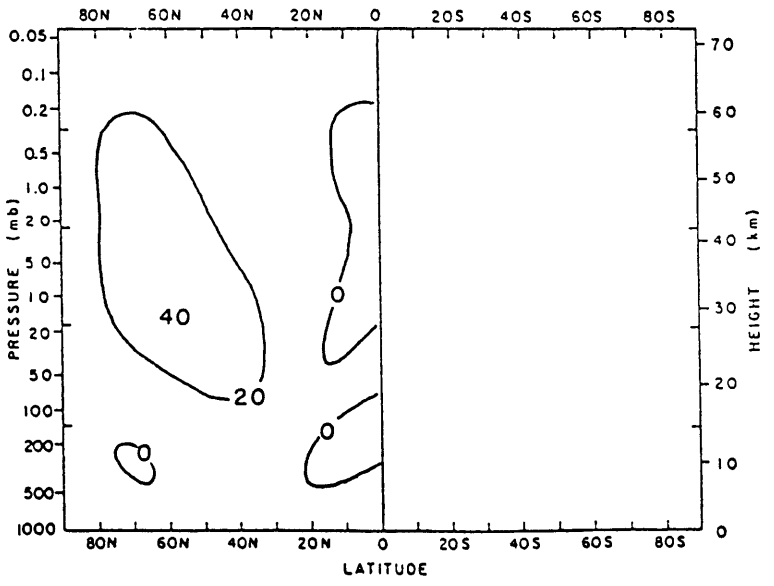

Fig. 3.44

Model X_M (10^{12} gm/s) for day 30

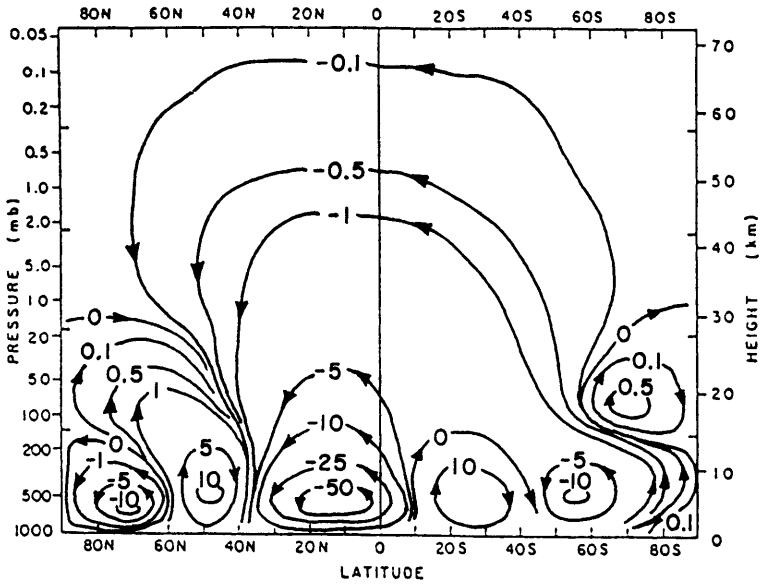

Fig. 3.45

Model $[n_{O_3}]$ (10^{11} cm^{-3}) for day 30

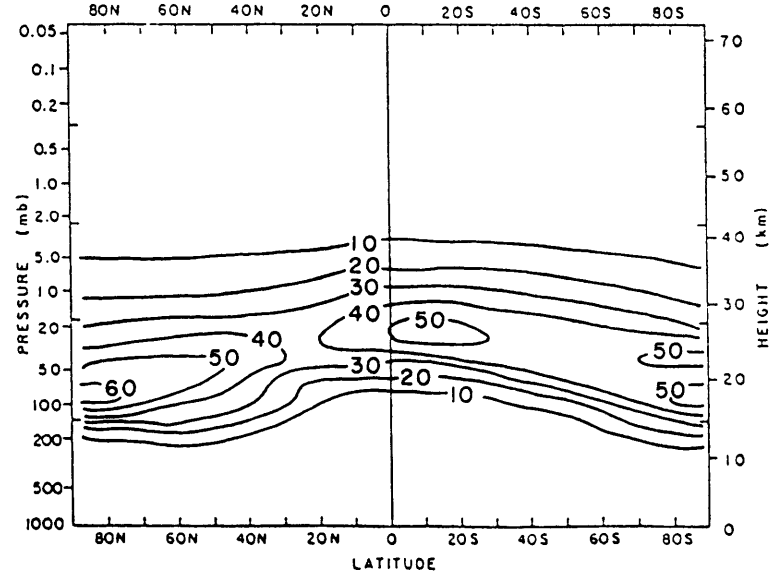

Fig. 3.46

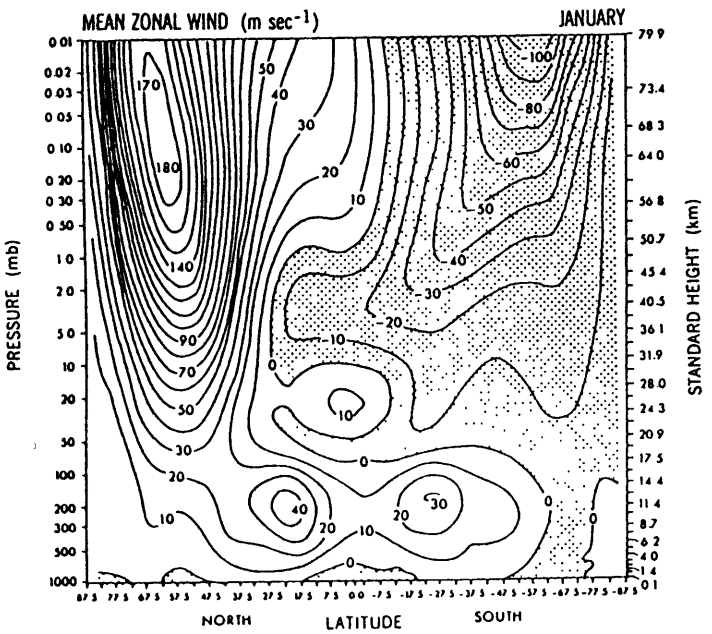

(a)

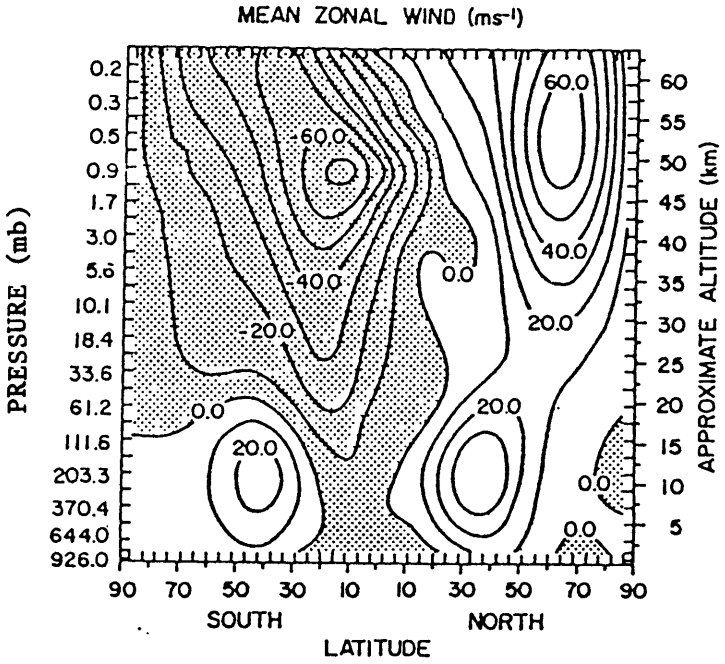

(b)

Figs. 3.47 January Average Mean Zonal Wind Profiles for: (a) GFDL "SKYHI" Model (Mahlman & Umscheid, 1984)
(b) NCAR Community Climate Model (Boville, 1986)

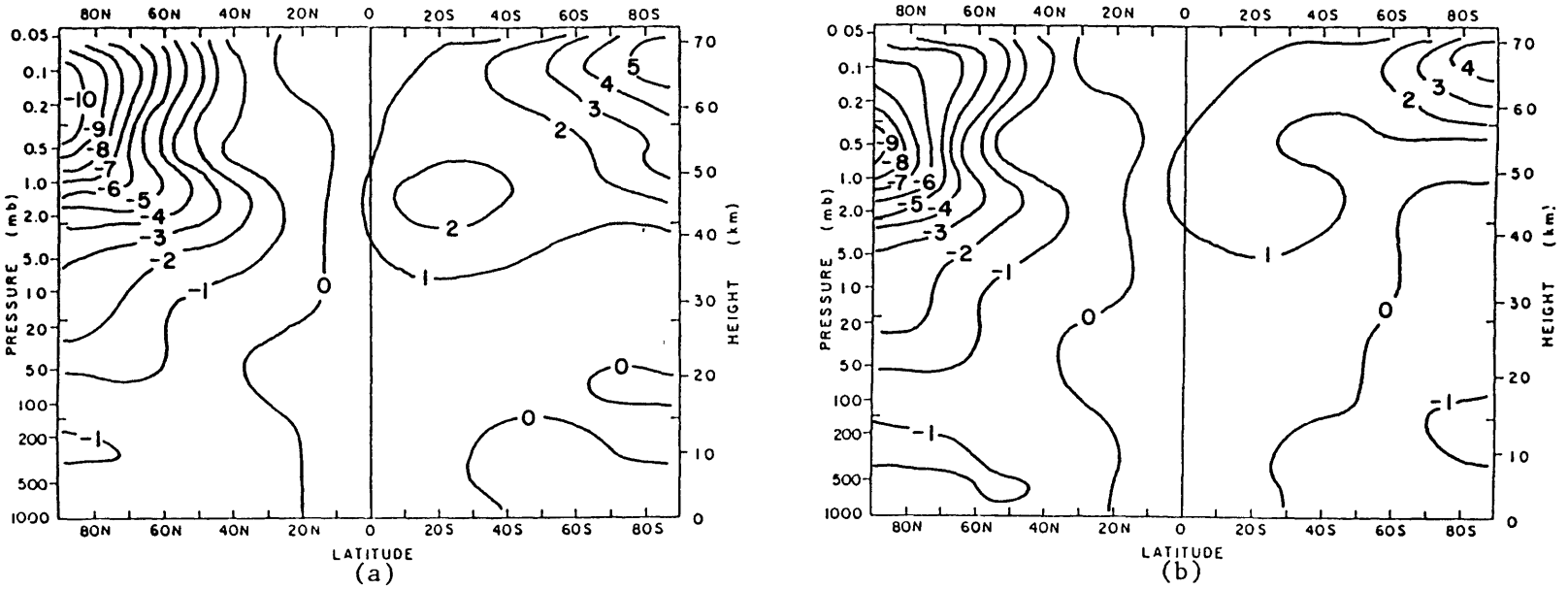

Figs. 4.1 Model [Q] (K/day) for: (a) January, (b) February, (c) March

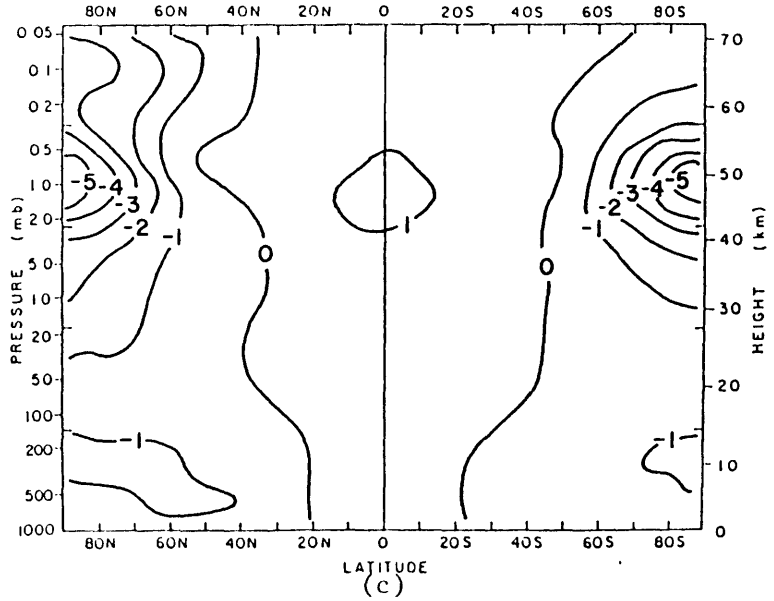

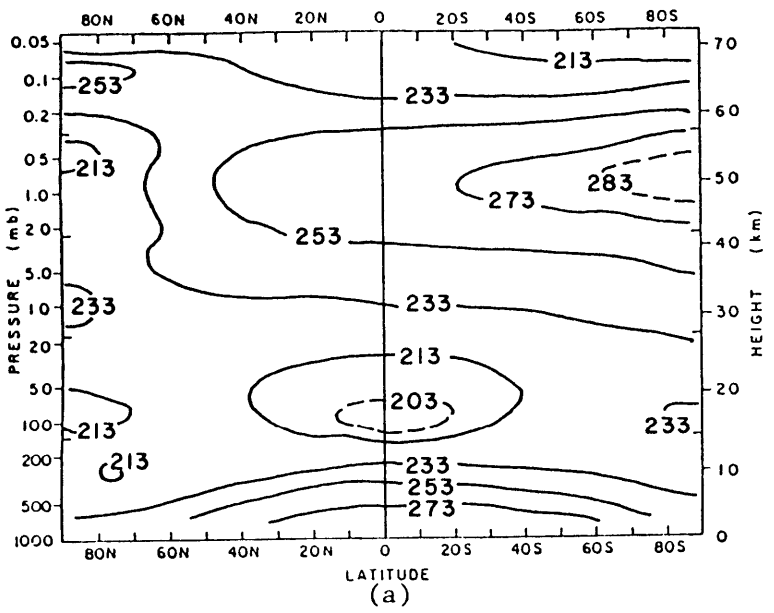

Figs. 4.2 Model [T] (K) for: (a) January, (b) February, (c) March

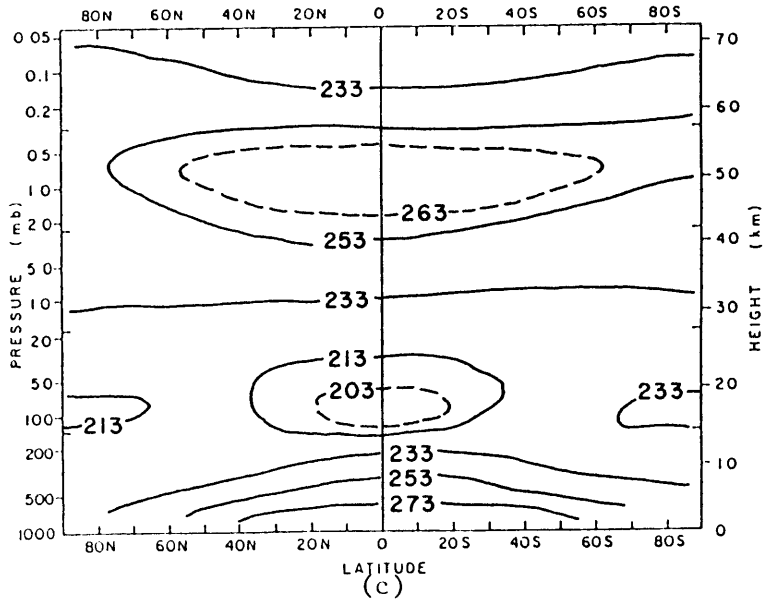

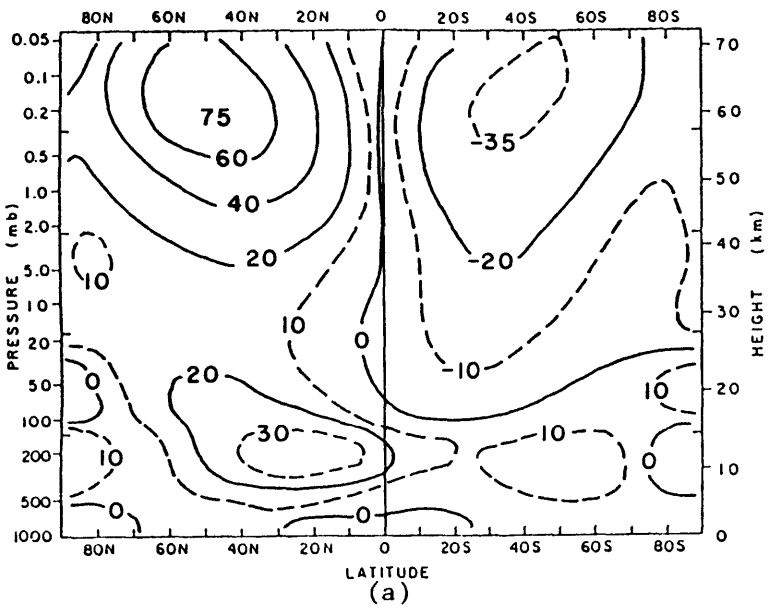

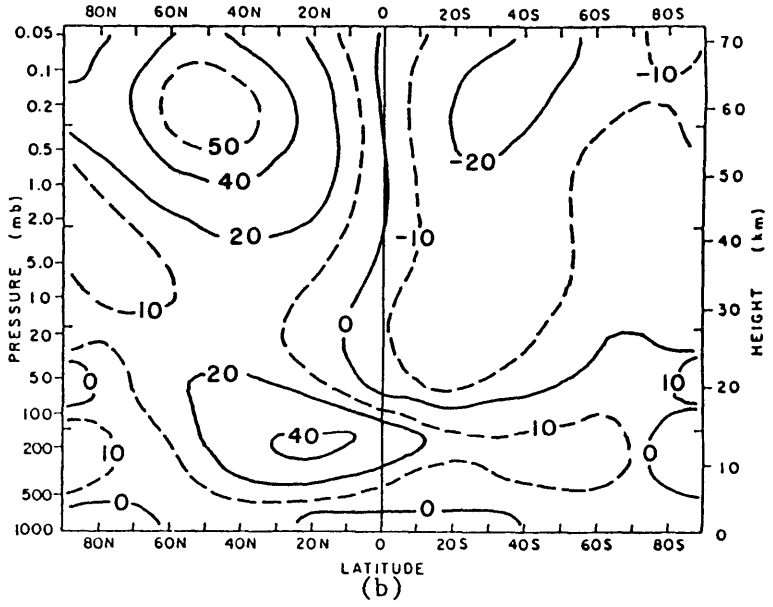

Figs. 4.3 Model [u] (m/s) for: (a) January, (b) February, (c) March

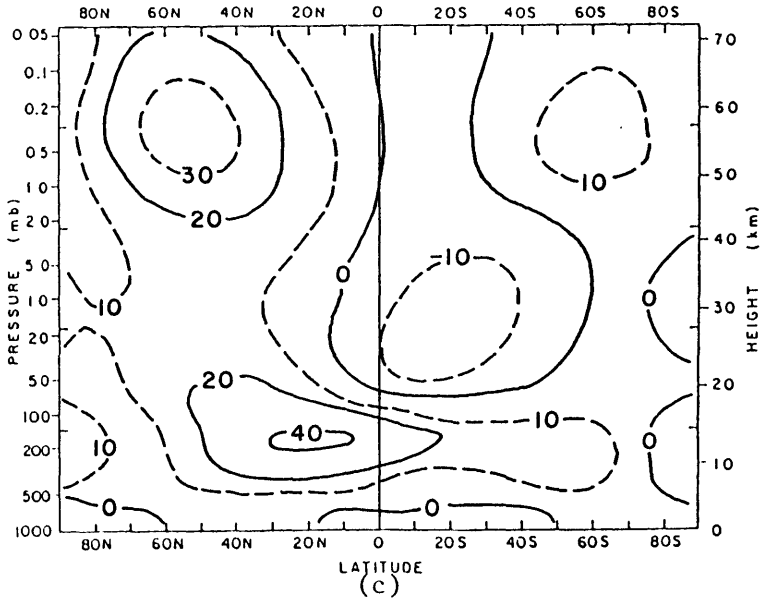

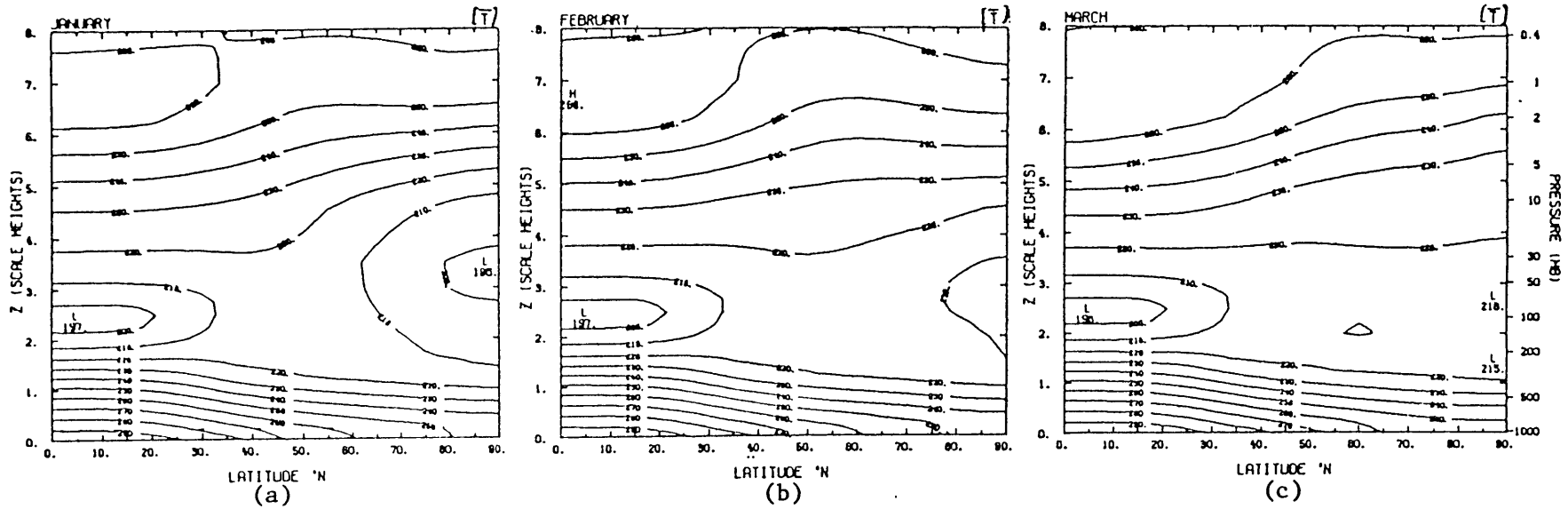

Figs. 4.4 Observed [T] (K) for: (a) January, (b) February, (c) March (after Wu, et al, 1984)

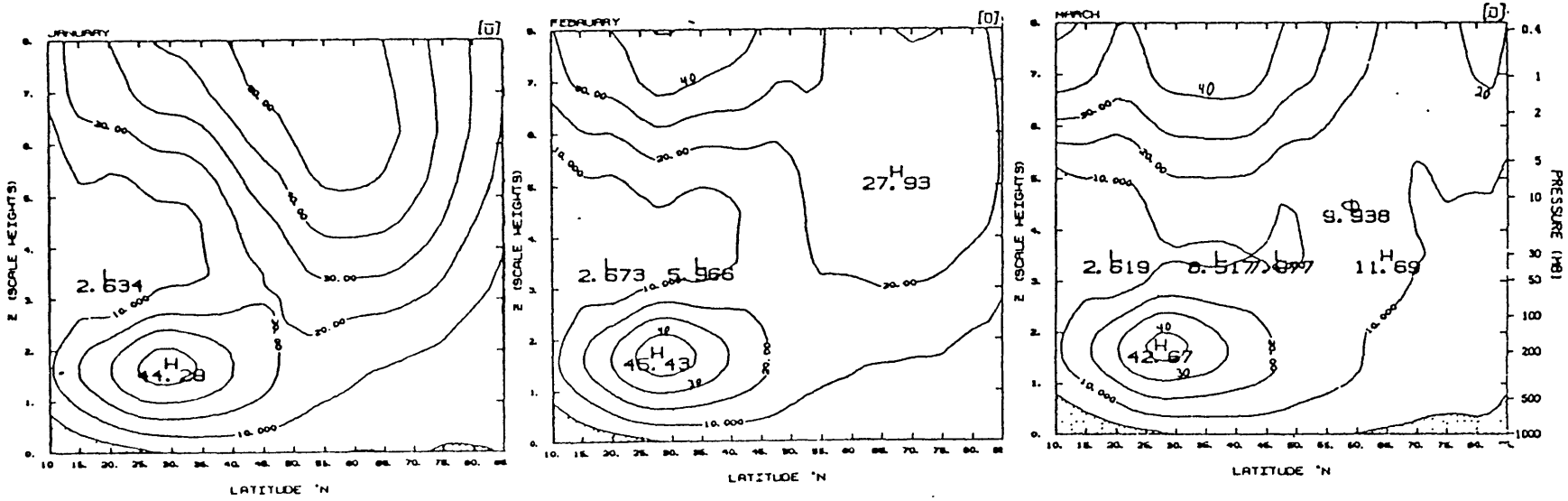

Figs. 4.5 Observed [u] (m/s) for: (a) January, (b) February, (c) March (after Wu, et al, 1984)

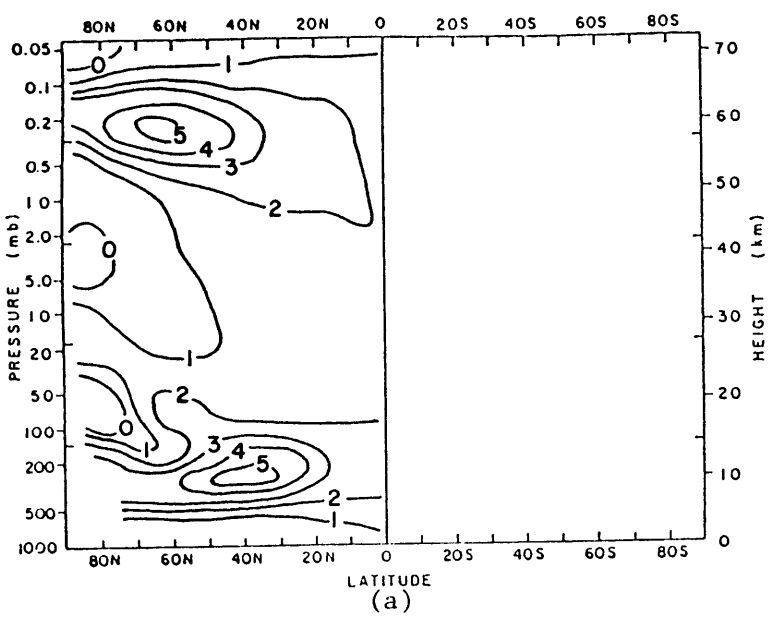

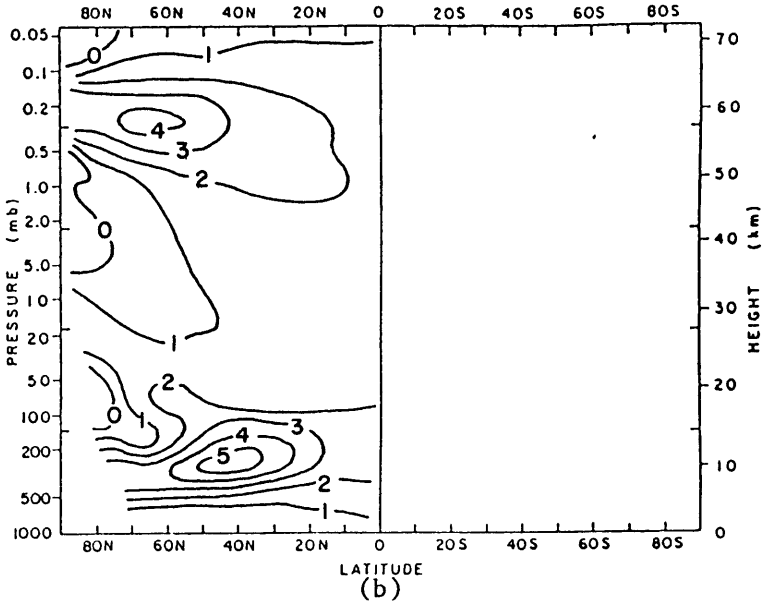

Figs. 4.6 Model Latitudinal gradient of potential vorticity (units of omega) for: (a) January, (b) February, (c) March

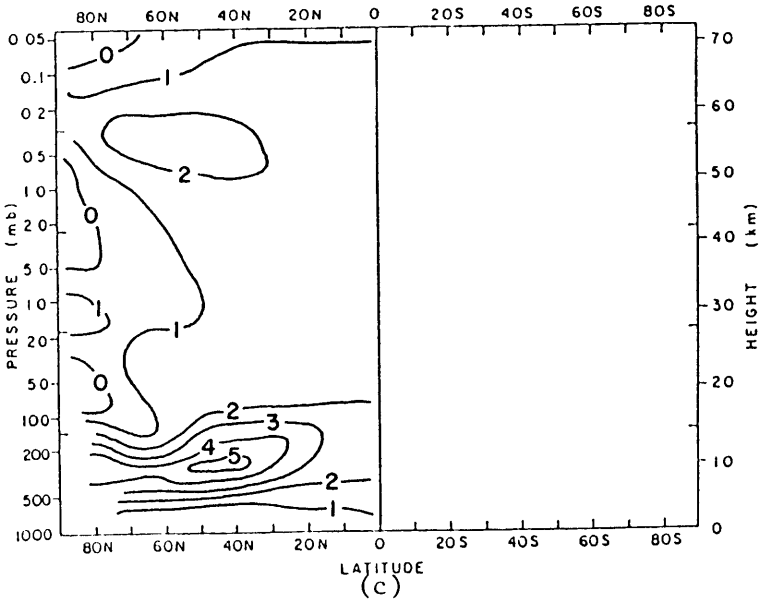

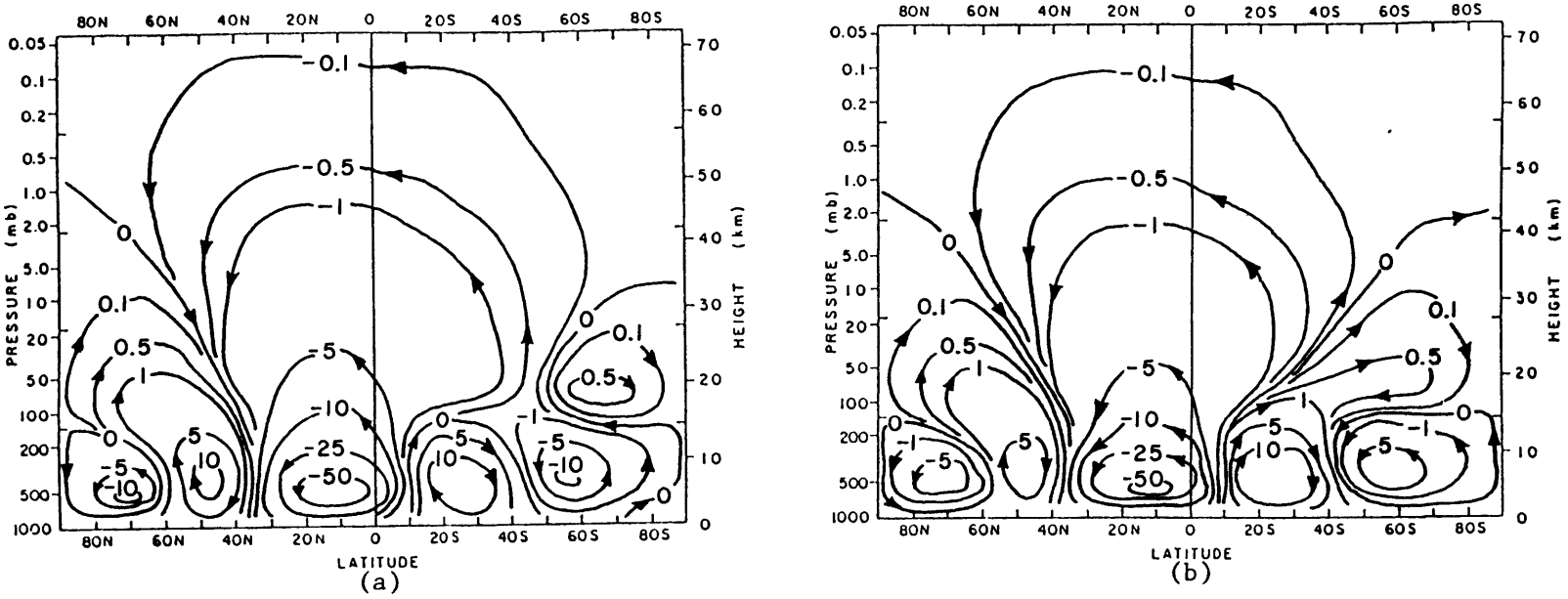

Figs. 4.7 Model X_M (10^{12} gm/s) for: (a) January, (b) February, (c) March

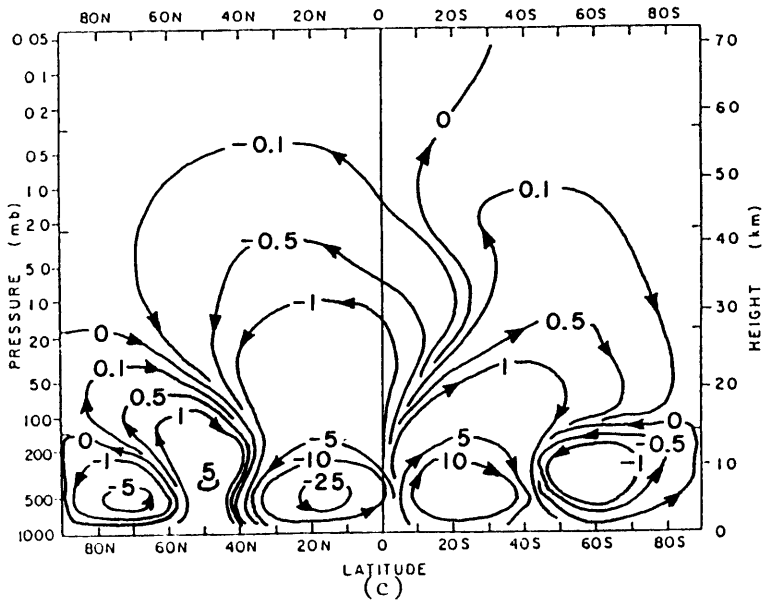

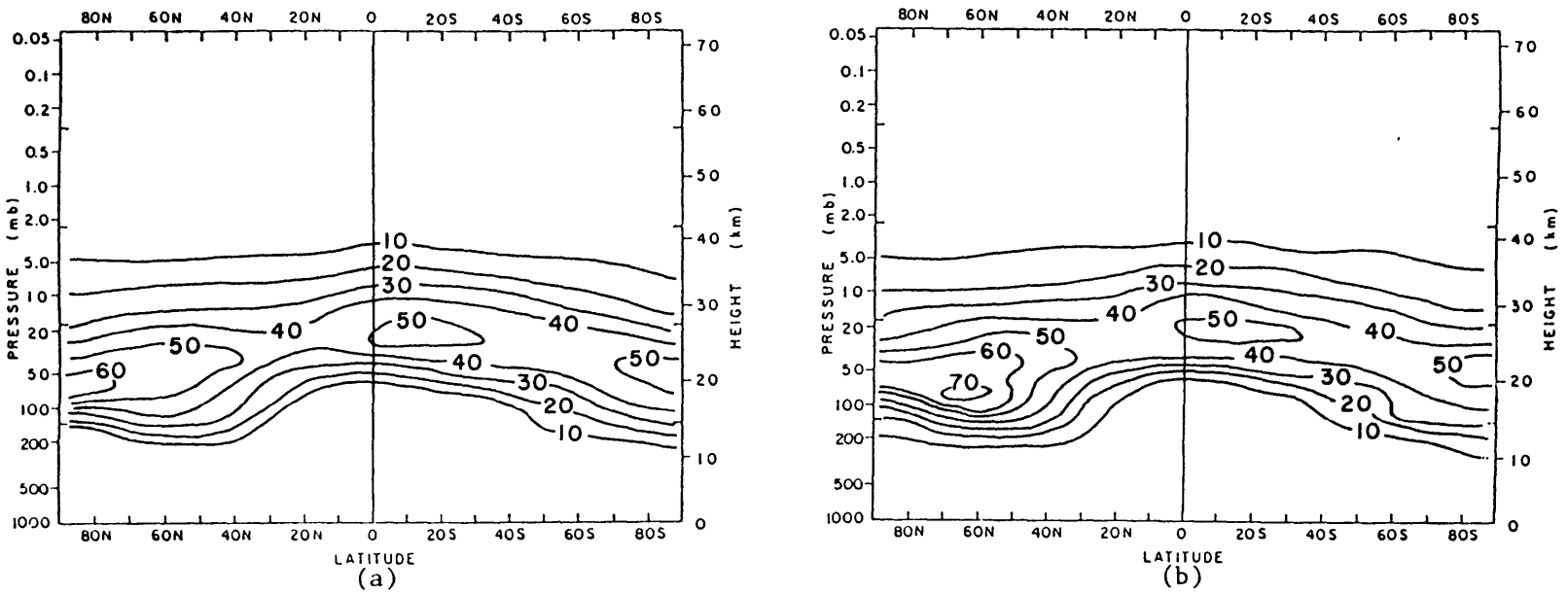

Figs. 4.8 Model $[n_{O_3}]$ (10^{11} cm^{-3}) for: (a) January, (b) February, (c) March

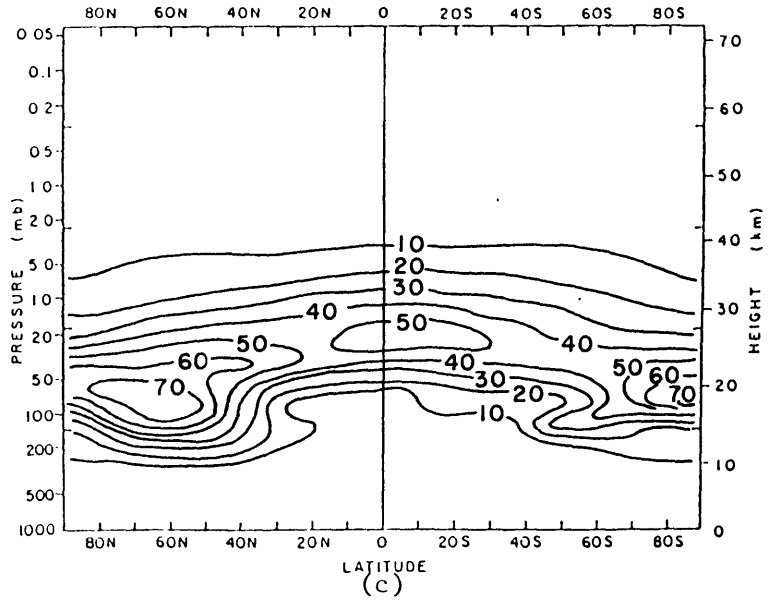

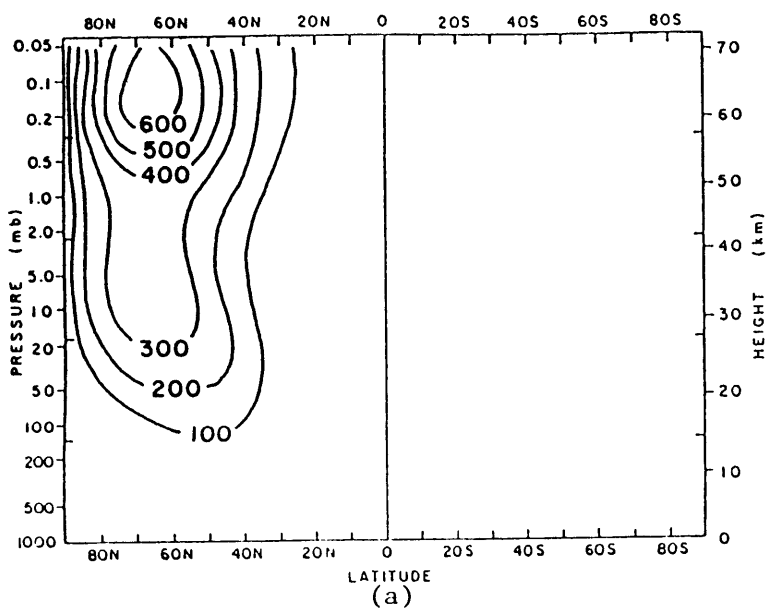

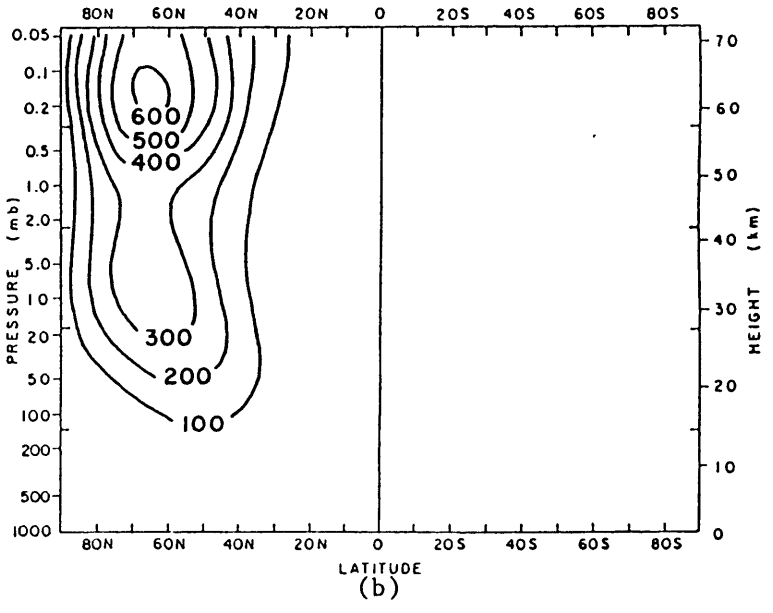

Figs. 4.9 Model Wavenumber 1 Amplitude (gpm) for: (a) January, (b) February, (c) March

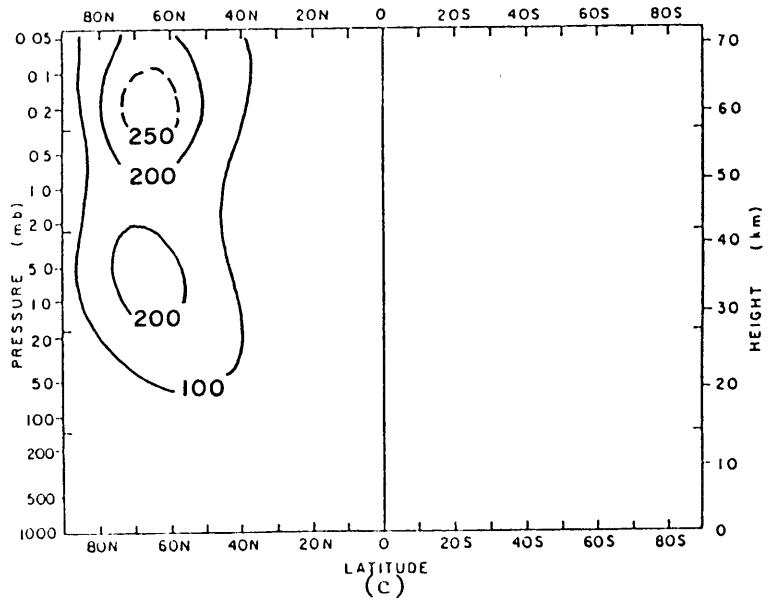

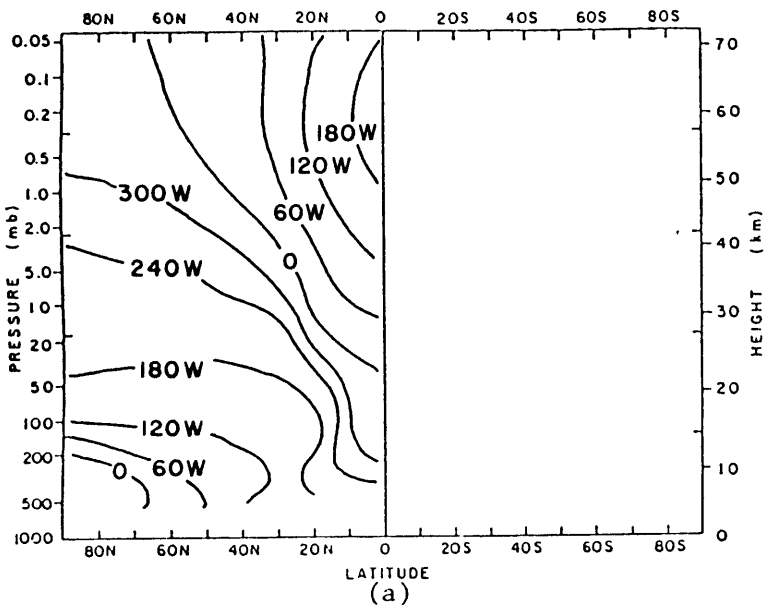

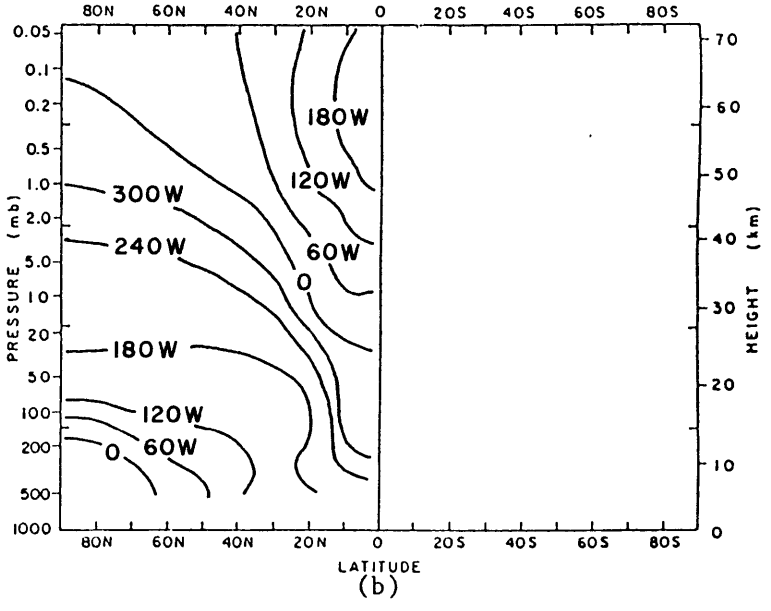

Figs. 4.10 Model Wavenumber 1 Phase (deg) for: (a) January, (b) February, (c) March

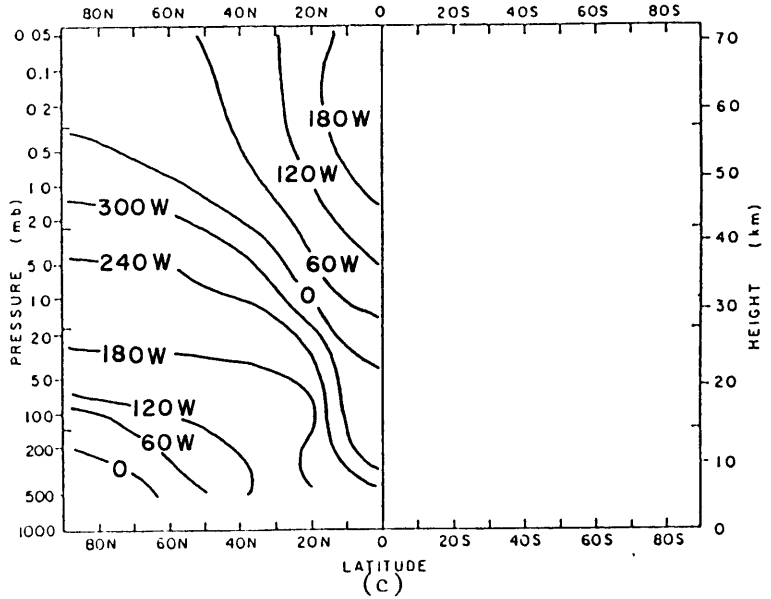

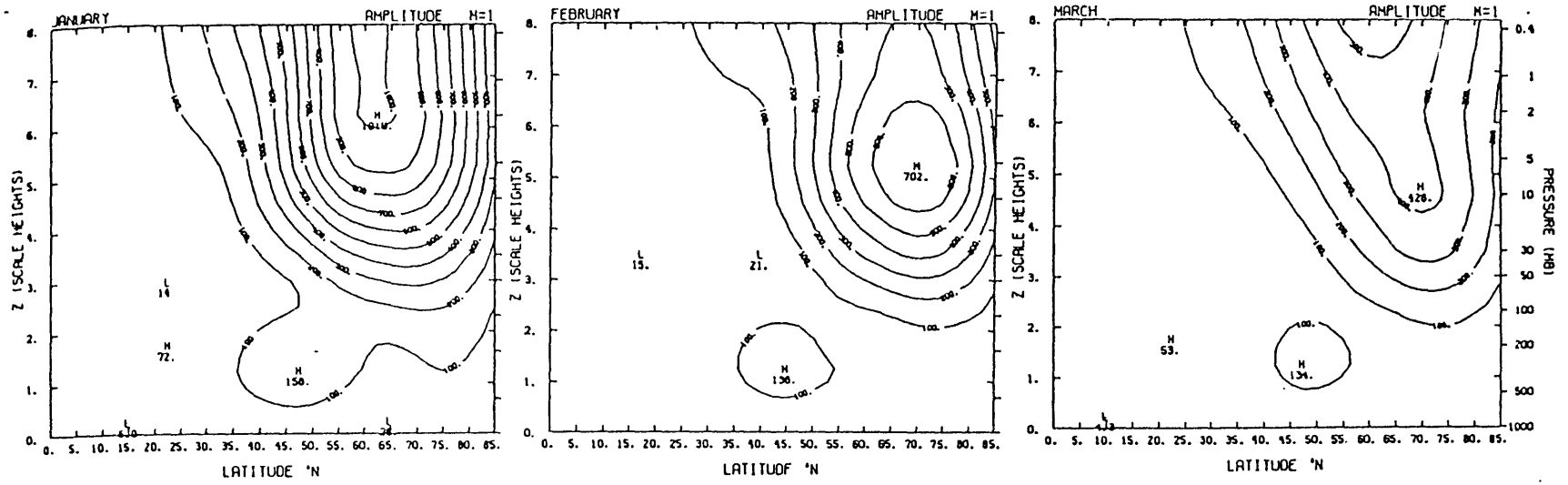

Figs. 4.11 Observed Wavenumber 1 Amplitude (gpm) for: (a) January, (b) February, (c) March (after Wu, et al, 1984)

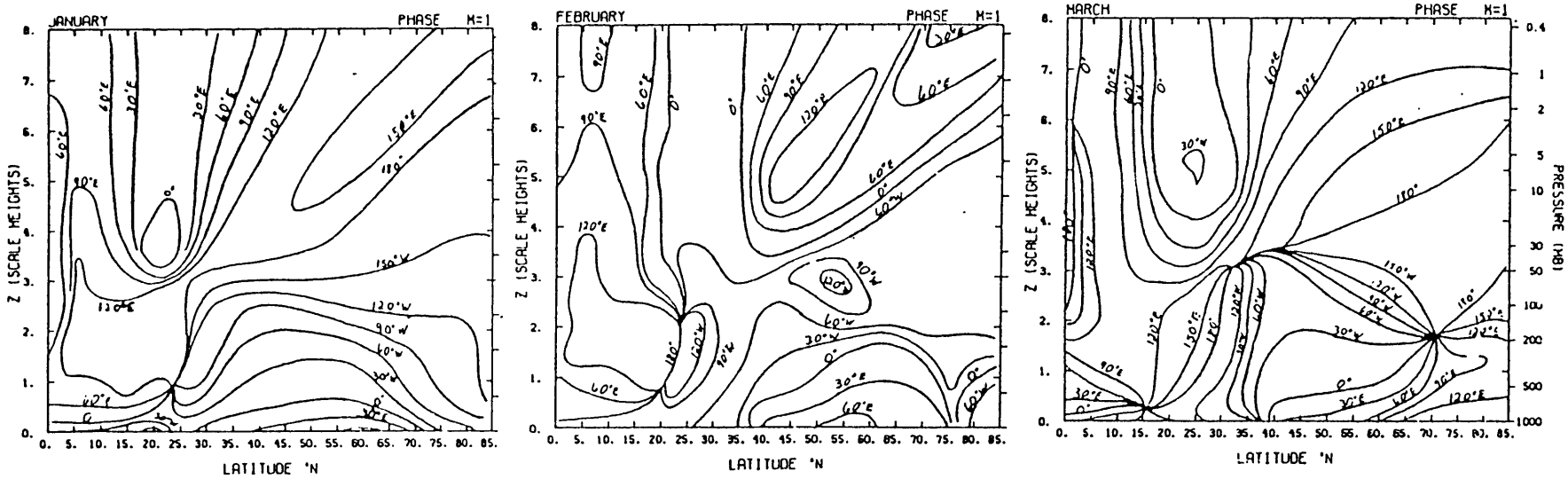

(a) (b) (c)

Figs. 4.12 Observed Wavenumber 1 Phase (deg) for: (a) January, (b) February, (c) March (after Wu, et al, 1984)

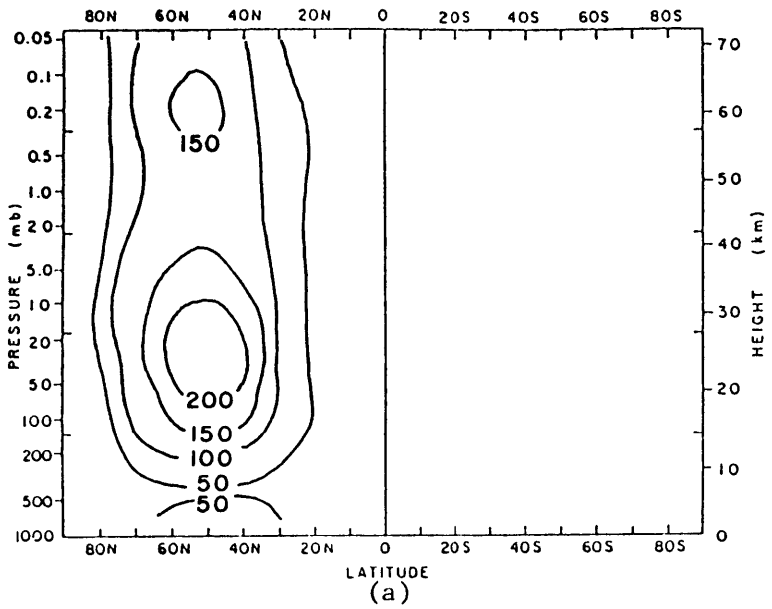

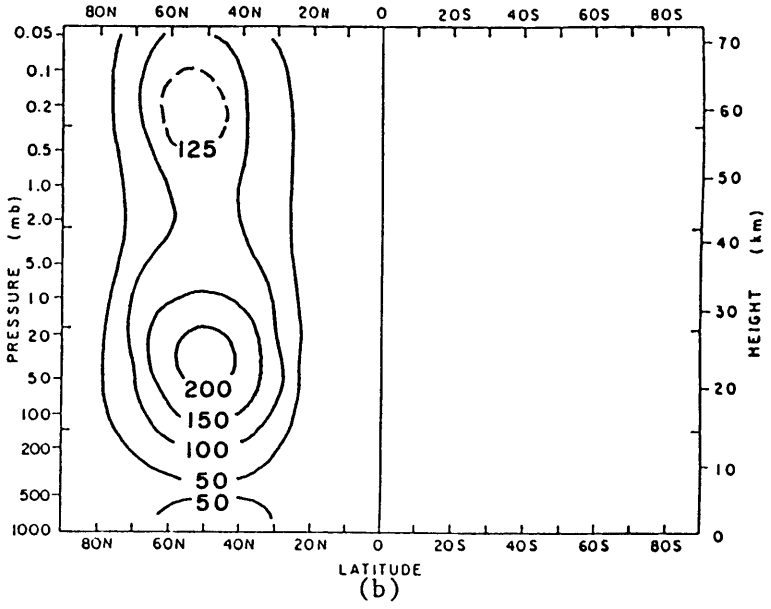

Figs. 4.13 Model Wavenumber 2 Amplitude (gpm) for: (a) January, (b) February, (c) March

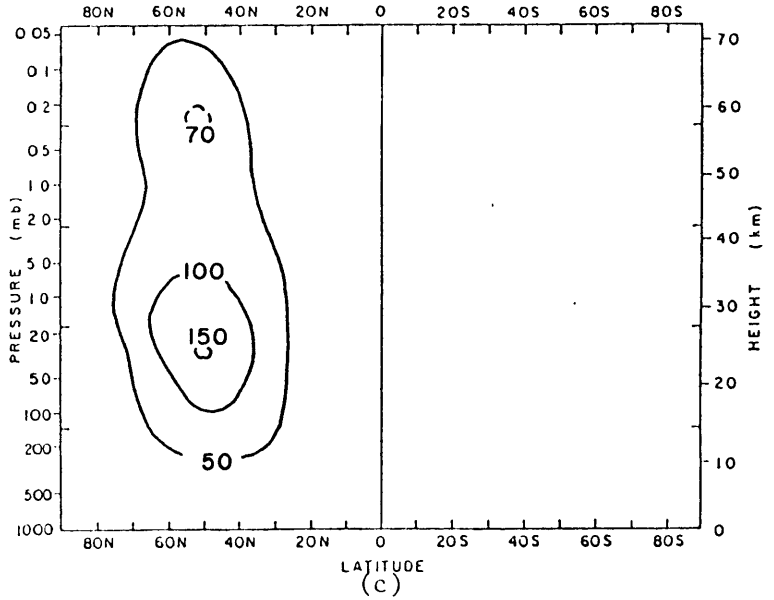

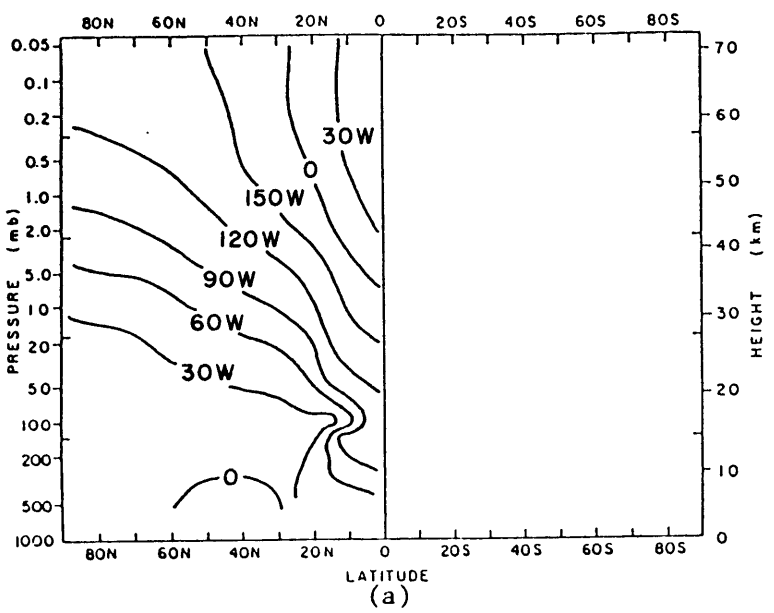

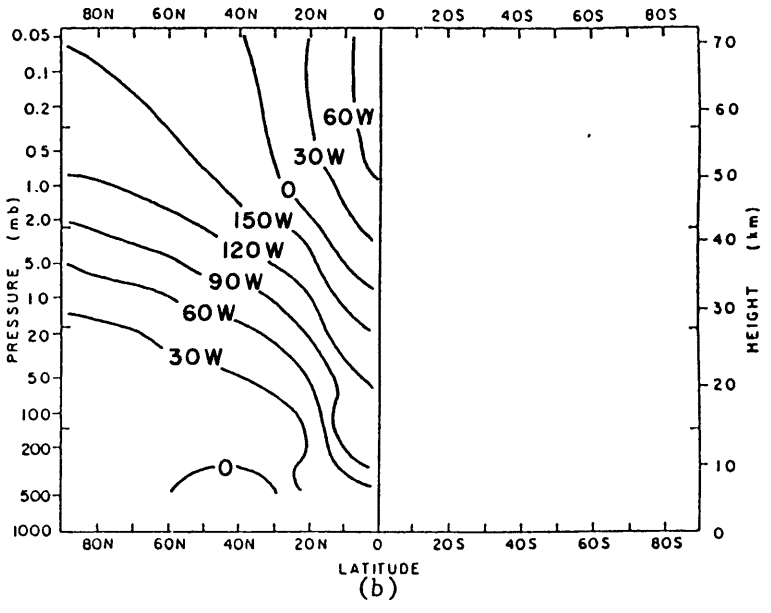

Figs. 4.14 Model Wavenumber 2 Phase (deg) for: (a) January, (b) February, (c) March

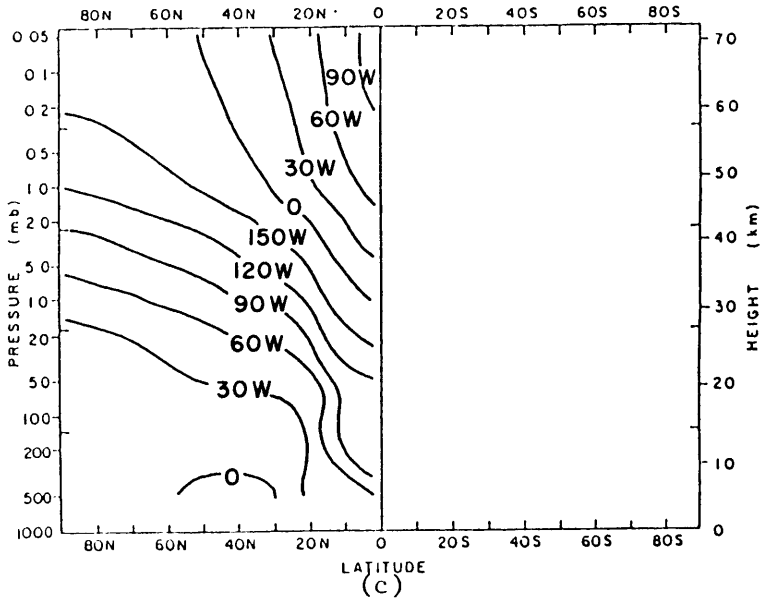

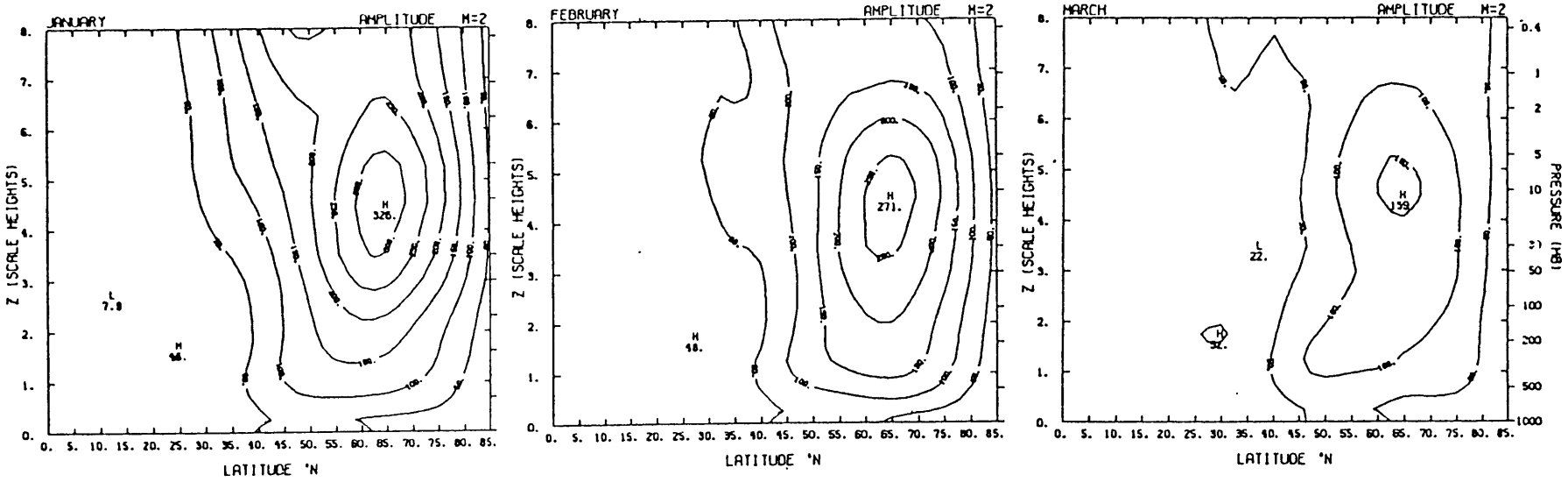

Figs. 4.15 Observed Wavenumber 2 Amplitude (gpm) for: (a) January, (b) February, (c) March (after Wu, et al, 1984)

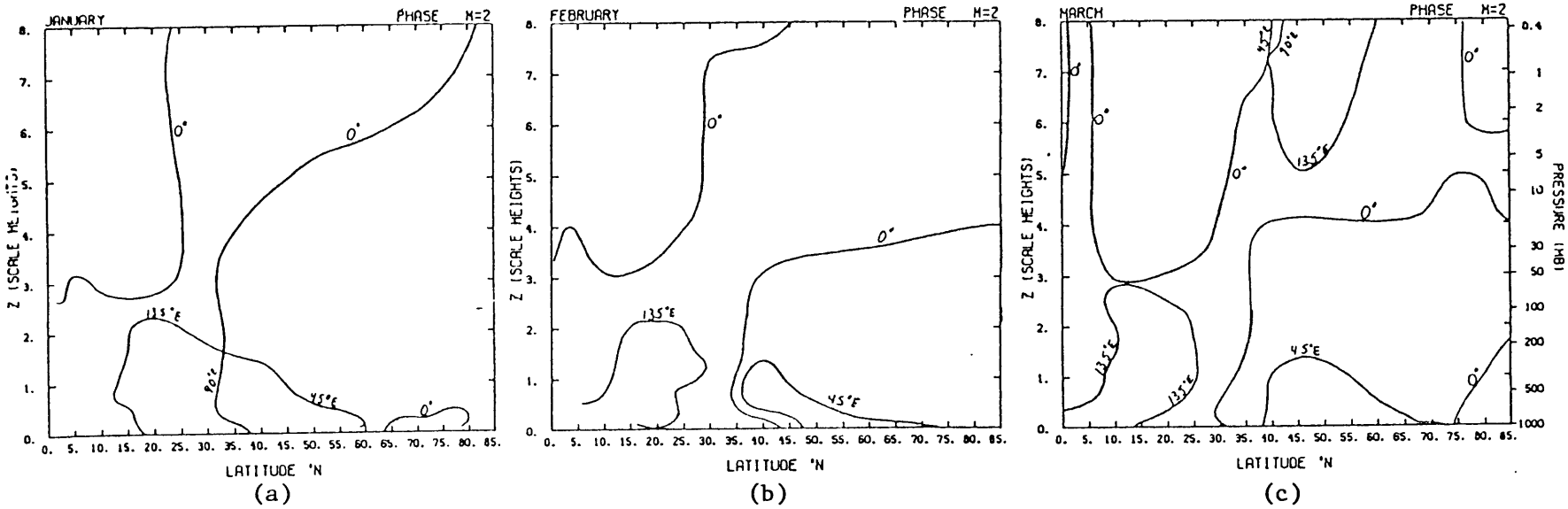

Figs. 4.16 Observed Wavenumber 2 Phase (deg) for: (a) January, (b) February, (c) March (after Wu, et al, 1984)

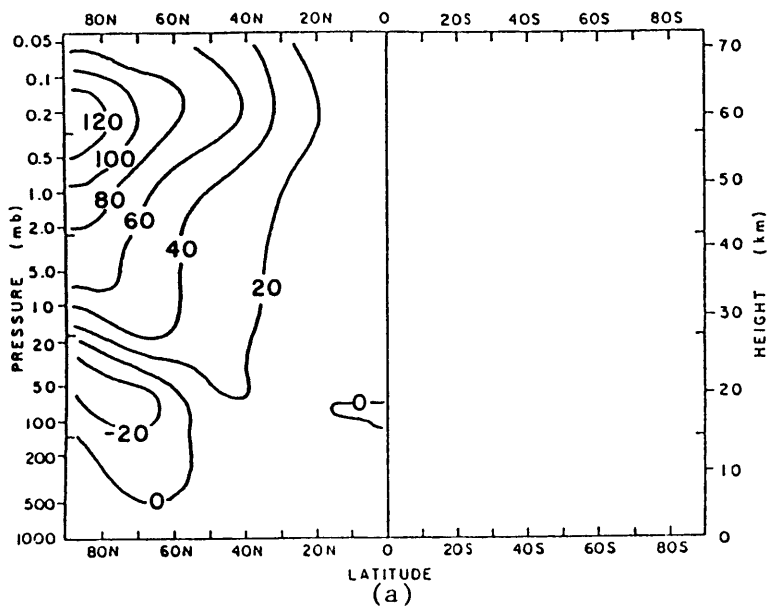

(a)

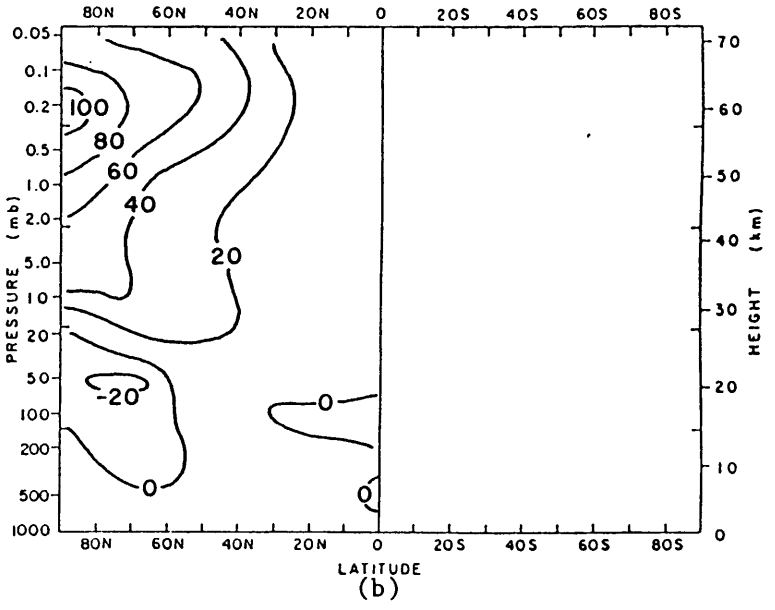

(b)

Figs. 4.17 Model $[u^* v^*]$ (m^2/s^2) for: (a) January, (b) February, (c) March

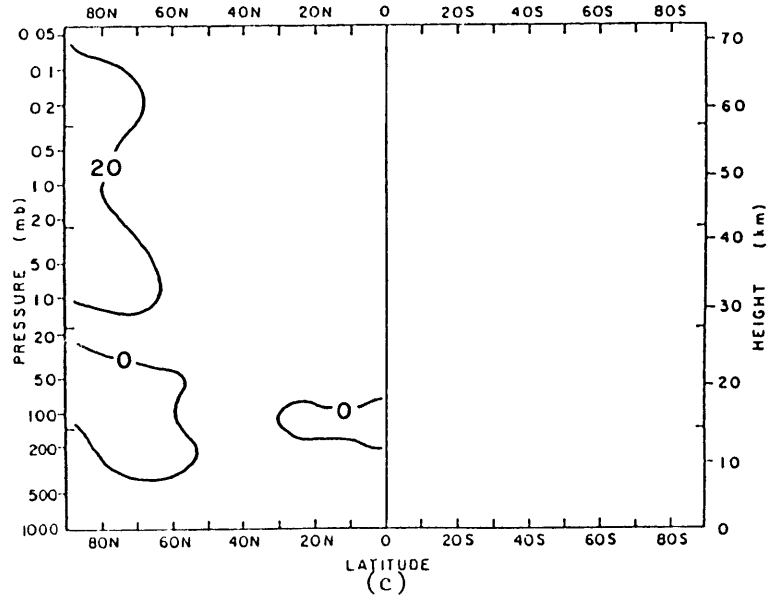

(c)

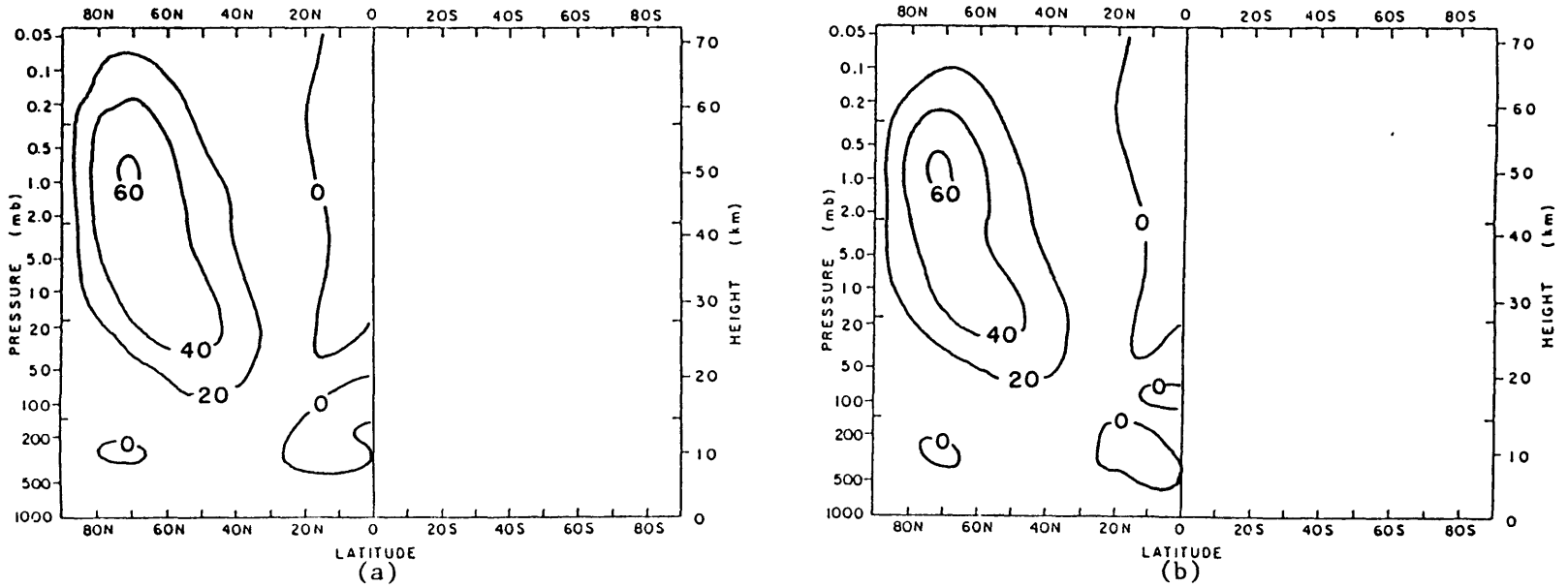

Figs. 4.18 Model $[v^{*}T^{*}]$ (K-m/s) for: (a) January, (b) February, (c) March

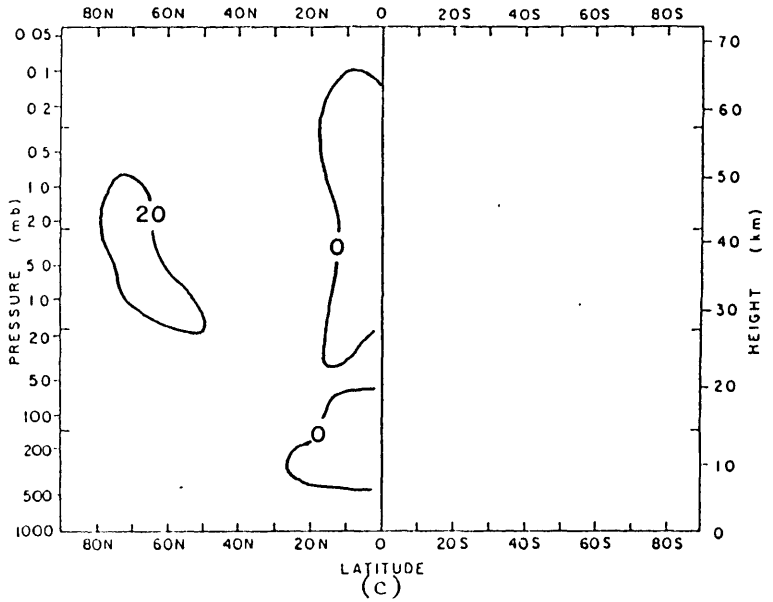

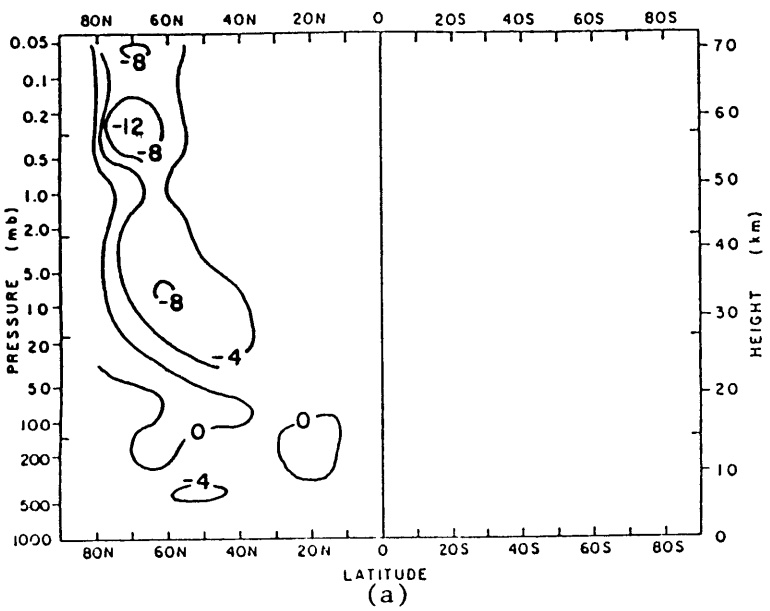

(a)

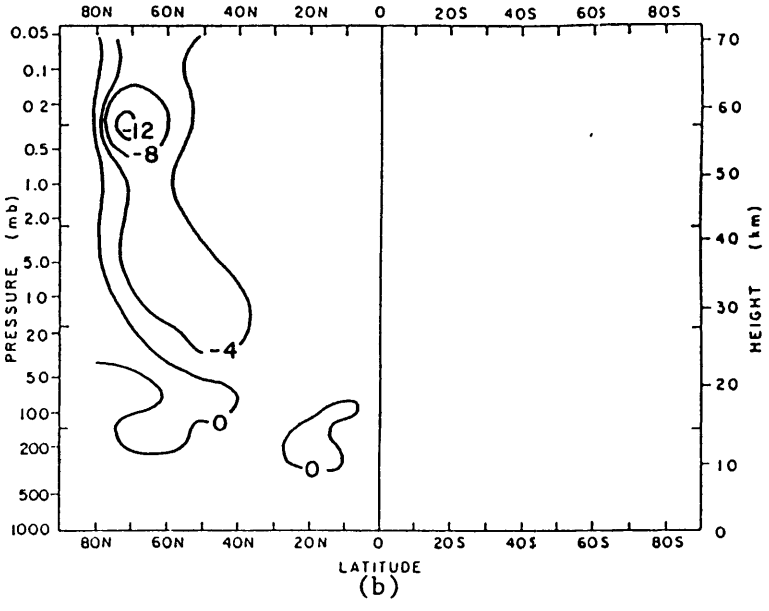

(b)

Figs. 4.19 Model Eliassen-Palm flux divergence (10^{-5} m/s^2) for: (a) January, (b) February, (c) March

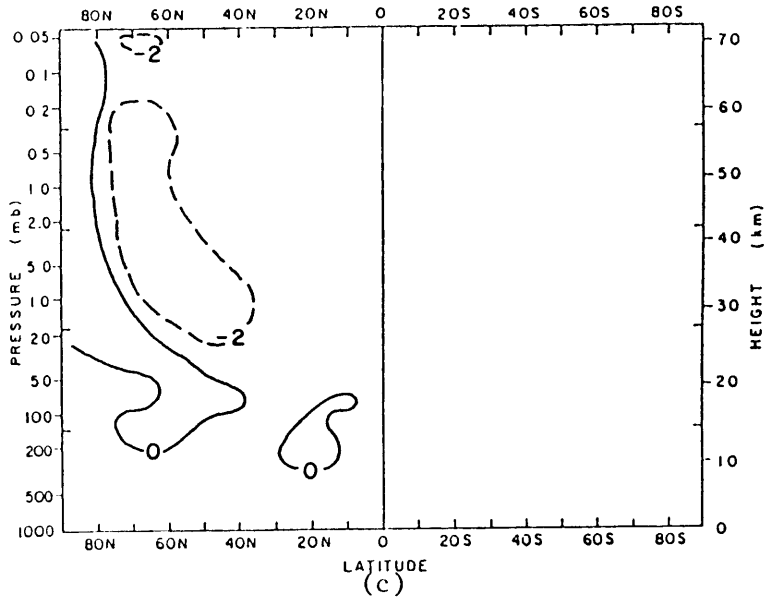

(c)

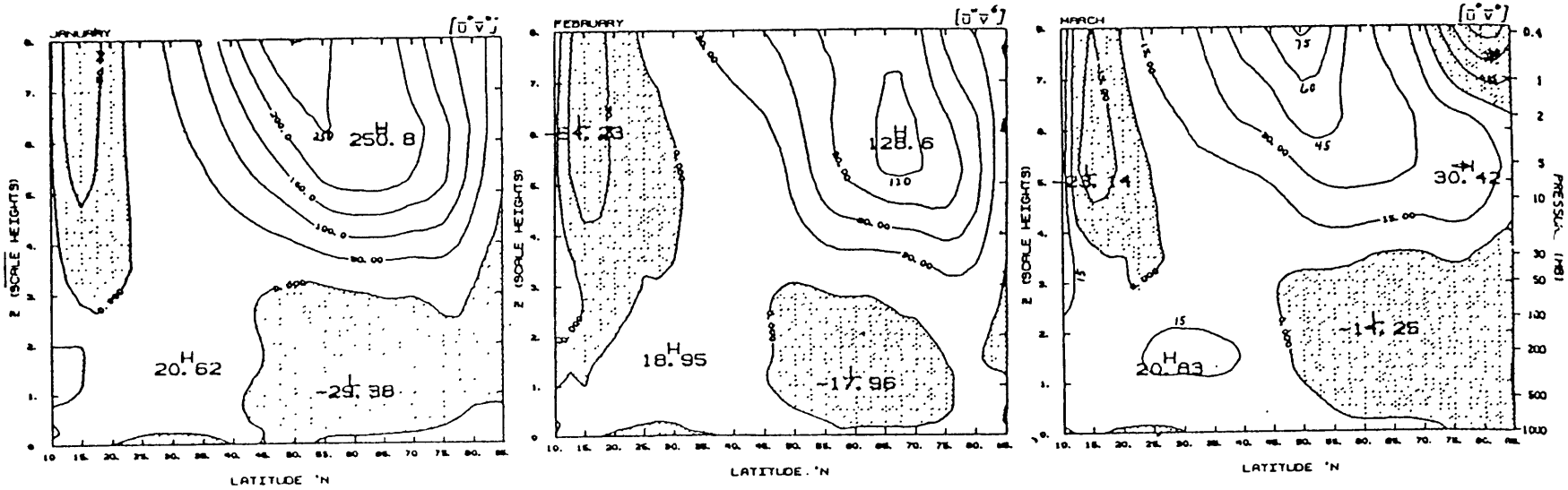

(a) (b) (c)

Figs. 4.20 Observed Standing Eddy Momentum Flux (m^2/s^2) for: (a) January, (b) February, (c) March (after Wu, et al, 1984)

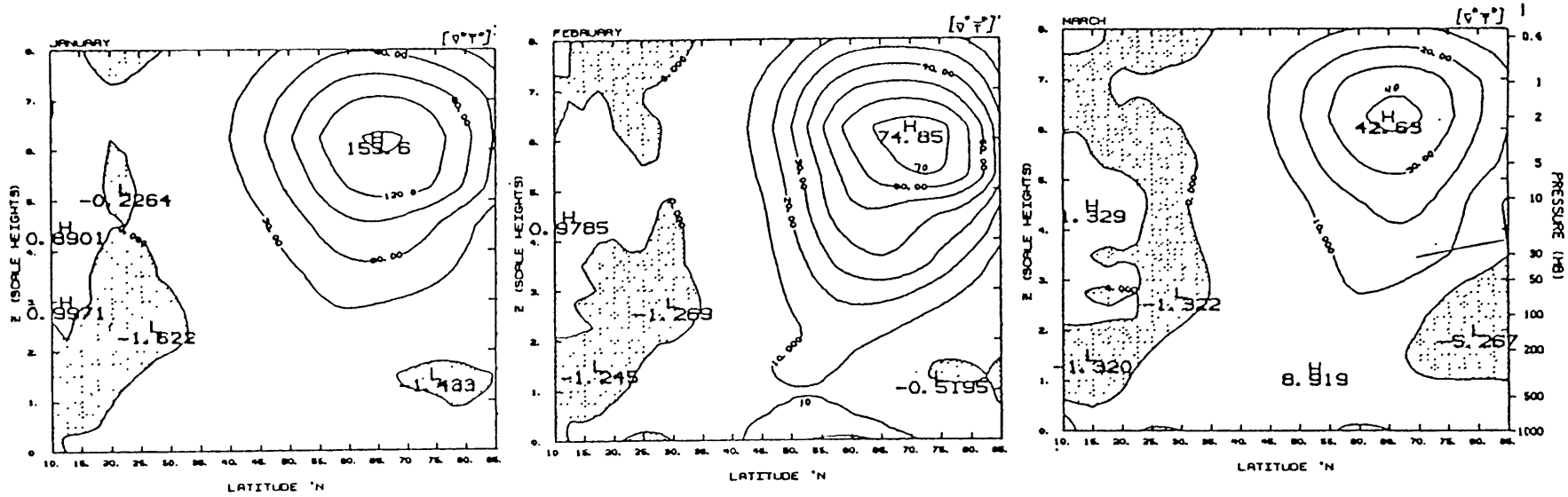

(a) (b) (c)

Figs. 4.21 Observed Standing Eddy Heat Flux (K-m/s) for: (a) January, (b) February, (c) March (after Wu, et al, 1984)

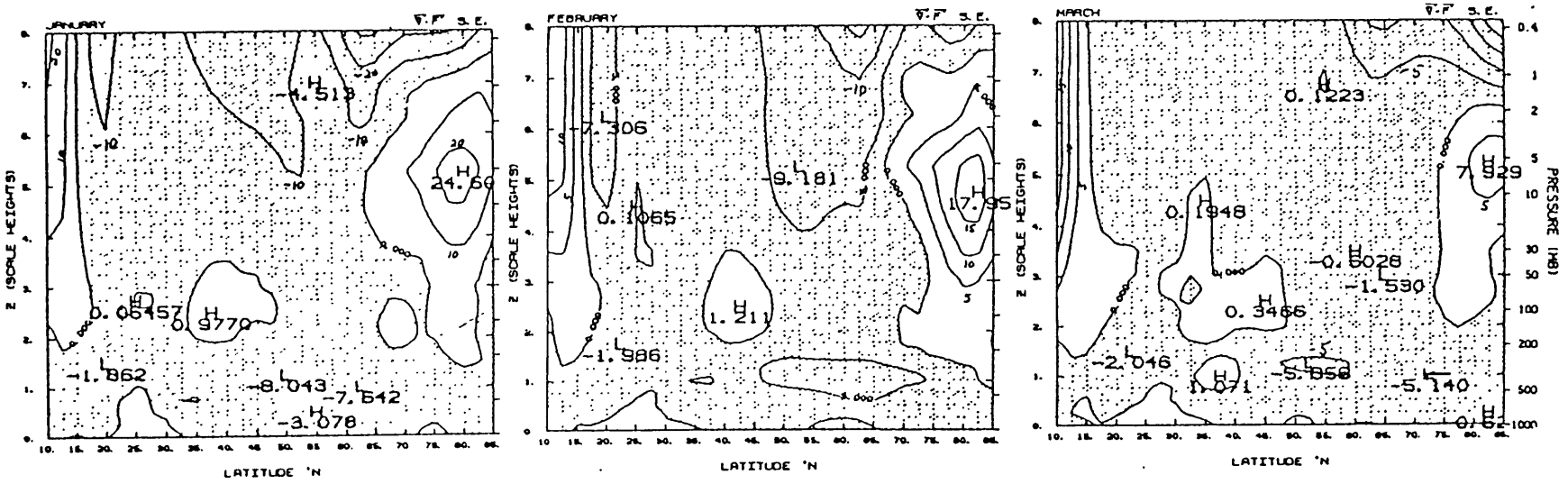

(a) (b) (c)

Figs. 4.22 Observed Standing Eddy Eliassen-Palm flux divergence (10^{-5} m/s^2) for: (a) January, (b) February, (c) March (after Wu, et al, 1984)

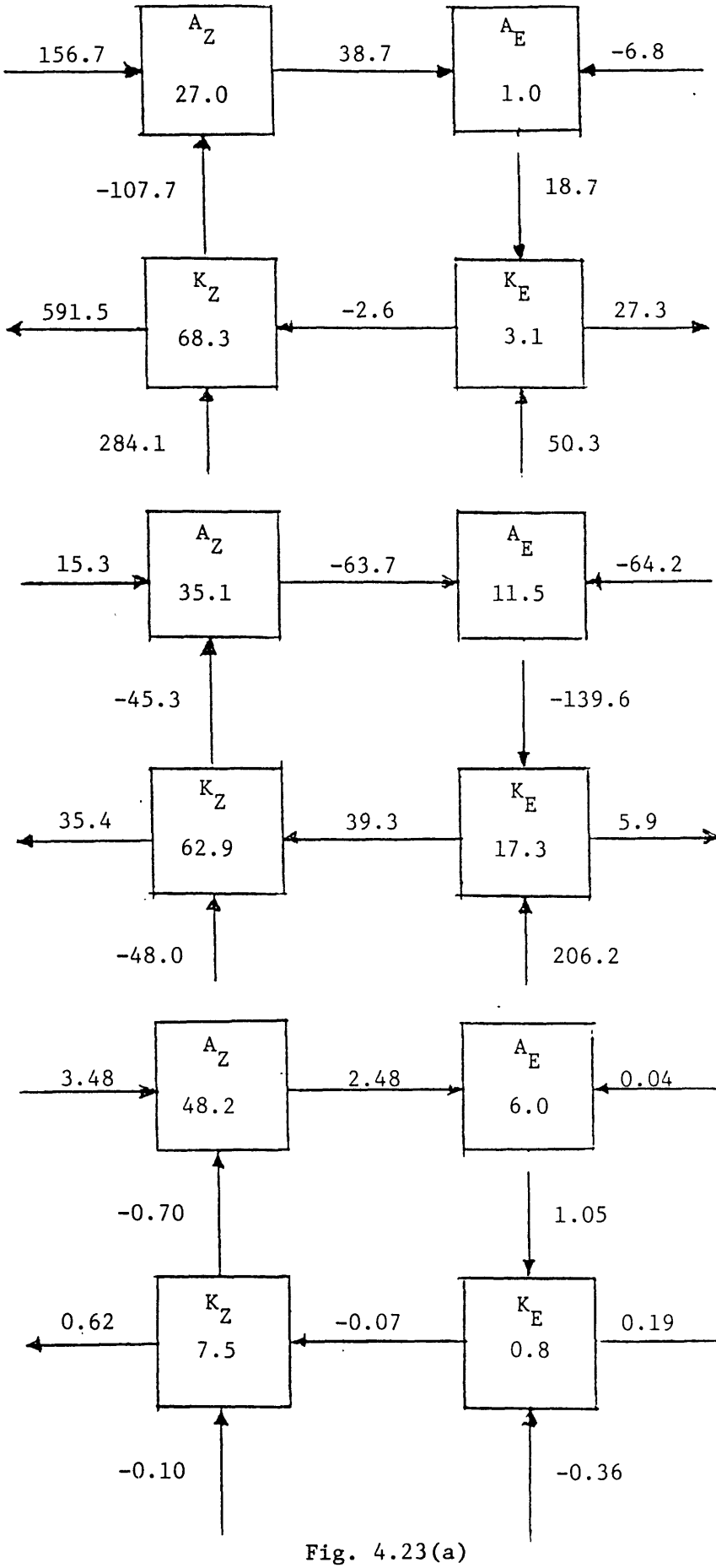

MESOSPHERE
(Levels 1-8)

Units: 10^2 J/m^2, 10^{-4} W/m^2

STRATOSPHERE
(Levels 9-19)

Units: 10^3 J/m^2, 10^{-3} W/m^2

TROPOSPHERE
(Levels 20-26)

Units: 10^5 J/m^2, W/m^2

Fig. 4.23(a)

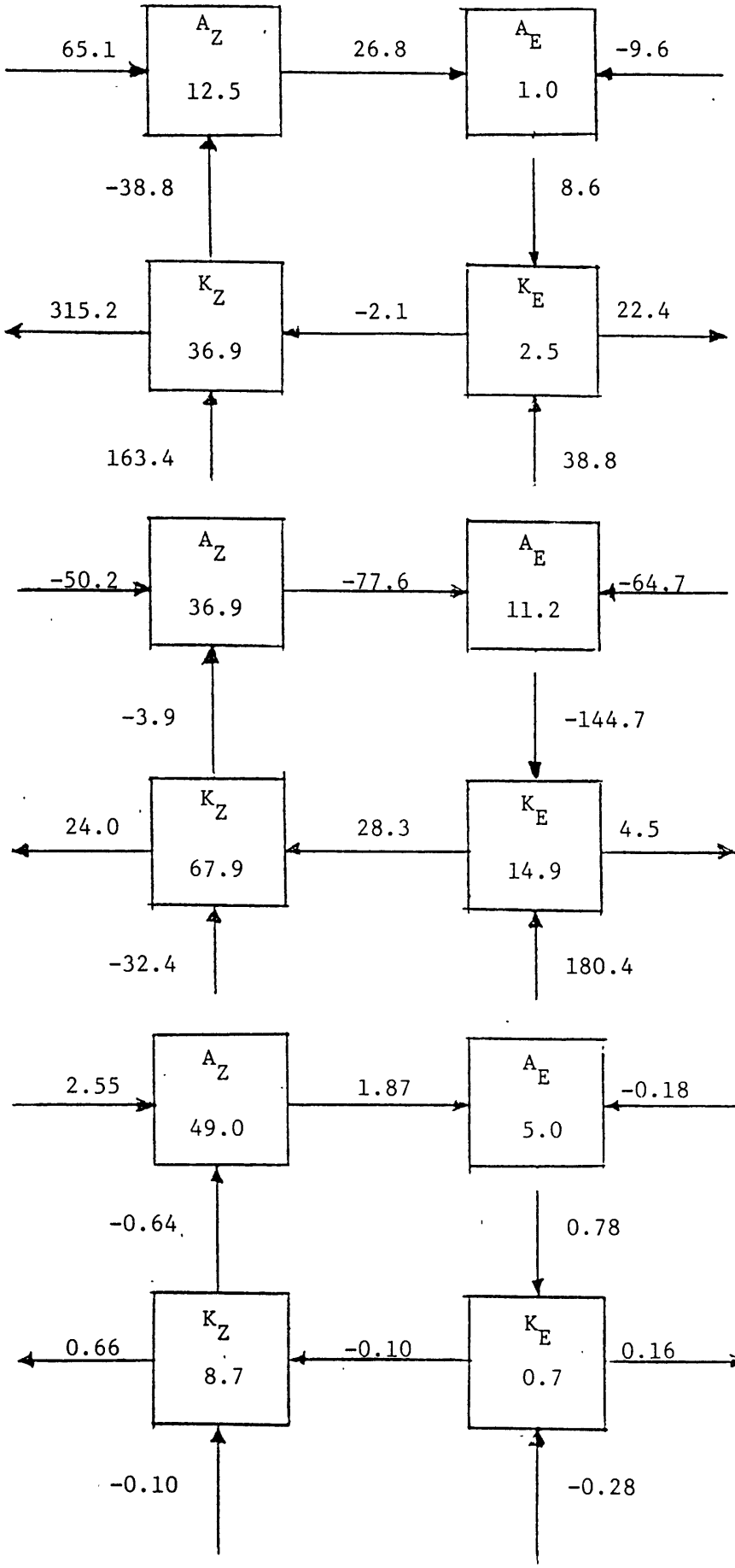

MESOSPHERE
(Levels 1-8)

Units: 10^2 J/m^2, 10^{-4} W/m^2

STRATOSPHERE
(Levels 9-19)

Units: 10^3 J/m^2, 10^{-3} W/m^2

TROPOSPHERE
(Levels 20-26)

Units: 10^5 J/m^2, W/m^2

Fig. 4.23(b)

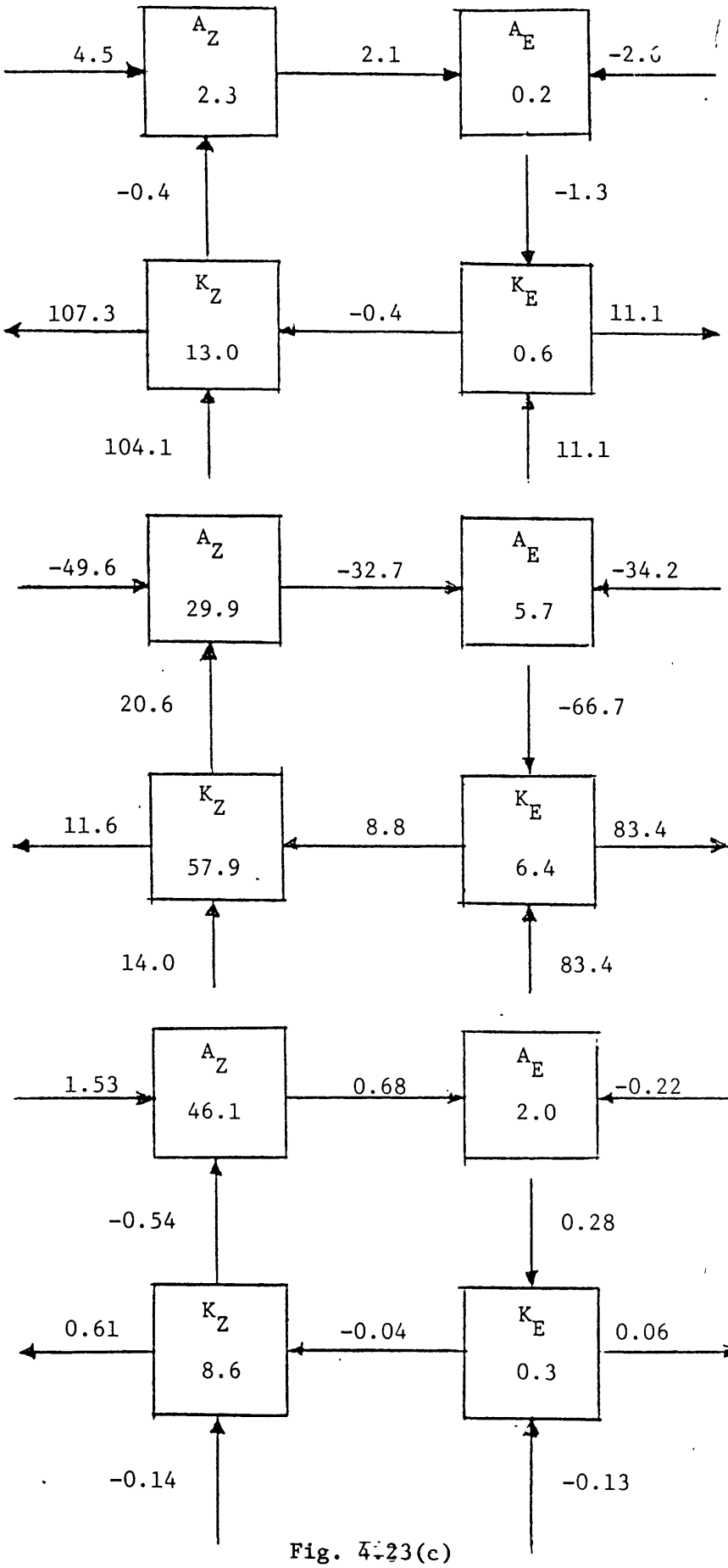

MESOSPHERE
(Levels 1-8)

Units: 10^2 J/m^2, 10^{-4} W/m^2

STRATOSPHERE
(Levels 9-19)

Units: 10^3 J/m^2, 10^{-3} W/m^2

TROPOSPHERE
(Levels 20-26)

Units: 10^5 J/m^2, W/m^2

Fig. 4.23(c)

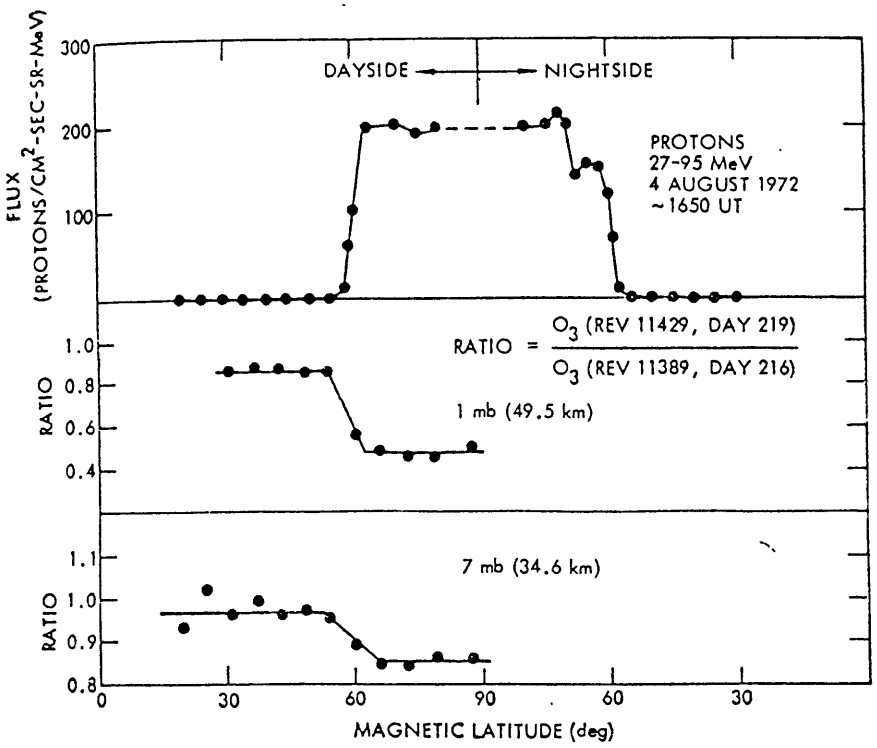

Fig. 5.1: Relationship between the polar cap region irradiated by the solar protons and the polar ozone cavity created by the former at 1- and 7-mbar altitudes during the August, 1972 SPE (after Reagan, et al, 1981).

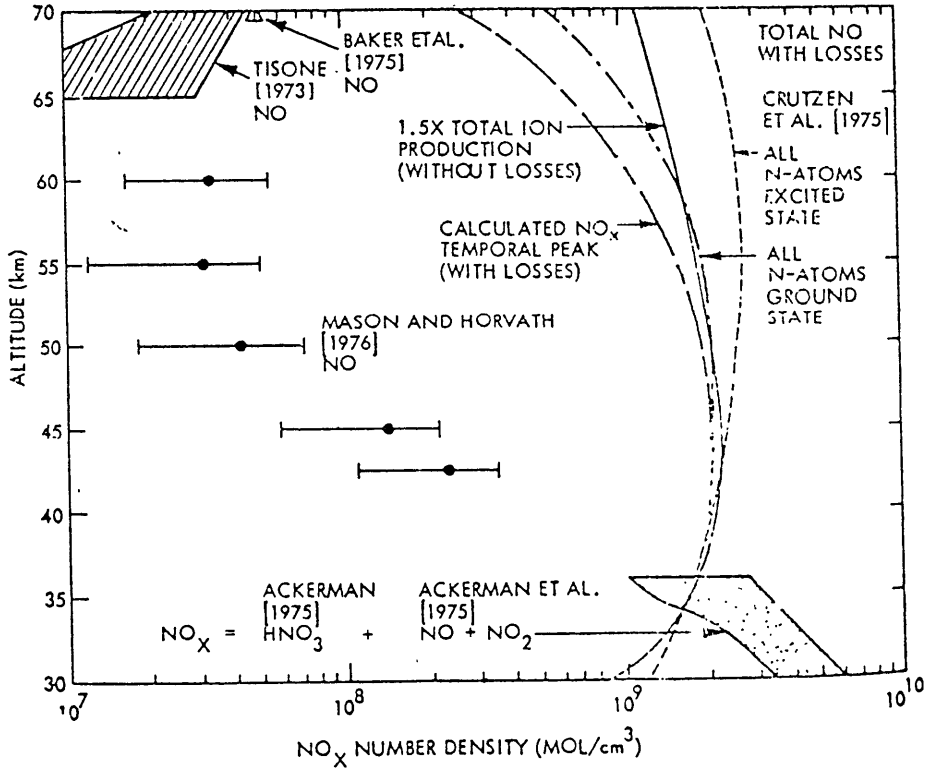

Fig. 5.2: Theoretical NO_x production during the August, 1972 SPE (after Reagan, et al, 1981). Mid-latitude ambient NO_x shown for comparison.

Fig. 5.3: Wavenumber 1 Amplitude Change (gpm) for February Solar-Terrestrial Experiment

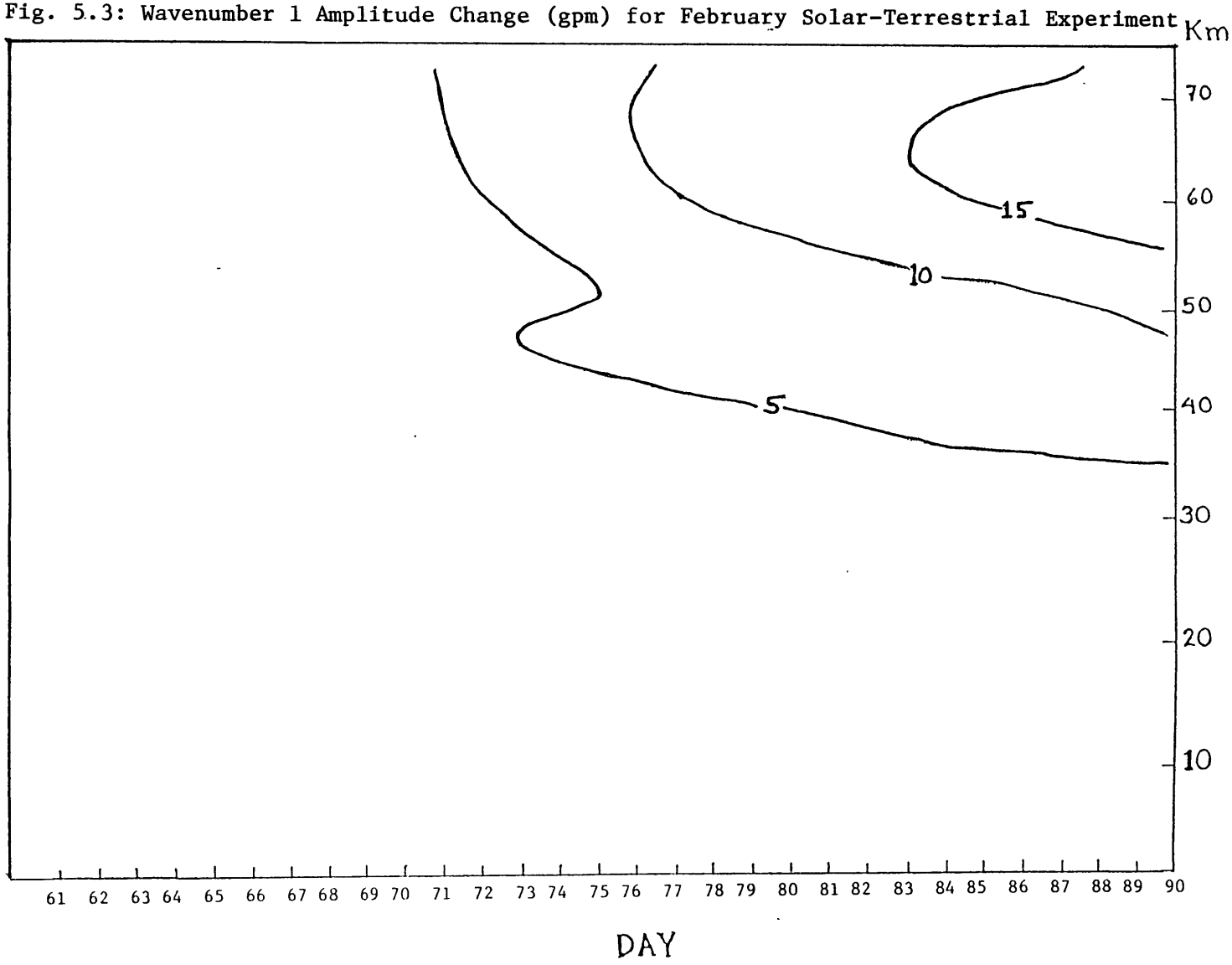

Fig. 5.4: Wavenumber 1 Phase Change (deg) for February Solar-Terrestrial Experiment

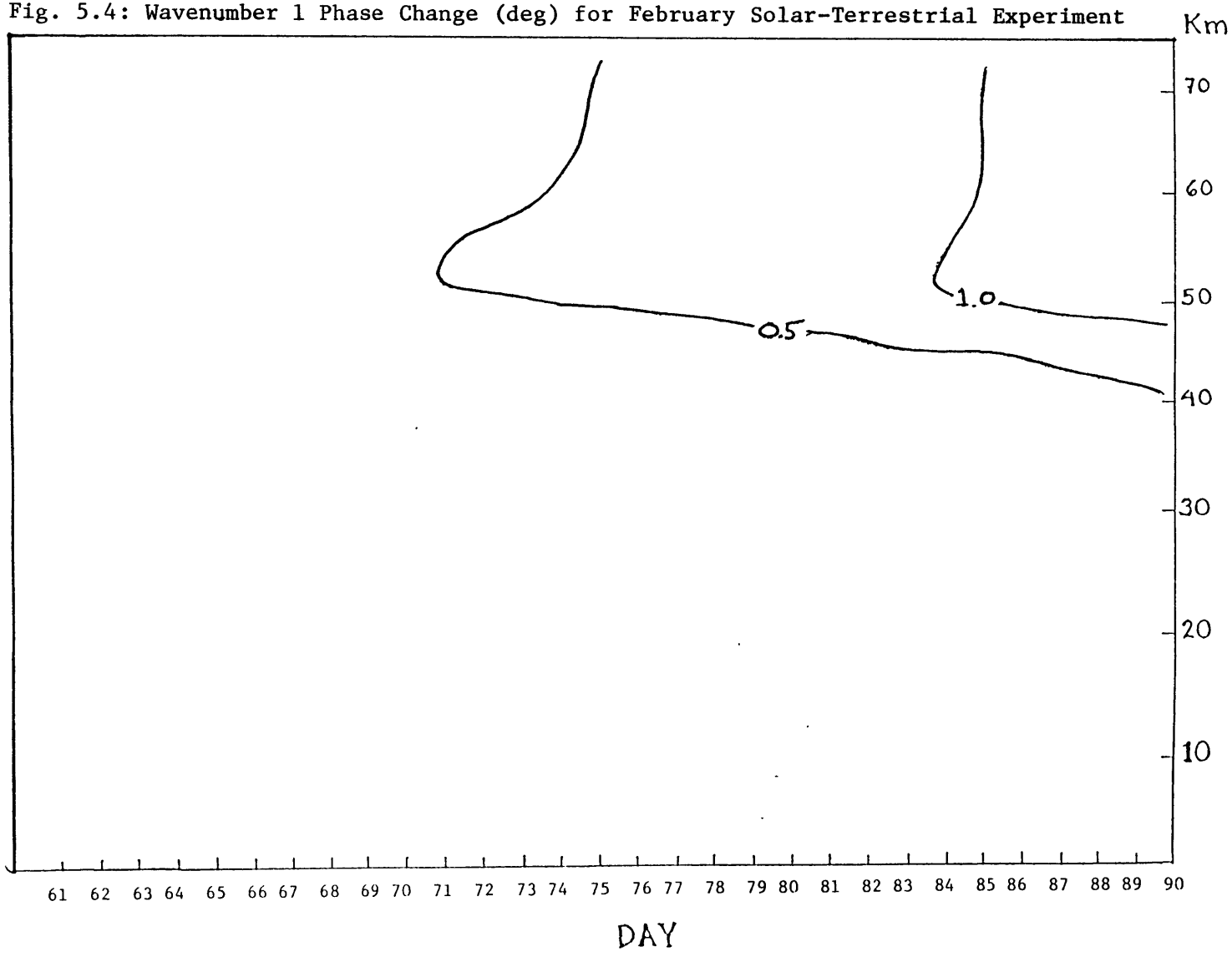

Fig. 5.5: Wavenumber 2 Amplitude Change (gpm) for February Solar-Terrestrial Experiment

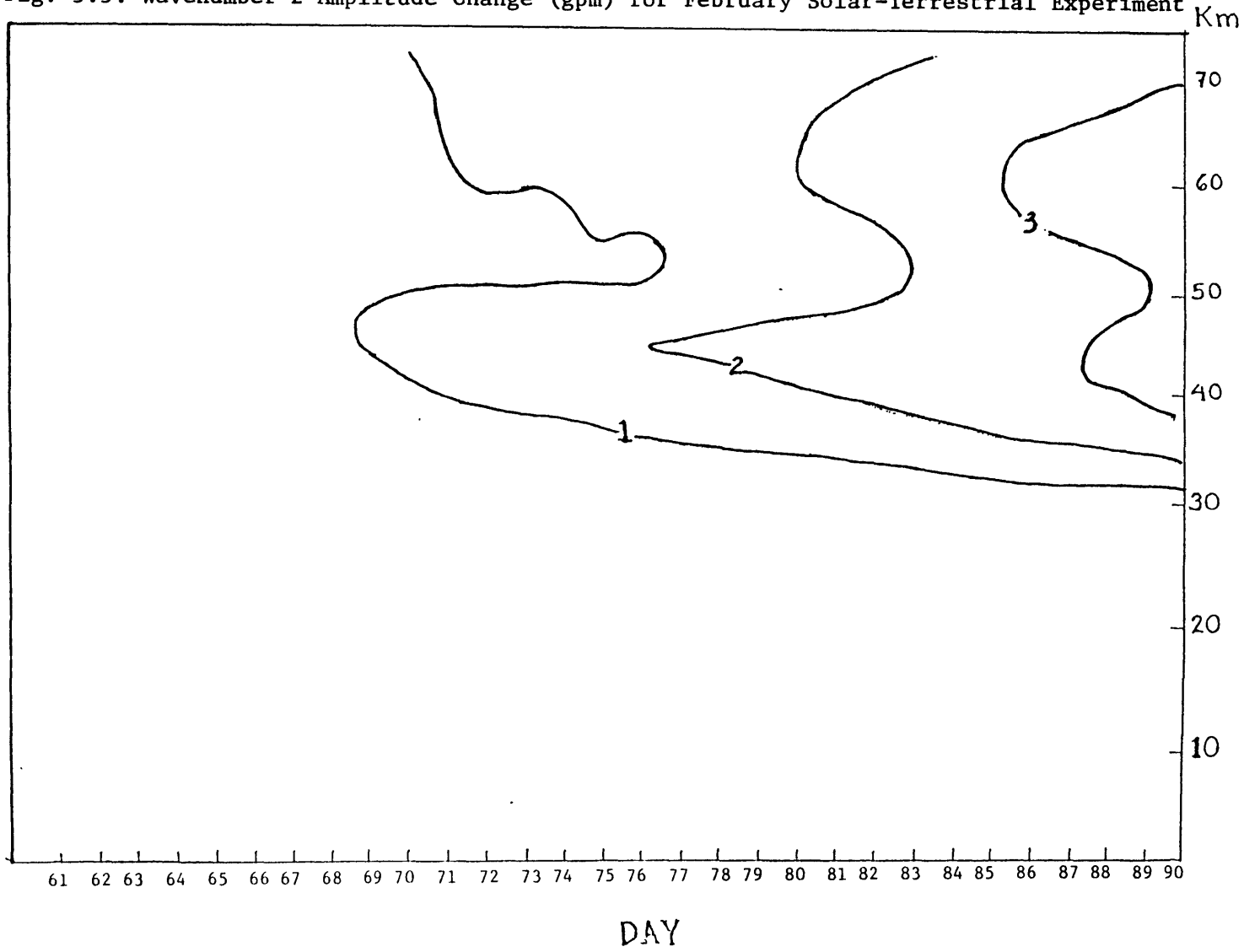

Fig. 5.6: Wavenumber 2 Phase Change (deg) for February Solar-Terrestrial Experiment

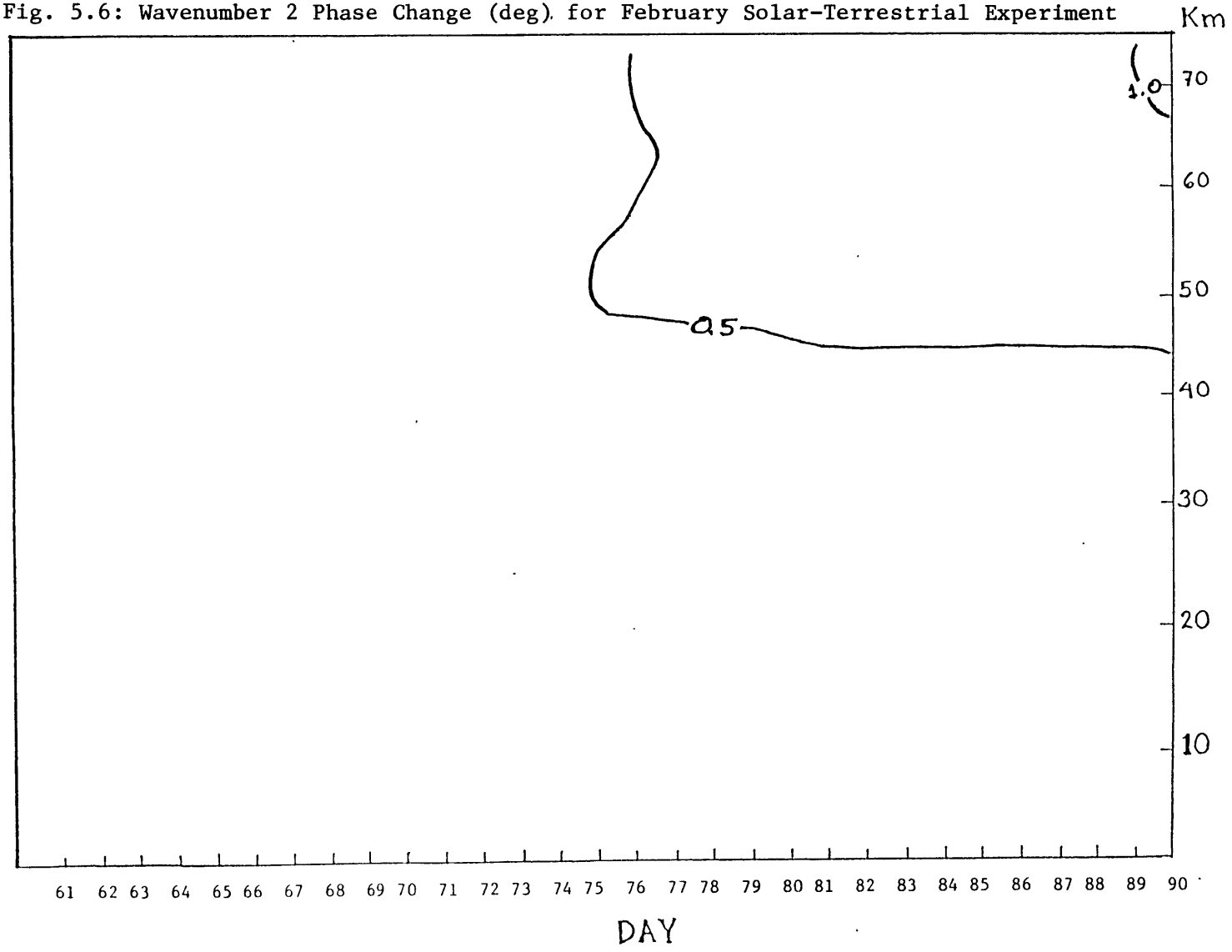

Fig. 5.7: Wavenumber 1 Amplitude Change (gpm) for March Solar-Terrestrial Experiment

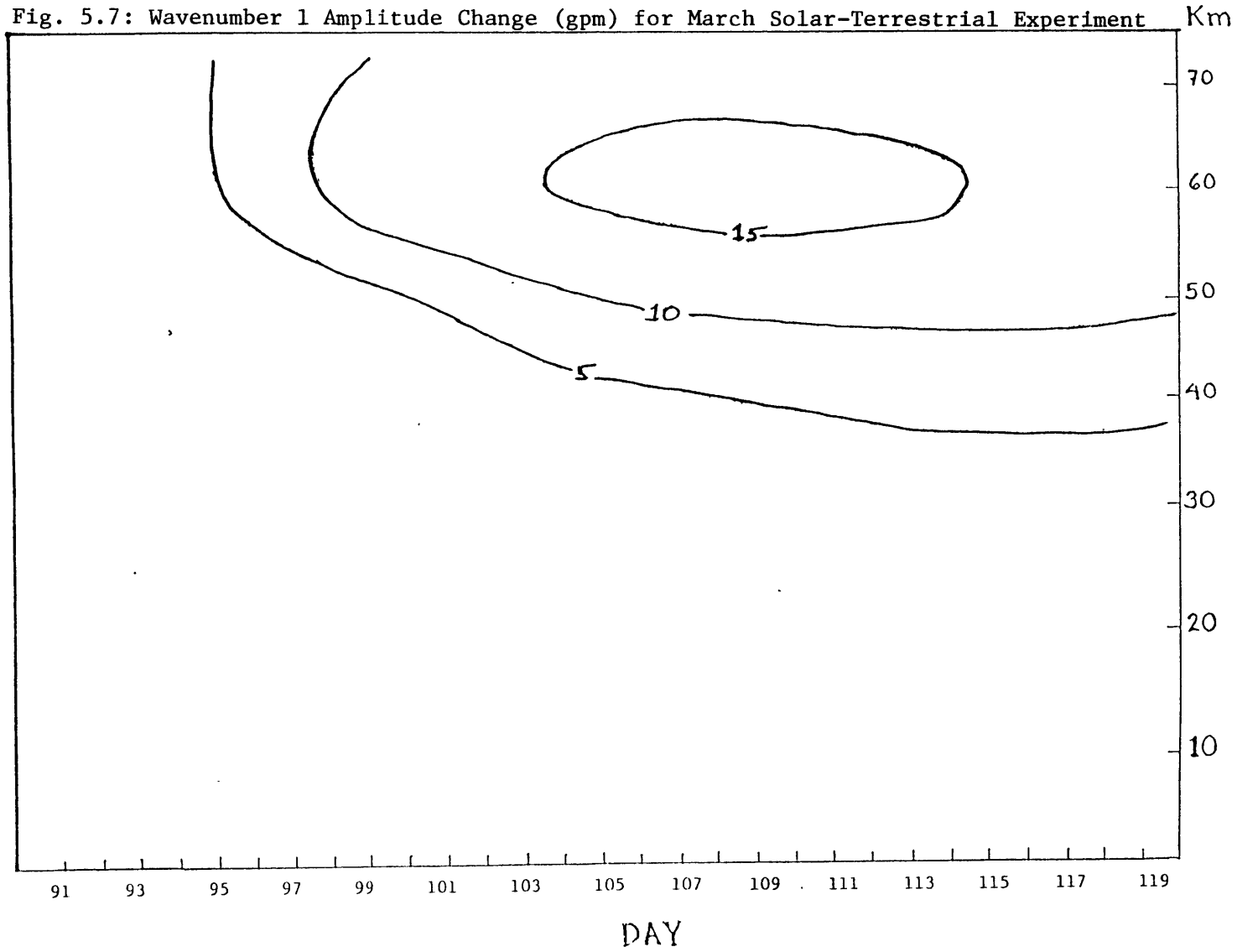

Fig. 5.8: Wavenumber 1 Phase Change (deg) for March Solar-Terrestrial Experiment

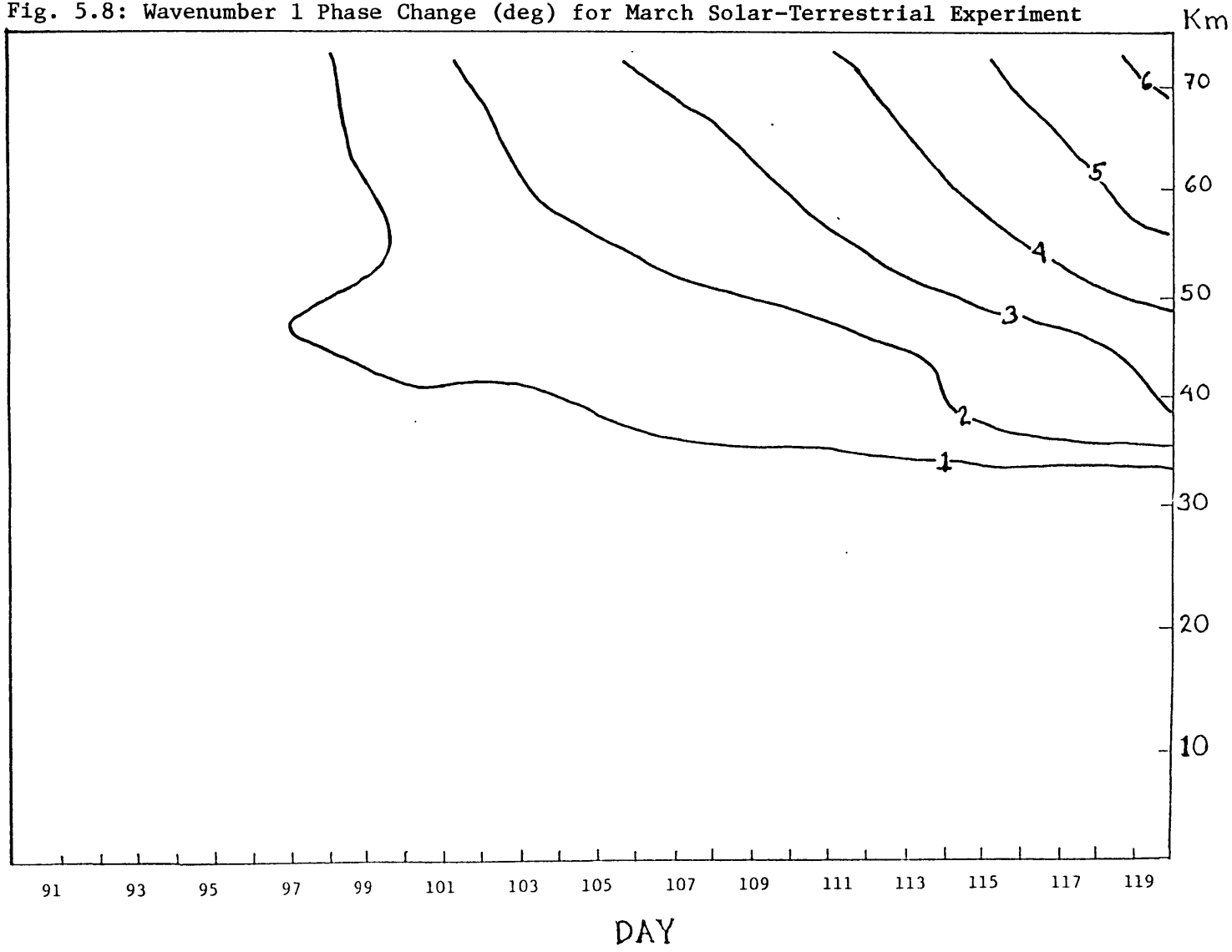

Fig. 5.9: Wavenumber 2 Amplitude Change (gpm) for March Solar-Terrestrial Experiment

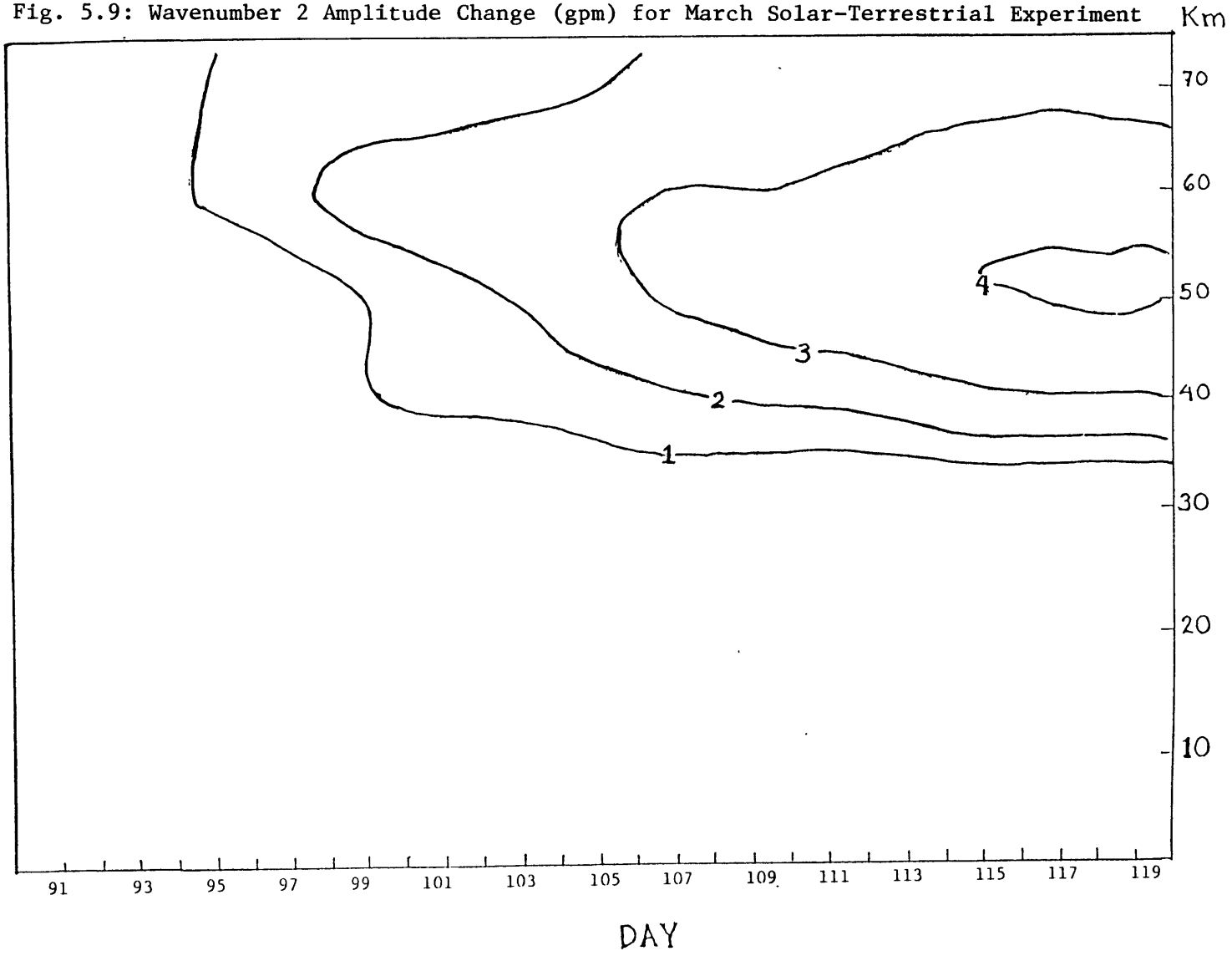

Fig. 5.10: Wavenumber 2 Phase Change (deg) for March Solar-Terrestrial Experiment

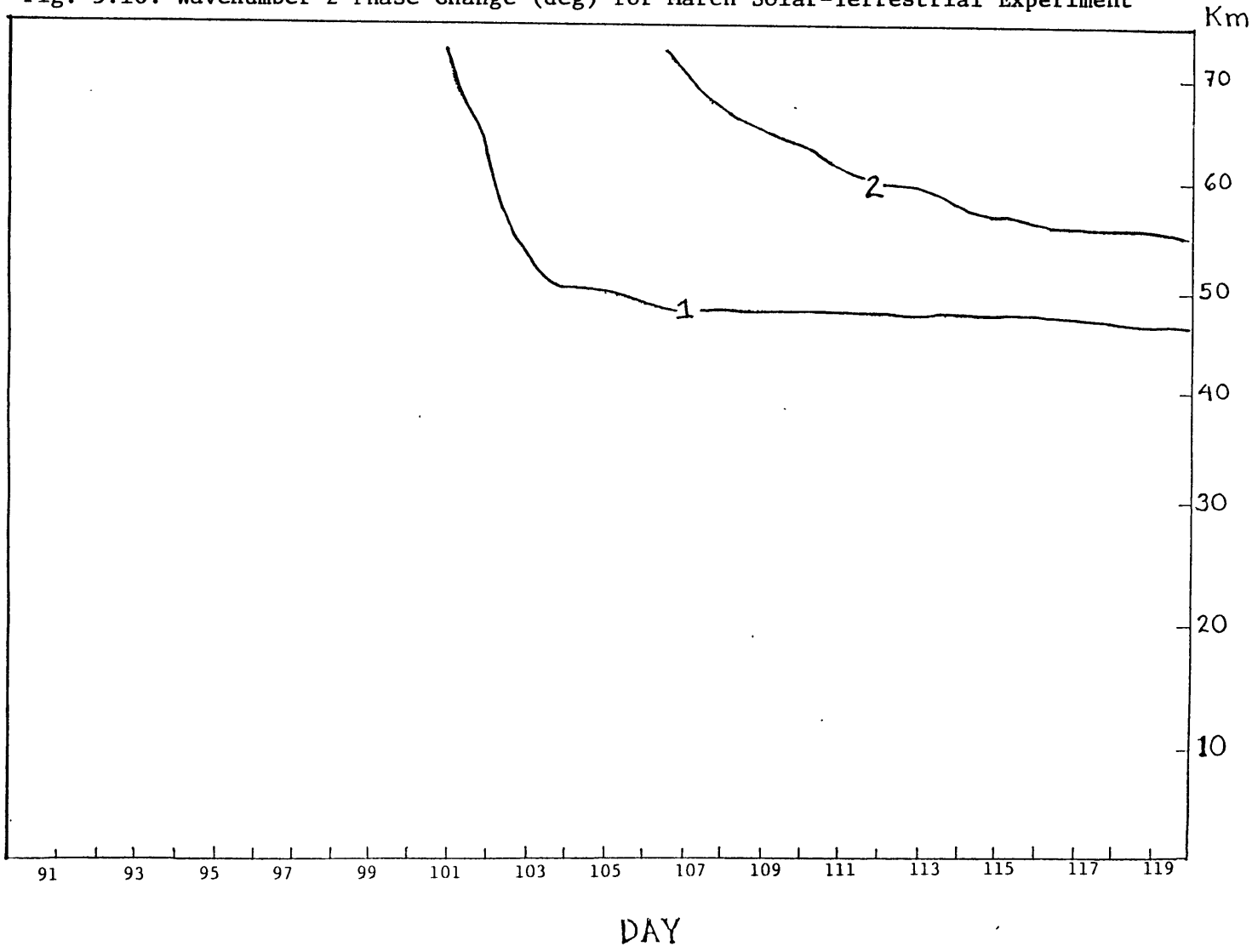

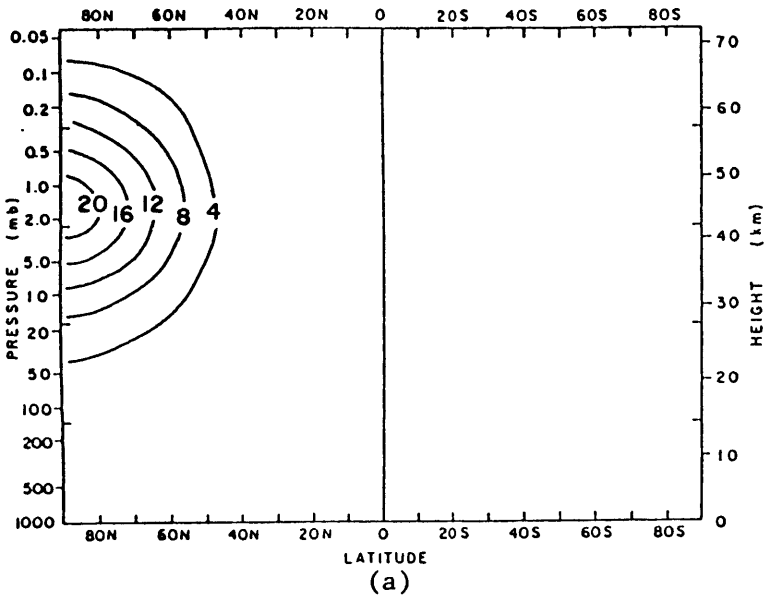

(a)

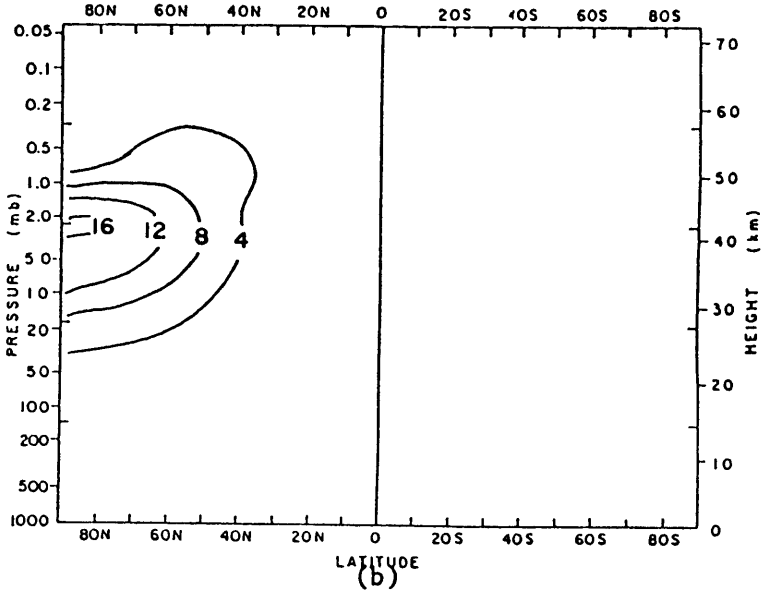

(b)

Figs. 5.11 Perturbation NO_x density (10^8 cm^{-3}) for: (a) day 93, (b) day 102, (c) day 111, (d) day 120

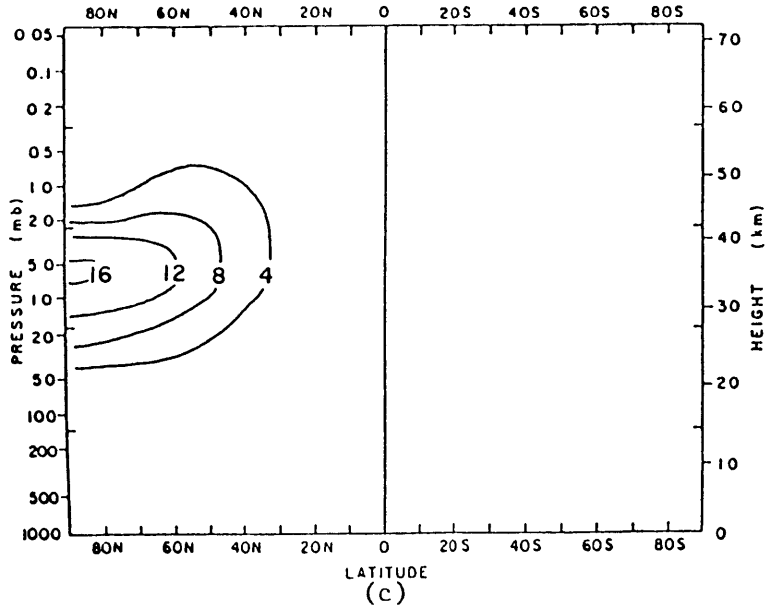

(c)

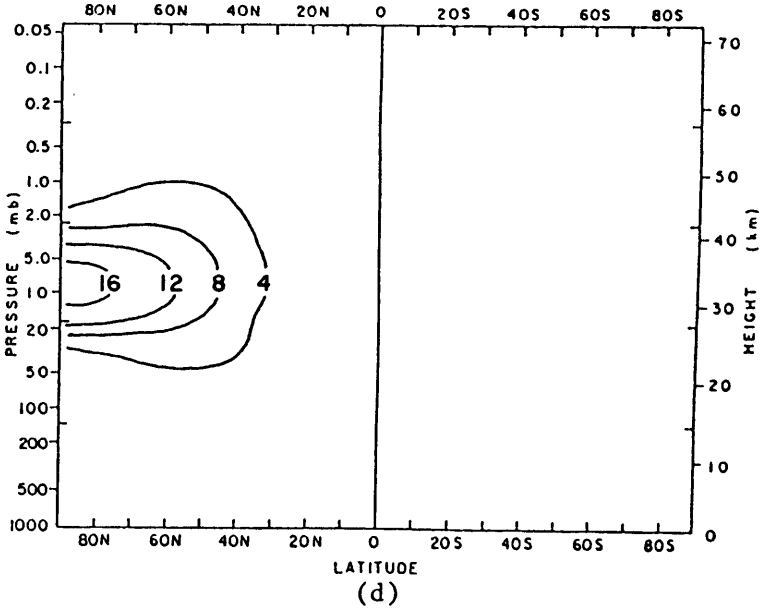

(d)

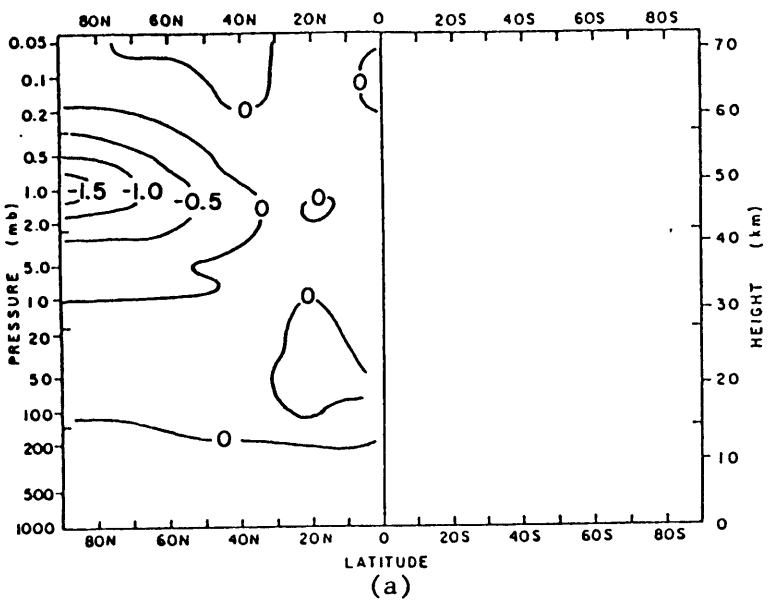

(a)

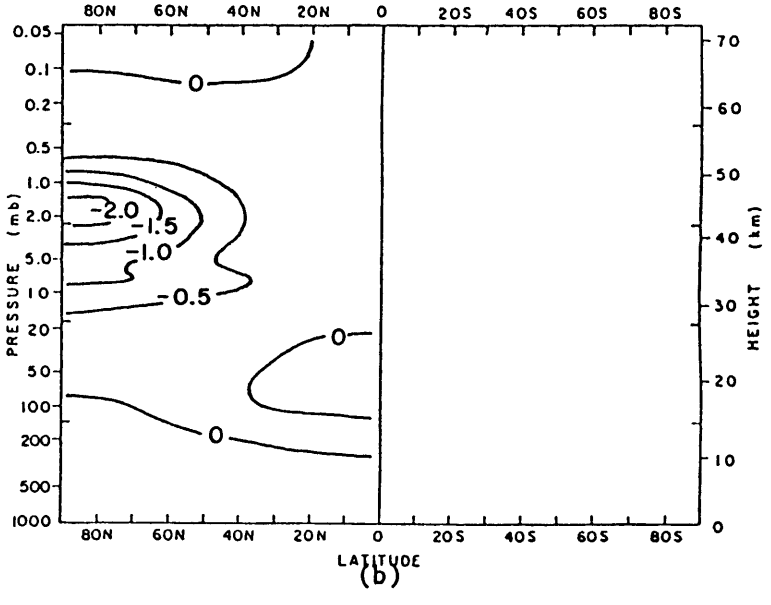

(b)

Figs. 5.12 Change in O_3 mixing ratio (ppmv) for: (a) day 93, (b) day 102, (c) day 111, (d) day 120

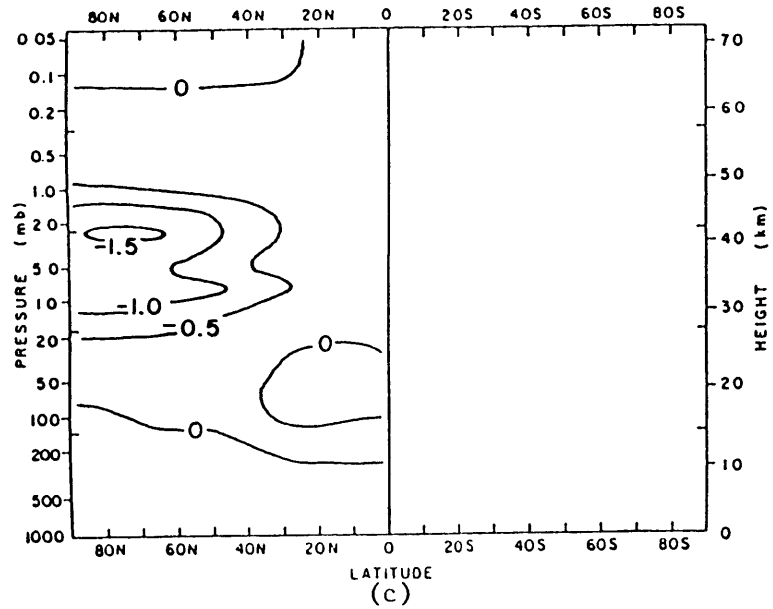

(c)

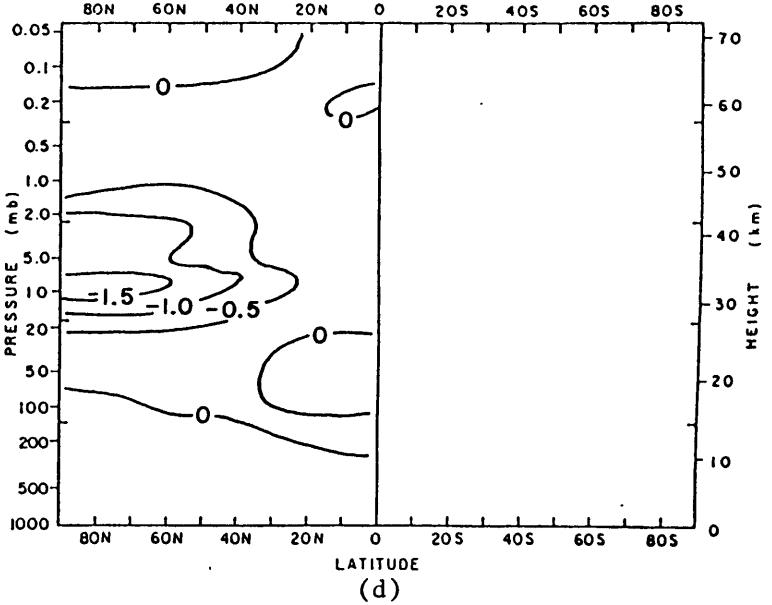

(d)

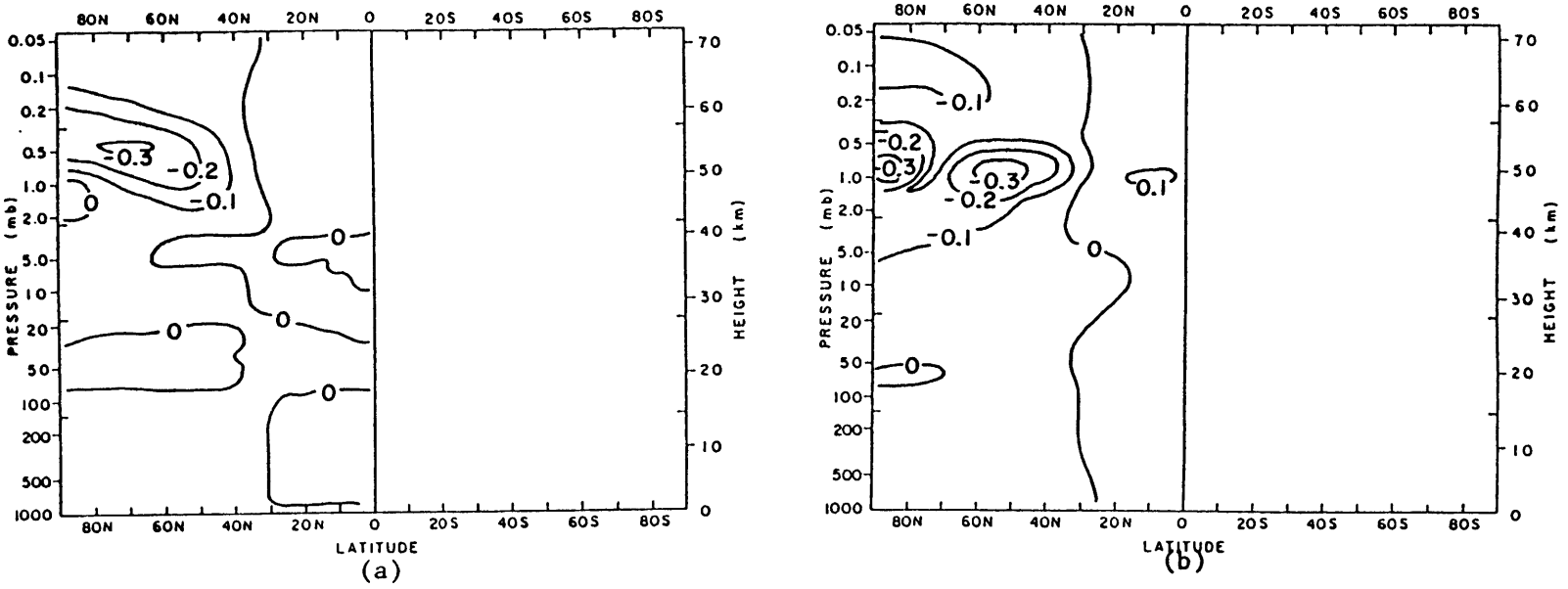

Figs. 5.13 Change in [Q] (K/day) for: (a) day 93, (b) day 102, (c) day 111, (d) day 120

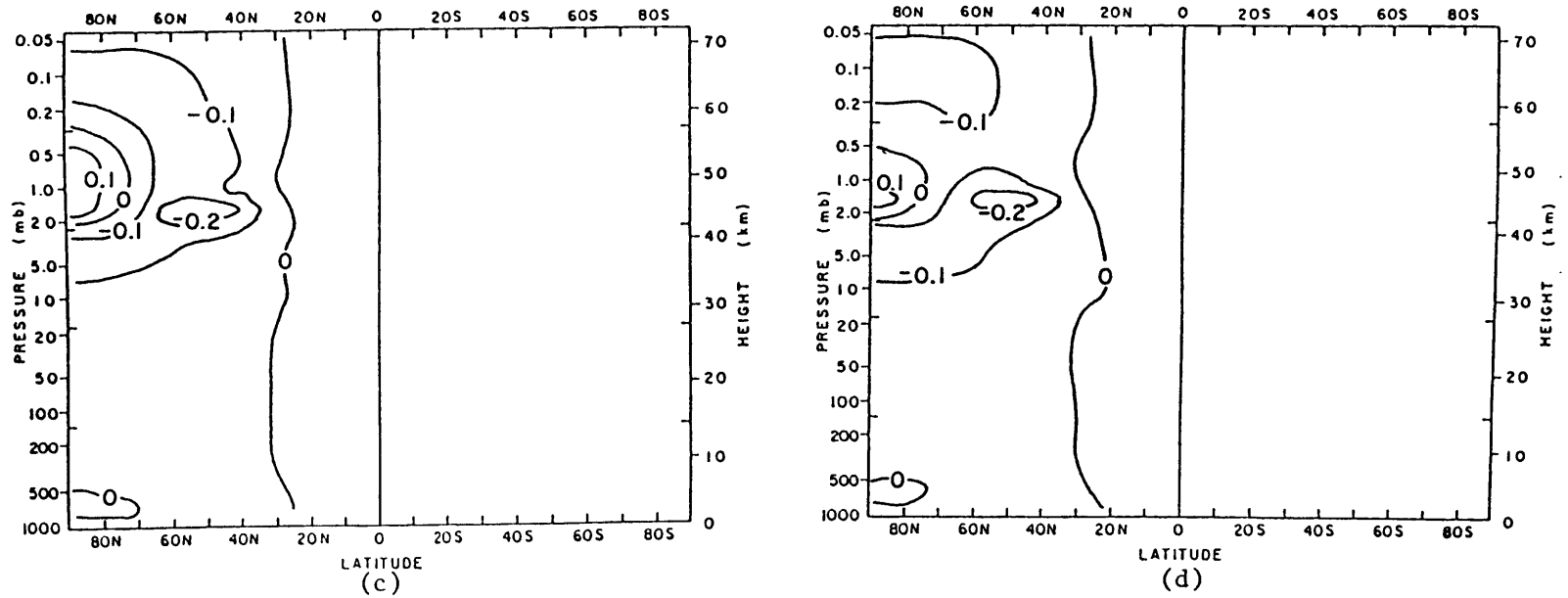

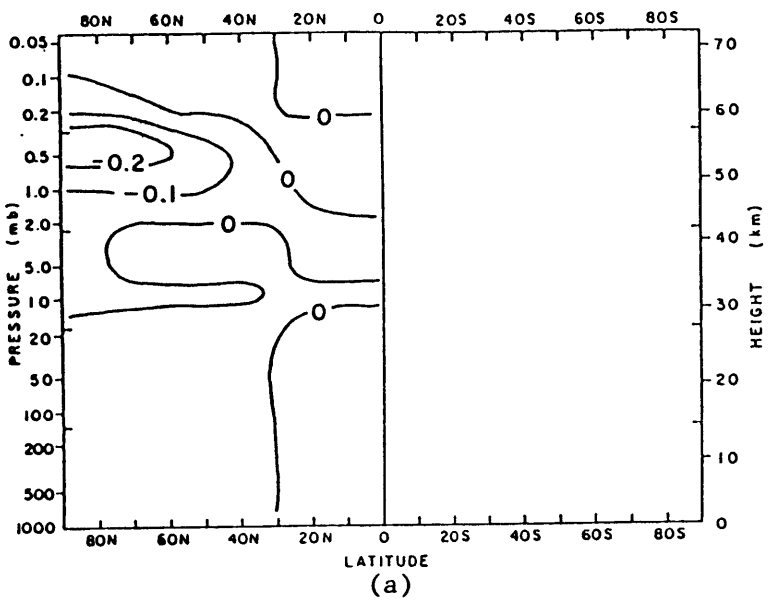

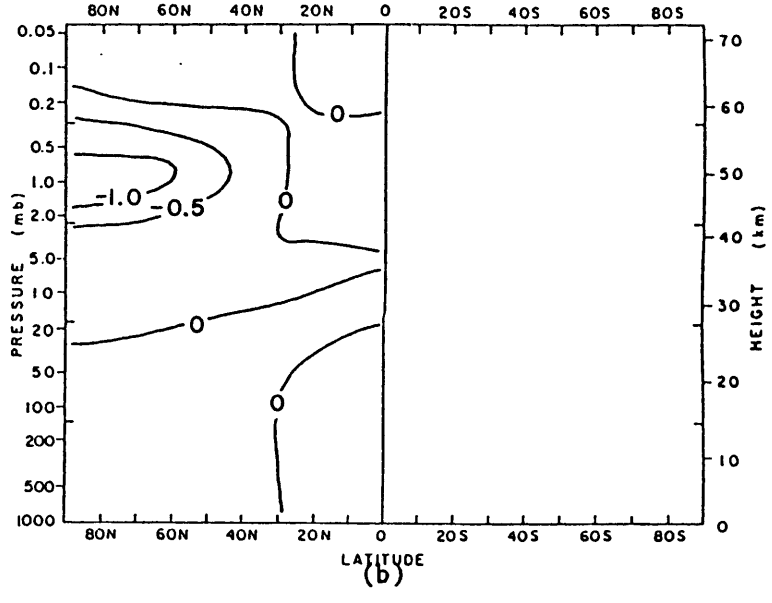

Figs. 5.14 Change in [T] (K) for: (a) day 93, (b) day 102, (c) day 111, (d) day 120

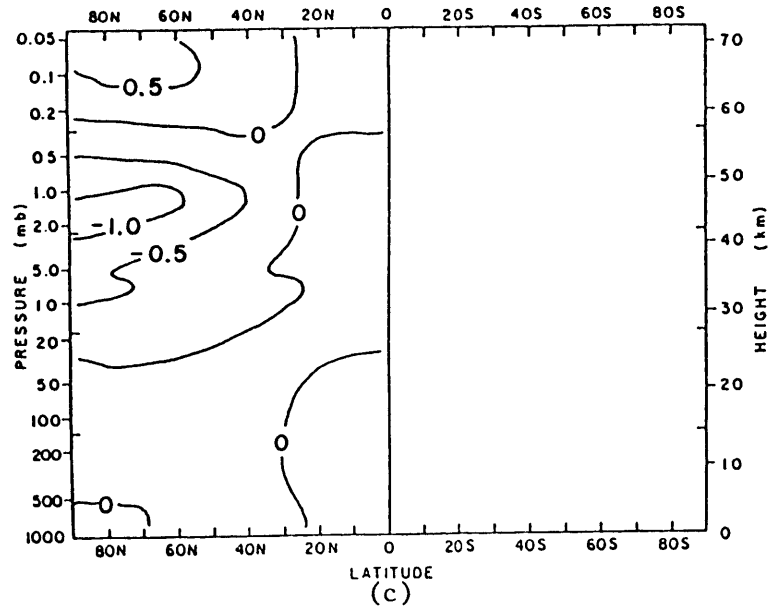

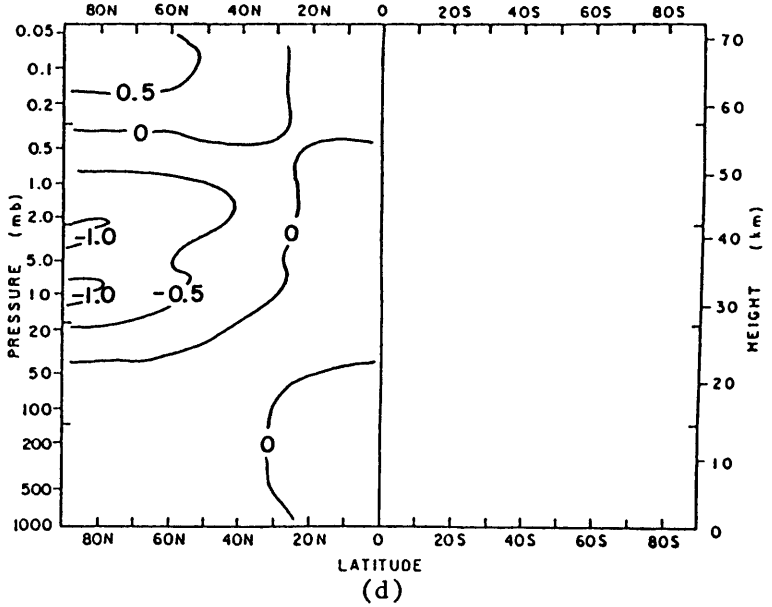

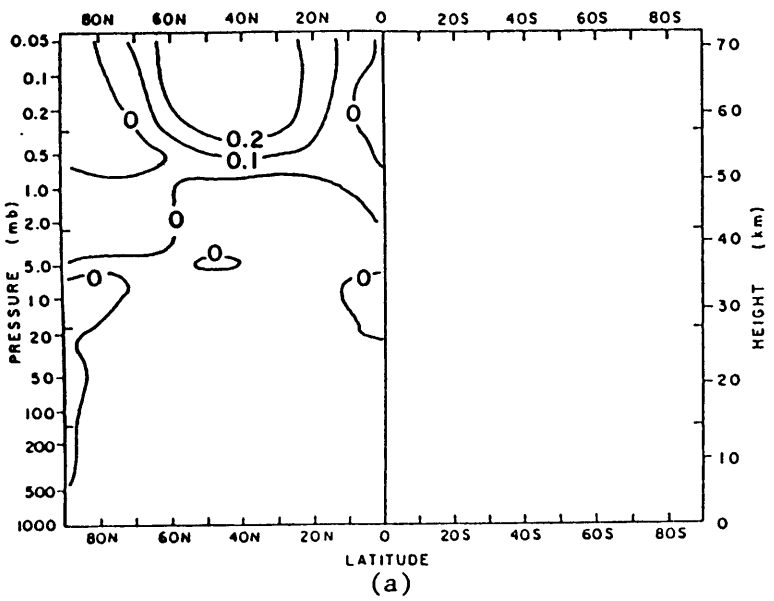

(a)

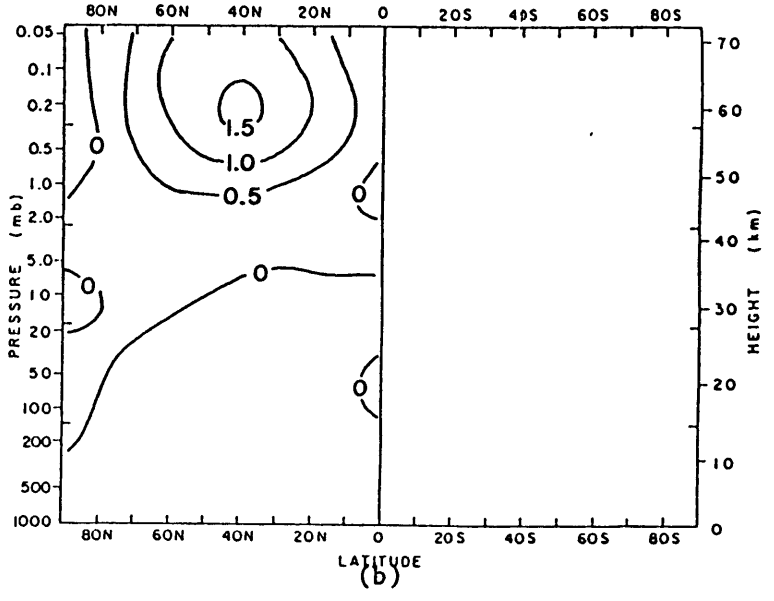

(b)

Figs. 5.15 Change in [u] (m/s) for: (a) day 93, (b) day 102, (c) day 111, (d) day 120

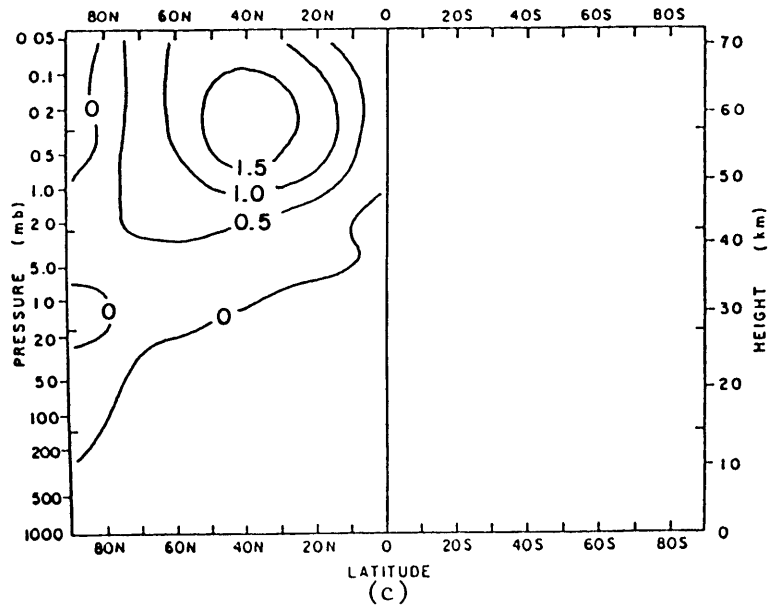

(c)

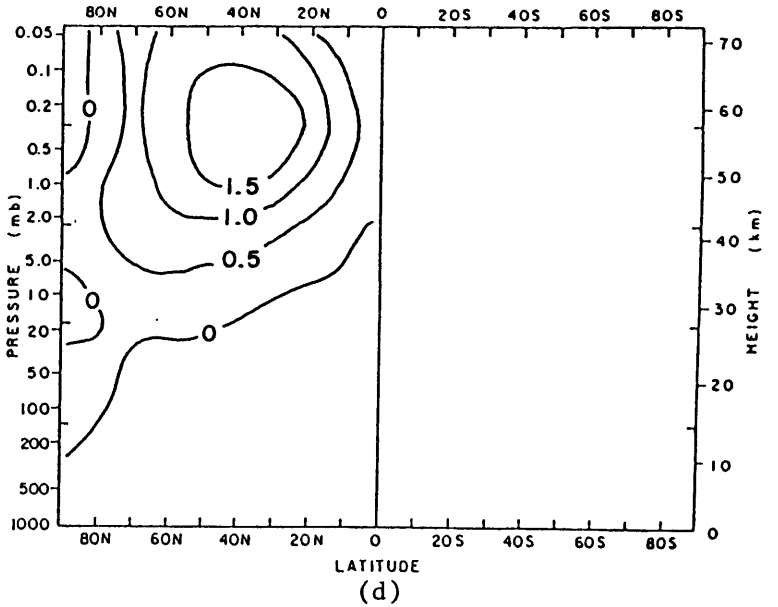

(d)

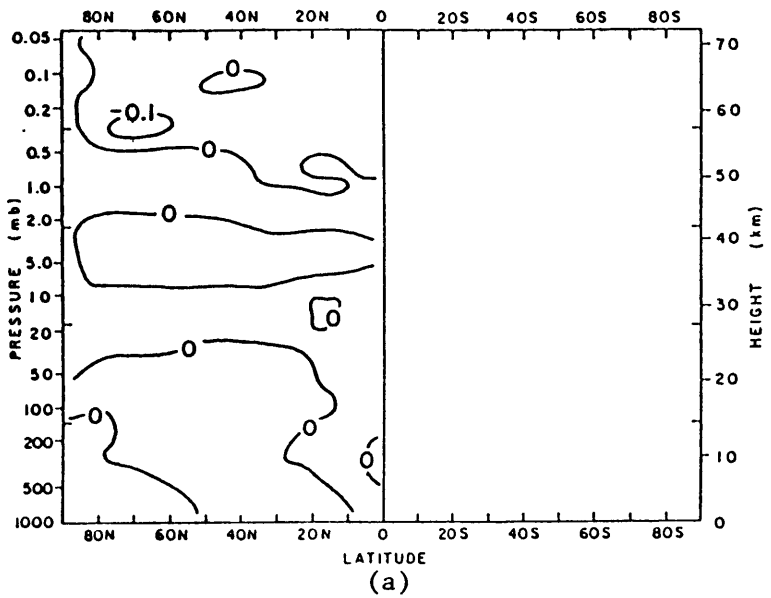

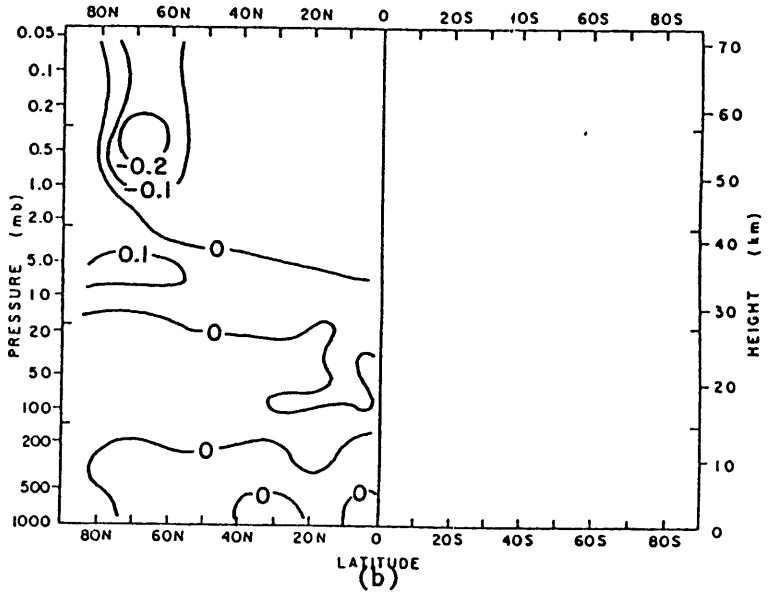

Figs. 5.16 Change in Eliassen-Palm flux divergence (10^{-5} m/s^2) for: (a) day 93, (b) day 102, (c) day 111, (d) day 120

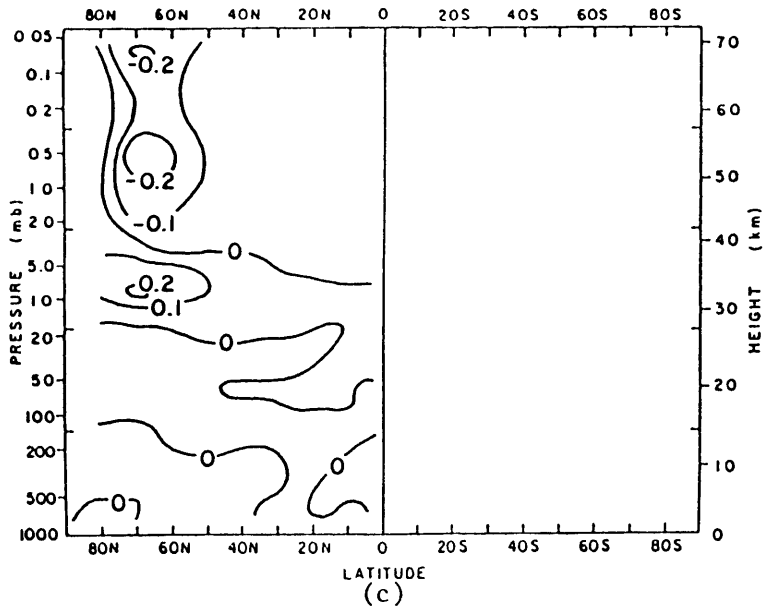

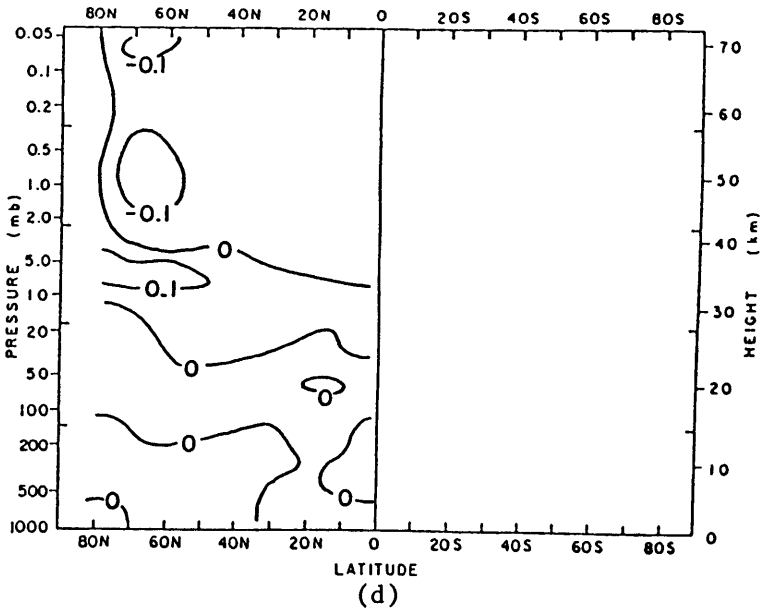

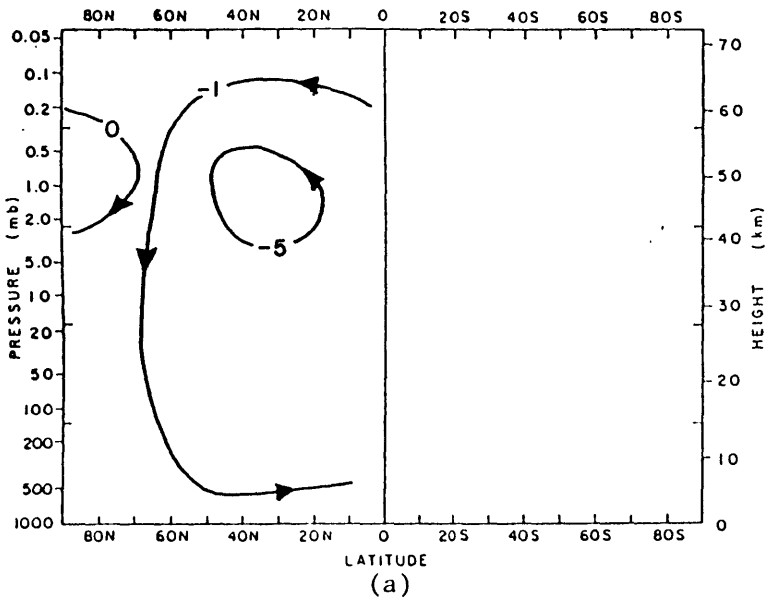

(a)

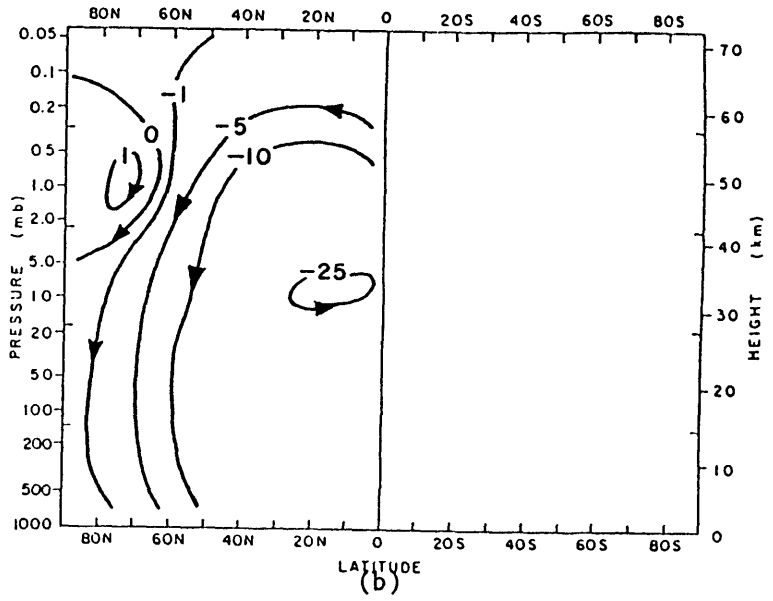

(b)

Figs. 5.17 Change in X_M (10^9 gm/s) for: (a) day 93, (b) day 102, (c) day 111, (d) day 120

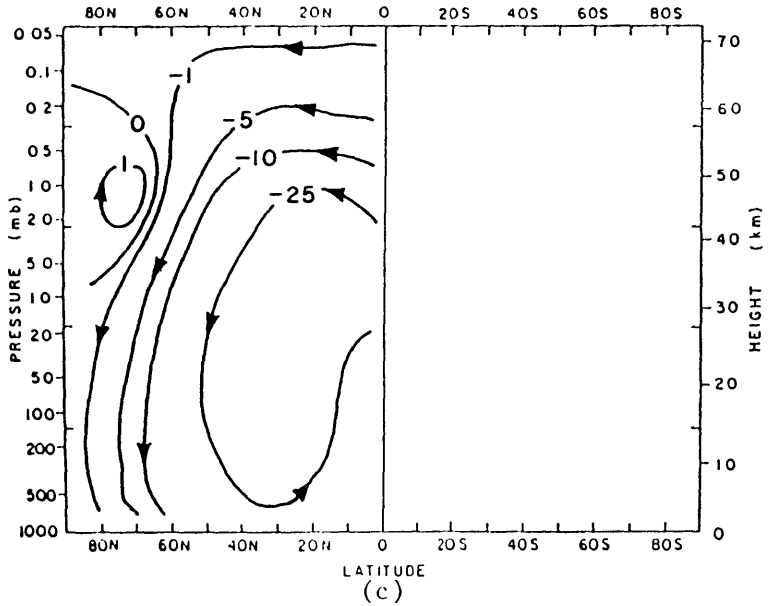

(c)

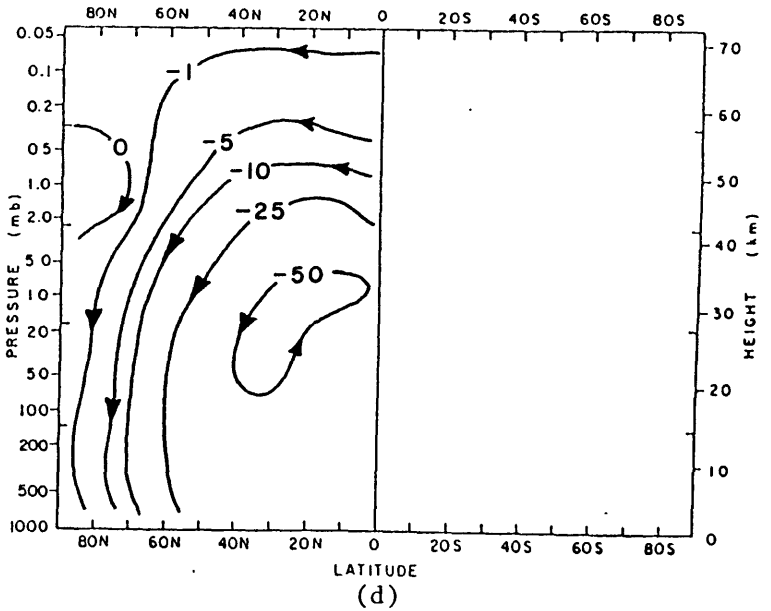

(d)

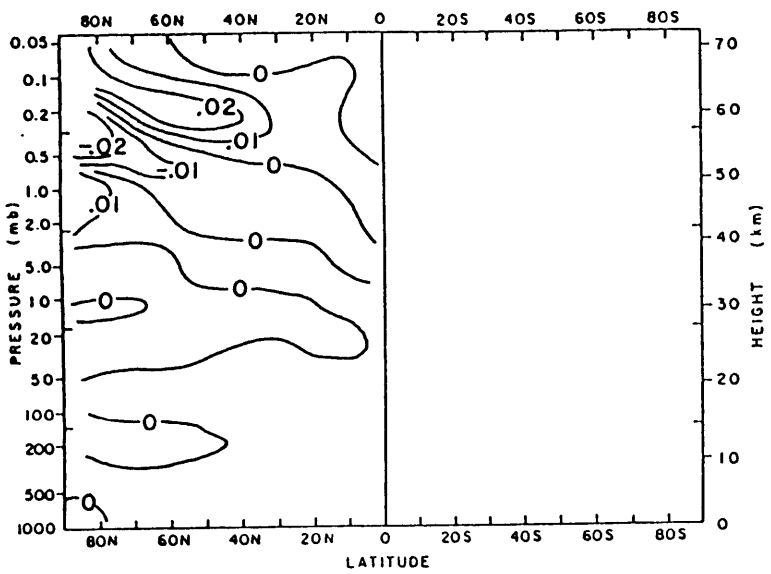

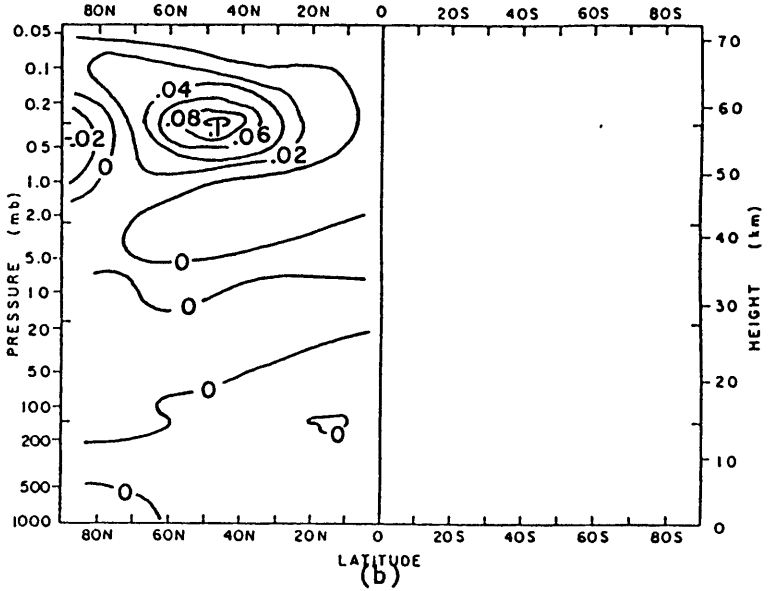

Figs. 5.18 Change in latitudinal gradient of potential vorticity (units of omega) for: (a) day 93, (b) day 102, (c) day 111, (d) day 120

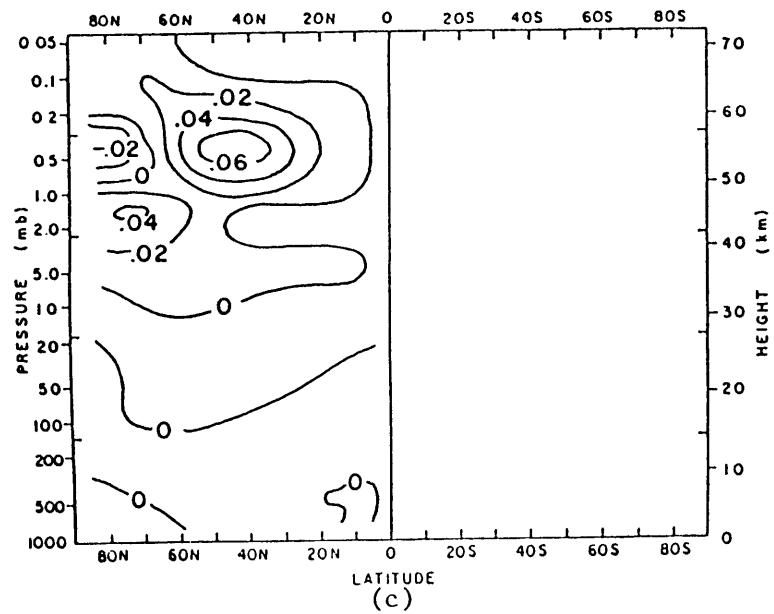

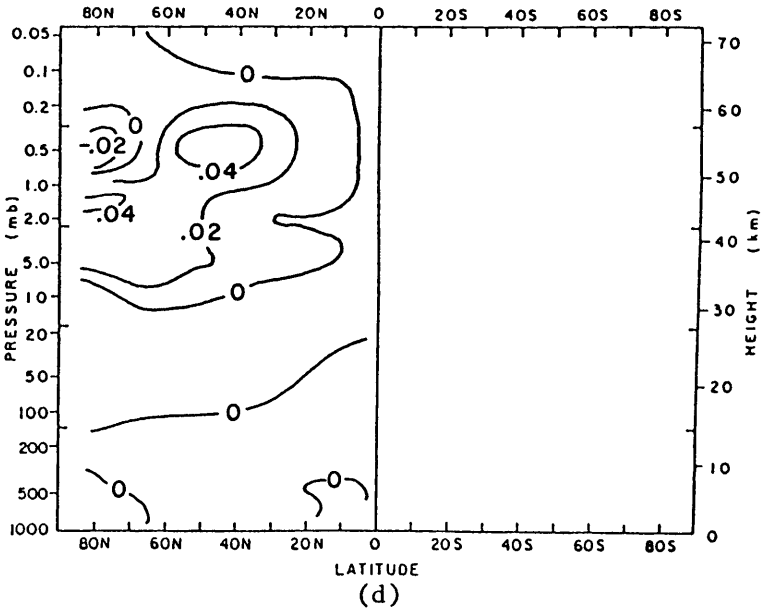

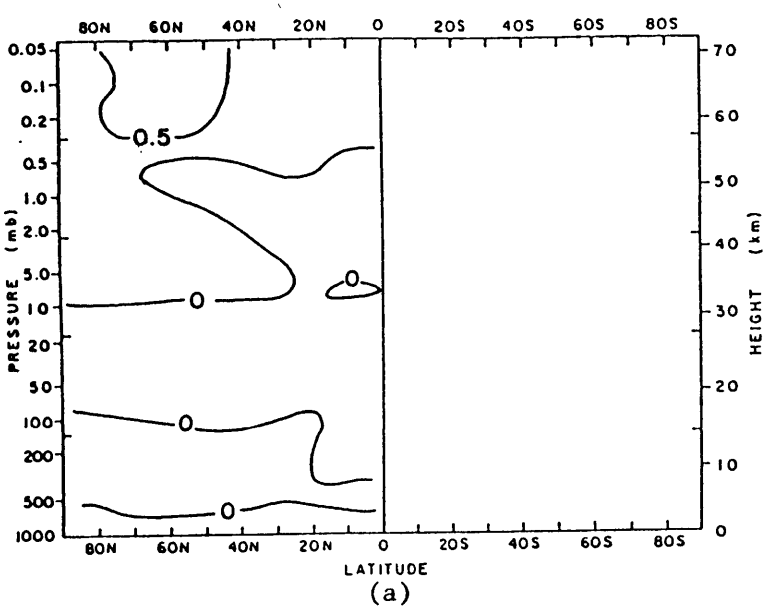

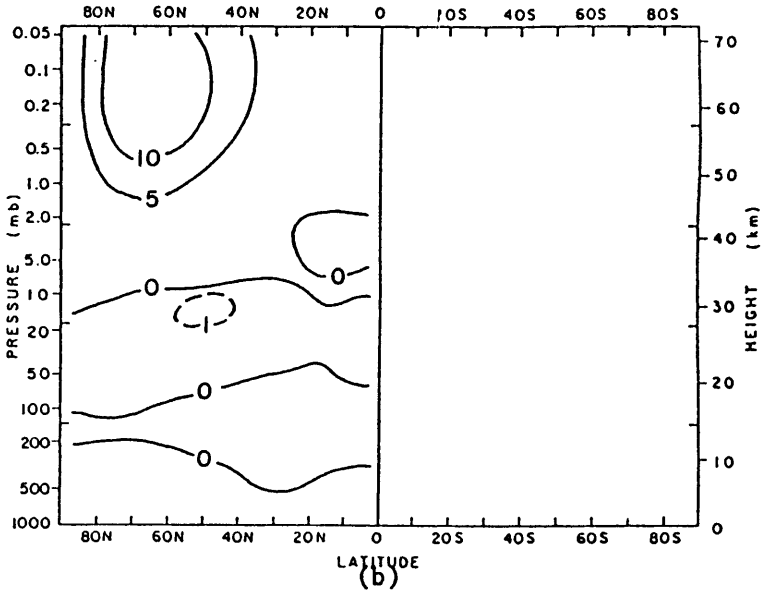

Figs. 5.19 Change in Wavenumber 1 Amplitude (gpm) for: (a) day 93, (b) day 102, (c) day 111, (d) day 120

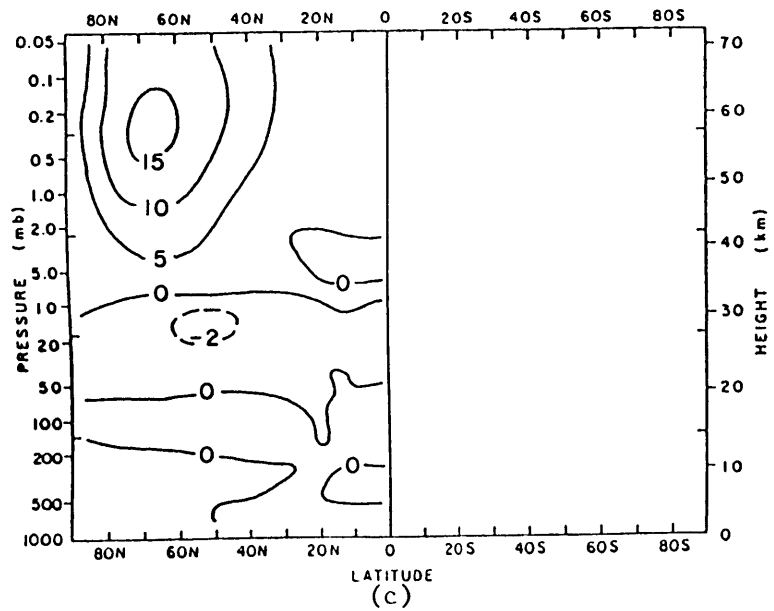

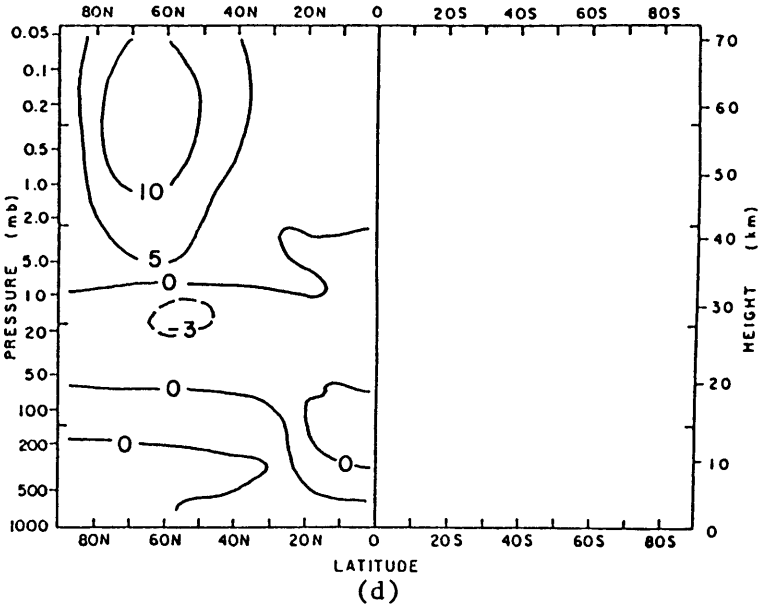

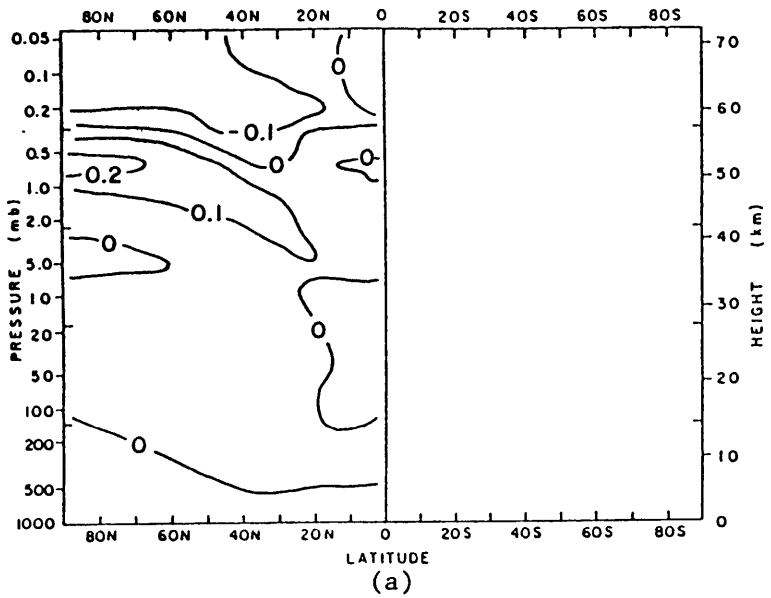

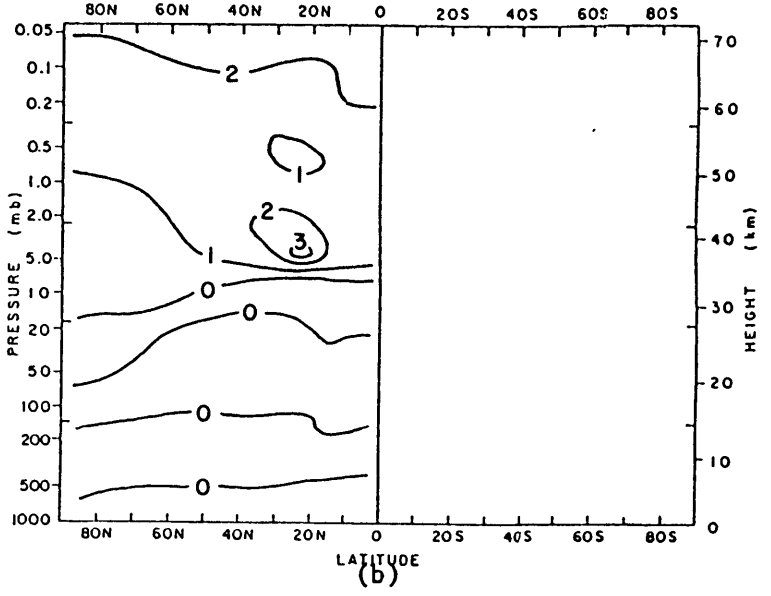

Figs. 5.20 Change in Wavenumber 1 Phase (deg) for: (a) day 93, (b) day 102, (c) day 111, (d) day 120

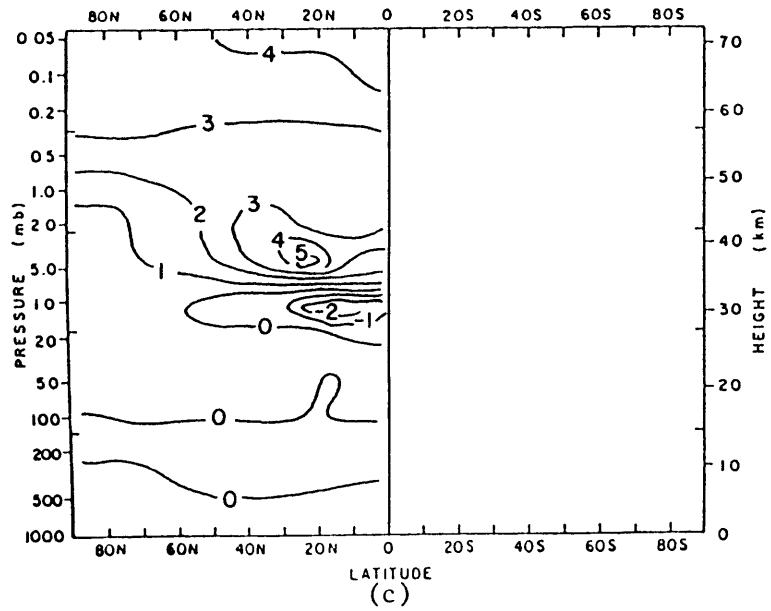

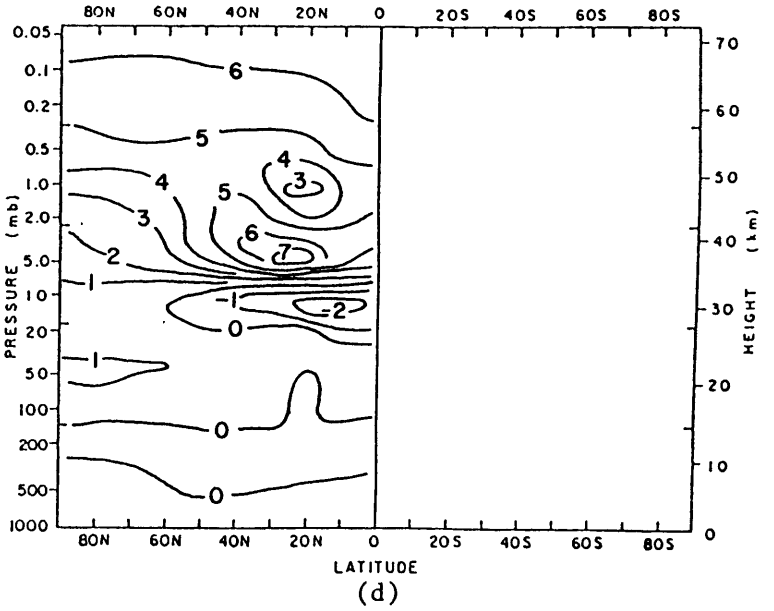

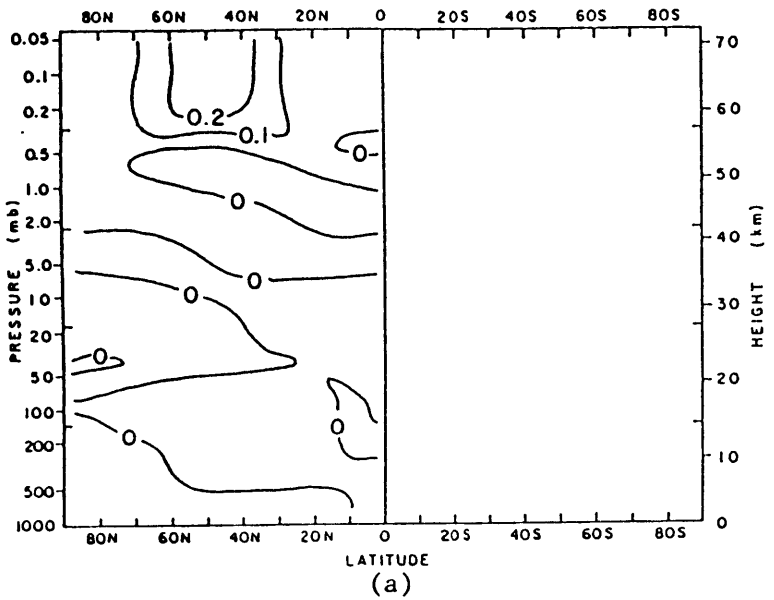

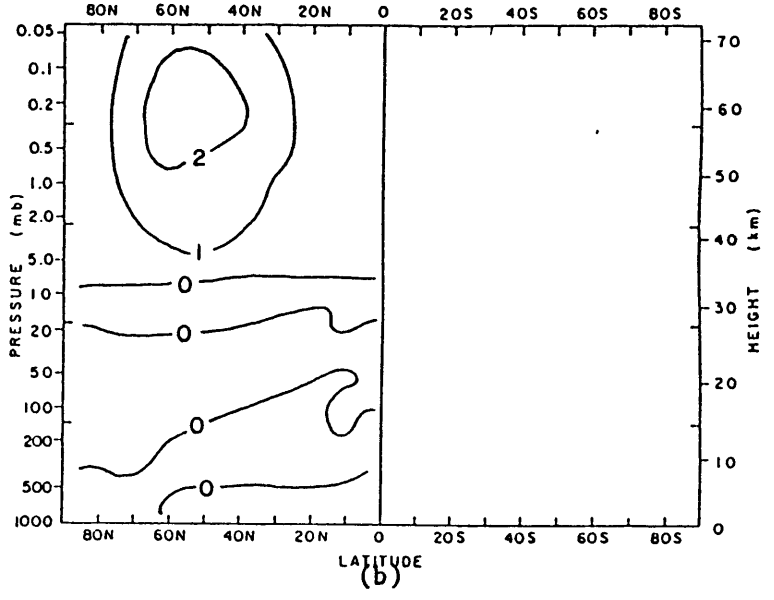

Figs. 5.21 Change in Wavenumber 2 Amplitude (gpm) for: (a) day 93, (b) day 102, (c) day 111, (d) day 120

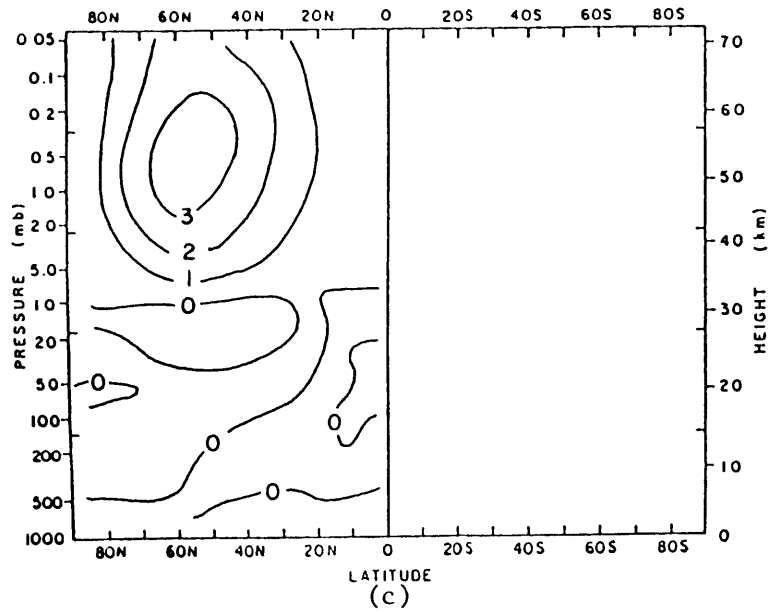

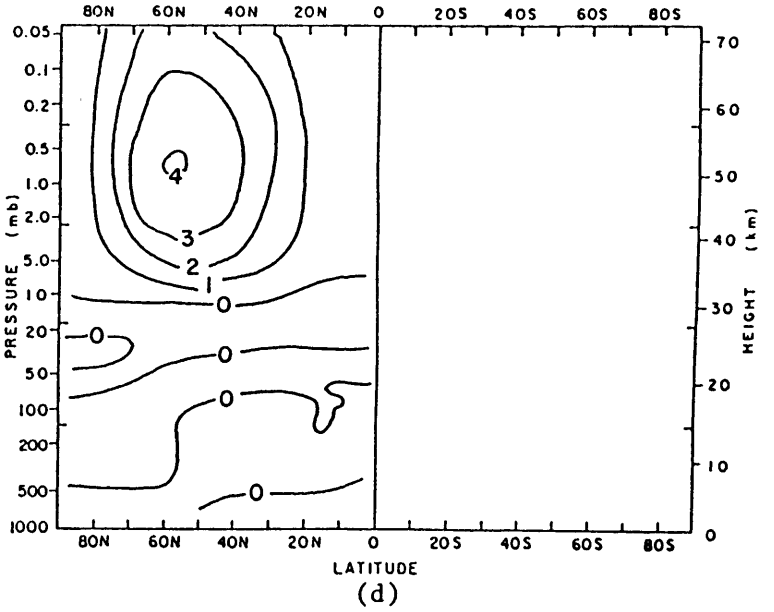

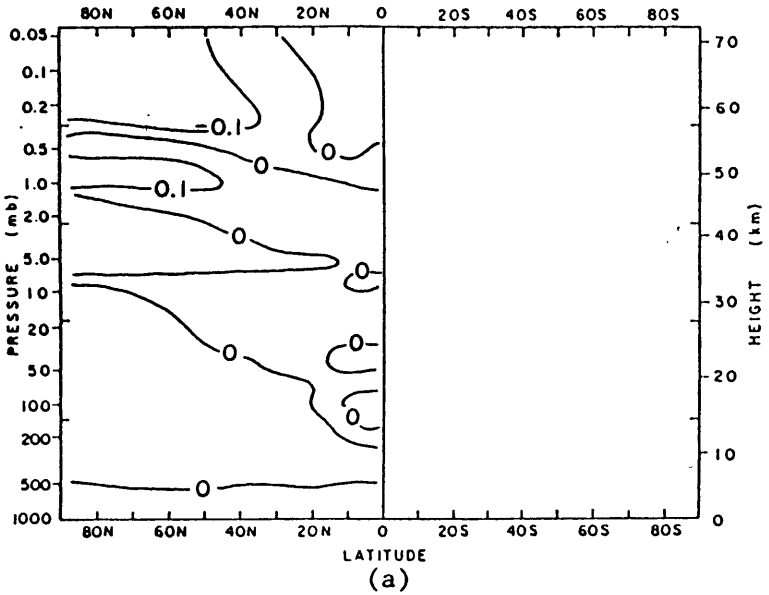

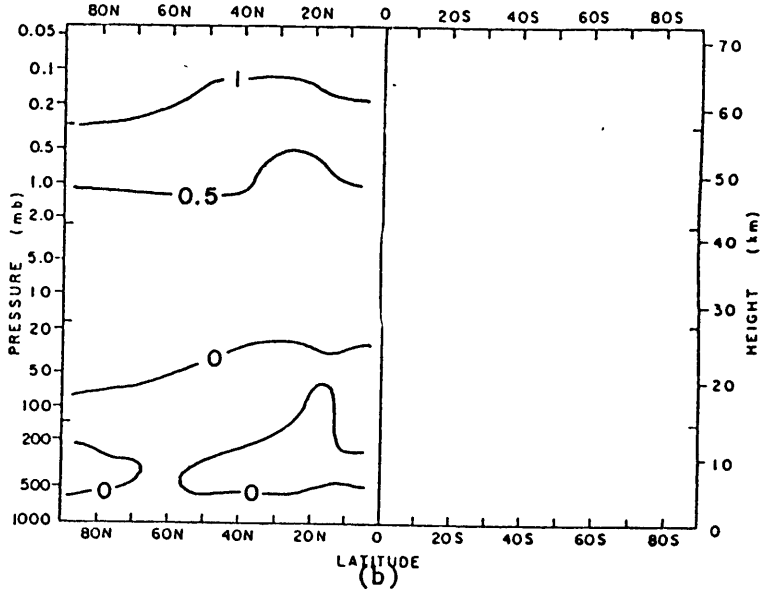

Figs. 5.22 Wavenumber 2 Phase Change (deg) for: (a) day 93, (b) day 102, (c) day 111, (d) day 120

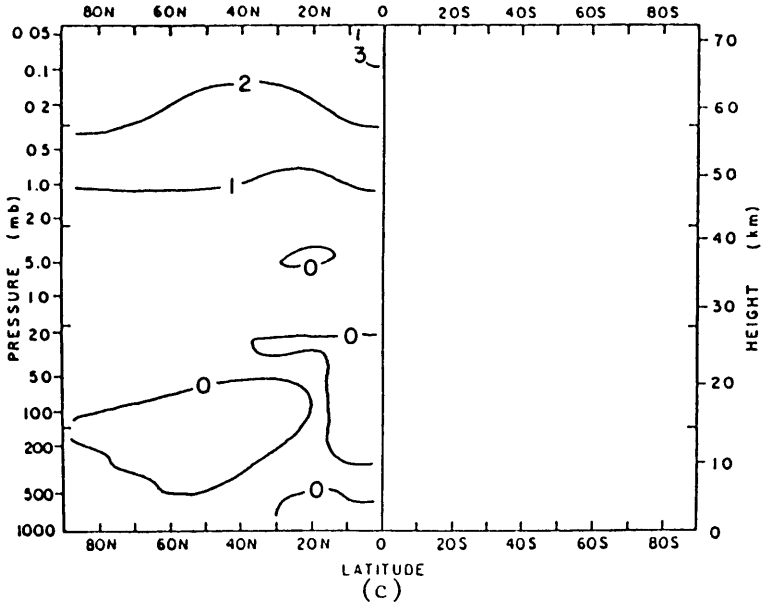

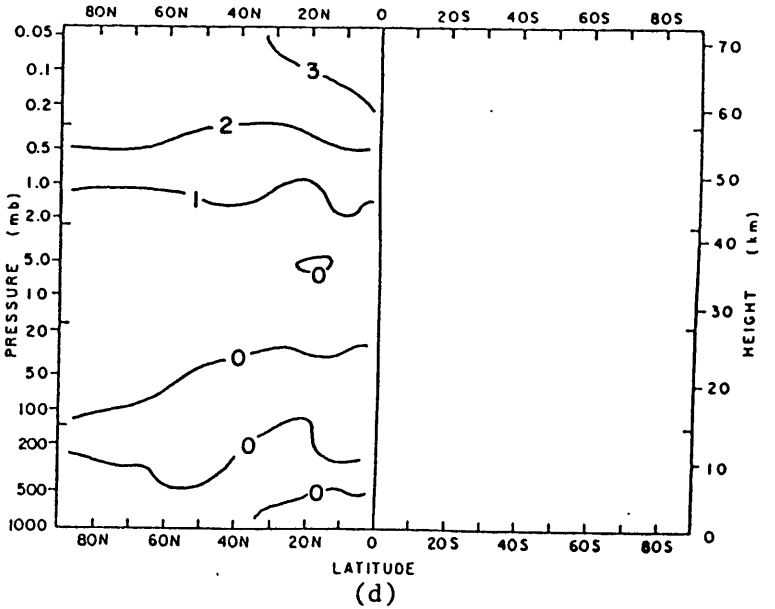

VIII. APPENDIX: EFFECTS OF RADIATIVE DAMPING ON PLANETARY WAVE PROPAGATION

The details of the following derivation are after Dickinson (1969). We begin with the linearized equation for perturbation potential vorticity on a mid-latitude β-plane with thermal dissipation- written in the notation of Chapter III as follows:

$$\partial q_0^*/\partial t + [u]\partial q_0^*/\partial x + \partial\psi^*/\partial x\ \partial[q_0]/\partial y = -(f_0^2/RP)\partial((P\alpha_T/\sigma)\partial\psi^*/\partial Z)/\partial Z \qquad \text{(A-1)}$$

where:

$x = (a\cos\theta)\lambda$

$y = a\theta$

f_0= Coriolis parameter at the center of the β-plane

α_T= radiative dissipation rate (including photochemical acceleration)

We assume that [u], σ, and α_T are all constant, and that the perturbation streamfunction has the form:

$$\psi^* = \Psi_0(Z)\exp[i(kx+ly-kct)+ Z/2] \qquad \text{(A-2)}$$

Substituting eq.(A-2) into eq.(A-1), we obtain the following equation for the vertical variation of ψ^*:

$$d^2\Psi_0/dZ^2 + n^2\Psi_0 = 0 \qquad \text{(A-3)}$$

where:

$n^2 = F/(1-i\varepsilon) - 1/4$

$F = (R\sigma/f_0^2)[\ \beta/[u] - (k^2+l^2)\ ]$

$\varepsilon = \alpha_T/[u]k$

The solution of eq.(A-3) which satisfies the radiation condition at $Z\to\infty$ is

$$\Psi_0(Z) = A\exp[(i\gamma-\Gamma)Z] \qquad \text{(A-4)}$$

where:

$\gamma = [|n^2| + (n^2)_r]^{1/2}/\sqrt{2}$

$\Gamma = [|n^2| - (n^2)_r]^{1/2}/\sqrt{2}$

$$(n^2)_r = F/(1+\varepsilon^2) - 1/4$$

Eqs.(A-2) and (A-4) may be combined to yield:

$$\psi^* = A \exp[(1/2 - \Gamma)Z]\exp[i(kx+ly+\gamma Z-kct)] \qquad (A-5)$$

Note that γ is a positive definite quantity, so that if $k>0$, then contours of the phase angle $\phi=kx+ly+\gamma Z-kct$ must have westward tilt with height. Furthermore, let

$$B = 2\gamma^2/F = 1/(1+\varepsilon^2) - 1/4F + [(1-1/2F)/(1+\varepsilon^2) + 1/16F^2] \qquad (A-6)$$

so that B is a measure of the westward phase tilt of the wave described by eq.(A-5). Clearly if radiative dissipation is present (ε is non-zero), the value of B will be reduced in comparison to when $\varepsilon=0$, so that the dissipation decreases the westward phase tilt of the wave.

IX. REFERENCES

Andrews, D.G. and M.E. McIntyre, 1976: Planetary waves in horizontal and vertical shear: the generalized Eliassen-Palm relation and the mean zonal circulation, J. Atmos. Sci., 33, 2031-2048.

Bates, J.R., 1977: Dynamics of ultra-long waves in middle latitudes, Quart. J. R. Met. Soc., 103, 397-430.

Bates, J.R., 1980: On the interaction between a radiatively damped planetary wave and the zonally averaged circulation in the middle atmosphere, Pageoph, 118, 266-283.

Baulch, D.L., R.A. Cox, P.J. Crutzen, R.F. Hampson, Jr., J.A. Kerr, J. Troe, and R.T. Watson, 1982: Evaluated kinetic and photochemical data for atmospheric chemistry: Supplement I. CODATA task group on chemical kinetics, J. Phys. Chem. Ref. Data, 11, 327-496.

Boville, B.A., 1986: Wave-mean flow interactions in a general circulation model of the troposphere and stratosphere, J. Atmos. Sci., 43, 1711-1725.

Boyd, J.P., 1976: The noninteraction of waves with the zonally averaged flow on a spherical earth and the interrelationships of eddy fluxes of energy, heat, and momentum, J. Atmos. Sci., 33, 2285-2291.

Brigder, A.F.C., 1981: Wave-mean flow interactions and solar-weather effects, Ph.D. thesis, Colorado State Univ., Fort Collins, Colorado.

Bushby, T. and C. Whitelam, 1961: A three-parameter model of the atmosphere suitable for numerical intergration, Quart. J. R. Met. Soc., 87, 374-392.

Butchart, N., J.A. Clough, T.N. Palmer, and P.J. Trevelyan, 1982: Simulations of an observed stratospheric warming with quasigeostrophic refractive index as a model diagnostic, Quart. J. R. Met. Soc., 108, 475-502.

Callis, L.B., J.C. Alpert, and M.A. Geller, 1985: An assessment of thermal, wind, and planetary wave changes in the middle and lower atmosphere due to 11-year UV flux variations, J. Geophys. Res., 90, 2273-2282.

Callis, L.B. and M. Natarajan, 1986: The Antarctic ozone minimum: relationship to odd nitrogen, odd chlorine, the final warming, and the 11-year solar cycle, J. Geophys. Res., 91, 10,771-10,796.

Cess, R.D. and S.N. Tiwari, 1972: Infrared radiative energy transfer in gases, in Advances in Heat Transfer, Vol.8, Academic, 229-283.

Chamberlain, J.W., 1977: A mechanism for inducing climactic variations through the stratosphere: screening of cosmic rays by solar and terrestrial magnetic fields, J. Atmos. Sci., 34, 737-743.

Chandra, S. and K. Maeda, 1980: A search for correlations between geomagnetic activity and stratospheric ozone, Geophys. Res. Lett., 7, 757-760.

Chandra, S., 1985: Solar-induced oscillations in the stratosphere: a myth or reality? J. Geophys. Res., 90, 2331-2339.

Charney, J.G., and P.G. Drazin, 1961: Propagation of planetary scale disturbances from the lower into the upper atmosphere, J. Geophys. Res., 66, 83-109.

Chivers, H.J.A. and J.K. Hargreaves, 1965: Conjugate observations of solar proton events: delayed ionospheric changes during twilight, Planet. Space Sci., 13, 583-592.

Cunnold, D., F. Alyea, N. Phillips, and R. Prinn, 1975: A three-dimensional dynamical-chemical model of atmospheric ozone, J. Atmos. Sci., 32, 170-194.

Cunnold, D.M., F.N. Alyea, and R.G. Prinn, 1980: Preliminary calculations concerning the maintenance of the zonal mean ozone distribution in the northern hemisphere, Pageoph, 118, 329-354.

Curtis, A.R., 1956: The computation of radiative heating rates in the atmosphere Proc. Roy. Soc. London, A236, 193-206.

Dickinson, R.E., 1969: Vertical propagation of planetary Rossby waves through an atmosphere with Newtonian cooling, J. Geophys. Res., 74, 929-938.

Dickinson, R.E., 1975: Solar variability and the lower atmosphere, Bulletin of the Amer. Meteor. Soc., 56, 1240-1248.

Dunkerton, T., C.-P.F. Hsu, and M.E. McIntyre, 1981: Some Eulerian and Lagrangian diagnostics for a model stratospheric warming, J. Atmos. Sci., 38, 819-843.

Ebel, A., B. Schwister, and K. Labitzke, 1981: Planetary waves and solar activity in the stratosphere between 50 and 10 mbar, J. Geophys. Res., 86, 9729-9783.

Ebel, A. and B. Schwister, 1983: Relations between stratospheric and tropospheric oscillations correlated with solar activity between 13 and 27 days, in Weather and Climate Responses to Solar Variations, B.M. McCormac, ed., Colorado Assoc. Univ. Press, 169-178.

Eckman, R.S., 1986a: Response of ozone to short-term variations in the solar ultraviolet irradiance, 1, A theoretical model, J. Geophys. Res., 91, 6695-6704.

Eckman, R.S., 1986b: Response of ozone to short-term variations in the solar ultraviolet irradiance, 2, Observations and interpretation, J. Geophys. Res., 91, 6705-6721.

Eliassen, A. and. E. Palm, 1961: On the transfer of energy in stationary mountain waves, Geofys. Publ., 22, 1-23.

Fabian, P. and C. Junge, 1970: Global rate of ozone destruction at the earth's surface, Arch. Meteor. Geophys. Bioklim., 19, 161-172.

Fels, S.B., J.D. Mahlman, M.D. Schwarzkopf, and R.W. Sinclair, 1980: Stratospheric sensitivity to perturbations in ozone and carbon dioxide: radiative and dynamical response, J. Atmos. Sci., 37, 2265-2297.

Freeman, K.P. and K.N. Liou, 1979: Climactic effects of cirrus clouds, Adv. Geophys., 21, 231-287.

Fritts, D.C., 1984: Gravity wave saturation in the middle atmosphere: a review of theory and observations, Rev. Geophys. Sp. Phys., 22, 275-308.

Fritts, D.C., B.B. Balsley, and W.L. Ecklund, 1984: VHF echoes from the Arctic mesosphere and lower thermosphere, Part II: Interpretations, in Dynamics of the Middle Atmosphere, J.R. Holton and T. Matsuno, eds., Terra Scientific Publ. Co., 97-116.

Geller, M.A. and Alpert, J.C., 1980: Planetary wave coupling between the troposphere and the middle atmosphere as a possible sun-weather mechanism, J. Atmos. Sci., 37, 1197-1215.

Gille, J.C., C.M. Smythe, and D.F. Heath, 1984: Observed ozone response to variations in solar ultraviolet irradiance, Science, 225, 315-317.

Golombek, A. and R.G. Prinn, 1986: A global three-dimensional model of the circulation and chemistry of CFCl , CF_2Cl_2, CH_3CCl_3, CCl_4, and N_2O, J. Geophys. Res., 91, 3985-4002.

Goody, R.M., 1964: Atmospheric Radiation I., Oxford Univ. Press, 436pp.

Grieger, N. and G. Schmitz, 1982: The structure of planetary waves up to the lower mesosphere based on data analyses and model calculations, J. Geophys. Res., 87, 11,255-11,264.

Hamilton, K., 1983: Diagnostic study of the momentum balance in the northern hemisphere winter stratosphere, Mon. Wea. Rev., 111, 1434-1441.

Hartmann, D.L., 1976: The dynamic climatology of the stratosphere in the southern hemisphere during late winter 1973, J. Atmos. Sci., 33, 1789-1802.

Heath, D.F., 1975: Relation of the observed far ultraviolet solar irradiance to the solar magnetic sector structure, Solar Physics, 45, 79-82.

Heath, D.F. and S.S. Prasad, 1976: Proc. Joint Symposium on Atmospheric Ozone, Dresden, Vol.2, p.91.

Heath, D.F., A.J. Krueger, and P.J. Crutzen, 1977: Solar proton event: influence on stratospheric ozone, Science, 197, 886-889.

Heath, D.F., and B.M. Schlesinger, 1985: Global response of stratospheric ozone to ultraviolet solar flux variations, in Atmospheric Ozone, Proc. Quadriennial Ozone Symposium, Halkidiki, Greece, C.S. Zerefos and A. Ghazi, eds., p.666.

Hines, C.O., 1974: A possible mechanism for the production of sun-weather correlations, J. Atmos. Sci., 31, 589-591.

Hines, C.O. and I. Halevy, 1977: On the reality and nature of certain sun-weather correlations, J. Atmos. Sci., 34, 382-404.

Hirota, I. and Y. Sato, 1969: Periodic variation of the winter stratospheric circulation and intermittent vertical propagation of planetary waves, J. Meteor. Soc. Japan, 47, 390-402.

Hirota, I., 1971: Excitation of planetary Rossby waves in the winter stratosphere by periodic forcing, J. Meteor. Soc. Japan, 49, 439-448.

Hirota, I. and J.J. Barnett, 1977: Planetary waves in the winter mesosphere-preliminary analysis of Nimbus 6 PMR results, Quart. J. R. Met. Soc., 103, 487-498.

Holton, J.R., 1975: The Dynamic Meteorology of the Stratosphere and Mesosphere, Meteor. Monogr., No. 37, Amer. Meteor. Soc., 218 pp.

Holton, J.R., 1980: The dynamics of sudden stratospheric warmings, Ann. Rev. Earth Planet. Sci., 8, 169-190.

Holton, J.R. and W.M. Wehrbein, 1980: The role of forced planetary waves in the annual cycle of the zonal mean circulation of the middle atmosphere, J. Atmos. Sci., 37, 1968-1983.

Holton, J.R., 1983: The influence of gravity wave breaking on the general circulation of the middle atmosphere, J. Atmos. Sci., 40, 2497-2507.

Holton, J.R. and Zhu, X., 1984: A further study of gravity wave induced drag and diffusion in the mesosphere, J. Atmos. Sci., 41, 2653-2662.

Hood, L.L., 1986: Coupled stratospheric ozone and temperature responses to short-term changes in solar ultraviolet flux: an analysis of Nimbus 7 SBUV and SAMS data, J. Geophys. Res., 91, 5264-5276.

Houghton, J.T., 1977: The Physics of Atmospheres, Cambridge Univ. Press, 203pp.

Hunt, B.G., 1981: An evaluation of a sun-weather mechanism using a general circulation model of the atmosphere, J. Geophys. Res., 86, 1233-1245.

Julian, P.R., and K, Labitzke, 1965: A study of atmospheric energetics during January and February 1963 stratospheric warming, J. Atmos. Sci., 22, 597-610.

Kanzawa, H., 1982: Eliassen-Palm flux diagnostics and the effect of the mean zonal wind on planetary wave propagation for an observed sudden stratospheric warming, J. Meteor. Soc. Japan, 60, 1063-1073.

Kanzawa, H., 1984: Four observed sudden warmings diagnosed by the Eliassen-Palm flux and refractive index, in Dynamics of the Middle Atmosphere, J.R. Holton and T. Matsuno, eds., Terra Scientific Publ. Co., 307-332.

Katayama, A., 1964: On the heat budget of the troposphere over the northern hemisphere, Ph.D. thesis, Tohoku Univ., Japan.

Keating, G.M., G.P. Brasseur, J.Y. Nicholson III, and M. Natarajan, 1985: Detection of the response of ozone in the middle atmosphere to short-term ultraviolet variations, Geophys. Res. Lett., 12, 449-452.

Kiehl, J.T. and S. Solomon, 1986: On the radiative balance of the stratosphere, J. Atmos. Sci., 43, 1525-1534.

King, J.W., A.J. Slater, A.D. Stevens, P.A. Smith, and D.M. Willis, 1977: Large-amplitude standing planetary waves induced in the troposphere by the sun, J. Atmos. Terr. Phys., 39, 1357-1367.

Ko, M.K.W., K.K. Tung, D.K. Weisenstein, and N.D. Sze, 1985: A zonal mean model of stratospheric tracer transport in isentropic coordinates: numerical simulations for nitrous oxide and nitric acid, J. Geophys. Res., 90, 2313-2329.

Ko, M.K.W., McElroy, M.B., Weisenstein, D.K., and N.D. Sze, 1986: Lightning: a possible source of stratospheric odd nitrogen, J. Geophys. Res., 91, 5395-5404.

Koermer, J.P., A. Kasahara, and S.K. Kao, 1983: Numerical studies of major and minor stratospheric warmings caused by orographic forcing, J. Atmos. Sci., 40, 1552-1570.

Labitzke, K., 1972: Changes in the mesosphere and stratosphere connected with circulation changes in winter, J. Atmos. Sci., 29, 756-766.

Labitzke, K., 1981: Stratospheric-mesospheric midwinter disturbances. A summary of observed characteristics, J. Geophys. Res., 86, 9665-9678.

Lindzen, R.S., 1981: Turbulence and stress owing to gravity wave and tidal breakdown, J. Geophys. Res., 86, 9707-9714.

Lorenz, E.N., 1955: Available potential energy and the maintenance of the general circulation, Tellus, 7, 157-167.

Lorenz, E.N., 1960: Energy and numerical weather prediction, Tellus, 12, 364-373.

Louis, J.F., 1975: Chap. 6, CIAP Monograph No. 1, E.R. Reiter, ed., U.S. Dept. of Transportation, Washington, D.C.

Madden, R.A., 1983: The effect of the interference of traveling and stationary waves on time variations of the large-scale circulation, J. Atmos. Sci., 40, 1110-1125.

Mahlman, J.D. and L.J. Umscheid, 1984: Dynamics of the middle atmosphere: successes and problems of the GFDL "SKYHI" general circulation model, in Dynamics of the Middle Atmosphere, J.R. Holton and T. Matsuno, eds. Terra Scientific Publ. Co., 501-526.

Matsuno, T., 1970: Vertical propagation of stationary planetary waves into the winter northern hemisphere, J. Atmos. Sci., 27, 871-883.

Matsuno, T., 1982: A quasi one-dimensional model of the middle atmosphere circulation interacting with internal gravity waves, J. Meteor. Soc. Japan, 60, 215-226.

Matsuno, T., 1984: Dynamics of minor stratospheric warmings and preconditioning in Dynamics of the Middle Atmosphere, J.R. Holton and T. Matsuno, eds. Terra Scientific Publ. Co., 333-351.

McClatchey, R.A., W.S. Benedict, S.A. Clough, D.E. Burch, R.F. Calfee, K. Fox, L.S. Rothman, and J.S. Garing, 1973: AFCRL atmospheric absorption line parameters compilation, Air Force Cambridge Research Laboratories Environmental Research Papers no. 434.

McInturff, R.M., 1978: Stratospheric warmings: synoptic, dynamic, and general circulation aspects, NASA Publication No. 1017, 166 pp.

McIntyre, M.E., 1982: How well do we understand the dynamics of stratospheric warmings? J. Meteor. Soc. Japan, 60, 37-65.

McPeters, R.D. and C.H. Jackman, 1985: The response of ozone to solar proton events during solar cycle 21: the observations, J. Geophys. Res., 90, 7945-7954.

Moura, A.D., 1976: The eigensolution of linearized balance equations over a sphere, J. Atmos. Sci., 33, 877-907.

Nastrom, G.D. and A.D. Belmont, 1978: Preliminary reports on the 27-day solar rotation variation in stratospheric zonal winds, Geophys. Res. Lett., 5, 665-668.

Newell, R., 1969: Radioactive contamination of the upper atmosphere, in Progress In Nuclear Energy- Series XII, Health Physics, Vol.2, A.M. Francis Duhamel, ed., Pergammon, 535-550.

Newell, R., D. Vincent, T. Dopplick, D. Ferruzza, and J. Kidson, 1972: The energy balance of the global atmosphere, in The Global Circulation of the Atmosphere, G.A. Corby, ed., p.42, Roy. Meteor. Soc.

O'Neill, A. and T.F. Taylor, 1979: A study of the major stratospheric warming of 1976/77, Quart. J. R. Met. Soc., 105, 71-92.

O'Neill, A. and C.E. Youngblut, 1982: Stratospheric warmings diagnosed using the transformed Eulerian-mean equations and the effect of the mean state on wave propagation, J. Atmos. Sci., 39, 1370-1386.

Oort, A.H. and J.P. Peixoto, 1983: Global angular momentum and energy balance requirements from observations, Adv. Geophys., 25, 355-490.

Padgaonkar, A.D. and B.R. Arora, 1981: Tropospheric vorticity responses to the solar magnetic sector structure and geomagnetic disturbances, Pageoph, 119, 893-900.

Palmer, T.N., 1981a: Diagnostic study of a wavenumber-2 stratospheric sudden warming in a transformed Eulerian-mean formalism, J. Atmos. Sci., 38, 844-855.

Palmer, T.N., 1981b: Aspects of stratospheric sudden warmings studied from a transformed Eulerian-mean viewpoint, J. Geophys. Res., 86, 9679-9687.

Palmer, T.N. and C.-P.F. Hsu, 1983: Stratospheric sudden coolings and the role of nonlinear wave interactions in preconditioning the circumpolar flow, J. Atmos. Sci., 40, 909-928.

Pittock, A.B., 1983: Solar variability, weather and climate: an update, Quart. J. R. Met. Soc., 109, 23-55.

Puri, K. and W. Bourke, 1974: Implications of horizontal resolution in spectral model integrations, Mon. Wea. Rev., 102, 333-347.

Ramanathan, V., 1976: Radiative transfer within the earth's troposphere and stratosphere: a simplified radiative convective model, J. Atmos. Sci., 33, 1330-1346.

Ramanathan, V., and W.L. Grose, 1978: A numerical simulation of seasonal stratospheric climate, Part I. Zonal thermal and dynamical structure, J. Atm. Sci., 35, 600-614.

Rao, K.S. and M.V.H. Nair, 1981: Possible linkage between atmospheric total ozone and solar magnetic sector boundary passage, J. Atmos. Terr. Phys., 43, 367-372.

Reagan, J.B., R.E. Meyerott, R.W. Nightingale, R.C. Gunton, R.G. Johnson, J.E. Evans, and W.L. Imhof, 1981: Effects of the August 1972 solar particle events on stratospheric ozone, J. Geophys. Res., 86, 1473-1494.

Reiter, R. and M. Litfass, 1977: Stratospheric-tropospheric exchange influenced by solar activity. Results of a 5-year study, Arch. Met. Geoph. Biokl. Ser. A, 26, 127-154.

Reiter, R., 1979: Influences of solar activity on the exchange intensity between the stratosphere and troposphere, in Solar-Terrestrial Influences on Weather and Climate, B.M. McCormac and T.A. Seliga, eds., D. Reidel, 289-296.

Robinson, W.A., 1985: A model of the wave 1-wave 2 vacillation in the stratosphere, J. Atmos. Sci., 42, 2289-2304.

Ruderman, M.A. and J.W. Chamberlain, 1975: Origin of the sunspot modulation of ozone: its implications for stratospheric NO injection, Planet. Space Sci., 23, 247-268.

Schoeberl, M.R. and M.A. Geller, 1977: A calculation of the structure of stationary planetary waves in winter, J. Atmos. Sci., 34, 1235-1255.

Schoeberl, M.R., 1978: Stratospheric warmings: observations and theory, Rev. Geophys. Sp. Phys., 6, 521-538.

Schoeberl, M.R. and D.F. Strobel, 1978: The response of the zonally averaged circulation to stratospheric ozone reductions, J. Atmos. Sci., 35, 1751-1757.

Schoeberl, M.R. and D.F. Strobel, 1980a: Numerical simulation of sudden stratospheric warming, J. Atmos. Sci., 37, 214-236.

Schoeberl, M.R. and D.F. Strobel, 1980b: Sudden stratospheric warmings forced by mountains, Geophys. Res. Lett., 7, 149-152.

Schoeberl, M.R., 1982: Vacillation, sudden warmings and potential enstrophy balance in the stratosphere, J. Atmos. Sci., 39, 1862-1872.

Schoeberl, M.R., D.F. Strobel, and J.P. Apruzese, 1983: A numerical model of gravity wave breaking and stress in the mesosphere, J. Geophys. Res., 88, 5249-5259.

Shah, G.N., 1981: Solar proton events and terrestrial weather, J. Atmos. Terr. Phys., 43, 147-150.

Smith, A.K., 1983a: Stationary waves in the winter stratosphere: seasonal and interannual variability, J. Atmos. Sci., 40, 245-261.

Smith, A.K., 1983b: Observation of wave-wave interactions in the stratosphere, J. Atmos. Sci., 40, 2484-2496.

Smith, A.K., J.C. Gille, and L.V. Lyjak, 1984: Wave-wave interactions in the stratosphere: observations during quiet and active wintertime periods, J. Geophys. Res., 89, 363-373.

Smith, A.K. and L.V. Lyjak, 1985: An observational estimate of gravity wave drag from the momentum balance in the middle atmosphere, J. Geophys. Res., 90, 2233-2241.

Solomon, S. and P.J. Crutzen, 1981: Analysis of the August 1972 solar proton event including chlorine chemistry, J. Geophys. Res., 86, 1140-1146.

Strobel, D.F., 1979: Parameterization of the thermal relaxation rate in the stratosphere, J. Geophys. Res., 84, 2469-2470.

Thorne, R.M., 1977: Influence of relativistic electron precipitation on the lower mesosphere and stratosphere, in Dynamical and Chemical Coupling between the Neutral and Ionized Atmospheres, B. Grandal and J. Holtet, eds., D. Reidel, p.161.

Thorne, R.M., 1980: The importance of energetic particle precipitation in the chemical composition of the middle atmosphere, Pageoph, 118, 128-151.

Trenberth, K., 1973: Global model of the general circulation of the atmosphere below 75 kilometers with an annual heating cycle, Mon. Wea. Rev., 101, 287-305.

Tung, K.K. and R.S. Lindzen, 1979: A theory of stationary long waves. Part II: Resonant Rossby waves in the presence of realistic vertical shears, Mon. Wea. Rev., 107, 735-750.

van Loon, H., R.L. Jenne, and K. Labitzke, 1973: Zonal harmonic standing waves, J. Geophys. Res., 78, 4463-4471.

Venne, D.E., G.D. Nastrom, and A.D. Belmont, 1982: Corrections to "Preliminary results on 27-day solar rotation variation in stratospheric zonal winds" by G.D. Nastrom and A.D. Belmont, Geophys. Res. Lett., 7, 759-760.

Wehrbein, W.M. and C.B. Leovy, 1982: An accurate radiative heating and cooling algorithm for use in a dynamical model of the middle atmosphere, J. Atmos. Sci., 39, 1532-1544.

Weinbeck, R.S. and D.N. Yarger, 1978: Relationship of atmospheric ozone profiles to solar magnetic activity, Pageoph, 116, 32-43.

Wescott, E.M., 1966: Magnetoconjugate phenomena, Space Sci. Rev., 5, 507-561.

Wilcox, J.M., P.H. Scherrer, L. Svalgaard, W.O. Roberts, R.H. Olson, R.L. Jenne, 1974: Influence of solar magnetic sector structure on terrestrial atmospheric vorticity, J. Atmos. Sci., 31, 581-588.

Willet, H.C., 1962: The relationship of total atmospheric ozone to the sunspot cycle, J. Geophys. Res., 67, 661-670.

Williams, R.G. and E.J. Gerety, 1978: Does the troposphere respond to day-to-day changes in solar magnetic field? Nature, 275, 200-201.

Williams, R.G., 1978: A study of the energetics of a particular sun-weather relation, Geophys. Res. Lett., 5, 519-522.

Williams, R.G. and E.J. Gerety, 1980: A further study of the tropospheric energetics of a particular sun-weather relation, J. Atmos. Terr. Phys., 42, 27-34.

Willis, D.M., 1976: The energetics of sun-weather relationships: magnetic processes, J. Atmos. Terr. Phys., 38, 685-698.

Wofsy, S. and M. McElroy, 1973: On vertical mixing in the upper stratosphere and lower mesosphere. J. Geophys. Res., 78, 2619-2624.

Wu, M.-F., 1973: Observations and analysis of trace constituents in the stratosphere, Annual Report, Contract DOT-05-20217, Environmental Res. Tech., Lexington, Mass.

Wu, M.-F., M.A. Geller, J.G. Olson, and M.E. Gelman, 1984: Tropospheric-stratospheric (surface-55 km) monthly general circulation statistics for the northern hemisphere- four year averages, NASA Technical Memorandum 86182, Goddard Space Flight Center, Greenbelt, Maryland, 129pp.

Zerefos, C.S., 1975: Circulation changes in the free atmosphere during proton events associated with Type IV radio bursts, Planet. Space Sci., 23, 1035-1043.